TECHNISCHE UNIVERSITÄT MÜNCHEN
Institut für Energietechnik

Lehrstuhl für Thermodynamik

Aspects of the Thermoacoustic Effect Considering Mean Flow

Tobias Holzinger

Vollständiger Abdruck der von der Fakultät für Maschinenwesen der Technischen Universität München zur Erlangung des akademischen Grades eines

DOKTOR – INGENIEURS

genehmigten Dissertation.

Vorsitzender:
Prof. Dr.-Ing. Oskar J. Haidn
Prüfer der Dissertation:
1. Univ.-Prof. Wolfgang Polifke, Ph.D. (CCNY)
2. Prof. Sjoerd S.W. Rienstra, Ph.D.
TU Eindhoven/ Niederlande

Die Dissertation wurde am 03.04.2013 bei der Technischen Universität München eingereicht und durch die Fakultät für Maschinenwesen am 25.06.2013 angenommen.

Ein Wiesel
saß auf einem Kiesel
inmitten Bachgeriesel.

Wißt ihr
weshalb?

Das Mondkalb
verriet es mir
im Stillen:

Das raffinier-
te Tier
tat's um des Reimes willen.

Christian Morgenstern

Vorwort

Die vorliegende Arbeit entstand am Lehrstuhl für Thermodynamik der Technischen Universität München im Rahmen meiner sechs jährigen Anstellung als akademischer Rat. Die Forschungsarbeit in diesem Zeitraum setzte sich zum Ziel selbst erregte Pulsationen an einem Wärmetauscher mit Hilfe des thermoakustischen Effekts zu erzeugen, um damit dessen Wärmeübertragung zu verbessern. Aus diesem Forschungsvorhaben kristallisierte sich die verbesserte eindimensionale Modellierung der Wechselwirkung zwischen mittlerer Strömung und thermoakustischen Grenzschichtphänomenen als wissenschaftlich besonders interessanter Aspekt heraus. Ihre Formulierung und Validierung gegen numerische und experimentelle Daten stellen den Kern dieser Doktorarbeit dar.

Um dieses Thema umfassend in dieser Promotion münden zu lassen, war die tatkräftige Unterstützung vieler Personen notwendig.

Vor allen gilt mein Dank meinem Doktorvater, Prof. Wolfgang Polifke, Ph.D., der mich über die gesamte Zeit mit kreativen fachlichen Anregungen und kritischen Fragen bei meinen Forschungen voranbrachte. Die Möglichkeit dabei meinen eigenen Weg zu gehen, ohne äußeren Restriktionen ausgesetzt zu sein, erlaubte mir auch auf unorthodoxe Herangehensweisen an das Thema zurückzugreifen. Seine große Spontanität sorgte dafür, dass nie Eintönigkeit aufkam.

Für die Chance, diese Arbeit kurzfristig mündlich verteidigen zu können bin ich dem Vorsitzenden der Kommission Prof. Dr.-Ing. Oskar J. Haidn und meinem Zweitprüfer Prof. Sjoerd W. Rienstra, Ph.D. zu Dank verpflichtet. Hier geht auch ein besonderer Dank an Frau Helga Basset. Ohne Ihre straffe Organisation wäre der Zeitplan nicht umsetzbar gewesen.

Neben den Herren Ralf Blumenthal und Christoph Jörg bin ich vor allem Frau Indu Sujith dankbar, dass sie es mir ermöglichte diese Arbeit in englischer Sprache abzufassen.

Die Bearbeitung des Forschungsthemas mit analytischen, numerischen und experimentellen Methoden wäre ohne die tatkräftige Unterstützung

vieler Studenten nicht möglich gewesen. Besonders möchte ich dabei die Arbeiten von Armin Baumgartner und Maximilian Sperling hervorheben, die die Erkenntnisse auf den Gebieten der eindimensionalen Modellierung und der numerischen Validierung besonders vorantreiben konnten.

Die Betreuung des Hochschulpraktikums "Grundlagen numerischer Simulation" bereitete mir stets große Freude. Dies lag nicht zuletzt an der großartigen Unterstützung durch Tutoren, die mir dabei halfen das Praktikum für die Teilnehmer stets kurzweilig zu gestalten.

Die positivste Erfahrung im Rahmen dieser Arbeit war die gegenseitige Unterstützung unter den Doktoranden. Für die großartige Hilfe bei großen und kleinen Problemen danke ich stellvertretend für alle nicht Genannten Klaus Mösl, Martin Hauser, Christoph Mayer, Volker Kaufmann, Daniel Morgenweck, Alejandro Cardenas und Johannes Weinzierl.

Diese Arbeit steht am Ende eines langen Ausbildungsweges. Dies wäre ohne die Unterstützung meiner Eltern undenkbar gewesen.

Zu guter Letzt gilt mein Dank meiner Frau Sandra und meinen Kindern Gabriel und Magdalena. Die geopferte Freizeit, die ich nicht mit ihnen sondern der Anfertigung dieser Dissertation verbracht habe, hätte ich lieber ihnen gewidmet. Ich danke ihnen von Herzen für ihr Verständnis und die abgenommene Last, die vor allem meine Frau für mich getragen hat.

München, im August 2013 Tobias Holzinger

Kurzfassung

Der weltweit steigende Energiebedarf und die strikter werdenden Anforderungen an die bei der Aufbereitung entstehenden Emissionen eröffnet die Nachfrage nach alternativen Ansätzen der Energiewandlung. Der Phasenversatz akustischer Schwankungsgrößen im Einflußbereich der thermischen und viskosen akustischen Grenzschicht erlaubt eine effiziente, teils reversible Umwandlung von Wärme in akustische Energie. Das Zusammenspiel mit den geringen treibenden Temperaturgefällen, die für diesen Prozess notwendig sind, führt zu einem gesteigerten Interesse, diesen Effekt kommerziell nutzbar zu machen. Die Wechselwirkung der zugrunde liegenden Mechanismen mit einer Grundströmung sind bis heute aber nur teilweise verstanden. Deshalb fokussieren sich bisherige Forschungen auf das Gebiet undurchströmter thermoakustischer Anlagen. Viele Technologien, für die ein Einsatz solcher Wandler denkbar wäre, gehen jedoch mit eben solchen Grundströmungen einher. Deshalb setzt sich diese Arbeit zum Ziel, für ein tieferes Verständnis der Interaktion zwischen mittlerem Strömungsfeld und thermoakustischer Energiewandlung zu sorgen. Ein eigens analytisch hergeleitetes, quasi eindimensionales Modell erlaubt eine Vorhersage des akustischen Übertragungsverhaltens. Die Validierung dieses Modells und der, zur Schließung des Gleichungssystems enthaltenen Modellierungsansätze erfolgt gegen generierte Vergleichsdaten aus CFD Simulationen und experimentellen Messungen. Die Ergebnisse dieser Arbeit ermöglichen einen tieferen Einblick in die thermoakustische Energiewandlung unter dem Einfluss mittlerer Strömung. Das validierte Vorhersagemodell erleichtert die Bestimmung optimaler Bedingungen für zukünftige durchströmte thermoakustische Anwendungen.

Abstract

The rising global demand for energy coinciding with increasingly stringent requirements for emissions, opens the field for alternative energy conversion processes. The phase lag of acoustic fluctuating quantities in the vicinity of the thermal and viscous acoustic boundary layer facilitates an efficient transformation of heat to acoustic power and vice versa. As the involved mechanisms come along with low thermal driving ratios, there is an increased interest in utilizing this effect in commercial applications. The interaction of this thermoacoustic conversion mechanism with mean flow is barely understood and hence no proper modeling approaches exist. Thus, the research activity is mostly restricted to thermoacoustic apparatuses operating in quiescent environment. Many technologies with a conceivable application of such converters are inherently employing mean flow. This thesis aims at providing a deeper understanding of the interaction of thermoacoustic boundary layer effects and mean flow. A quasi one-dimensional predictive model is derived analytically. This model is validated against both CFD data and experimental measurement accomplished in this study. Generating a deeper insight into the interaction of thermoacoustic energy conversion and providing an improved low-order modeling tool, this thesis facilitates the identification of an optimum combination of thermoacoustic energy conversion and mean flow conditions.

Contents

List of Figures

List of Tables

1 Introduction

Energy has been a perennial topic since the beginning of the industrial revolution in the 18th century. From that time on its worldwide demand has risen steadily. Today, especially emerging markets and developing countries insist on a rising amount of resources for domestic and industrial use. This trend will lead to increasing environmental problems that have to be faced. The industrial nations tackle this problem by forcing their industry to reduce their CO_2 equivalent by self-dictated restrictions. Consequently, the interest in efficient energy conversion has been a current topic in research activity in the recent decades. Traditional energy conversion techniques have been exploited up to their efficiency limits. Hence, the investigation of less common methods becomes more and more interesting for special applications like waste heat recovery or efficient cooling.

Thermoacoustic (TA) boundary layer interaction causes energy conversion effects that can be exploited in both power generation and thermal management. This type of energy conversion combines positive aspects, such as theoretical high efficiency and low maintenance costs because of the absence of moving parts and low minimum driving levels. These promising issues have pushed the research activity in TAs over almost three decades. They have yielded, among other innovations, analytical descriptions of the effect. However, the performance of the technology achieved in practice is still far from the theoretical potential. Additional research effort is needed to improve the applicability of this form of energy conversion.

Existing analytical formalisms that describe this mechanism are based on simplifications and hence do not account for several technically inevitable effects. One of the most restricting assumptions is ignoring the mean flow impact on acoustic transport inside TA regenerators. The goal of this study is to expand the understanding of the influence of mean flow on TA boundary layer interaction, focusing on the transmission and

back scattering of acoustic waves in components experiencing such conditions. Analytical considerations yield a fast quasi one-dimensional prediction tool for future technical applications. This approach is validated against numerical and experimental results obtained for a generic problem.

The research field of thermoacoustics focuses on effects that originate from thermal and acoustic background. The most common topic is the investigation of the energy feedback between acoustics and heat release in systems containing enclosed flames. Apart from this undesired effect this thesis treats a research topic that handles a deliberate coupling of thermal and acoustic mechanisms. In modern literature this effect is more and more referred to as "*the thermoacoustic (TA) effect*" [77, 115, 174], which causes a transformation from acoustic power into steady state heat flux in the vicinity of rigid walls or vice versa.

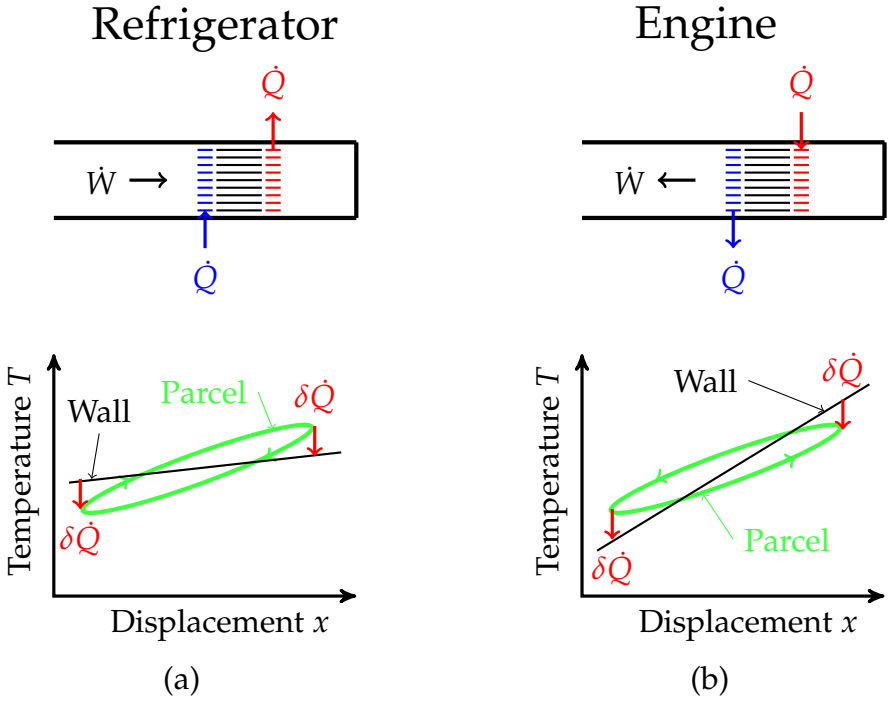

Figure 1.1: Operating types of TA applications: If the change in fluid parcel temperature over its displacement is larger than the temperature change in the solid part of a stack a) heat is transported against the natural gradient. This situation is called a TA refrigerator or heat pump. If the situation is contrary b) the oscillation of the fluid parcel is amplified. Such applications are known as TA engines.

The most simple TA apparatus consists of a module of two heat exchangers adjacent to a porous media – so called stacks or regenerators – which are located near the closed end of a wide duct. The two sketches displayed in the top part of Figure 1.1 depict the energy transport for both configurations. If heat $\dot{Q}$ is pumped from a cold region to a hot reservoir (Fig. 1.1a), acoustic power $\dot{W}$ has to be fed into the system. Depending on the application, apparatuses employing this kind of energy conversion are distinguished as TA "refrigerators" or "heat pumps" [60]. If the TA energy conversion process is reverted (Fig. 1.1b), a part of $\dot{Q}$ being transported from the hot to the cold reservoir is converted into $\dot{W}$. As acoustic power is generated, such systems are referred to as "TA engines" and "prime movers".

An intuitive explanation of the TA effect can be given by an idealized consideration of a fluid volume parcel oscillating inside a part of the porous media, which for simplicity is modeled as a channel of constant height. Acoustic perturbations in gases at stagnant conditions usually lead to reversible, isentropic changes of thermodynamic state. In wide ducts the adiabatic compression and expansion of a fluid parcel cause an oscillatory displacement in axial direction, which coincides with an acoustic temperature fluctuation T_1. With decreasing duct diameter this fluctuation is affected by the local temperature of the solid wall. In the vicinity of the wall the temperature undergoes a cycle, which is sketched by the green ellipses in the lower part of Figure 1.1. When traveling towards larger x-values, the compression due to the increasing acoustic pressure p_1 causes an increase in T_1. If the local temperature of the wall is lower than the actual fluid parcel value, heat is transfered to the wall, which is rejected when the parcel travels in negative x-direction. Hence the fluid transports a certain amount of heat in the direction opposite to the axial temperature gradient of the wall. Using parts of the acoustic power of the fluid, heat is pumped from a cold to a hot reservoir. This is shown in the top part of Figure 1.1a. The effect is reversed when the mean temperature gradient $\partial T_0/\partial x$ is steeper than the gradient experienced by the fluid parcel. In the configuration displayed in Figure 1.1b a part of the heat flux is converted into acoustic power, which may lead to an acoustic instability.

If mean flow affects the oscillation of the volume parcel, the thermodynamic cycle it undergoes is no more closed. As long as the displacement caused by the mean velocity u_0 is much smaller than the oscillatory counterpart, the system still performs at similar conditions. When $u_0 > u_1$ is reached not only the mean field conditions change, but also the changes of state cannot be described by the idealized consideration presented above. Furthermore, the analytical models which are derived for stagnant mean flow conditions are no more valid. Thus these models have to be adapted to non-zero mean flow conditions.

1.1 Thermoacoustic Applications

The theoretically high conversion efficiency of such processes produced a large variety of ideas for its possible technical applications. However, the technical efficiencies achieved so far are not at all competitive with

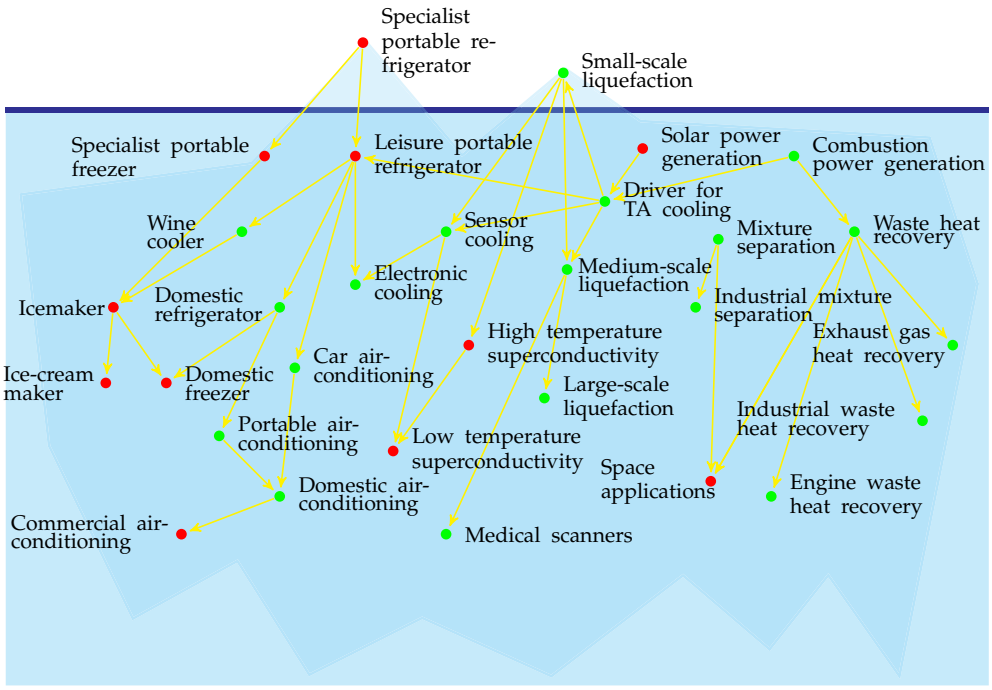

Figure 1.2: Applicability of mean flow thermoacoustics in future TA applications. The figure of the thermoacoustic iceberg is based on the sketch of Altenborkum [8] and extended to TA engine applications. The green dots denote potential applicability of mean flow affected thermoacoustics and hence the quasi one-dimensional models developed in this thesis.

established energy conversion processes of heat engines and cooling devices. This ongoing challenge led to an analogy presented in 2008 [8]. It visualizes the commercial applicability of existing and future TA applications by comparing the research field to an iceberg of which only a small part is lifted above the surface. In Figure 1.2 Altenborkum's [8] sketch[1] is expanded for applications using the TA effect in engine operation mode. The "water surface" separates the commercially provided applications from ideas for technical devices and research activities. Using the iceberg analogy, it has to be stated that most of the research field is below the water level. Besides special refrigeration applications only small-scale liquefaction concepts like the QDrive cryocooler [33] depicted in Figure 1.3 are established, because of the advantage of avoiding solidification problems by the absence of moving parts. Other technical devices are either not competitive to current applied technologies in the corresponding activity field or in an early stage of development.

The arrangement of the items depicted in Figure 1.2 is also a part of the iceberg analogy. Items located at greater "depths" are expected to need longer time spans of development before being ready for the market. The

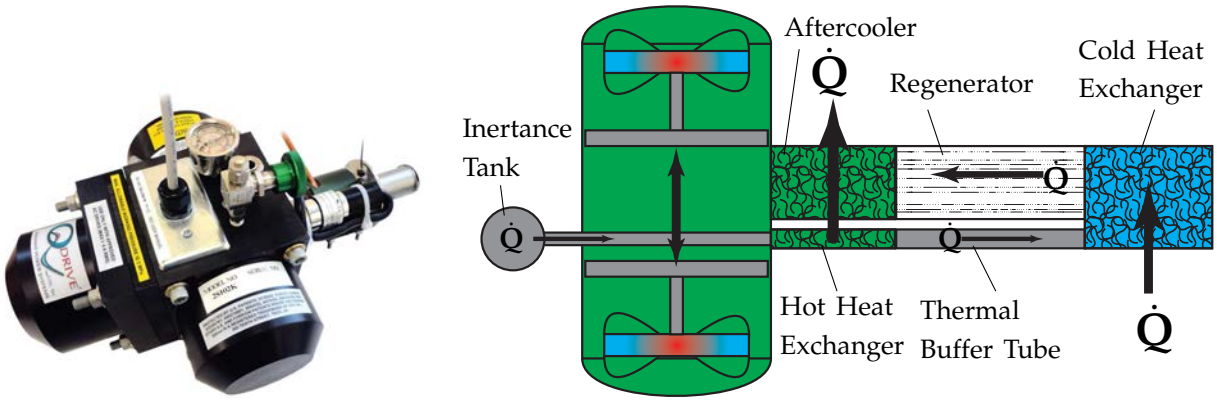

Figure 1.3: The QDrive Cryocooler: One of the few established products applying TA energy conversion technology [33]. It reaches up to 50 K cooling temperature.

[1] This is secondary literature: Altenborkum [8] gives reference to the original source of his figure. As the citation is incomplete, this original publication could not be found. He refers to *Clever Fellows Innovation Consortium, 2003*.

yellow arrays give an idea of the evolution steps that have to be processed before certain devices could reach their break-through.

For example the generation of acoustic power from a biomass combustor with the aim of developing a stove with a stand-alone source for electrical power is an ongoing project [34, 119]. If the production costs per apparatus are reduced by half, the project denoted as SCORE [162] is ripe for the market. The same accounts for waste heat recovery systems which have already been mounted as prototypes to small industrial applications [43].

On the bottom of the iceberg medical scanners are listed. The application of TA tomography [98] is an alternative to technologies using ultrasonic sound. Although the mathematical theory is fully provided [99], further research activity is needed to make this technology competitive to existing technologies. Further as TA liquefaction plays a certain role in this technology, a stable medium-scale liquefaction should be established on the market first. Therefore, TA tomography is far away from being used commercially.

The huge discrepancy between the number of commercially established and theoretically conceivable TA devices shows the long way TA research still has to go. The wide range of the applicability of the TA technology provides space for promising niche applications.

One area investigated only in a cursory manner is the application of TA energy conversion in combination with mean flow. Existing ideas mainly focus on stagnant mean flow conditions. In many applications the large oscillations at operating conditions cause undesired streaming effects which limit the efficiency of many devices. Some of the topics listed in Figure 1.2 are related to mean flow effects. The green dots indicate fields of research where non-stagnant conditions may either occur or can even be used beneficially. TA mixture separation only works if the products can be transported towards the separation device. Thus a certain mean flow inside such applications occurs necessarily. Car air-conditioning and exhaust gas heat recovery are also linked to convection dominated energy flux. Under certain circumstances, a direct coupling of the gas stream with TA energy conversion in the latter example may

lead to an extra conversion of heat and hence an increase in efficiency of the device.

A further conceivable application is the recovery of heat at very low exergy levels. The recuperation from waste heat is often restricted by global design parameters of higher priority. Sometimes huge losses are tolerated as long as the energy is at least partially recovered. Especially if the driving temperature difference reaches low values the residual heat is hard to recover economically by common techniques. This also accounts for almost all existing technical and experimental TA setups that deal with fluids at rest, because of the indirect heat supply. If the TA energy conversion process could be established directly inside the mean flow dominated enthalpy flux, this direct heating might lead to an economically interesting application.

Empirical experiences show that mean flow affects the TA energy conversion in a negative way. The ”blow-off” of the necessary temperature gradient and turbulence effects can even kill the desired energy transformation effect. Due to the lack of experimental data, numerical investigation and consequently analytical modeling of mean flow affected configurations, the prediction of the impact of mean flow on the TA energy conversion is rather inaccurate. Mean flow effects are not fully taken into account in the low-order models used for the design of TA devices. This thesis provides information about the acoustic transfer at non-zero mean flow conditions obtained from both fields numerical simulations and experimental measurements. It further demonstrates the derivation of an improved semi-analytical low-order model to predict the operating conditions of such processes. These findings form a scientific basis for future technical TA applications including mean flow.

1.2 Thermodynamic Cycles of Thermoacoustic Energy Conversion

So far, using Figure 1.1, the basic mechanism of TA energy conversion was explained. Following this consideration allows for a differentiation of TA applications in apparatuses consuming or generating acoustic

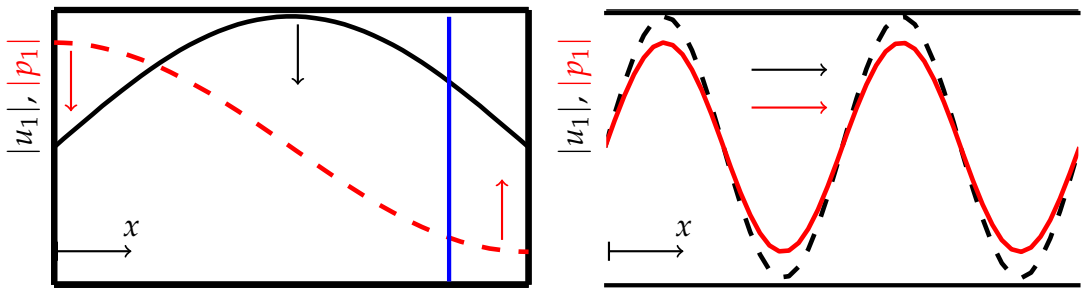

(a) (b)

Figure 1.4: a) Standing vs. b) traveling wave conditions. In contrast to synchronized oscillations of p_1 and u_1 at traveling wave conditions, standing waves are characterized by a phase shift of $\pm\frac{\pi}{2}$.

power. This section provides a more detailed explanation by considering the idealized thermodynamic cycles of the volume parcel followed in the lower part of Figure 1.1. The separation into engines and prime movers of devices generating acoustic power originates from the idealized cycle they are considered to operate at.

The spatial distribution of the $p_1(x)$ and $u_1(x)$ depicted in Figure 1.4a is typical for TA engines. This situation denoted as standing wave conditions is characterized by a phase shift of $\pm\frac{\pi}{2}$ of the complex-valued acoustic pressure p_1 and velocity u_1 fluctuations. The thermodynamic cycle that accounts for devices exposed to standing wave conditions is approximated by a Joule cycle [207]. Apart from the difference in heat addition – heat transfer vs. internal heat release – gas turbine engines are approximated by a similar thermodynamic cycle[2] [120]. These standing wave conditions describe a physical limit the real acoustic field inside a TA device never experiences.

The opposite limit in terms of acoustic conditions is described by traveling wave conditions. Figure 1.4b displays the in-phase spatial propagation of $p_1(x)$ and $u_1(x)$ inside a TA device. The thermodynamic cycle caused by such acoustic conditions is idealized by a Stirling cycle [31, 207]. This is the reason why TA prime movers are often denoted by

[2] Strictly speaking this thermodynamic cycle is called Brayton cycle [121].

TA Stirling engines. Sometimes such devices are also called “traveling wave engines”.

Neither of these two operating conditions are reached in TA applications. As they form the limit conditions an oscillating which a volume parcel experiences, investigating it under these two idealized conditions leads to a deeper qualitative insight to TA energy conversion. In the next two sections we follow such a parcel located in the region marked by the blue line in Figure 1.4 for both limit conditions. In order to make the investigation more intuitive, the changes of displacement, acoustic pressure p_1 and acoustic velocity u_1 of the parcel are idealized by square wave signals. Here we focus on acoustic power generation, i.e. TA engine and heat pump applications. The same ideas can be applied to the consideration of acoustic power consumption. If so, the inverse temperature differences to the wall cause a change in the direction of the fluxes of heat and power.

1.2.1 Standing Wave Thermoacoustics

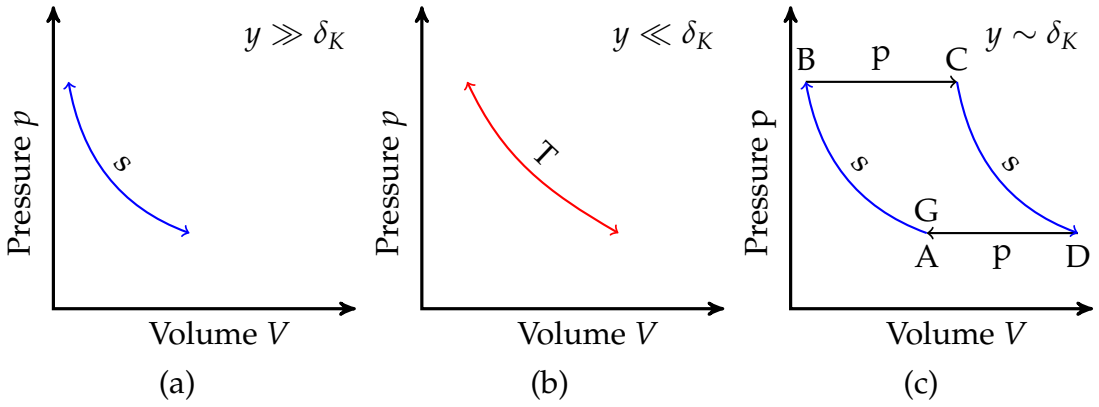

Figure 1.5: $p - V$ diagrams of a standing wave fluid element near a non-isothermal wall. a) Far away from the wall the element experiences isentropic compression and expansion. b) For very small distances the parcel is thermally coupled to the wall and thus is subject to isothermal changes of state. c) For non-perfect thermal contact a phase delay causes isobaric heating and cooling.

As shown in the introduction, the interaction between the fluid and the solid wall is crucial for TA energy conversion. The length scales characterizing this problem are the viscous acoustic penetration depth

$$\delta_\nu = \sqrt{\frac{2\nu}{\omega}} \tag{1.1}$$

and thermal acoustic penetration depth

$$\delta_K = \sqrt{\frac{2K}{\omega c_p \varrho_0}}. \tag{1.2}$$

Both quantities scale with the inverse square root of angular frequency ω and the material properties of the fluid. The viscous acoustic penetration depth δ_ν depends on the kinematic viscosity ν. The fraction of thermal conductivity K and the product of specific capacity of heat c_p and mean density ϱ_0 is denoted as thermal diffusivity and forms the equivalent for the thermal penetration depth δ_K. Here, we consider the ratio of the distance y between the volume parcel and the wall to the thermal penetration depth δ_K as the measure allowing for a classification into three different situations:

$y \gg \delta_K$: General acoustics deals with parcels that are not affected by the wall. Due to the poor contact to the wall, the isentropic change of state of the parcel is not affected by the solid temperature. The blue line(s) in the $p - v$ diagram presented in Figure 1.5a depicts all acoustic states such a parcel experiences. As no area is enclosed by the changes of state, acoustic energy is neither consumed nor generated.

$y \ll \delta_K$: The fluid parcel is in perfect thermal contact to the wall. Hence, the compression it experiences when being displaced towards higher acoustic pressure at larger x-values leads to a simultaneous heating. The hotter solid wall passes heat to the fluid parcel at lower temperature. When the parcel travels in the opposite direction, it is cooled while it expands to the lower acoustic pressure at its original position. Figure 1.5a displays the thermodynamic states of such a parcel in terms of a red line (T). Again, they form a line which is insufficient for energy conversion. Like parcels the

first situation, this change of state is not restricted to the region near the blue line depicted in Figure 1.4a.

$y \approx \delta_K$: The thermal contact of the fluid volume to the corresponding wall location is imperfect. This causes a time delay between the expansion/compression and the addition/subtraction of heat by the solid wall. If a parcel located right of the blue line in Figure 1.4a is exposed to a positive axial mean temperature gradient, the pressure fluctuation is larger than the velocity counterpart. This leads to small but non-negligible axial movements of the parcel that are in phase with the pressure oscillation. During one oscillation period it experiences a four step process that is displayed in Figure 1.5. Additionally the location, volume and temperature of the parcel is visualized in the left column of Figure 1.6:

1. The parcel is compressed (A $\rightarrow$ B) while being displaced towards higher pressure.
2. If acoustic power is generated, the hot wall at this location heats ($\delta Q_1 > 0$) the parcel (B $\rightarrow$ C). In addition the change in volume does work at the system ($\delta W_1 < 0$).
3. Next, the parcel expands while being displaced towards its original position (C $\rightarrow$ D).
4. Finally it is cooled (D $\rightarrow$ A) to its original state ($\delta Q_1 < 0$) while work is freed $\delta W_2 < 0$.

This thermodynamic cycle is known as Joule cycle [207]. As the imperfect thermal contact is crucial for the energy conversion process, TA devices operating with this cycle use porous media with hydraulic radii R larger than the thermal penetration depth δ_K.

1.2.2 Traveling Wave Thermoacoustics

The characteristic thermodynamic cycle a traveling wave engines is operating with is shown in Figure 1.7. Additionally the parcel with perfect thermal wall contact $\delta_K \ll y$ is sketched on the right column of Figure 1.6. In contrast to the phase shift of $\pi/2$ between acoustic pressure and velocity in a standing wave application, the acoustic variables oscillate simul-

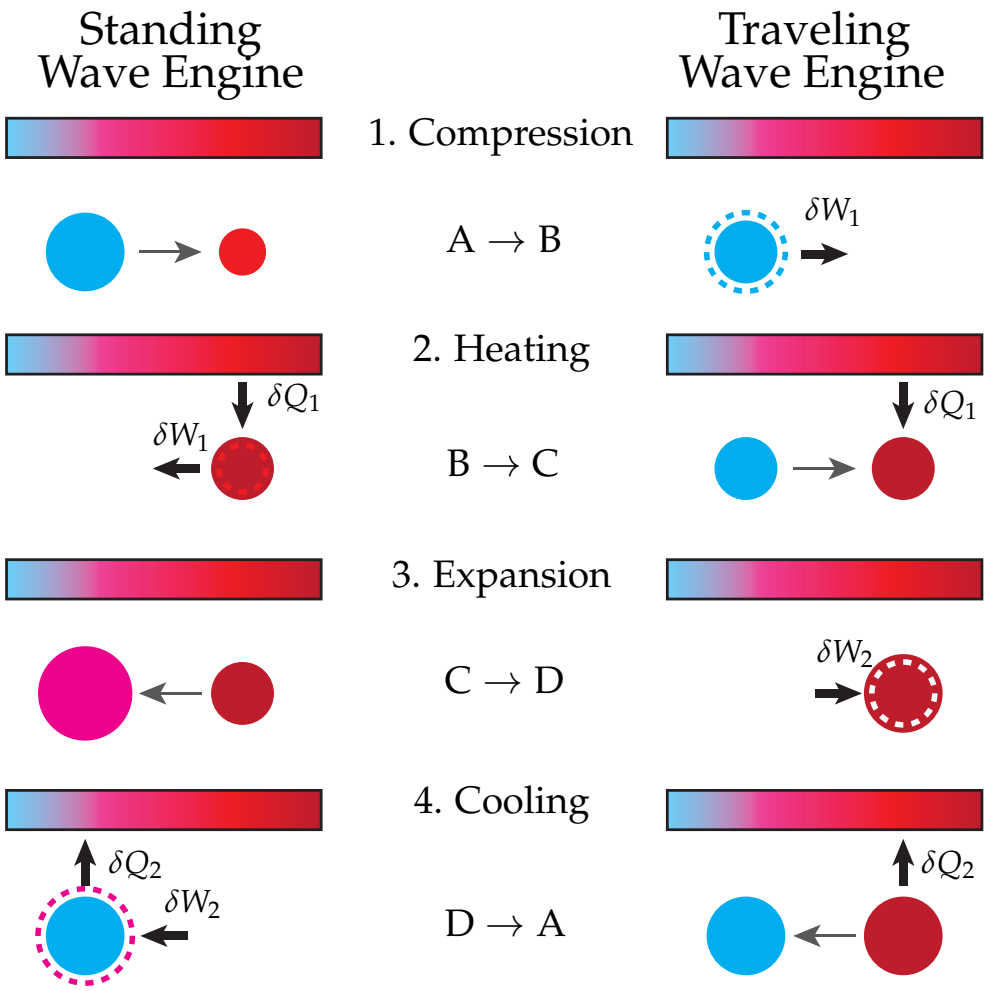

Figure 1.6: Idealized thermodynamic states of a volume parcel inside a stack of a standing wave (left) and a traveling wave engine (right). If heat pumps are considered, the input and output of power and heat fluxes in step 2. and 4. are reversed.

taneously. Hence, the thermodynamic cycle does not depend on its axial location. As the velocity is per definition the time derivative of the parcel displacement, the compression/expansion process is decoupled from the movement of the parcel. This phase shift of the acoustic quantities changes the cycle the parcel undergoes:

1. As the parcel does not move when the acoustic pressure rises, it is compressed (A $\rightarrow$ B) under isothermal conditions (T) while doing work on the parcel ($\delta W_1 > 0$).

2. Due to the perfect thermal contact to the wall, the parcel is displaced at constant volume, following the temperature of the solid wall. This

isochoric change of state causes an input of heat ($\delta Q_1 > 0$) into the parcel.

3. In the maximum positive deflection, the parcel expands (C $\rightarrow$ D) keeping the temperature of the wall. Mechanic power ($\delta W_2 < 0$) is freed by the fluid volume.

4. When it travels back to the negative point of deflection (D $\rightarrow$ A) leads to a heat release ($\delta Q_1 < 0$) into the wall.

1 This clockwise Stirling like process of a traveling wave engine acts ideally with Carnot's efficiency

$$\xi_{\text{Stirling}} = 1 - \frac{T_{\text{cold}}}{T_{\text{hot}}}. \tag{1.3}$$

As TA prime movers do not require an imperfect wall contact, they typically operate at $R \ll \delta_K$. In comparison to this theoretically high efficiency, the standing wave Joule cycle yields a lower performance

$$\xi_{\text{Jou}} < \xi_{\text{Stirling}}. \tag{1.4}$$

For both cases, standing and traveling wave, the acoustic displacement is small with respect to the geometrical length of the wall. However, even if a single parcel transports heat or acoustic power over a very small distance, the train of adjacent elements shifts this small amount of energy along the entire range of the temperature gradient. Analogous to water

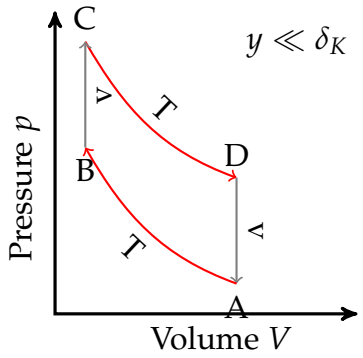

Figure 1.7: $p - V$ diagram of a traveling wave fluid element in the vicinity of a solid wall with imposed temperature gradient. The thermodynamic cycle of a parcel with perfect wall contact is considered to be of the Stirling type.

buckets being passed from person to person to bridge the distance from a well to the scene of fire, this effect is referred to as bucket-brigading.

These idealized considerations are only valid for stagnant flow conditions. As soon as mean flow is present, the fluid parcel does not return to the initial condition after one loop. In his Ph. D. thesis [158], Reid provides an improved idealized condition for moderate mean flow condition. If the mean velocity increases to small values, the original ellipses in Figure 1.1 degenerate toward spirals that propagate along the mean flow gradient. Only as long as the mean velocity u_0 is that low, it affects the mean flow field and does not interfere directly with acoustic propagation. While isobaric heat exchange in the standing wave cycle seems to be quite unaffected by this effect, the expansion and compression process in the traveling wave configuration are no longer isothermal. Therefore, the thermodynamic cycle of the latter is expected to be affected more strongly by mean flow effects.

Using the model of Reid, the impact of mean flow is accounted for by solving a convection/diffusion equation for the cross-sectionally averaged mean flow temperature $\langle T_0 \rangle (x)$. A solution for such a problem with constant material properties has an exponential shape. With increasing Peclet number Pe of the mean flow field, the narrow geometry consists of a larger region at approximately uniform temperature. Here, the thermoacoustic energy conversion is clearly in the heat pumping regime. The rest of the duct is dominated by large mean temperature gradients. As these gradients $\partial T_0(x)/\partial x$ lead to higher acoustic power production, this part annihilates at least a part of the first conversion from power to heat. The integral impact of this combination on the acoustic propagation has not been investigated so far.

In technical applications the temperature profile is not fixed by boundary conditions of the first kind. Thus using similar heat exchangers, parts of the steep profile are shifted inside the heat exchanger and do not cause TA interaction. Furthermore, mean flow leads to the formation of shear layers. They especially form at the in- and outlet of the duct and are not accounted for in the scope of this thesis. These shear layers interact with acoustic propagation in a dissipative way. The impact of mean flow inside the duct is partially accounted for in later investigations in

this thesis. It will be shown that the transversal mean velocity profile plays a minor role for the acoustic propagation in the cases. Summarizing the ideas of possible mean flow impact on TA energy conversion, no benefiting effect can be identified. Technical applications also could not generate conditions that improve the basic mechanism. Wherever mean flow occurs, the efficiency of the device is reduced.

1.3 Thermoacoustic Stacks and Regenerators

The simplified explanation of the TA energy conversion presented in the last sections reveals the main requirement for the technical segment of TA energy conversion. Both traveling and standing wave conversion cy-

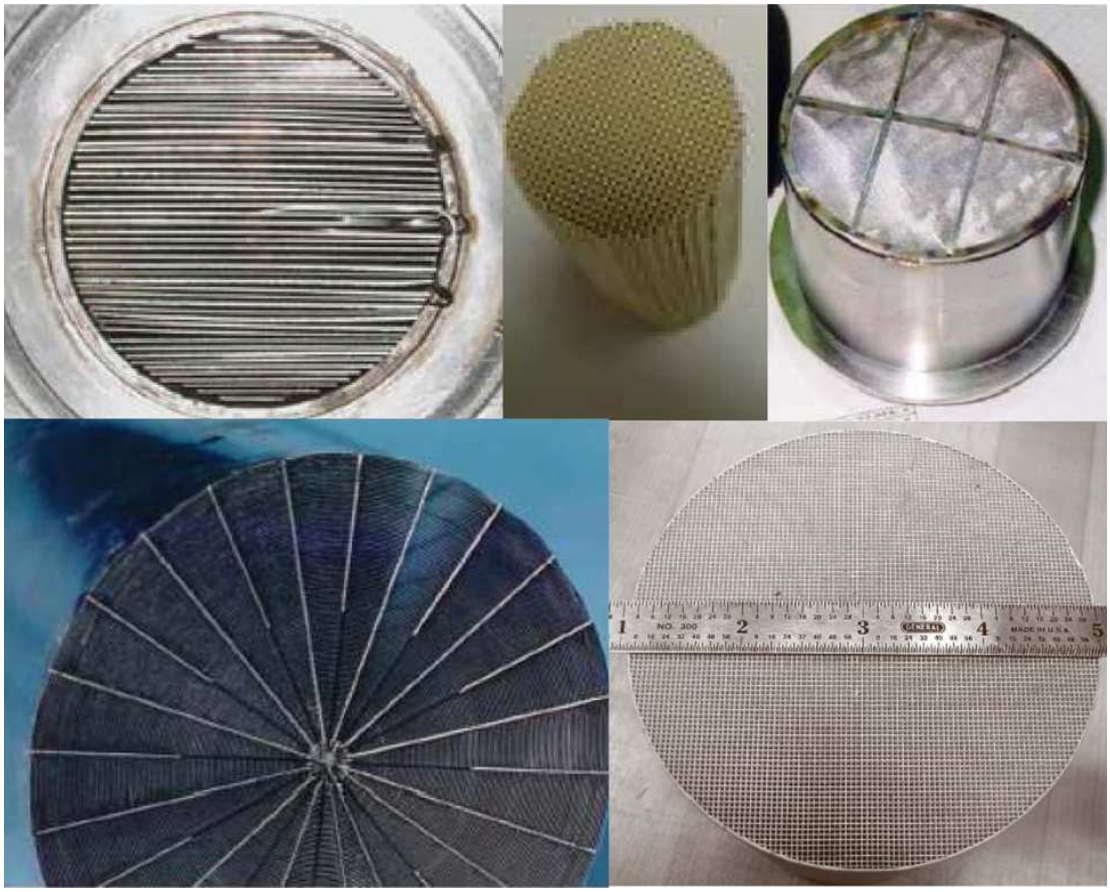

Figure 1.8: Pictures of some stacks and regenerator components [21, 140, 153, 163]. Mesh screens, slab plates, rectangular and circular pores of metal or ceramic material are most commonly used.

cles are characterized by the thermal acoustic boundary layer thickness. The hydraulic radius R of the selected component has to be at least of a similar order of magnitude as δ_K. As this geometric restriction leads to small amounts of power per pore, an efficient application of the effect implies a parallel utilization of such components. A wide variety of materials and forms were proposed by different authors; some are shown in Figure 1.8. Thermally low charged devices often operate with bundles of plastic pipes or packages of equally spaced plates [16]. Most of the applications use a slab-shaped pore geometry or other simple shapes such as bundles of circular [184] or rectangular pipes [158]. Besides these regular shaped geometries, arbitrary porous media with similar average pore diameters also support the TA effect and can even be modeled analytically [105]. Due to their wider thermal stability, copper [71], stainless steel [15] or ceramic based [212] devices are utilized in applications with high temperature differences. As long as the Lautrec number

$$\mathrm{La} = \frac{R_h}{\delta_K}, \tag{1.5}$$

i.e. the ratio of hydraulic to acoustic length scale, is of the order of unity or smaller, the pore shape can be chosen arbitrarily. For example, steel wool [2] and even rice [129] were used for the energy conversion.

TA standing wave devices typically operate with porous media with $1 < \mathrm{La} < 10$. In the literature they are denoted as *stacks*, as their first prototypes consisted of stacks of parallel plates. As explained in the previous section, the fluid outside the thermal boundary layer of traveling wave applications does not contribute to the energy conversion. Therefore a Lautrec number of $\mathrm{La} < 1$ is required for this operation mode. The idealized Stirling cycle suggests a direct comparison to the homonymous type piston engines. Thus, the heat conversion unit is called *regenerator*. Nevertheless these various denominations describe the same component and, depending on the operating frequency and the acoustic state, even identical components are referred to by different wordings. In this work the acoustic scattering behavior of these components is investigated. This means the transmitted and back scattered components are related to the incident acoustic waves. In general this is a frequency dependent problem. As this thesis does not distinguish frequency ranges, regenerator and stack are used as synonyms here.

1.4 Thesis Overview

The knowledge about thermoacoustic energy conversion in mean flow affected pores, investigated only fleetingly so far, is improved by providing data sets and analytical prediction tools for this combination. The conversion performance of mean flow affected devices in all hitherto investigated configurations always decreased with increasing Mach number. High Peclet numbers Pe cause an reduction of the axial temperature gradient inside the regenerators. The change in mean temperature is shifted towards the heat exchanger. No driving mean temperature gradient in the pore establishes and the TA energy conversion breaks down. High pore Reynolds numbers Re lead to turbulent perturbations and therewith distortion or deterioration of both acoustic boundary layers. Thus, researchers with the focus on constructing high efficient devices, which are particularly based on TA energy conversion, always concentrate on suppressing turbulent effects. Designing economically reasonable applications operating in this regime requires a detailed knowledge of the interaction of the TA effect and non-stagnant mean conditions. Improving this understanding demands a universal approach. Thus, the thesis is structured in an analytical, numerical and experimental investigation of one generic reference configuration.

Chapter 2 briefly reviews the literature published on TA boundary layer interaction. Starting from its discovery, the analytical, numerical and experimental developments are presented. It focuses on publications which either contribute to the general understanding of TAs or provide information on mean flow affected devices. The problem considered in this thesis is presented based on the investigation techniques applied.

The investigations processed in the main part of this thesis demand some theoretical background. These include the basics of fluid dynamics, thermodynamics and acoustics. Their fundamental equations are provided in Chapter 3. The theory of the latter topic is treated in detail. The description of technical components in terms of acoustic multi-ports, their transmission behavior and instability potentiality (IP), a newly derived acoustic power balance criterion, is explained by simple configurations. The chapter finally presents the derivation of a Green's function (GF) for

a form of ordinary differential equation that is encountered in subsequent chapters.

The interaction of thermoacoustic energy conversion and mean flow is treated theoretically in Chapter 4. The scope of this chapter is to provide a quasi one-dimensional set of differential equations that describe such configurations with higher accuracy than previous methods. The new approach extends the formulation found by Peter in't panhuis [82] using the same derivation strategy. At first, the fluid transport equations accounting for viscous friction and thermal diffusion are non-dimensionalized using characteristic parameters from boundary layer theory. In a second step the resulting equations experience a series expansion in terms of acoustic Mach number. The first order set of equations is simplified by assuming this quantity to be of the order of the ratio of dimensions of the pore considered. Applying the method of separation of variables to these equations, the GF presented in Chapter 3 allows for an analytical solution for the transversal components of the acoustic quantities. The cross-sectionally averaged[3] form of the set of equations strongly depends on two closure assumptions that have to be found during the derivation. For the purpose of keeping the resulting system of equations short, two different approaches are selected. These final equations are implemented in a numerical tool, which is later used to compute linear scattering matrices for given mean field configurations of the TA stack. The description of the implementation is followed by a discussion of closure assumptions of higher complexity.

For validating the scattering matrix results of the one-dimensional tool, a multi-dimensional numerical approach is carried out in Chapter 5. Computational fluid dynamics (CFD) is used to describe the TAs inside regenerators affected by mean flow. The accuracy of CFD simulations scales with the precision of the geometric model and the exactness of resolution of the dominating effects. Consequently, resolving all scales dominating the problem leads to a highly accurate prediction of the flow field inside the domain. As CFD is hosted in the time domain, system identification (SI) methods are needed for post processing. The theory of the

[3] The application of the words "mean" and "average" are strictly distinguished: All parameters denoted as mean parameters are constant in time, while averaging refers to computed spatial (mostly cross-sectional) averaging of a quantity.

technique used in this work is laid out in Section 5.1. Using this so-called CFD/SI method, the scattering behavior in the observed frequency range can be predicted in a single simulation run. The results of this method enable a direct validation of the scattering matrices predicted by the one-dimensional tool.

Numerical and semi-analytical results are always based on modeling assumptions. In general only experimental results are assumed to be valid within the accuracy of measurement errors. For this purpose an experimental test rig was set up for generating reference data. In Chapter 6 its setup components and the measurement techniques applied are demonstrated. The multi-microphone technique, an improvement of the two-source location method of Munjal and Doige [123], delivers the acoustic scattering behavior for the thermoacoustic core, a regenerator flanked by two heat exchangers. The use of recursive methods allows the determination of the acoustic scattering matrices of the TA stack.

Chapter 7 discusses the predicted acoustic scattering behavior of the generic stack for stagnant mean flow conditions. The chapter considers the acoustic scattering predicted by all three approaches. The frequency dependent scattering matrix values are further compared against a network model that approaches a stack pore by two viscous ducts enclosing a discrete temperature change. This simple model matches the scattering behavior in the high frequency regime. Whenever the thermoacoustic energy conversion is active, it deviates from the real matrix values and hence provides an insight into the impact of the TA effect to the scattering behavior of the stack. An implementation of the computed scattering matrices into a network stability analysis tool facilitates a comparison with experimentally investigated TA engine operating conditions. The modeled growth rate as well as the mode shape are investigated. Finally a parameter variation yields information about an optimum stack configuration in terms of IP. Applying this criterion facilitates the determination of the limit amplification or attenuation of the observed acoustic two-port.

The impact of mean flow on the acoustic scattering behavior is discussed in Chapter 8. The good qualitative agreement of the experimental and CFD/SI data forms a base for validation of the one-dimensional predic-

tion models. The improvements of the newly derived over their predecessors are demonstrated. The chapter finally discusses the influence of different closure assumptions.

The thesis concludes with a brief outlook on the applicability of TA devices affected by mean flow and their importance is classified in the field of thermoacoustics.

2 Investigations of the Thermoacoustic Effect

The discovery of thermoacoustics dates back more than 200 years. The report of Higgins [69] on "singing flames"gave birth to TA research. He observed the occurrence of unstable acoustic modes when hydrogen flames were located in certain regions in open pipes. Rijke [161] replaced the flames by a wire framed mesh and showed that in this case the TA phenomenon is linked to convection dominated energy conversion processes. Although Sondhauss [182] is considered to be the first investigator of spontaneous acoustic sounds emitted during the glass blowing process, Pinaud [139] and Carl Marx [112] tried to capture its physics to some extent. Their publications even refer to investigations carried out at the beginning of the 18th century, which mainly focus on musical aspects of the construction of a thermal organ pipe. While Pinaud related the spontaneous loud emission of tones to local condensation phenomena, Marx, discovered a certain dependency on the glass pipe diameter and the location of heating. In contrast to his predecessors, Sondhauss [182] was the first to provide technical data. Moreover, he investigated a correlation of the axial temperature gradient with the observed sound levels. This publication led to an immense amount of publications over the last two centuries. They approach the problem of understanding these mechanisms from three different directions. The experimental observations published for various configurations provide the data to validate the investigations carried out with numerical simulations. The third type of publications provides simplified analytical models that lead to a better understanding of the basic mechanisms. The literature referenced here is also presented in three parts. At first, the history of analytical modeling is reviewed. The second section treats the most important experimental contributions, before Section 2.3 gives a brief overview over the milestones achieved by numerical simulations of the thermoacoustic effect. For detailed information the reader is referred to review articles [25, 52, 53], the resource letter of Garrett [60], the book of Swift [187] and the literature discussed therein.

Finally, Section 2.4 discusses the generic reference setup, which is used for the existing one-dimensional analytical models as well as for the new model developed in Chapter 4.

2.1 Analytical Modeling

Rayleigh [157] himself claimed that his general criterion for the occurrence of any TA oscillation – an in-phase oscillation of pressure and heat release fluctuation – is fulfilled for the process described by Sondhauss [182], because *"(...) the adjustment of air takes time, and thus the temperature (...) deviates from that of neighbouring parts. (...) From this it follows, that at the phase of greatest condensation heat is received by the air, and at the phase of greatest rarefaction, heat is given up from it, and thus there is the tendency to maintain the vibrations."* However, he provided no analytical description for this phenomenon. Kirchhoff [92] was the first to consider the impact of thermal diffusion on acoustic propagation. He found that like viscous friction, this damping mechanism affects the propagation of acoustic waves in terms of shifting the wave number from the real axis into the complex plane. Almost one century later Kramers [96] published a profound mathematical model to describe thermally damped and driven oscillations in terms of acoustic pressure p_1 and cross-sectionally averaged velocity $\langle u_1 \rangle$. Like his predecessor, he considered an idealized pipe. His approach was the first attempt to completely describe thermo-viscous boundary layer interaction, but he could not explain the acoustic amplification in the presence of mean temperature gradients $\partial T_0 / \partial x$. A few years later, Clement and Gaffner [37] derived a similar model, which was based on observed oscillations in cryogenic devices.

In the following decades, Merkli and Thomann [115] and especially Rott refined Kramers model in a series of publications [164–171]. Using the method of separation of variables, he found analytical solutions $h_\nu(y)$ for the transversal (y-dependent) profile of the acoustic velocity u_1 in the linearized axial momentum equation including viscous frictions and $h_K(y)$ of the temperature fluctuation T_1 in the energy transport equation including thermal diffusion. For the description of circular pipes, he incorporated these solutions into the one-dimensional ODEs describing

the axial acoustic propagation of p_1 and the transversally averaged form of the acoustic velocity $\langle u_1 \rangle$. Furthermore, the second-order analysis of enthalpy flux revealed a correlation of the mean temperature distribution to acoustic quantities. Applying a harmonic ansatz, his observations yielded a system of ordinary differential equations (ODEs) in frequency domain. These ODEs are formulated in terms of acoustic pressure p_1, transversally averaged velocity oscillation $\langle u_1 \rangle$, mean parameters and two functions $f_{\nu,K} = \langle h_{\nu,K} \rangle$ accounting for the cross-sectionally averaged impact of viscous friction (index ν) and thermal diffusion (index K).

Wheatley and his successors [187, 206, 207] established the idea to apply Rott's model to one pore located in the center of the TA regenerator (see Fig. 1.8). In this region, the transversal boundaries of the pore are approximately symmetric, which makes Rott's formulations applicable. They further improved the understanding of the TA effect by providing several analytical explanations. Amongst others, Olson and Swift [130] presented a non-dimensional set of parameters for TA problems. Besides explaining the effects by the application of the acoustic compactness assumptions, Swift also established the standard formulation for the TA transport ODEs

$$\frac{\partial p_1}{\partial x} = - \underbrace{\mathrm{i}\omega \frac{\rho}{1 - f_\nu}}_{A_{12}} \langle u_1 \rangle, \tag{2.1a}$$

$$\begin{aligned} \frac{\partial \langle u_1 \rangle}{\partial x} = & - \underbrace{\frac{\mathrm{i}\omega}{\gamma p} \left(1 + \frac{(\gamma - 1) f_K}{(1 - \epsilon_S)} \right)}_{A_{21}} p_1 \\ & + \underbrace{\frac{(f_K - f_\nu)\beta}{(1 - f_\nu)(1 - \epsilon_S)(1 - \mathrm{Pr})} \frac{\partial T}{\partial x}}_{A_{22}} \langle u_1 \rangle \end{aligned} \tag{2.1b}$$

for zero mean velocity conditions [187][1]. They are traditionally used in the design process of standard TA devices. The thermal and viscous boundary layer contribution is captured by the transversally averaged Rott functions f_K, f_ν. Those functions originally were provided for distinct cross-sectional geometries (circular, rectangular, parallel plates,

[1] For reasons of comparability, the denominations A_{ij} of the right hand side terms are similar to the naming of the system matrix elements in Equation (4.63).

etc.), before Arnott et al. [9] derived a general solution for these quantities for arbitrarily shaped cross-sections. The system of Equations (2.1) includes the contribution of viscous dissipation as well as thermal diffusivity and the TA interaction. The viscous dissipation is taken into account by the viscous Rott function f_ν in A_{12} of the acoustic pressure transport Equation (2.1a) originating from the linearized axial momentum equation. Thermal diffusivity scales the energy transport (Eq. (2.1b)) in terms of p_1 and the thermal Rott function f_K in A_{21}. The third term A_{22} is controlled by a combination of the Rott functions. The compressibility β and the mean temperature gradient also affect the TA interaction. The influence of thermal oscillations inside the solid region was added by Swift's student Ward [189] using the scaling parameter ϵ_S, a product of the ratio of thermal diffusivities and geometrical functions.

The attempt of Reid and Swift [159] to take mean flow into account has already been introduced in Section 1.2.2. They considered the mean velocity to be of second order. Thus terms containing u_0 do not appear in the linearized system of equations. To account for the changes in axial mean temperature distribution, their steady state enthalpy equation includes second-order energy fluxes and thus is affected by the mean flow velocity. As stated in the previous section, Peter in't panhuis [80–82] derived Swifts system of TA transport Equations (2.1) form a dimensionless set of Navier-Stokes equations by applying Green's function (GF) techniques. This technique is also the base for the improved modeling derived in Chapter 4, where mean flow impact of zeroth order is incorporated.

The recent review of Bamman et al. [22] shows that the system of Equations (2.1) is still state of the art for the prediction of mean flow contribution in TA devices. Further considerations of mean flow effects, for example by Backhaus and Swift [18, 19, 131, 186, 188], only considered second-order effects in terms of different types of acoustic streaming. As existing TA analysis does not incorporate mean flow, technical TA design approaches do not attempt to exploit possible benefits from mean flow. This may be restricted to the low predicting accuracy of the acoustics inside a mean flow affected device by the existing models. A more accurate modeling may open the research field for technical TA applications affected by mean flow.

2.2 Experimental Milestones

In 1918, Knipp [93] extended the measurements of Sondhauss [182] and presented the first quantitative results of his device. Although incapable to explain the phenomenon, he was the first to state that this effect could be used to provide a constant source of sound. Three decades later, Taconis [190] discovered similar sound occurrences in the pipe system of cryogenic coolers. Although often named after its discoverer, Taconis oscillations are based on the same acoustic thermo-viscous boundary layer effects as those of the Sondhauss type.

The idea of technically exploiting TA energy conversion dates back fifty years. Carter [30] was the first who suggested to transform the acoustic energy obtained from a TA engine into electricity. For this purpose, his Ph. D. student Feldman [51] extensively studied the pressure distribution in several experimental standing wave setups and different working fluids. The first standing wave heat pump prototype was proposed by Merkli and Thomann [115]. They reached temperature differences of up to 30 K in an air filled 100 Hz resonance tube and pressure amplitudes of 2000 Pa. Hofler's [206] pressurized and helium filled refrigerator was one of the first to use a TA stack. He measured a mean temperature difference of up to 50 K over his 5 cm long stack.

Due to the higher complexity, traveling wave based applications appeared later. In 1979, Ceperley [31] proposed the first traveling wave engine. It was capable of producing a ratio of acoustic power input to output of 1.16 by applying a temperature difference of 60 K.

In the beginning of this century, Backhaus and Swift[17] published a small review of existing TA devices. The refrigerator of Reid [158] is of big interest in the scope of this thesis. The setup of his experiment is displayed in Figure 2.1. It facilitates the replacement of some heat exchangers by applying a mean gas flow and thus convective transport of enthalpy. He experimentally demonstrated that the net performance of his engine could be improved by this substitution. Reid restricted his measurements to very low Pe numbers. Nevertheless, the comparison to the model data obtained by applying Equations (2.1) reveal deviations of more than 15% in the computed heat loads. Unfortunately, the pre-

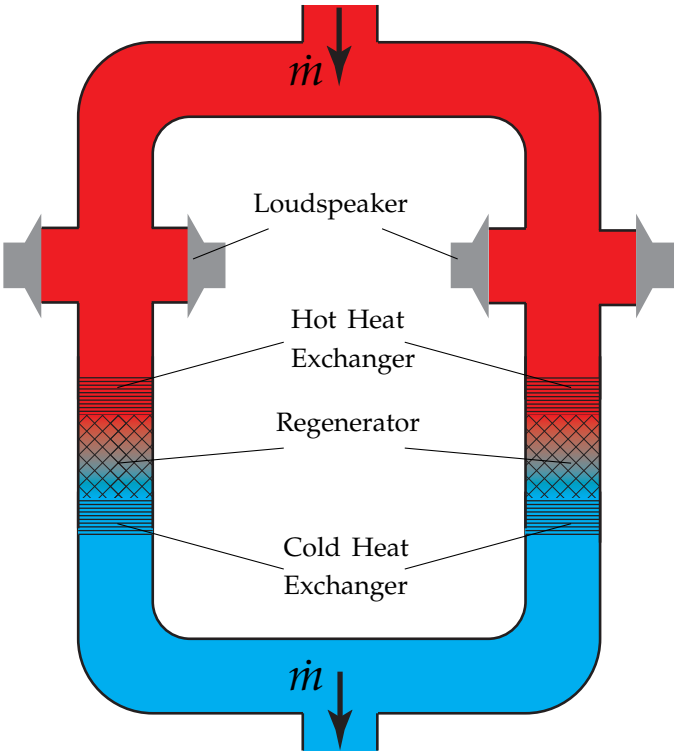

Figure 2.1: Redrawn sketch of Reid's [159] refrigerator: The torus shaped traveling wave application is capable of including mean velocity. The incoming enthalpy flow replaces the energy supply from the upstream heat exchangers.

sented acoustic data are not very extensive. Based on this work, Weiland [205] constructed a combustion driven thermoacoustic engine with mean flow in some parts of the engine. He achieved less than 20% of thermal to acoustic energy conversion efficiency for a temperature difference of more than 1000 K. The lumped capacity model he introduced predicted the spacial profile of the acoustic pressure with more than 10% deviation to the experimentally determined values. Like Reid, he also assumed his flow of combustion reactants through the regenerator to be of second order, which may be a reason for these deviations.

The experimental investigation of the acoustic power distribution is mostly restricted to operating conditions of the complete TA device. Fusco et al. [59] presented power measurements based on the two sensor method for one operating frequency. Bailliet et al. [20] published coupled laser doppler anemometry and microphone measurements that also yielded the acoustic power flux for their setup. In 1998, Adeff et

al. [5] investigated stacks made of reticulated vitreous carbon [2] applying Fusco's technique. One year later Petrulescu et al. [138] experimentally determined the working compressibilities of a circular pore with good agreement to analytically modeled data.

The acoustic scattering caused by TA components is rarely considered in literature. Only Guedra et al. [66] published very recently acoustic transfer measurement data of a complete *thermoacoustic core* that is the regenerators flanked by two heat exchangers, a thermal relaxation tube and an additional cold heat exchanger to maintain the outlets at cold conditions. They aimed to theoretically derive a criterion leading to instability in different applications with the same mounted TA core. The investigated frequency ranges from 50 to 200 Hz. In acoustic boundary layer theory the Womersley number

$$\mathrm{Wo} = \frac{R}{\delta_\nu}, \tag{2.2}$$

that is the ratio of hydraulic radius R to viscous boundary layer thickness δ_ν is taken to be the dimensionless number representing the impact of frequency. Substitution into Equation (1.1) leads to a square root scaling of the frequency to this dimensionless number. Thus, Guedra et al. [66] investigate a very small range of $\frac{1}{6} \lesssim \mathrm{Wo} \lesssim \frac{1}{2}$.

2.3 Numerical Developments

The immense increase in computational resources over the last decades caused a flood of publications treating full and partial numerical simulations of TA devices.

The numerical prediction of TA phenomena started in 1994 with the one-dimensional computational tool developed by Swift's student Ward [203]. This tool works on a coupled system of acoustic network elements and components describing the regenerators in terms of Rott's equations for one sample pore. Applying a shooting method [154] for some optimization parameters, the operating conditions of a TA device can be

[2] Reticulated Vitreous Carbon or RVC is a foam of glassy carbon, which consists of completely repeatable, regular, and uniform cells. It is a rigid, highly porous and permeable structure.

predicted. An updated version of the tool[3] is used for validation of the model presented in Chapter 4, which is common for state of the art publications [32]. Although the Reverse Polish Notation and the numerical methods applied are outdated, no other one-dimensional approach is competitive to this tool. It is still the choice of most scientists for the first stage of designing TA devices [1].

Up to now, the computational costs for resolving all relevant length scales that are geometry, acoustics and boundary layers, are too high for simulating a full TA device. Therefore, particular components of the engine are considered, the regenerator and heat exchangers are modeled or the dimensions are reduced. Nijeholt et al. [128] for example performed a full CFD simulation of a traveling wave engine describing the regenerator in terms of porous media. Hiereche et al. [70] considered the onset of a TA engine numerically. Typically, this onset, defined as the initial destabilization of a TA device if a critical temperature gradient is exceeded, is often discussed in experimental investigations [137]. Hiereche and his co-authors compared the onset of a of a quasi one-dimensional model to a two-dimensional finite volume based simulation of a single stack pore flanked by two idealized heat exchangers. The attached resonator tubes were described by impedance boundary conditions located at a certain distance away of the core elements. The same approach was used by Blanc et al. [26, 113] to investigate their TA refrigerator components. Worlikar and Knio [210, 211] described the thermoacoustics inside one pore by a finite difference approach of a linearized dimensionless system of equations.

The first full 2D-CFD simulation of a very simple TA engine was performed in 2007 by Yu et al. [215]. They managed to resolve all scales with less than one million cells. The timestep of their simulation was far beyond the critical acoustic Courant-Friedrichs-Lewis (CFL) number

$$\mathrm{CFL} = \frac{c\Delta t}{\Delta y} \tag{2.3}$$

of unity. Nevertheless, their computational results were quite accurate. The group of Zink investigated the influence of different resonators in a two dimensionally resolved simple TA engine [219] and demonstrated

[3] DeltaEC, Version 6.2, 2008 [202]

the capability of simulating TA cooling with a commercial CFD code [220]. For the latter, they performed their simulations at a super computer. The time step used was orders of magnitudes smaller than the time step of Yu [215]. It was still too high (CFL$\gtrsim$10) to capture all acoustic effects.

2.4 Generic Reference Problem

Previous sections demonstrated the necessity of significant computational capacities for the complete description of TA apparatuses. Especially in the early design stages, one-dimensional considerations are preferred because of their reduced computational costs. The multi-dimensional fluid flow problem inside the TA pore has to be approximated for such purposes. In this regard, the author follows the approach of Swift and his successors to consider a central pore of the TA stack for the derivation of the quasi one-dimensional model derived in Chapter 4. An extrapolation from the results obtained for one single pore to a device consisting of an arrangement of multiple pores is a good approximation for most thermoacoustic stacks and regenerators. For comparability, the multi-dimensional simulations carried out for validation in this thesis are based on the same geometry. Thus, their model is presented before discussing the methods of investigation.

Common devices utilizing TA energy conversion mechanisms, like those displayed in Figure 1.8, consist of porous media of different form. A typ-

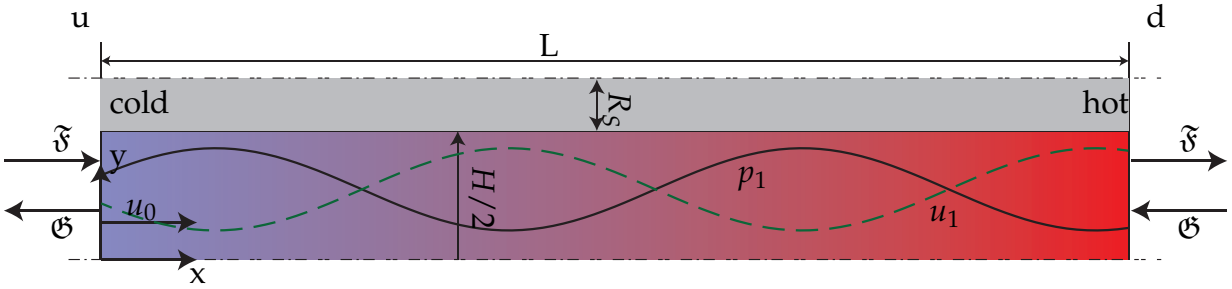

Figure 2.2: Sketch of the investigated problem: The acoustics in a stacked slab pore, that is a narrow channel of length L and constant hydraulic radius $R = H$ are illustrated. The pore is subjected to a laminar mean flow from the cold upstream to the hot downstream end.

ical, rather regular form of porosity is a combination of narrow channels, that is a stack of parallel plates. In this study, one of the channels of such a TA stack with imposed mean flow and preliminarily determined temperature profiles is considered. The geometry of this problem is depicted in Figure 2.2. As the problem is symmetric, only half a pore and the corresponding half of a solid plate have to be considered. The inlet and outlet planes of the domain are located at the ends of the solid medium. In this generic configuration, the impact of gravity is ignored as well as entrance or streaming effects. The air flow inside the domain of length L and hydraulic radius $R = H$ is assumed to be laminar [18].

The solid component with a thickness of $2R_S$ is of cordierite with preset constant material properties. The origin of the Cartesian coordinate system is located at the cold – or upstream (index u) – end of the channel. The opposite hot end at $x = L$ is also denoted as the downstream (d) end of the pore. The reference values at the cold end of the slab pore are fixed to standard ambient temperature and pressure (SATP [124]).

The propagation of acoustic waves inside the domain under investigation are considered in terms of acoustic pressure p_1 and transversally averaged velocity $\langle u_1 \rangle$. The incoming and outgoing values are further described in terms of characteristic wave amplitudes $\mathfrak{F}, \mathfrak{G}$. For further details, please refer to Section 3.2.3.

Literature on thermoacoustics [18, 131, 158, 167, 187] indicates an impact of second-order acoustics on the mean parameter distribution inside narrow geometries. Both fields have to be considered using a hybrid approach, which is sequentially solving for the mean and the acoustic field quantities. The acoustic feedback correlates with the product of amplitudes of the acoustic pressure p_1 and velocity u_1. Taking these effects into account in the hybrid approach implies an iterative solution of the mean field and its acoustic pendant. To avoid this procedure, the thesis is mainly restricted to the low amplitude regime with prescribed fixed mean parameters, although the methods presented are not a priori restricted to this limitation. The cross-sectionally averaged – including the fluid and solid part– mean temperature profile $\langle T_0 \rangle (x)$ is determined by the mean flow conditions and the temperatures upstream T_u and downstream T_d of the pore. Figure 2.3 illustrates transversally averaged mean

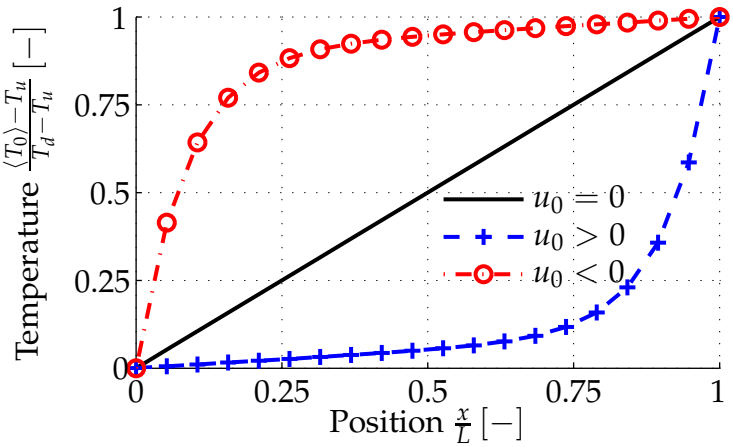

Figure 2.3: Cross-sectionally averaged mean temperature profiles $\langle T_0 \rangle(x)$ (including the solid temperature) inside a narrow pore. Depending on the mean flow velocity profile $u_0(x)$, the temperature distribution is linear (black) or exponential shaped.

temperature profiles $\langle T_0 \rangle(x)$ for three different flow conditions. If heat conduction inside the solid and fluid media dominates (e.g. $u_0 = 0$), the cross-sectionally averaged temperature gradient $\partial \langle T_0 \rangle / \partial x$ is nearly constant. Otherwise, if the Peclet number

$$\mathrm{Pe} = \frac{\varrho_0 c_p u_0 L}{K} \tag{2.4}$$

is not negligible ($u_0 \neq 0$), the temperature profile follows a mixed convection/ diffusion transport equation.

Assuming temperature independent thermophysical properties allows for an analytical solution of the transversally averaged problem. Given two temperature boundary conditions leads to quasi exponential axial temperature profiles $\langle T_0(x) \rangle$ (a more detailed consideration is presented in Section 4.3). Depending on the direction of the flow, the curve is either convex (blue crosses) for positive velocity or concave (red circles) if for the counter directed case. The mathematical formulations for these correlations read

$$\frac{\partial^2 T_0(x)}{\partial x^2} > 0 \quad \text{for} \quad u_0 > 0 \tag{2.5}$$

$$\frac{\partial^2 T_0(x)}{\partial x^2} < 0 \quad \text{for} \quad u_0 < 0. \tag{2.6}$$

The real shape of the curve is always determined from a steady state solution with non-constant thermophysical properties, leading to small deviations from the depicted profiles.

3 Theoretical Background

This chapter gives an introduction to the theoretical background of the analytical models used throughout this thesis. The first section provides different forms of basic equations of fluid dynamics. Starting from the most general formulations of high complexity, they are simplified to account for special conditions. The description of the aeroacoustic transport in isentropic conditions is one of these cases. This thesis concentrates on (thermo-)acoustic problems. The corresponding equations are discussed in detail in Section 3.2. These formulations form the fundamentals for acoustic network modeling. An efficiency criterion based on acoustic two-ports is introduced, whic facilitates a comparison of different configurations. The chapter concludes with a review of the GF method, which yields a model reduction in Chapter 4.

3.1 Basic Equations of Fluiddynamics

As stated in Section 1.4, this thesis deals with different approaches of fluidmechanics and acoustics to describe the physics in TA regenerators and its surrounding parts. The most complex approach used here is the finite volume based CFD technique applied in Chapter 5. The basic equations discretized by this technique as well as the one-dimensional linearized transport equations derived in Chapter 4 are based on the same set of conservation equations describing continuous fluid flow. The resulting formalisms arise from different simplifications and discretization methods. As the problem considered does not include any chemical reactions, heat addition or energy production by thermal or nuclear radiation, no source terms need to be considered. Many thermoacoustic apparatuses experience streaming effects which are initiated by inhomogeneities caused by gravity. As these effects are beyond the scope of this thesis, gravity effects are also neglected. Nevertheless, the corresponding equations include a general volume force term b. These equations are part of many textbooks, in which various notations are used. In this

thesis, the notation of Landau and Lifshitz [103] in combination with the Einstein summation convention (see e.g. Kundu et al. [100]) is used.

3.1.1 Conservation of Mass

The conservation of mass

$$\frac{D\varrho}{Dt} = -\varrho \frac{\partial u_i}{\partial x_i} \tag{3.1}$$

describes the coupling of fluid density ϱ to flow velocity u_i while being transported through the domain. Here $\frac{D\Psi}{Dt}$ stands for the substantial derivative of the transported variable Ψ. If incompressibility is assumed, the pressure dependency of $\varrho = \varrho(p)$ is neglected.

3.1.2 Navier-Stokes Equations

Considering the specific momentum conservation of a Newtonian fluid element [103] and simplifying the resulting equation by substituting Equation (3.1) yields

$$\varrho \frac{Du_i}{Dt} = -\frac{\partial p}{\partial x_i} + \frac{\partial \tau_{ij}}{\partial x_j} + \varrho b_i, \tag{3.2}$$

where the stress tensor τ_{ij} represents the viscous shear forces. The flow is either driven by a pressure gradient $\frac{\partial p}{\partial x_i}$ or a volume force b_i. In the absence of magnetic fields, gravity effects and chemical reactions, this force term vanishes.

The stress tensor for Newtonian fluids can be expressed in terms of bulk kinematic viscosity μ and volume viscosity ζ by

$$\tau_{ij} = \mu \left(\frac{\partial u_j}{\partial x_i} + \frac{\partial u_i}{\partial x_j} \right) + \zeta \delta_{ji} \frac{\partial u_k}{\partial x_k}, \tag{3.3}$$

where ζ is negligible for incompressible and weakly compressible fluids and can usually be neglected for small expansion processes [44]. The combination of Equation (3.3) and Equation (3.2) are denominated as Navier-Stokes equations (NSE).[1]

3.1.3 Euler Equations

In the absence of shear layers that is in free stream flows or if compressibility effects dominate the flow field, viscous effects are often neglected. Within this assumption, the NSEs (Eq. (3.2)) simplify to

$$\varrho \frac{Du_i}{Dt} = -\frac{\partial p}{\partial x_i} + \varrho b_i. \tag{3.4}$$

The literature refers to this set of equations as the Euler equations. These equations govern the field of aerodynamics. For example, their irrational form is the basis for the computation of potential flows [218].

3.1.4 Energy Conservation

The first law of thermodynamics states that energy can neither be produced nor destroyed. In other words, the rate of change of the sum of internal and kinetic energy equals the sum of work done and the heat flux q addition to a material volume. Substituting Fourier's law

$$q_i = K \frac{\partial T}{\partial x_i} \tag{3.5}$$

and the Newtonian stress tensor (Eq. (3.3)) yields an energy equation in terms of internal energy, temperature T, density ϱ and velocity u_i. Rewriting the internal energy in terms of enthalpy and applying some thermodynamic relations [120] yields a temperature T transport equation

$$\varrho c_p \frac{DT}{Dt} = \beta T \frac{Dp}{Dt} + \frac{\partial}{\partial x}\left(K \frac{\partial T}{\partial x}\right) + \frac{\partial}{\partial x_j}\left(u_i \tau_{ij}\right). \tag{3.6}$$

When the Euler formalism (Eq. (3.4)) is used for describing the momentum transport, the viscous and heat conductive terms in this transport equation are also neglected.

[1] Some authors, especially gas dynamics scientists, include the full set of continuity equation, momentum and energy conservation for Newtonian fluids into the denotation of Navier-Stokes equations. The same also accounts for the Euler Equation (3.4).

3.1.5 Closure by Gas Laws

The number of transported variables $(\varrho,\ p,\ T,\ u_i)$ is larger than the number of transport equations ((3.1), (3.2) and (3.6)). Consequently, a further equation is needed for problem closure. Typically a pressure-density-entropy relation is used. In case of gaseous fluids, these formulations are denoted as gas law. The consideration of generic fluids in the region of standard conditions allows the application of the simplest – ideal gas – approximation, which relates the fluid density in terms of

$$p = \varrho \mathfrak{R} T. \tag{3.7}$$

$\mathfrak{R}$ denotes the specific gas constant of the medium. For low temperature applications, or under conditions in which phase changes may occur, more accurate real gas formulations are recommended.

As first estimations, constant basic thermophysical properties are assumed. For more accurate results, the thermal conductivity K and dynamic viscosity μ have to be adapted. The changes in mean temperature over the regenerators and pressurization cause changes in orders of magnitudes of those two decisive parameters. These dependencies have to be taken into account, either by modeling or interpolating their values.

The Sutherland formula [24] is applied to describe the temperature dependency of these quantities in many CFD codes. It is mainly used to scale the temperature dependency relative to a reference temperature T_{ref}

$$\mu = \mu_{\text{ref}} \frac{T_{\text{ref}} + C}{T + C} \left(\frac{T}{T_{\text{ref}}} \right)^{\frac{3}{2}} \tag{3.8}$$

for the dynamic viscosity. K is also found in the same manner. An alternative choice is the polynomial description of the properties, which mostly accounts for a certain range of pressure and temperature. In contrast to these methods, the data from measurement tables yield a very accurate approximation of the real values. Standard data are available from the National Institute of Standards and Technology (NIST) [124] or the VDI Atlas [201].

3.2 Acoustic Theory

The interdisciplinary science of acoustics deals with the propagation of sound and vibrations in any media. This section mainly focuses on the propagation of sound waves in compressible media. The first modern works on acoustics stem from Helmholtz [68] and Rayleigh, whose "Theory of Sound" [157] is still one of the most common books in the field of aeroacoustics.

This section is divided into two main parts. At first, the basic equations of wave propagation are outlined. Additional assumptions lead to aeroacoustic standard formulations for the mathematical description of sound. The second part considers the so-called acoustic two-ports and network models which allow for simplified investigations of complex acoustic systems. Here the notation mainly follows Rienstra and Hirschberg [160] and Munjal [122].

3.2.1 Linearized Euler Equations

Sound, that is the propagation of a pressure wave through any medium, is commonly described as a frictionless form of fluid motion. The pressure wave amplitude $|p_1|$ is assumed to be small compared to the mean pressure. So are the relative motions $|u_1| \ll c$ of a gas parcel and thus viscous losses can be neglected.

The assumption of small variations from their mean quantities allows the application of linearization techniques to Equations (3.1), (3.4) and any formulation of energy conservation (e.g. Eq. (3.6)). The formulation for such an expansion in A reads

$$\Psi(x_i, t) = \Psi_0(x_i, t) + A\Psi_1(x_i, t) + A^2\Psi_2(x_i, t) + ... \; A \ll 1. \tag{3.9}$$

The dimensionless form of the basic system of equations suggests to relate the terms by the acoustic Mach number $\mathrm{Ma} = \frac{u_1}{c} \approx \mathcal{O}\left(\frac{p_1}{p_0}\right)$, which is a valid expansion for $\mathrm{Ma} \ll 1$ [81]. The mean component (index 0) of the asymptotic expansion of any quantity Ψ in terms of A is assumed to be constant in time, i.e. $\Psi_0(x_i, t) \equiv \Psi_0(x_i)$. Therefore, the zeroth-order terms

have to separately fulfill the expanded set of equations. For $\mathrm{Ma_a} \ll 1$, this also accounts for all collections in the different orders of $\mathrm{Ma_a}$.

For characteristic Mach numbers

$$\mathrm{Ma} = \frac{u_0}{c} \tag{3.10}$$

lower than 0.2 and in the absence of shear layers, entropy waves etc., mean velocity contributions play a minor role in the resulting first-order set of equations. This approach leads to

$$\frac{\partial \varrho_1}{\partial t} + u_{1,i}\frac{\partial \varrho_0}{\partial x_i} = -\varrho_0 \frac{\partial u_{1,i}}{\partial x_i} \tag{3.11a}$$

$$\varrho_0 \frac{\partial u_{1,i}}{\partial t} = -\frac{\partial p_1}{\partial x_i} \tag{3.11b}$$

for the linearized mass (3.1) and momentum conservation (3.4).

3.2.2 Isentropic Acoustics – The Wave Equation

If the fluid is considered to be isothermal, the second term on the left hand side of Equation (3.11a) vanishes. The equation of state for an ideal gas states that the pressure is a pure function of entropy s and density ϱ. A Taylor expansion for isentropic conditions yields

$$p(x_i, t) = p_0 + \left.\frac{\partial p}{\partial \varrho}\right|_s \varrho_1 + \mathcal{O}(\varrho_1). \tag{3.12}$$

Within the ideal gas assumption (Eq. (3.7)), the speed of sound c defined as the square root of this isentropic variation of pressure with density

$$c^2 = \left.\frac{\partial p}{\partial \varrho}\right|_s \tag{3.13}$$

reduces to

$$c = \sqrt{\gamma \Re T}. \tag{3.14}$$

Here γ stands for the specific heat ratio (or isentropic exponent). Substituting this simplification into the linearized mass conservation (Eq. (3.11a)) directly yields

$$\frac{\partial p_1}{\partial t} = -\varrho_0 c^2 \frac{\partial u_{1,i}}{\partial x_i}. \tag{3.15}$$

Differentiating Equation (3.15) with respect to time t and computing the gradient of Equation (3.11b) in space cause an elimination of the acoustic velocity terms. Doing so directly yields the standard wave equation

$$\frac{\partial^2 p_1}{\partial t^2} - c^2 \frac{\partial^2 p_1}{\partial x_i^2} = 0. \tag{3.16}$$

3.2.3 Characteristic Wave Amplitudes

For one-dimensional acoustics, the special form of the linear operator on the pressure fluctuation can be factorized to

$$\left[\frac{\partial}{\partial t} - c\frac{\partial}{\partial x_i}\right]\left[\frac{\partial}{\partial t} + c\frac{\partial}{\partial x_i}\right] p_1 = 0. \tag{3.17}$$

The general solution of this equation

$$p_1 = \varrho_0 c \left[\mathfrak{f}(x - ct) + \mathfrak{g}(x + ct)\right] \tag{3.18a}$$

in terms of Riemann Invariants[2] describes the transport of any shape of perturbation along the characteristics $x = \pm ct$ in time and space. In a more extensive derivation, the contribution of mean velocity, which is neglected in the presented form, results in a similar equation where $\pm(c \pm u_{0,i})$ replaces the prefactor $\pm c$ of the operators in Equation (3.17).

The same derivation as above used for the acoustic velocity directly yields

$$u_1 = \mathfrak{f}(x - ct) - \mathfrak{g}(x + ct). \tag{3.18b}$$

For harmonic waves in isentropic fluid, the solution of these equations yields

$$\mathfrak{f}(x - ct) = \mathfrak{F} e^{\mathrm{i}\omega\left(t - \frac{x}{c}\right)} \tag{3.19a}$$

$$\mathfrak{g}(x + ct) = \mathfrak{G} e^{\mathrm{i}\omega\left(t + \frac{x}{c}\right)}, \tag{3.19b}$$

with $\mathfrak{F}$ and $\mathfrak{G}$ denoting the characteristic wave amplitudes. As long as isentropic acoustics are considered, these quantities are constant. For planar waves the change of the complex-valued functions is described by the argument of the exponential function containing the parameters of angular frequency ω, time t and the ratio of space x to the characteristic transport velocity c.

[2] This notation indicates that both solutions propagate independently and do not interfere.

3.2.4 Network Modeling and Acoustic Two-Ports

Network theory was first developed in electrical engineering for the description of electrical transmission circuits. An analogy between the frequency domain description of such systems and the gray box approach [122] for complex acoustic systems can be drawn. The idea of modeling combustion driven thermoacoustic systems using a one-dimensional network was introduced by Bohn and Deucker [28]. In the beginning, TA stability analysis mainly focused on predicting combustion instabilities of academic configurations [45, 46]. Most geometry and even combustion dominated problems are modeled based on analytical considerations. Poinsot and Veynante [141] provide a good overview for the analytical description of the acoustic transfer of laminar and turbulent flames and academic configurations for combustion engines. More sophisticated burner configurations are displayed using general models that contain control parameters. As these parameters sometimes are not based on physics, they often have to be determined using experimental [135, 178, 179] or numerical [87, 180] methods. During the last two decades these models were expanded from the investigation of academic single burner configurations [114] to annular combustion chambers [50, 149, 183]. Irrespective of the complexity of the system, generating a representative network model of all those configurations requires splitting up the system into compact acoustic elements. These so-called multi-ports describe the transformation of acoustic parameters from side to side. The assembly of these complex-valued linear combinations of input variables leads to a prediction of stability. For example, the predicted sign of the complex eigenfrequencies of the system defines the corresponding eigenmode to be stable or unstable.

In contrast to models based on the frequency domain, newer developments use time domain low-order network models [64, 177]. They even facilitate predictions of limit cycle oscillations and modal interactions.

Also the frequency based one-dimensional integration tool DeltaEC uses acoustic two-ports for the description of some aeroacoustic elements. Straight ducts and discrete area changes, for example, are described using standard network model elements. In contrast to stability prediction tools, DeltaEC was designed to compute the spatial distribution of

limit cycle oscillations in thermoacoustic applications. The inclusion of nonlinearities and damping effects facilitates a forecast of the operating conditions of such systems. The constraints of linear stability analysis of acoustic networks neglect such factors. Still, the information obtained about the growth rate can be used for a comparison of different configurations. The exponential growth rate of an unstable mode scales with the energy fed into the system. Hence, the acoustic power generation can be optimized by a comparison of the imaginary part of the unstable eigenfrequencies. The stability analysis allows a wider parameter variation while consuming little computational costs. The results obtained for the linear regime have to be investigated by a single frequency investigation of promising system configurations. Hence, it is advisable to combine both methods to find an optimized configuration of the planned device.

In some cases, detailed considerations of acoustic two-ports that dominate the network already enable a first estimate of the system performance. As will be demonstrated in Section 3.2.5, a quantitative prediction of the growth rate of simple thermoacoustic engines can be found by considering the transmission and reflection behavior of the crucial elements, i.e. the stack.

Figure 3.1 sketches a typical acoustic two-port in its black-box representation. The in- and output parameters denoted in terms of p_1, u_1 or characteristic wave amplitudes $\mathfrak{F}$ and $\mathfrak{G}$ are either arranged such that the transport is predicted from one port (1) to the other (2) or, in a causal formulation, the output is a combination of transmitted and reflected incident waves. Due to the identity of the parameter spaces, all formulations can be mapped. The coefficients of matrix entries are based on simplified an-

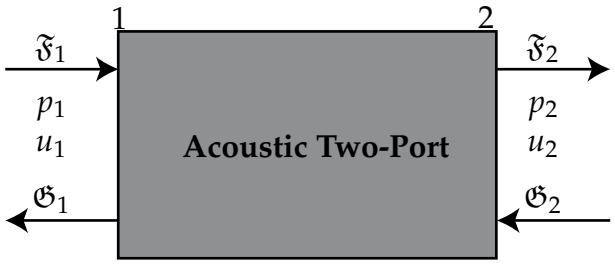

Figure 3.1: The black-box model of an acoustic two-port. In network theory, the acoustic transport between two ends of an acoustic element are often approached by a linear black-box model.

alytical considerations as well as numerical and experimental measurements.

Using combinations of such acoustic two-ports, more complex problems can be approximated to achieve a first estimate of their acoustic transfer behavior. For example, a combustor geometry may be discretized by a combination of analytically modeled ducts, area discontinuities and a two-port description of the flame obtained numerically or experimentally [28]. Applying the same technique, a thermoacoustic regenerator may be modeled by the set of acoustic two-ports displayed in Figure 3.2. The area changes (AC) represent the ends of the porous material. In these positions, the acoustics experience a change of the cross-sectional area that scales with the porosity

$$\phi = \frac{A_F}{A_F + A_S} \tag{3.20}$$

of the TA regenerator. The inner two viscous ducts (Duct) mainly contribute to phase shifting of the waves traveling through the regenerator. The center element, a temperature discontinuity (TC) accounts for the discrepancy of the hot and cold resonator temperatures. The analytical two-port approaches of these components are a simplistic representation and will be presented in this section. In comparison to the numerical and experimental data demonstrated later, the resulting scattering behavior of this set serves as a limit approximation.

3.2.4.1 Acoustic Two-Port Theory

The description of acoustic transmission in terms of two-port elements holds in both states, the acoustic transport variables p_1, u_1 and the char-

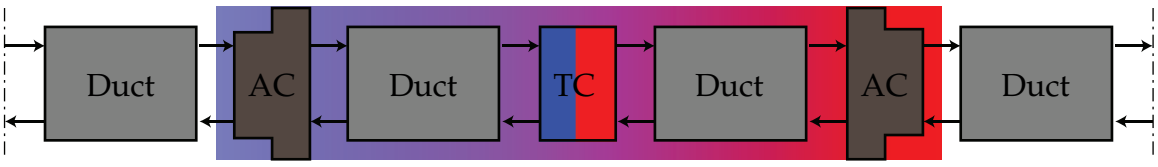

Figure 3.2: An example of a simple network model approach for a TA regenerator. The acoustics are approximated by five two-port elements accounting for the porosity, the spatial transport and the experienced temperature change.

acteristic wave space $\mathfrak{F}$, $\mathfrak{G}$. This section provides the relations between the different notations.

Transfer Matrices

The port to port transmission formulation through a black box element is generally referred to as transfer matrix $\mathbf{T}$. Scaling the acoustic pressure $p_1$with the specific acoustic impedance $\varrho_0 c$ leads to non-dimensional matrix entries in

$$\begin{pmatrix} \frac{p_1}{\varrho_0 c} \\ u_1 \end{pmatrix}_2 = \begin{bmatrix} T_{11} & T_{12} \\ T_{21} & T_{22} \end{bmatrix} \begin{pmatrix} \frac{p_1}{\varrho_0 c} \\ u_1 \end{pmatrix}_1 = \mathbf{T}_{\mathfrak{pu}} \begin{pmatrix} \frac{p_1}{\varrho_0 c} \\ u_1 \end{pmatrix}_1 . \tag{3.21}$$

In general, the complex-valued coefficients in $\mathbf{T}_{\mathfrak{pu}}$ are functions of frequency f and problem-dependent parameters. This formulation is often used, because of its plausibility. It allows a direct identification of characteristic parameters in analytical models for some network elements. The transfer matrix of a flame in a burner for example is often approximated using Rankine-Hugoniot relations [141]. Some terms of these equations scale with characteristic mean temperature ratios or the Mach number of the mean flow.

The formulation of Equation (3.21) in the characteristic wave amplitude space

$$\begin{pmatrix} \mathfrak{F} \\ \mathfrak{G} \end{pmatrix}_2 = \begin{bmatrix} \mathfrak{T}_{11} & \mathfrak{T}_{12} \\ \mathfrak{T}_{21} & \mathfrak{T}_{22} \end{bmatrix} \begin{pmatrix} \mathfrak{F} \\ \mathfrak{G} \end{pmatrix}_1 = \mathbf{T}_{\mathfrak{FG}} \begin{pmatrix} \mathfrak{F} \\ \mathfrak{G} \end{pmatrix}_1 \tag{3.22}$$

is mostly used to display short analytical formulations, for example for ducts and channels. Introducing the conversion matrix

$$\mathbf{\Omega} = \frac{1}{2} \begin{bmatrix} 1 & 1 \\ 1 & -1 \end{bmatrix}, \tag{3.23}$$

it directly couples with the transfer matrix in pu notation by

$$\mathbf{T}_{\mathfrak{FG}} = \mathbf{\Omega} \mathbf{T}_{\mathfrak{pu}} \mathbf{\Omega}^{-1}. \tag{3.24}$$

One advantage of these notations is their simple mathematical coupling. The matrix product of the series of acoustic elements is equivalent to the transport through the technical components represented by these elements.

Scattering Matrices

If the observer's interests focuses on the impact of the incoming waves on the output of the acoustic element, a scattering matrix notation directly yields this causality. While the diagonal elements t_{12}, t_{21} in

$$\begin{pmatrix} \mathfrak{F}_2 \\ \mathfrak{G}_1 \end{pmatrix} = \begin{bmatrix} t_{12} & r_{11} \\ r_{22} & t_{21} \end{bmatrix} \begin{pmatrix} \mathfrak{F}_1 \\ \mathfrak{G}_2 \end{pmatrix} = \mathbf{S} \begin{pmatrix} \mathfrak{F}_1 \\ \mathfrak{G}_2 \end{pmatrix} \tag{3.25}$$

describe the transmission of waves, the off-diagonal elements r_{ii} display the contribution of the reflections to the outgoing wave.

Except for the case of vanishing wave transmission in negative coordinate direction, $\mathbf{S}$ is directly related to the characteristic wave space transfer matrix $\mathbf{T}_{\mathfrak{F}\mathfrak{G}}$. Rearranging the matrix components in terms of

$$\mathbf{S} = \frac{1}{\mathfrak{T}_{22}} \begin{bmatrix} \mathfrak{T}_{11}\mathfrak{T}_{22} - \mathfrak{T}_{12}\mathfrak{T}_{21} & \mathfrak{T}_{12} \\ -\mathfrak{T}_{21} & 1 \end{bmatrix}, \tag{3.26}$$

yields a scattering matrix formulation.

3.2.4.2 Analytical Two-Port Models

The last section provided the basic correlations for acoustic network modeling. This section discusses the three analytical approaches, which are applied in the remainder of this thesis.

Thermo-Viscous Ducts

Formulating the one-dimensional characteristic wave propagation under isentropic conditions (Eqs. (3.19)) in terms of scattering matrices, the independence of solutions $\mathfrak{F}$ and $\mathfrak{G}$ directly yields

$$\begin{pmatrix} \mathfrak{F} \\ \mathfrak{G} \end{pmatrix}_2 = \begin{bmatrix} \exp\left(-\mathrm{i}k^+x\right) & 0 \\ 0 & \exp\left(\mathrm{i}k^-x\right) \end{bmatrix} \begin{pmatrix} \mathfrak{F} \\ \mathfrak{G} \end{pmatrix}_1. \tag{3.27}$$

Here the wave numbers $k^{\pm}$ are defined by $\frac{\omega}{c \pm u}$. The sign notation is chosen, such that waves traveling in positive flow direction from x_1 to x_2 are

denoted by $+$. In duct acoustics, losses in pipes are generally not negligible. The damping influence is mostly taken into account by manipulating the wave number with an additional complex-valued term d that scales the $k^{\pm}$ in terms of

$$k^{\pm} = d\frac{\omega}{c \pm u}. \tag{3.28}$$

As damping strongly depends on the geometric conditions, a wide variety of approaches can be found in literature [122, 197]. Preliminary experimental investigations by Alemela [7] and Neunert [127] at the Lehrstuhl für Thermodynamik at TU München revealed good results with the application of Kirchhoff's [92] formulation. Using Neunert's [127] formulation and an expected roughness coefficient of unity, the damping coefficient

$$d = 1 + \frac{(1-i)}{\sqrt{2}\,\mathrm{Sh}}\left(1 + \frac{\gamma - 1}{\sqrt{\mathrm{Pr}}}\right) \tag{3.29}$$

is a function of the Womersley number, Wo, the Prandtl number, Pr and the Shear number, Sh combining the material properties of the fluid. The nature of this damping model causes a generation of complex-valued $k^{\pm}$, which lead to an exponential decrease of the characteristic wave amplitudes while traveling through the duct.

Non-Constant Cross-Sectional Areas

Technical applications of duct acoustics exhibit non-constant cross-sectional areas. Provided that the assumption of acoustic compactness holds, i.e. as long as the acoustic wave length

$$\lambda = \frac{c}{f} \tag{3.30}$$

is much larger than the geometric length scale, the change in cross-sectional area is considered as an abrupt change in A. If this assumption is too restrictive, for example for continuously varying cross-sections, a distributed area change can be approximated by a discretized series of ducts and area changes [143].

Such area changes often generate acoustic losses by mean flow interaction, for example in the shear layers occurring in the region mean flow expansion. Such losses are hard to handle qualitatively. Most of them

scale with Mach number, Ma and are even apparent for Ma ~ 0.1. Only if mean flow follows potential flow descriptions, here Ma $\lesssim 0.01$, these effects are negligible. These conditions are assumed to be valid in the problems considered. Other dissipative effects that are generally taken into account revealed no influence in the network representation applied later. These terms are neglected for the derivation of the transfer matrix $\mathbf{T}_{AC}$ of a discrete change in cross-sectional area.

The transfer matrix of a discrete area change is based on the integral conservation of acoustic mass and momentum (Eqs. (3.11)). The latter states that the pressure fluctuation p_1 is unaffected by the change in cross-section. For constant acoustic mass flux, the acoustic velocity ratio is reciprocally proportional to the area ratio α, that is

$$u_{1,2} = \frac{A_1}{A_2} u_{1,1} = \alpha u_{1,1}. \tag{3.31}$$

Expressing these relations in terms of transfer matrix notation leads to

$$\begin{pmatrix} \frac{p_1}{\varrho_0 c} \\ u_1 \end{pmatrix}_2 = \begin{bmatrix} 1 & 0 \\ 0 & \alpha \end{bmatrix} \begin{pmatrix} \frac{p_1}{\varrho_0 c} \\ u_1 \end{pmatrix}_1 . \tag{3.32}$$

Changes in Mean Temperature

Technical applications often deal with non-constant mean temperature conditions. Here, we deal with non-reactive mean flow conditions that are free from internal heat release as they occur in the tail pipe of combustors. For modeling the acoustics in these regions, the changes in mean temperature have to be taken into account [126].

Due to the lack of analytical solutions of the linearized Euler Equations (3.11), the temperature profile is discretized in the same way as continuous variations of the cross-section are approached. Using the linearized Rankine-Hugoniot relations [141] to describe each discrete temperature change leads to a linear relation between the acoustic pressure and velocity upstream (index u) and downstream (index d) of tempera-

ture discontinuity. According to the derivation of Chu [36] the acoustic quantities are related by

$$\begin{aligned}\left(\frac{p_1}{\varrho_0 c}\right)_d &= \frac{\varrho_{0,u}c_u}{\varrho_{0,d}c_d}\left(\frac{p_1}{\varrho_0 c}\right)_u - \\ &\quad \frac{\varrho_{0,u}c_u}{\varrho_{0,d}c_d}\left(\frac{T_{0,d}}{T_{0,u}}-1\right)\mathrm{Ma}_u u_{0,u}\left(\frac{\dot{Q}_1}{\dot{Q}_0}+\frac{u_{1,u}}{u_{0,u}}\right), \qquad (3.33)\\ u_{1,d} &= u_{1,u}+\left(\frac{T_{0,d}}{T_{0,u}}-1\right)u_{0,u}\left(\frac{\dot{Q}_1}{\dot{Q}_0}+\frac{p_{1,u}}{p_{0,u}}\right). \qquad (3.34)\end{aligned}$$

In the absence of heat release $\dot{Q}$ and assuming small mean flow velocities, the second terms on the right hand side of Equations (3.33) and (3.34) vanish.

Using the equation of state for an ideal gas (3.7) , the prefactor of the first term in Equations (3.33) is rewritten in terms of mean temperature

$$\frac{\varrho_{0,u}c_u}{\varrho_{0,d}c_d} = \sqrt{\frac{T_{0,d}}{T_{0,u}}} = \Theta. \qquad (3.35)$$

Substituting Θ into Equation (3.33) and rewriting the linearized Rankine-Hugoniot relations in matrix notation yields

$$\begin{pmatrix} \frac{p_1}{\varrho_0 c} \\ u_1 \end{pmatrix}_d = \begin{bmatrix} \Theta & 0 \\ 0 & 1 \end{bmatrix} \begin{pmatrix} \frac{p_1}{\varrho_0 c} \\ u_1 \end{pmatrix}_u . \qquad (3.36)$$

Modeling continuous mean temperature variations by a combination of Equation (3.36) and Equation (3.27) lead to an accurate approach for the description of acoustic transfer in wide geometries. Based on the idea stated by Ffowcs and Dowling [47], Neunert et al. [126] demonstrated that acoustic measurements inside an exhaust gas tract with strongly varying mean temperature can be accurately approximated using the approach of a series of isothermal ducts and temperature changes.

3.2.5 Instability Potentiality of an Acoustic Two-Port

Generally acoustic two-ports are used in network models to approximate the acoustics inside a technical device. The interaction of the acoustic

elements plays a crucial role when an accurate prediction of the stability of the system is sought. The local investigation of the acoustic powers P of distinct elements facilitates the determination of possible reason for unstable eigenfrequencies of the system. It is defined by

$$P = \frac{1}{2} A \mathfrak{Re} \left[p_1 u_1^* \right], \tag{3.37}$$

i.e. the product of the cross-sectional area and the flux of acoustic energy. Here, the asterisk denotes the complex conjugate.

This approach was carried out by Aurégan and Starobinsky [13]. In 1999 they presented the "acoustical energy dissipation/production potentiality" concept. In aeroacoustics this formalism was successfully applied to estimate the "whistling potentiality" of several aeroacoustic duct elements [89, 102, 194]. The acoustic power P at each port is separated into right- (P^+) and leftwards (P^-) traveling energy fluxes which are depicted in Figure 3.3. The whistling potentiality relates the outgoing acoustic energy fluxes $P_1^- + P_2^+$ of an acoustic multi-port to its ingoing equivalents $P_1^+ + P_2^-$ using the acoustic scattering matrix formulation. The acoustic states at the ports, which define this power ratio η, are functions of the incoming characteristic wave amplitudes and, computed by the scattering matrix, their outgoing counterparts. Determining the worst and best case power ratios and the corresponding acoustic states at the ports leads to an estimation of the "instability potentiality" (IP) of the acoustic element considered. This terminology was introduced by Polifke [145], who transformed the acoustic exergy and mass velocity based formulation of Aurégan and Starobinski into the standard characteristic wave amplitude form and computed the IP of a premix swirl burner [61]. This thesis uses

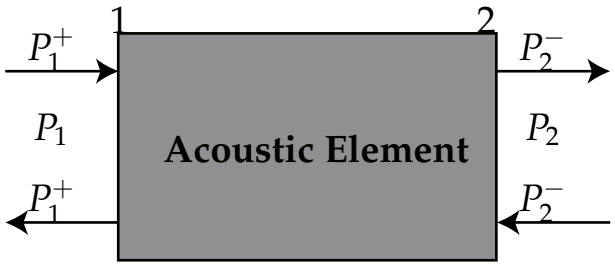

Figure 3.3: The black-box model of an acoustic two-port. In network theory, the acoustic transport between two ends of an acoustic element are often approached by a linear black-box model.

the formalism to demonstrate the influence of certain parameters on the limit power ratios of TA stacks. The corresponding acoustic states are not considered. A deeper investigation of the relevance of these quantities for TA applications can be found in Holzinger et al. [73]. As the characteristic wave formalism is used in this thesis, the main derivation steps of IP are briefly repeated in this section maintaining the notation of Polifke [145].

Using the characteristic waves, the acoustic sound power at the port of an acoustic element defined by Equation (3.37) reads

$$P = \frac{1}{2}\varrho_0 c A \left(\mathfrak{F}\mathfrak{F}^* - \mathfrak{G}\mathfrak{G}^*\right). \tag{3.38}$$

Defining the variable

$$\chi = \sqrt{\frac{\varrho c A}{2}}, \tag{3.39}$$

and inserting

$$P^+ = \chi\mathfrak{F}, \qquad P^- = \chi\mathfrak{G}, \tag{3.40}$$

enables an interpretation of the terms in brackets in Equation (3.38) as the sum of incoming and outgoing acoustic fluxes at this port. Summing up the sound powers of all ports yields the net production Π of an acoustic multi-port. Defining the input and output vector of a two-port system as

$$\boldsymbol{r} = \begin{pmatrix} P_1^+ \\ P_2^- \end{pmatrix}, \qquad \boldsymbol{z} = \begin{pmatrix} P_1^- \\ P_2^+ \end{pmatrix}, \tag{3.41}$$

this quantity Π reads

$$\Pi = \boldsymbol{r}^\dagger \boldsymbol{r} - \boldsymbol{z}^\dagger \boldsymbol{z}. \tag{3.42}$$

Next, the order of output wave amplitudes of the scattering matrix notation is changed, such that

$$\hat{\mathbf{S}} = \begin{bmatrix} r_{11} & t_{12} \\ t_{21} & r_{22} \end{bmatrix}. \tag{3.43}$$

A multiplication of $\hat{\mathbf{S}}$ by

$$\mathbf{V} = \begin{bmatrix} \chi_1 & 0 \\ 0 & \chi_2 \end{bmatrix} \tag{3.44}$$

from the left hand side and its inverse from the right-hand side yields

$$\Pi = z^{\dagger} \underbrace{\left((\mathbf{V}\hat{\mathbf{S}}\mathbf{V}^{-1})^{\dagger}\mathbf{V}\hat{\mathbf{S}}\mathbf{V}^{-1}\right)}_{\mathbf{U}} z - z^{\dagger}z. \tag{3.45}$$

The eigenvalues λ_i of the system matrix $\mathbf{U}$ correlate the amplification of the acoustic power production in terms of their eigenvectors ϵ_i by

$$z^{\dagger}\mathbf{U}z = \sum_{i=1}^{2} \lambda_i |\epsilon_i|^2. \tag{3.46}$$

They stand for two relations of incoming waves, that are normal in this space. Given these values and the scattering matrix of the two-port also defines outgoing characteristic wave amplitudes. If the acoustic state matches one of these conditions, the other eigenvalue has no contribution to the acoustic power ratio. Furthermore, the eigenvalues λ_i correspond to the minimum as well as maximum possible ratio of outgoing versus incident acoustic power for any state vector $\boldsymbol{a}$ defined by

$$\eta = \frac{P_{\text{out}}}{P_{\text{in}}} = \frac{\boldsymbol{a}^{\dagger}\mathbf{U}\boldsymbol{a}}{||\boldsymbol{a}||_2^2}. \tag{3.47}$$

The amplification or attenuation caused by the acoustic element is a direct result of the scattering behavior and the acoustic state applied. When the power ratio η exceeds unity the component causes acoustic amplification. Values lower than one, indicate a damping of the acoustic wave by this element.

The solid lines in Figure 3.4 display maximum eigenvalues of the acoustic two-ports presented so far for a frequency range of 1 to 500 Hz. The dashed lines indicate the minimum IP of these elements. Air, treated as ideal gas at standard conditions is used as transport medium. The considered damped duct is 0.05 m wide and 10 m long, the applied mean velocity corresponds to Ma $= 0.5$. The area ratio and temperature ratio both have a fixed value of $\Theta = \alpha = 1.5$.

The eigenvalues of a discrete change in temperature depicted in red are both neutral, which means all eigenvalues are unity. Considering the derivation of the applied model, zero acoustic energy change was postulated. This means that any change in mean temperature can either inherently cause or suppress an acoustic instability[3].

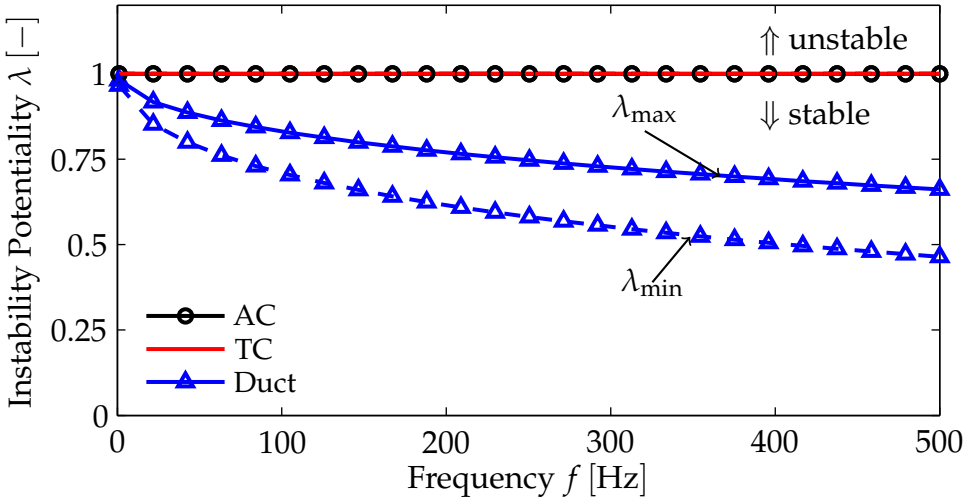

Figure 3.4: The instability potentiality of the acoustic two-ports described in the Section 3.2.4.2: a duct ($L = 10$m, $d_h = 0.05$m,$u_0 = 0.5c$), an area change ($\alpha = 1.5$) and a temperature discontinuity ($\Theta = 1.5$). All elements are not active because their maximum eigenvalue does not exceed unity.

Although energy conservation is not directly considered in the derivation of area changes (black lines & circles), these two-ports do not alter the acoustic energy content. Taking into account the damping effects in the description of discrete area changes, which are neglected here results in a decrease of λ_{min} below unity[4].

If both eigenvalues are less than unity, the element shifts from an acoustically neutral to passive behavior, because of energy dissipation. The investigated viscous duct is such a passive element. The damping effects due to viscous wall friction inside ducts scale with frequency. Moreover, the damping coefficient d scales with the inverse of the acoustic transport velocity $c \pm u_0$. The resident time of the wave traveling in the opposite direction of the mean flow velocity is larger than the one of the wave being transported with $c + u_0$. The wave experiences more cycles, which are each damped exponentially. Hence, the eigenvalues of the duct (blue lines & triangles), decay with different slope.

[3] The reader should be aware that the element still influences the reflection and transmission of $\mathfrak{F}$ and $\mathfrak{G}$ and thus contributes to the input control of other potentially unstable parts of the system.

[4] Combined area changes are generally capable of causing $\lambda_{\text{max}} > 1$. Thus, for example orifices and side branches have a certain "whistling potentiality".

The resonators and most of the thermoacoustic core components allow a network description in terms of the three two-ports considered. In classic thermoacoustic engines the stack or regenerator (and for certain configurations the heat exchangers) is the only expected acoustic amplifier. The instability potentiality of these acoustic elements is a qualitative indication for the amount of acoustic power generated by the complete device.

3.2.6 Analytical Solutions Obtained by the Green's Function Method

Special conditions allow for a partial simplification of the acoustic equations (NSE and EE) by substituting analytical solutions. In general, these formulations are derived from solving inhomogeneous linear differential equations. One of the most powerful tools to produce such solutions is the application of the Green's function (GF) method. Its advantage compared to most other techniques is that once the solution for the differential operator is obtained, the influence of any right-hand side term can be obtained by a convolution process. Besides finding analytical solutions for acoustic problems, it is applied in various other scientific fields: potential theory [90] and heat conduction [38] problems are investigated as well as differential equations describing quantum physics [49]. Here, this method is used to reduce the linearized NSEs derived in Chapter 4 from a multi-dimensional problem into a set of quasi one-dimensional ordinary differential equations describing the acoustic transport through a TA regenerator.

The characteristic GF $G(y|\hat{y})$ of a problem describes the response of the system to a Dirac impulse $\delta(y-\hat{y})$, i.e. a unit impulse located at $\hat{y}$. Due to the nature of this special right-hand side inhomogeneity, the convolution of $G(y|\hat{y})$ with any other kind of inhomogeneity $b(y)$ yields the corresponding response of the field.

In mathematical terms, the GF is the solution of the linear differential operator $\mathcal{L}(y)$ acting on a certain domain $y \in [y_{\min}, y_{\max}]$ following

$$\mathcal{L}(y)G(y|\hat{y}) = \delta(y-\hat{y}). \tag{3.48}$$

If the same operator $\mathcal{L}(y)$ is acting on $\vartheta(y)$ in combination with any arbitrary inhomogeneity $b(y)$, the solution of $\vartheta(y)$ can be easily found by

$$\vartheta(y) = \int_{y_{\min}}^{y_{\max}} G(y|\hat{y}) b(\hat{y})\, d\hat{y}. \tag{3.49}$$

There are different ways for obtaining the GF for a certain $\mathcal{L}$. Various methods are provided in textbooks [38, 41, 48], but their presentation is beyond the scope of this thesis. As the derivation process does not always lead to analytical formulations and sometimes is very cumbersome, the GFs determined are also listed in the references provided.

In Chapter 4, this thesis treats problems with a differential operator of the form

$$\mathcal{L}\left[\vartheta(y)\right] = \left[1 - \frac{1}{\alpha^2}\frac{\partial^2}{\partial y^2}\right] \vartheta(y). \tag{3.50}$$

Here, the complex-valued parameter α is constant in y. With this assumption, the corresponding GF reads

$$G(y|\hat{y}) = -\alpha\, \mathrm{H}(y-\hat{y})\, \sinh(\alpha(y-\hat{y})) + C_1(\hat{y})e^{\alpha y} + C_2(\hat{y})e^{-\alpha y}. \tag{3.51}$$

Here, $\mathrm{H}(y-\hat{y})$ denotes the Heaviside function. The integration constants C_i are determined by the required boundary conditions (BC). Including BCs of first kind (Dirichlet)

$$\vartheta(y_j) = g_j \tag{3.52}$$

and second kind (Neumann)

$$\left.\frac{\partial \vartheta}{\partial y}\right|_{y_k} = h_k, \tag{3.53}$$

the solution for $\vartheta(y)$ reduces to [38]

$$\vartheta(y) = \int_{\hat{y}=0}^{\hat{y}=L} G(y|\hat{y}) b(\hat{y})\, d\hat{y} + \frac{1}{\alpha^2}\sum_j g_j G(y|\hat{y}_j) - \frac{1}{\alpha^2}\sum_k h_k \left.\frac{\partial G(y|\hat{y})}{\partial \hat{y}}\right|_{\hat{y}=y_k}. \tag{3.54}$$

The first term describes the impact of the inhomogeneity. The contributions of all BC types scale with α^{-2}. In the investigated problem, the

field is fixed by a Dirichlet condition at the solid/fluid interface. The center of the pore displayed in Figure 2.2 is represented by a symmetry plane. With this BC at $y_k = 0$, h_k becomes zero and the third term in Equation (3.54), accounting for Neumann conditions, vanishes.

4 Inclusion of Mean Flow in Quasi One-dimensional Thermoacoustic Transport Equations

In this chapter, the one-dimensional TA modeling equations used hitherto are extended by explicitly considering mean flow. The existing system of ODEs have been derived by various authors applying different mathematical techniques. The traditional methods used by Rott [164, 165] or Swift [187] are restricted to the zero mean flow assumptions. Starting from the most general equations describing fluid flow – the Navier-Stokes Equations – , Peter in't panhuis [82] applies a series of general mathematical methods, which allow for different approximations in the intermediate steps. The schematic sketch of Figure 4.1 displays his

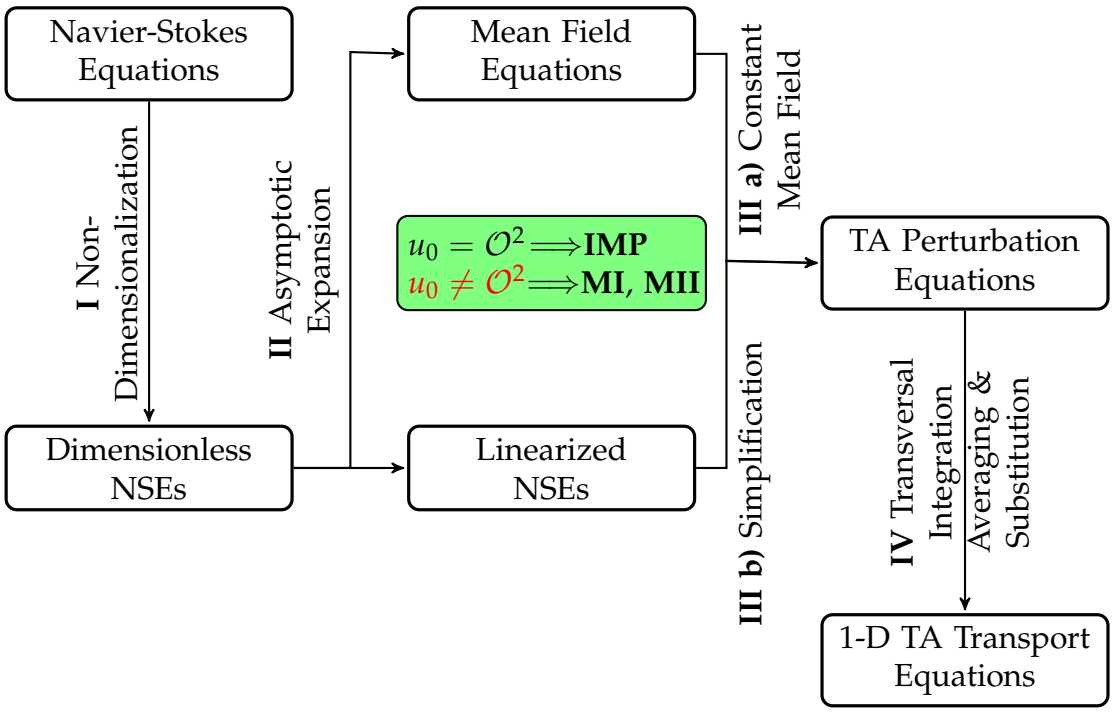

Figure 4.1: Derivation adapted from Peter in't panhuis [82]. In contrast to his procedure, the mean velocity u_0 inside the pore is not neglected a priori.

general procedure. After a problem specific non-dimensionalization (**I**) of the NSE, he applies a simplified asymptotic expansion (**II**) to the dimensionless NSEs by assuming u_0 being a quantity of second order in Ma. In the third step an analytical solution for the mean field quantities is found. Substituting the temporally constant mean field values (**III a)**) to the linearized NSEs (LNSEs) leads to a set of TA perturbation equations (TAPEs). A transversal integration and averaging of these ODEs by applying GF methods allows for substituting (**IV)**) all acoustic quantities except pressure p_1 and the cross-sectionally averaged velocity $\langle u_1 \rangle$ in the TAPEs. This leads to a description of the acoustic propagation in a one-dimensional model in terms of p_1 and the cross-sectional average of the velocity fluctuation $\langle u_1 \rangle$. This model is denoted as TA transport equations (TATEs).

The derivation presented here follows the same procedure. Section 4.1 repeats the non-dimensionalization step **I** of the derivation without differing from the former process. The formalism of the asymptotic expansion discussed in Section 4.2 is also similar to step **II** in Figure 4.1. However, the mean flow assumption is not invoked, which leads to different mean field equations and additional terms in the LNSEs containing explicit mean flow contribution, which are presented in Section 4.3 and Section 4.4. In the following, Section 4.5 provides a description of the way to an analytical formulation similar to the existing TA equations. For finding a solution, these changes require the introduction of modeling approximations that are discussed in Section 4.5.2. These simplifications are applied in step **III b)** of the derivation. Using these closure assumptions enables the application of the GF technique to cross-sectionally average the TAPEs **IV)**. In combination with the substitution, these processes are shown in detail in Section 4.5.3, following the process applied by in't panhuis [82]. This procedure leads to one-dimensional TA transport equations (TATEs) containing contributions of mean flow velocity u_0.

These TATEs describe the acoustic transmission through a narrow pore in the presence of a temperature gradient and mean flow. Using this set of equations, a numerical tool is implemented that facilitates the one-dimensional computation of scattering matrices of TA stacks affected by mean flow. Before the implementation of this tool is discussed in Section 4.6, the impact of the optional simplifications, which were intro-

duced in the modeling approaches is demonstrated and more accurate assumptions are incorporated in Section 4.5.4.

4.1 Dimensionless Two-Dimensional Navier-Stokes Equations

This section treats step **I** of the derivation, the non-dimensionalization of the general fluid transport equations. Due to the fact that the acoustic thermo-viscous boundary layer plays the most important role in generating the phase lag necessary for energy conversion in the TA effect, thermal diffusion and friction have to be considered in the modeling equations [170]. Thus, the NSE (Eqs. (3.2)) in combination with the conservation of mass (Eq. (3.1)) and the energy equation formulated in terms of Equation (3.6) are the basis of the derivation model.

A dimensionless consideration of the problem yields direct insight into the main parameter combinations controlling the transport behavior. Based on the Buckingham Π theorem [29], Olson and Swift [130] derived a dimensionless set quantifying the influence of the TA effect. As mean flow is neglected in their considerations, we follow Peter in't panhuis et al. [81], where the set of equations is first non-dimensionalized and then the terms containing mean flow contribution are neglected.

The system of equations is formulated in Cartesian coordinates x, y, z. As the problem considered is two-dimensional, the governing equations, that is mass continuity (Eq. (3.1)), NSEs (Eqs. (3.2)) and the energy Equation (3.6), are reduced to their two-dimensional form in space. Body forces, especially buoyancy effects, are neglected in this approach. Nevertheless, if convective effects dominate the mean flow field, these terms should be considered carefully.

The set of parameters describing the problem are

$$t,\ \boldsymbol{x} = (x,y)^T,\ \boldsymbol{v} = (u,v)^T,\ \varrho,\ p,\ T,\ \beta,\ K,\ c_p,\ \boldsymbol{\tau},\ \mu,\ \zeta \tag{4.1}$$

for the fluid domain and

$$K_S,\ c_S,\ \varrho_S \tag{4.2}$$

for the solid domain. Those quantities are non-dimensionalized by the set of reference parameters

$$L,\ R,\ c_{\mathrm{ref}},\ K_{\mathrm{ref}},\ \varrho_{\mathrm{ref}},\ c_{p,\mathrm{ref}},\ \mu_{\mathrm{ref}},\ \zeta_{\mathrm{ref}},\ K_{S,\mathrm{ref}},\ c_{S,\mathrm{ref}} \text{ and } \varrho_{S,\mathrm{ref}}. \tag{4.3}$$

As the boundary layers play a crucial role in the investigated geometries, we follow the non-dimensionalization technique from boundary-layer theory [175] and scale transversal and viscous components by a second geometrical length scale, that is the pore radius R. Introducing the ratio of (geometric) dimensions

$$\varepsilon = \frac{R}{L}, \tag{4.4}$$

the dimensionless parameters ($\tilde{}$) are defined by

$$\begin{aligned}
&x = L\,\tilde{x} \qquad y = R\,\tilde{y} \qquad t = \frac{L}{c_{\mathrm{ref}}}\,\tilde{t} \qquad u = c_{\mathrm{ref}}\,\tilde{u} \quad v = \varepsilon c_{\mathrm{ref}}\,\tilde{v}\\
&\varrho = \varrho_{\mathrm{ref}}\,\tilde{\varrho} \quad p = \varrho_{\mathrm{ref}} c_{\mathrm{ref}}^2\,\tilde{p} \quad T = \frac{c_{\mathrm{ref}}^2}{c_{p,\mathrm{ref}}}\,\tilde{T} \qquad c = c_{\mathrm{ref}}\,\tilde{c} \quad \beta = \frac{c_{p,\mathrm{ref}}}{c_{\mathrm{ref}}^2}\,\tilde{\beta}\\
&K = K_{\mathrm{ref}}\,\tilde{K} \quad c_p = c_{p,\mathrm{ref}}\,\tilde{c}_p \qquad \boldsymbol{\tau} = \frac{\mu_{\mathrm{ref}}\, c_{\mathrm{ref}}}{R}\,\tilde{\boldsymbol{\tau}} \quad \mu = \mu_{\mathrm{ref}}\,\tilde{\mu} \quad \zeta = \zeta_{\mathrm{ref}}\,\tilde{\zeta}.
\end{aligned} \tag{4.5}$$

As shown in Section 1.2, the non-isentropic changes of thermodynamic state in the acoustic boundary layers cause the phase shifts necessary for the occurrence of the thermoacoustic effect. Their characteristic length scales δ, that is the viscous δ_ν, δ_ζ and the thermal δ_K, δ_S boundary layer thicknesses are defined by

$$\begin{aligned}
\delta_\nu &= \sqrt{\frac{2\mu_{\mathrm{ref}}}{\omega\,\varrho_{\mathrm{ref}}}}, & \delta_\zeta &= \sqrt{\frac{2\zeta_{\mathrm{ref}}}{\omega\,\varrho_{\mathrm{ref}}}},\\
\delta_K &= \sqrt{\frac{2K_{\mathrm{ref}}}{\omega\,\varrho_{\mathrm{ref}}\,c_{p,\mathrm{ref}}}} \qquad \text{and} & \delta_S &= \sqrt{\frac{2K_S}{\omega\,\varrho_S\,c_S}}.
\end{aligned} \tag{4.6}$$

Comparing these quantities to the pore height R and the pore length L are typical dimensionless parameters for similarity considerations of TA devices. Using these parameters leads to the typical set of dimensionless numbers displayed in Table 4.1. Note that the Lautrec number La is related to the Womersley number Wo by the Prandtl number, that is

$$\mathrm{Pr} \equiv \frac{\mu_{\mathrm{ref}} c_{p,\mathrm{ref}}}{K_{\mathrm{ref}}} = \frac{\delta_\nu^2}{\delta_K^2} = \frac{\mathrm{La}^2}{\mathrm{Wo}^2}. \tag{4.7}$$

Symbol	Formula	Description
γ	$\frac{c_p}{c_v}$	heat capacity ratio
ε	$\frac{R}{L}$	ratio of dimensions
ϕ	$\frac{R}{R+R_S}$	porosity
σ	$\frac{K_S}{K_{\mathrm{ref}}}$	thermal conductivities ratio
κ	$\frac{\omega L}{c}$	Helmholtz number
Ma	$\frac{u}{c}$	Mach number
La	$\frac{R}{\delta_K}$	fluid Lautrec number
La_S	$\frac{R}{\delta_S}$	stack Lautrec number
Wo	$\frac{R}{\delta_\nu}$	Womersley number based on δ_ν
Wo_ζ	$\frac{R}{\delta_\zeta}$	Womersley number based on δ_ζ

Table 4.1: Dimensionless numbers of narrow pores

The Strouhal number Sr, which is often used in duct acoustics, is identical to

$$\mathrm{Sr} \equiv \frac{\omega R}{U} = \frac{\kappa\varepsilon}{\mathrm{Ma}}. \tag{4.8}$$

For ease of presentation, all thermophysical properties are considered to be constant for the presented set of equations. Nevertheless, in the implemented application this simplification is not applied and the data are taken from tabulated values [201]. Furthermore, the tildes denoting non-dimensional parameters are removed.

Applying the non-dimensional set of reference quantities given in Table 4.1 to the governing equations (Eq. (3.1), Eqs. (3.2) and Eq. (3.6)) and the equation of state (Eq. (3.7)) yields

$$\frac{D\varrho}{Dt} = -\varrho\left(\frac{\partial u}{\partial x} + \frac{\partial v}{\partial y}\right), \tag{4.9a}$$

$$\begin{aligned}\varrho\frac{Du}{Dt} = &-\frac{\partial p}{\partial x} + \frac{\kappa}{\mathrm{Wo}^2}\frac{\partial^2 u}{\partial y^2} \\ &+ \varepsilon\left[\frac{\kappa}{\mathrm{Wo}_\zeta^2}\left(\frac{\partial^2 v}{\partial y^2} + \frac{\partial^2 u}{\partial x \partial y}\right) + \frac{3\kappa}{\mathrm{Wo}^2}\frac{\partial^2 u}{\partial x \partial y}\right] + A_1\left(\mathcal{O}\left(\varepsilon^2\right)\right),\end{aligned} \tag{4.9b}$$

$$0 = -\frac{\partial p}{\partial y} + \varepsilon \frac{\kappa}{\mathrm{Wo}^2} \frac{\partial^2 u}{\partial y^2} + A_2 \left(\mathcal{O}\left(\varepsilon^2\right) \right), \tag{4.9c}$$

$$\varrho \frac{DT}{Dt} = \beta\, T \frac{Dp}{Dt} + \frac{\kappa}{2\mathrm{La}^2} \frac{\partial^2 T}{\partial y^2} + \frac{\kappa}{\mathrm{Wo}^2} \frac{\partial u}{\partial y}^2 + A_3 \left(\mathcal{O}\left(\varepsilon^2\right) \right), \tag{4.9d}$$

$$p = \frac{\gamma - 1}{\gamma}\, T\, \varrho. \tag{4.9e}$$

In this formulation, the transversal momentum equation (Eq. (4.9c)) was divided by ε^2 in order to obtain terms of order zero in ε.

Choosing an alternative coordinate system (x, y_S) at the center of the solid part (see Fig. 2.2) and R_S as transversal parameter of non-dimensionalization, the porosity vanishes in the energy equation of the solid:

$$\varrho_S \frac{\partial T}{\partial t} = \frac{\kappa}{2\mathrm{La}_S^2} \frac{\partial^2 T}{\partial y_S^2} + A_4 \left(\mathcal{O}\left(\varepsilon^2\right) \right). \tag{4.9f}$$

Here, the terms $A_i \left(\mathcal{O}\left(\varepsilon^2\right) \right)$ contain higher-order contributions of the ratio of pore dimensions. In the following section, these quantities are neglected. Please refer to Section A.1 for further information on these terms.

The transversal boundary conditions for the geometric setup with constant pore cross-section are non-dimensionalized in the same way as the governing equations. For the velocity and temperature field they read

$$u(x, y = \pm 1) = 0, \tag{4.10a}$$

$$v(x, y = \pm 1) = 0, \tag{4.10b}$$

$$T(x, y = \pm 1) = T_S(x, y_S = \pm 1), \tag{4.10c}$$

$$\left.\frac{\partial T}{\partial y}\right|_{y=\pm 1} = \sigma \left.\frac{\partial T_S}{\partial y_S}\right|_{y_S=\pm 1}, \tag{4.10d}$$

$$\left.\frac{\partial T_S}{\partial y_S}\right|_{y_S=0} = 0. \tag{4.10e}$$

4.2 Asymptotic Expansion

As stated in Section 3.2.1, carrying out an asymptotic expansion of the basic set of equations assuming mean properties constant in time lead

to the set of governing equations describing acoustic wave propagation. This technique is applied out in step **II** of the derivation depicted in Fig. 4.1. Different expansion techniques can be found in literature. The linearization techniques applied in most TA publications are rather restrictive [187], decomposing all transported scalars in terms of

$$\Psi(x,y,t) = \Psi_0(x) + \mathfrak{Re}\left[\Psi_1(x,y)\,\mathbf{e}^{\mathrm{i}\omega t}\right] + \dots . \tag{4.11}$$

This formulation only accounts for the values acquired during the measurement of acoustic quantities. Additionally, not considering the imaginary components in the resulting equations prohibits a stability analysis of any problem considered. The harmonic ansatz $\mathbf{e}^{i\omega t}$ in time separates acoustic oscillations from turbulent fluctuations. As the laminar regime is treated, the latter magnitudes are estimated to be orders of magnitudes smaller than the acoustic counterpart.

Moreover, the expansion of the velocity vector v has no mean contribution. Most authors justify this assumption by trying to suppress mean flow without providing any physical justification. In the present work, this limitation is removed by adopting a different approach. The zeroth-order quantity of v is only a function of the axial coordinate x. As long as mean flow is neglected, this approach is valid for inner pores with a mean temperature field that is not affected by multi-dimensional heat conduction effects due to heat transfer to the periphery.

The non-dimensionalization entails a transformation of the harmonic oscillation in time into the Helmholtz number (κ) space. The general asymptotic expansion similar to Equation (3.9) then reads for an arbitrary variable, i.e. the transport variables p, u, v, T, ϱ, but also the thermophysical properties of the solid and fluid region

$$\begin{aligned}\Psi(x,y,t) = {} & \Psi_0(x,y) + \mathrm{Ma_a}\,\Psi_1(x,y)\mathbf{e}^{i\kappa t} \\ & + \mathrm{Ma_a}^2\left(\Psi_{2,0}(x,y) + \Psi_{2,1}(x,y)\mathbf{e}^{2i\kappa t}\right) + \mathcal{O}(\mathrm{Ma_a}^3).\end{aligned} \tag{4.12}$$

The first term scaling with $\mathrm{Ma_a}^2$ (index 0,2) is constant in time. It results from the squared exponent of the complex valued frequency.

Thermophysical properties of fluids and solids are often assumed to be constant. If this approach is too inaccurate for the considered problem, these quantities are computed as smooth functions of temperature and

pressure (Section 3.1.5). As their relative change is always smaller than the change in the corresponding primary variables, all thermophysical property contributions other than zeroth order are negligible. Thus, they are considered as pure functions of the mean quantities, which in particular leads to

$$\beta = \frac{1}{T_0(x,y)} \tag{4.13}$$

for the compressibility β of the gas.

In the present derivation, the asymptotic expansion is simplified further by assuming

$$\Psi_0(x,y,t) = \langle \Psi_0 \rangle. \tag{4.14}$$

The angle brackets of the right hand side term indicate a transversal average over the channel height H

$$\langle \Psi \rangle = \frac{2}{H} \int_0^{H/2} \Psi(x,y)\, dy. \tag{4.15}$$

This renders the mean quantities independent of the y-direction, which is only valid for zero mean flow conditions. All preceding one-dimensional models from Reid's [158, 187] and in't panhuis [80], which consider the impact of mean flow follow the same approach for the mean flow quantities they take into account. The assumption of only considering mean parameters to be cross-sectionally constant is per se not physical and thus a modeling approach, which is necessary to keep the resulting system of equations of the order of $\mathrm{Ma_a}$ manageable. Only if certain conditions of comparably negligible mean flow boundary layers arise in the problem, the error impact of the modeling approach is small.

The choice of this assumption causes the intermediate steps of the derivation to be enhanced by one single parameter $\langle u_0 \rangle(x)$ compared to the derivation of in't panhuis [80]. mean velocity must be justified by physical considerations: A comparison between the laminar velocity profiles inside a channel and the acoustic profiles of Rott's solution (Eqs. (2.1)) yields some insight into the interaction of acoustics and mean flow in the thermoacoustic boundary layers. The mean velocity profiles $u_0(x,y)$

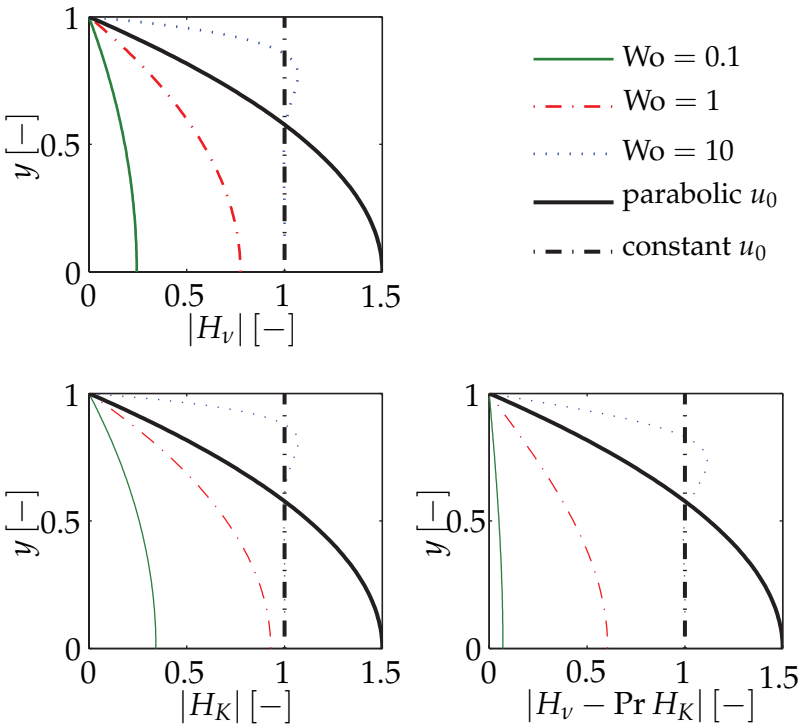

Figure 4.2: The three spatial contributions to the acoustic parameters under zero mean conditions for air and $Wo = 0.1, 1, 10$ and two different mean flow profiles.

(solid lines) and $\langle u_0 \rangle(x)$ (dashed lines) are depicted in Figure 4.2 by thick curves. The analytical solution of a Poiseuille flow inside a channel reads

$$u_0(x,y) = \langle u_0 \rangle(x) \frac{3}{2} \left(1 - \frac{2y}{H}\right)^2 . \tag{4.16}$$

The spatially resolved thermoacoustic equations implying stagnant mean flow contain three terms which change in y-direction [187]:

1. Viscous dissipation due to wall friction scales with H_ν in the conservation of axial momentum[1].

[1] Strictly speaking, the viscous contribution is described by the term scaling with $1 - H_\nu$. The same accounts for thermal diffusion.

2. Thermal diffusion H_K to the walls is taken into account in the energy equation. Using a dimensionless transversal coordinate y, those terms read

$$H_\nu = 1 - \frac{\mathrm{Cosh}\left((1+i)\mathrm{Wo}\, y\right)}{\mathrm{Cosh}\left((1+i)\mathrm{Wo}\right)}$$
$$H_K = 1 - \frac{\mathrm{Cosh}\left((1+i)\mathrm{La}\, y\right)}{\mathrm{Cosh}\left((1+i)\mathrm{La}\right)} \tag{4.17}$$

   in dimensionless form. Their absolute values are displayed in the left plots of Figure 4.2 by thin lines.

3. The TA conversion term also depends on these functions in terms of

$$H_\nu - \mathrm{Pr}\, H_K, \tag{4.18}$$

   which has a similar shape.

For low Wo the corresponding profiles are almost parabolic. Higher Wo lead to a narrower non-constant region near the wall and a quasi-constant profile near the center line. A product of these terms with a constant mean velocity field $\langle u_0 \rangle(x)$ enhances the near wall contribution compared to the more physical parabolic profile. The acoustic boundary layer effects are thus overestimated for such combinations. These products are additional terms that are smaller than the existing terms in the laminar, low Ma regime. However, the reader should keep in mind that the approximation of constant mean velocity $u_0(x, y) = \langle u_0 \rangle(x)$ overestimates these contributions.

The transversal profile of the mean temperature T_0 for Poiseuille conditions is also parabolic. In contrast to the mean velocity u_0 its value does not become zero at the solid interface. Thus, the mismatch obtained in terms containing the product of T_0 and the transversal acoustic profiles is smaller. Furthermore, the influence of axial temperature changes onto the generic problem is orders of magnitude larger than the changes in cross-sectional contribution.

4.2.1 Narrow Pore and Linear Acoustics Assumption

The full system of Equations (4.9) is a general formulation affected by the geometrical ratio of dimensions of the pore

$$\varepsilon = \frac{R}{L}. \tag{4.19}$$

If $\varepsilon \approx 1$ and friction or thermal diffusion terms are of similar order, the full system of equations needs to be considered. In contrast, in narrow pores with $\varepsilon \ll 1$ as they occur in TA regenerators, these terms become negligible.

Acoustic quantities are generally of the order of [160]

$$\mathrm{Ma}_a \approx \frac{p_1}{p_0} \lesssim 0.05. \tag{4.20}$$

Thus, the terms scaling with either ε or Ma_a have a similar contribution in the expanded system of equations. Here, we follow Peter in't panhuis [80], assuming

$$\mathrm{Ma}_a \sim \varepsilon^2, \tag{4.21}$$

which accounts for a low ratio of ε and linear acoustics. This approach yields a combined influence of geometric and acoustic streaming effects in one system of equations of higher order, where combinations of $c_0 {\mathrm{Ma}_\mathrm{a}}^n + c_1 {\mathrm{Ma}_\mathrm{a}}^{n-1}\varepsilon + ... + c_m {\mathrm{Ma}_\mathrm{a}}^{n-m}\varepsilon^m + ...c_n\varepsilon^n$ balance. Findings based on this system provide information about the impact of both parameters.

Applying Equation (4.21) and Equation (4.20) to the asymptotically expanded system of governing Equations ((4.9a)-(4.9e)), the system is separated in groups of terms scaling with the order of Ma_a. As the zeroth-order group is time invariant and we consider the linear acoustic regime, the mean parameters have to fulfill the corresponding set of equations. Applying the same argument to the first-order terms directly yields a linearized system of equations describing the spatial and temporal evolution of acoustic parameters.

4.3 Determination of Mean Field Quantities

The mean flow field is a set of temporally constant values providing background information for the acoustic transport equations. It is the result of step **II** of this derivation, the asymptotic expansion. With the chosen asymptotic expansion (3.9) and (4.14) , all transversal derivative terms become zero and the full system of equations describing mean transport processes reads

$$\langle u_0 \rangle \frac{\partial \langle \varrho_0 \rangle}{\partial x} = -\langle \varrho_0 \rangle \frac{\partial \langle u_0 \rangle}{\partial x}, \tag{4.22a}$$

$$\langle \varrho_0 \rangle \langle u_0 \rangle \frac{\partial \langle u_0 \rangle}{\partial x} = -\frac{\partial \langle p_0 \rangle}{\partial x}, \tag{4.22b}$$

$$\langle \varrho_0 \rangle \langle u_0 \rangle \frac{\partial \langle T_0 \rangle}{\partial x} = \beta \, \langle T_0 \rangle \langle u_0 \rangle \frac{\partial \langle p_0 \rangle}{\partial x}, \tag{4.22c}$$

$$\langle p_0 \rangle = \frac{\gamma - 1}{\gamma} \, \langle T_0 \rangle \, \langle \varrho_0 \rangle. \tag{4.22d}$$

The form of this system of equations is especially attributed to the cross-sectional means approach of (4.14). The cross-sectional average is only exact, if it is carried out for each term of the equations, e.g. the first term of (4.22a) should read $\langle u_0 \frac{\partial \varrho_0}{\partial x} \rangle$. Thus, Equation (4.22a) only accounts for conditions of $u_0(x, y) = u_0(x)$ or $\varrho_0(x, y) = \varrho_0(x)$. The problems considered here are always related to wall interaction. Unless the mean flow velocity becomes zero, the contact condition leads to cross-sectional variations in u_0. Equation (4.9c) directly yields a constant pressure distribution in this direction, hence

$$\langle p_0(x, y) \rangle = p_0(x). \tag{4.23}$$

Thus, the ideal gas law (Eq. (4.9e)) states, that cross-sectional shape of $\varrho_0(x, y)$ is a function of the transversal mean temperature profile. Comparing the spatial changes in these two quantities, the axial variation always exceeds the transversal changes. Hence, this approach may be valid under certain conditions.

Under these assumptions, the transversal velocity component $\langle v_0 \rangle$ vanishes, because the flow field is confined by the stack walls.

An integral consideration of Equation (4.9a) states that the mass flux at the reference position is conserved and thus,

$$\langle u_0(x)\varrho_0\rangle(x) = \langle u_0\rangle(0)\langle\varrho_0\rangle(0) = \mathrm{Ma} \tag{4.24}$$

is exact, if the inlet quantities have block profile. The profile of the mean density scales with the inverse of the cross-sectional temperature variation. The ratio of

$$\frac{R\lambda}{\varrho_{\mathrm{ref}} c_{p,\mathrm{ref}} c_{\mathrm{ref}} \mathrm{Ma}} \tag{4.25}$$

scales the variation of the magnitude of this profile. In common thermoacoustic devices this quantity is very small. Thus, assuming

$$\varrho_0 \approx \langle\varrho_0\rangle \tag{4.26}$$

is a good approximation as well as expecting the mean temperature to be transversally constant with respect to its variation in axial direction. The form of the axial momentum equation (Eq. (4.22b)) is totally inappropriate for the computation of the axial pressure gradient, which is the driving force for the mean flow. In the conditions observed, a shear stress rather than inertia balances the pressure gradient. Hence, neglecting the left hand side of Equation (4.9b), it states that

$$\frac{\partial p_0(x)}{\partial x} \simeq \frac{\kappa}{\mathrm{Wo}^2}\frac{\partial^2 u_0}{\partial y^2} = \frac{1}{\mathrm{Re}_c \varepsilon}\frac{\partial^2 u_0}{\partial y^2}. \tag{4.27}$$

Here, the Reynolds number

$$\mathrm{Re}_c = \frac{cR}{\nu} \tag{4.28}$$

is computed using the speed of sound. Moderate ratios of dimensions $1 \gg \varepsilon \gg \frac{1}{Re_c}$ cause small pressure gradients. Further, computing the second transversal derivative of the dimensionless form of Equation (4.16) leads to

$$\frac{\partial^2 u_0}{\partial y^2} = \frac{3}{2}u_0. \tag{4.29}$$

Hence, if the first condition coincides with low Mach numbers, this term has a smaller contribution than other terms that scale with mean flow and thus may be neglected.

Although the transversal mean temperature dependency is neglected, the averaged mean temperature distribution $\langle T_0 \rangle(x)$ includes the impact of the different thermal conductivities inside solid material and the fluid. These two quantities are replaced by a mean conductivity $\langle K \rangle$

$$\langle K \rangle = (1 - \phi)\, K_{S,\mathrm{ref}} + \phi K_{\mathrm{ref}}, \tag{4.30}$$

in a one-dimensional energy transport equation in terms of the mean temperature $\langle T_0 \rangle(x)$. Merging this approach into the conductive term of the temperature transport equation in dimensional form reads

$$c_p \varrho u \frac{d\langle T_0 \rangle}{dx} = \frac{d}{dx}\left[\langle K \rangle \frac{d\langle T_0 \rangle}{dx} \right]. \tag{4.31}$$

Introducing the Peclet number

$$\mathrm{Pe} = \frac{c_{p,\mathrm{ref}} \varrho_{\mathrm{ref}} c_{\mathrm{ref}} L}{\langle K \rangle_{\mathrm{ref}}}, \tag{4.32}$$

the dimensionless form of this equation reads

$$c_p \mathrm{Ma}\, \mathrm{Pe} \frac{d\langle T_0 \rangle}{dx} = \frac{d}{dx}\left(\frac{\langle K \rangle}{\langle K \rangle_{\mathrm{ref}}} \frac{d\langle T_0 \rangle}{dx} \right). \tag{4.33}$$

Material properties are solely functions of the mean temperature $\langle T_0 \rangle$ at constant pressure p_0. In this thesis, the axial temperature profile is determined in terms of upstream and downstream Dirichlet BCs $T(x = 0) = T_u$ and $T(x = L) = T_d$. Applying the parameters of non-dimensionalization from Equation (4.5), the mean temperature $\langle T_0 \rangle$ profile is fixed by the boundary values

$$\langle T \rangle|_0 = \frac{1}{\gamma - 1} \tag{4.34a}$$

$$\langle T \rangle|_1 = \frac{T_d}{(\gamma - 1)\, T_u}. \tag{4.34b}$$

If constant thermophysical properties are assumed an analytical solution for this differential equation can be found. Inserting the boundary conditions leads to

$$\langle T \rangle_0(x) = \frac{\left[\left(\frac{T_d}{T_u} - 1 \right) e^{\mathrm{Pe}x}) + \left(e^{\mathrm{Pe}} - \frac{T_d}{T_u} \right) \right]}{(\gamma - 1)\left(1 + e^{\mathrm{Pe}} \right)}. \tag{4.35}$$

Assuming small changes in the thermophysical properties leads to small variations from this profile.

If the transversal temperature profile is not assumed to be constant, Equation (4.33) still accounts for the averaged mean temperature. Nevertheless, under some assumptions an analytical solution can be obtained. The solution of a Poiseuille flow that is a fully developed incompressible flow through a channel with walls of constant temperature yields a parabolic cylinder solution [79] (see also Eq. (4.16)). If the thermal penetration depth is larger than the hydraulic radius of the pore, this profile can be used as an approximation for transversal profile of $u_0(x,y)$ and $T_0(x,y)$ inside the compressible flow with axially varying wall temperatures.

4.4 Linearized Navier-Stokes Equations

Substituting the results obtained for the mean parameters into the linearized NSEs (Eqs. (4.9)) yields a simplified system of equations. Further, applying the harmonic approach $\Psi_1(x,y,t) = \Psi_1(x,y)\mathbf{e}^{i\kappa t}$ to the time derivatives $\frac{\partial \Psi_1}{\partial t}$, enables a transformation of the system of equations into frequency space:

$$\varrho_1 = \frac{\gamma}{c^2} p_1 - \frac{\varrho}{T} T_1 \tag{4.36a}$$

$$\left(\mathrm{i}\kappa + \frac{\partial u}{\partial x}\right) \varrho_1 + u\frac{\partial \varrho_1}{\partial x} = -\varrho \left(\frac{\partial v_1}{\partial y} + \frac{\partial u_1}{\partial x}\right) - \frac{\partial \varrho}{\partial x} u_1 \tag{4.36b}$$

$$\varrho \left(\mathrm{i}\kappa + \frac{\partial u}{\partial x}\right) u_1 + \underbrace{u\varrho\frac{\partial u_1}{\partial x}}_{\mathbf{\Lambda}_1} = -\frac{\partial p_1}{\partial x} + \frac{\kappa\mu}{\mathrm{Wo}^2}\frac{\partial^2 u_1}{\partial y^2} \tag{4.36c}$$

$$0 = -\frac{\partial p_1}{\partial y} \tag{4.36d}$$

$$\mathrm{i}\kappa c_p \varrho T_1 + \underbrace{u\varrho c_p \frac{\partial T_1}{\partial x}}_{\mathbf{\Lambda}_2} = -c_p \frac{\partial T}{\partial x}\varrho u_1 - c_p \frac{\partial T}{\partial x} u \varrho_1 + \mathrm{i}\kappa p_1 + T u \frac{\partial p_1}{\partial x} + \frac{\kappa K}{2\mathrm{La}^2}\frac{\partial^2 T_1}{\partial y^2} \tag{4.36e}$$

$$- \boxed{\tfrac{u}{T}\tfrac{\partial p}{\partial x} T_1} - \boxed{\tfrac{\partial p}{\partial x} u_1}$$

$$\mathrm{i}\kappa c_S \varrho_S \, T_{S,1} = \frac{\kappa K_S}{2\mathrm{La}_S^2} \frac{\partial^2 T_{S,1}}{\partial y^2}. \tag{4.36f}$$

In the following, this system of equations is referred to as the thermoacoustic perturbation equations (TAPEs). Here and from now on, the index Ψ_0 as well as the spatial averaging $\langle \Psi \rangle$ symbol is dropped for all mean quantities.

The gray boxed terms in Equations (4.36) (explicitly) include contributions from mean velocity u. They have not been considered in previous studies [80, 170, 187]. All these terms describe the explicit impact of a transversally averaged mean flow onto the acoustic fields inside a narrow pore. If those gray boxed terms are dropped from Equations (4.36), the system of equations of Peter in't panhuis et al. [82] is recovered.

4.5 One-Dimensional Thermoacoustic Transport

This section treats the steps denoted by **III b)** and **IV** in the sketch of the derivation displayed in Figure 4.1. They treat the cross-sectional averaging process and substitution of parts of the equations obtained, which lead to the TATEs, i.e. one-dimensional transport equations in p_1 and u_1.

An analytical solution for the set of acoustic transport Equations (4.36) is not known. Thus, further simplifications and closure assumptions are introduced in order to develop an analytical description of the y-dependent components in the set of Equations (4.36) by following the sequence of steps listed in Table 4.2. Averaging these equations over the cross-section yields a one-dimensional description of the axial transport of all acoustic variables. Eliminating v_1, T_1, $T_{S,1}$ and ϱ_1 from this set of equations leads to a set of ODEs in terms of p_1, u_1 describing the averaged acoustic transport through a narrow geometry affected by mean flow $u(x)$ and non-constant temperature field $T(x)$.

Step	Equations	Methods Applied	Result
1	(4.36d)	Transversal Integration	$p_1(x,y) = p_1(x)$
2	(4.36c)	a) Modeling of $\mathbf{\Lambda}_1$ b) Green's Function Method c) Transversal Integration	$\frac{\partial p_1}{\partial x} = A_{11}(x)u_1(x)$
3	(4.36e) & (4.36f)	a) Modeling of $\mathbf{\Lambda}_2$ b) Green's Function Method c) Boundary Coupling d) Transversal Integration	$T_1(x) = f(u_1(x), p_1(x))$
4	(4.36a)	a) Transversal Integration b) Substituting	$\varrho_1(x) = f(u_1(x), p_1(x))$
5	(4.36b)	a) Transversal Integration b) Substituting	$v_1(x) = 0$ $\frac{\partial u_1}{\partial x} =$ $A_{21}(x)u_1(x) + A_{12}(x)p_1(x)$
6		Combination of Step 2 & 5	$\frac{d}{dx}\begin{pmatrix} p_1 \\ \langle u_1 \rangle \end{pmatrix} = \boldsymbol{A}(x)\begin{pmatrix} p_1 \\ \langle u_1 \rangle \end{pmatrix}$

Table 4.2: Overview of the segregated mathematical steps applied to the TAPEs that lead to a system of ODEs (TATEs) in terms of p_1 and u_1 .

4.5.1 Simplification Approaches

Determining the order of magnitude of the nine gray-boxed terms in the TAPEs (Eqs. (4.36)) is not trivial. Some terms scale with ϱu, which is the reference Mach number (see Eq. (4.24)). Their contribution should be retained if a high accuracy in the predicted results is required.

Both terms in the third line of Equation (4.36e) scale with the mean pressure gradient. Following Equation (4.27) the pressure gradient is proportional to $\frac{\mathrm{Ma}}{\mathrm{Re}_c \varepsilon}$, which is small in the cases considered here. The first term, which is a function of T_1, even scales with Ma^2 is very small for $\mathrm{Ma} \ll 1$. The second term scales with the acoustic velocity and also plays a minor role under the conditions met in the reference problem. Both are omitted in the further derivation but still allow for following the same derivation procedure presented here.

4.5.2 Closure Assumptions

For the solution steps (2 & 3) listed in Table 4.2, two closure assumptions need to be found. This section discusses the nature of these assumptions and suggests modeling approaches, which are applied in the later derivation.

The derivation of Peter in't panhuis et al. [80] involves the application of the GF method on the axial momentum Equation (4.36c) to find an analytical solution for the transversal profile of the velocity oscillation $u_1(x,y)$. Proceeding in the same manner implies finding a GF for the differential operator

$$\mathcal{L}_\nu = \varrho\left(\mathrm{i}\kappa + \frac{\partial u}{\partial x}\right) + \underbrace{\mathrm{Ma}\frac{\partial}{\partial x}}_{\mathbf{\Lambda}_1} - \frac{\kappa\mu}{\mathrm{Wo}^2}\frac{\partial^2}{\partial y^2}. \tag{4.37}$$

In contrast to the derivation for stagnant flow conditions, this differential operator $\mathcal{L}_\nu$ contains a x-derivative term denoted by $\mathbf{\Lambda}_1$. Thus, the operator is no exclusive operator in the transversal direction. No proper analytical GF can be found for this operator. For finding an analytical one-dimensional description of the TA transport through the pore, a closure assumption has to be made by modeling this term.

The same technique applied to Equation (4.36d) is used to solve the energy equations (Eqs. (4.36e) and (4.36f)). Again, the first of those two equations contains an axial derivative term $\mathbf{\Lambda}_2$ that is part of the differential operator

$$\mathcal{L}_k = \left[\mathrm{i}\kappa c_p\varrho + \underbrace{\mathrm{Ma}\, c_p\frac{\partial}{\partial x}}_{\mathbf{\Lambda}_2} - \frac{\kappa K}{2\mathrm{La}^2}\frac{\partial^2}{\partial y^2}\right], \tag{4.38}$$

acting on the fluid temperature oscillation T_1. Due to the similarity of those terms, the second necessary closure assumption should be chosen in accordance with the modeling of $\mathbf{\Lambda}_1$.

The modeling of $\mathbf{\Lambda}_i$ has to fulfill certain requirements:

- The assumed model should be as physical as possible.

Term	Character	Model	
		MI	**MII**
$\frac{\partial u_1}{\partial x}$	$\mathbf{\Lambda}_1$	0	$\frac{\partial \langle u_1 \rangle}{\partial x}\Big\vert_{u_0=0}$
$\frac{\partial T_1}{\partial x}$	$\mathbf{\Lambda}_2$	0	$\frac{\partial \langle T_1 \rangle}{\partial x}\Big\vert_{u_0=0}$

Table 4.3: Overview over the modeled terms. Choosing different closure assumptions leads to different results in the one-dimensional transport equations (**MI**, **MII**).

- The basic shape of the GF for the $\mathcal{L}_i$ considered should not be dominated by the modeled term. Thus, if parts of the model contribute to $\mathcal{L}_i \Psi_1$, they should be formulated in terms of Ψ_1 and its second transversal derivative $\frac{\partial^2 \Psi_1}{\partial y^2}$.
- Such model terms do not have to be constant in y but their mathematical formulation should lead to an analytical GF.
- The y-profile of the source terms has to be known before Equation (3.54) can be applied to find an analytical solution. Therefore, the transversal evolution of all contributions that do not include the sought variable Ψ should be given.

With these restrictions, two different basic assumptions can be found to model the closure terms in a first step:

MI: As the terms $\mathbf{\Lambda_i}$ scale with Ma, their contribution can be neglected and both terms vanish. This approach keeps the resulting system of equations short. However, this approach is not consistent, because other mean flow terms in Equation (4.36) also scale with Ma.

MII: The analytical solution for stagnant mean conditions is known. As this thesis deals with laminar mean flow conditions, the low velocity limit is described by these equations. The accuracy of this approach is estimated to decrease in the same way as the first approach. This initial approach is simplified here, such that only a transversally averaged version of the terms is applied.

Iteratively substituting the results of these approaches may lead to more accurate results unless an intermediate solution does not fulfill the re-

quirements stated before. The mathematical formulation for the terms $\mathbf{\Lambda}_i$ of these two models are gathered in Table 4.3.

Using these closure assumptions, an analytical solution may be obtained from Equations (4.36). To keep the derivation more general, the terms are not explicitly substituted, but replaced by two placeholders $\mathbf{\Lambda}_i$ in the derivation in the next section.

4.5.3 Spatial Averaging of the TAPEs

Here, the cross-sectional averaging of the system of Equations (4.36) is treated. Due to the huge amount of terms that occur in this process, the pertinent terminology is briefly explained. The blackboard bold capital letters (e.g. $\mathbb{E}$) indicate the equation into which the replacement character is introduced. The overbar ($\overline{\Phi}$) marks the terms stemming from transversally averaged equations. The indices refer to different issues. They either indicate the corresponding prefactors the term multiplies with (e.g. p_1) or stand for specially included parameters. The latter are for example the cross-sectional impact functions F_ν, F_K or the modeled closure terms ($\mathbf{\Lambda}_i$). Table 4.4 lists the abbreviations and indices and offers a reference to the corresponding equations. All terms are defined and related to the corresponding equations in Section A.2. The cross-sectional averaging of the parameter u_1, T_1 and ϱ_1 is processed by applying Equation (4.15) to the analytical definition obtained for the quantities.

A brief look at the transversal momentum conservation (Eq. (4.36d)) reveals that not only the mean pressure field is constant over the cross-section of the channel, but also the acoustic pressure $p_1(x, y) = p_1(x)$ (step 1 in Tab. 4.2).

Merging the closure assumptions of the last section into the y-momentum Equation (4.36c) and using the differential operator of Equation (4.37) facilitates rewriting the acoustic velocity problem as

$$\mathcal{L}_\nu\left[u_1\right] = \mathbb{X}_{\mathbf{\Lambda}_1} + \mathbb{X}_{p_1'}\frac{\partial p_1}{\partial x}, \tag{4.39}$$

$$u_1\big|_{\pm 1} = 0. \tag{4.40}$$

Char.	Eq.	Description	Ind.	Description
$\mathbb{E}$	(4.36e)	Energy conservation	p_1	Acoustic pressure
$\mathbb{G}$	(4.36a)	Gas law	p_1'	Axial derivative of p_1
$\overline{\mathbb{G}}$	(4.36a)	Averaged gas law	u_1	Acoustic velocity
$\overline{\mathbb{k}}$	(4.36b)	Intermediate averaged	u_1'	Axial derivative of u_1
		continuity	T_1	Acoustic temperature
$\overline{\mathbb{K}}$	(4.36b)	Averaged continuity	ϱ_1	Acoustic density
$\mathbb{T}$	(4.36e)	Solution of energy	ϱ_1'	Axial derivative of ϱ_1
	(4.36f)	conservations	ε_S	Containing ε_S (Eq. (4.56))
$\mathbb{X}$	(4.36c)	Axial momentum	F_ν	Transversal viscous part
		conservation	F_K	Transversal thermal part
$\mathbf{\Lambda}_1$	(4.36c)	Closure assumption 1	$\mathbf{\Lambda}_1$	Containing modeled term 1
$\mathbf{\Lambda}_2$	(4.36e)	Closure assumption 2	$\mathbf{\Lambda}_2$	Containing modeled term 2

Table 4.4: Left: replacement characters. Right: indexing. These replacement characters facilitate the readability of the resulting system of equations.

Here α_ν^2 in the differential operator $\mathcal{L}_\nu\left[u_1\right]$ (see Eq. (3.50)) standing for

$$\varrho\left(\mathrm{i}\kappa + \frac{\partial u}{\partial x}\right)\frac{\mathrm{Wo}^2}{\kappa\mu}. \tag{4.41}$$

This formulation implies that the closure assumption for $\mathbf{\Lambda}_1$ has no contribution in terms of u_1 and its transversal derivatives, which is valid for both model approaches and their first iterative solutions. Arnott et al. [9] obtained a solution for this problem by applying the GF of Equation (3.51) to the general solution (Eq. (3.54)) with a constant inhomogeneity term and a value of zero for the Dirichlet BCs. Introducing the Arnott function

$$F_j(y) = 1 - \frac{\cosh(\alpha_j\, y)}{\cosh(\alpha_j)}, \tag{4.42}$$

the solution of the transversal component reads

$$u_1 = F_\nu\left(\mathbb{X}_{\mathbf{\Lambda}_1} + \mathbb{X}_{p_1'}\frac{\partial p_1}{\partial x}\right). \tag{4.43}$$

Averaging in y-direction yields

$$\left\langle u_1\right\rangle = \left(1 - f_\nu\right)\mathbb{X}_{\mathbf{\Lambda}_1} + \underbrace{\left(1 - f_\nu\right)\mathbb{X}_{p_1'}}_{A_{12}}\frac{\partial p_1}{\partial x}. \tag{4.44}$$

The lowercase f_j stands for the Rott function

$$f_j = 1 - \langle F_j \rangle = \frac{\tanh\left(\alpha_j\right)}{\alpha_j}. \tag{4.45}$$

The latter formulation already occured in a general form in the Equations (2.1) of Rott [170]. The stagnant mean flow equivalent of Equation (4.44) is given by Equation (2.1a), and the corresponding term is consequently denoted by A_{12}. Depending on the chosen modeling for $\mathbf{\Lambda}_1$, $\mathbb{X}_{\mathbf{\Lambda}_1}$ has contributions for both A_{11} and A_{12} of the later system matrix $\mathbf{A}(x)$ (see Eq. (4.63)). Hence, after finishing step 2 of Table 4.2 the first ODE of the new set of TATEs including explicit mean flow u contribution is obtained. Furthermore, the transversal profile of p_1 and u_1 is described in terms of analytical expressions.

In step 3 of Table 4.2 a formulation for the fluid temperature oscillation T_1 and its solid counterpart $T_{1,S}$ is sought. The density oscillation ϱ_1 in the energy Equation (4.36e) is eliminated by applying the equation of state (Eq. (4.36a)). Again, the closure assumption for $\mathbf{\Lambda}_2$ is considered to have no contributions in terms of temperature oscillations. With these assumptions, the differential operator $\mathcal{L}_K$ for Equation (4.36e) is similar to the one of Equation (4.36d).

Together with the solid energy Equation (4.36f), which is identical to the derivation for negligible mean flow, the transversally constant coefficients read

$$\alpha_K^2 = \left[\varrho c_p \left(-\mathrm{i}\kappa + \frac{u}{T}\frac{\partial T}{\partial x}\right)\right] \frac{2\mathrm{La}^2}{\kappa K} \tag{4.46}$$

$$\alpha_S^2 = \mathrm{i} c_S \varrho_S \frac{2\mathrm{La}_S^2}{K_S}. \tag{4.47}$$

Introducing the corresponding differential operators $\mathcal{L}_K$, $\mathcal{L}_S$ in Eqs. (4.36e), (4.36f) in combination with their coupling conditions yields

$$\begin{aligned}
\mathcal{L}_K\left[T_1\right] &= \mathbb{E}_{\mathbf{\Lambda}_2} + \mathbb{E}_{\mathbf{\Lambda}_1,F_\nu} F_\nu && (4.48)\\
&\quad + \left(\mathbb{E}_{p_1} + \mathbb{E}_{p_1,F_\nu} F_\nu\right) p_1 + \left(\mathbb{E}_{p_1'} + \mathbb{E}_{p_1',F_\nu} F_\nu\right) \frac{\partial p_1}{\partial x} \\
\mathcal{L}_S\left[T_{1,S}\right] &= 0 && (4.49)\\
T_1\big|_{y=\pm 1} &= T_{1,S}\big|_{y_S=\pm 1} = T_b && (4.50)\\
\left.\frac{\partial T_1}{\partial y}\right|_{y=\pm 1} &= \sigma \left.\frac{\partial T_{1,S}}{\partial y}\right|_{y_S=\pm 1}. && (4.51)
\end{aligned}$$

The solution of the differential equations with symmetry conditions at $y = 0$ and $y = 1 + \frac{2R_S}{H}$ leads to formulations of the temperature oscillations T_1, $T_{1,S}$ containing the coupling wall boundary temperature T_b

$$\begin{aligned}
T_1 &= \mathbb{E}_{\mathbf{\Lambda}_2} F_K + \mathbb{E}_{\mathbf{\Lambda}_1,F_\nu} F_{K,\nu} + \left(\mathbb{E}_{p_1} F_K + \mathbb{E}_{p_1,F_\nu} F_{K,\nu}\right) p_1 && (4.52)\\
&\quad + \left(\mathbb{E}_{p_1'} F_K + \mathbb{E}_{p_1',F_\nu} F_{K,\nu}\right) \frac{\partial p_1}{\partial x} + \left(1 - F_K\right) T_b \\
T_{1,S} &= \left(1 - F_S\right) T_b. && (4.53)
\end{aligned}$$

This wall temperature T_b and the solid temperature fluctuation $T_{1,S}$ can be replaced by substituting Equation (4.52) and Equation (4.53) in the coupling conditions (Eqs. (4.50), (4.51)). The constant term reveals again thermal Arnott functions, which only differ in the factor $\alpha_{K,S}$. The mixed term

$$F_{K,\nu} = \frac{-F_K + \mathfrak{Pr} F_\nu}{-1 + \mathfrak{Pr}} \tag{4.54}$$

expresses the convolution of the GF and the viscous Arnott function. Here, the square ratio of the operator constants $\frac{\alpha_K^2}{\alpha_\nu^2}$ is designated by $\mathfrak{Pr}$ with respect to the zero mean flow solution of in't panhuis [80], where this ratio reduces to the Prandtl number Pr of the fluid.

Next, the Neumann condition (4.51) can be used to find

$$\begin{aligned}\frac{T_b}{\mathbb{E}_{\epsilon_S}} &= \mathfrak{Pr}\mathbb{E}_{\mathbf{\Lambda}_2} + \mathbb{E}_{\mathbf{\Lambda}_1,F_\nu}\left(\frac{f_{K,\nu}}{f_K}-1\right) \\ &+ \left[\mathfrak{Pr}\mathbb{E}_{p_1} + \mathbb{E}_{p_1,F_\nu}\left(\frac{f_{K,\nu}}{f_K}-1\right)\right] p_1 \\ &+ \left[\mathfrak{Pr}\mathbb{E}_{p_1'} + \mathbb{E}_{p_1',F_\nu}\left(\frac{f_{K,\nu}}{f_K}-1\right)\right] \frac{\partial p_1}{\partial x},\end{aligned} \tag{4.55}$$

whereas the substitutions $\mathbb{E}_{\epsilon_S}$ and ϵ_S are

$$\mathbb{E}_{\epsilon_S} = \frac{\epsilon_S}{\mathfrak{Pr}\,(1+\epsilon_S)} \tag{4.56}$$

$$\epsilon_S = \frac{K\mathfrak{Pr}f_K}{K_S\,\mathrm{Pr}\,f_S}. \tag{4.57}$$

Substituting Equation (4.55) into Equation (4.53) and introducing new variables $\mathbb{T}$, $\mathbb{E}$ (see Sec. A.2) finally yields the expression for the temperature fluctuation

$$\begin{aligned}T_1 &= \mathbb{T}_{\mathbf{\Lambda}_1} + \mathbb{T}_{\mathbf{\Lambda}_2F_K}F_K + \mathbb{E}_{\mathbf{\Lambda}_1,F_\nu}F_{K,\nu} \\ &+ \left(\mathbb{T}_{p_1} + \mathbb{T}_{p_1,F_K}F_K + \mathbb{E}_{p_1,F_\nu}F_{K,\nu}\right) p_1 \\ &+ \left(\mathbb{T}_{p_1'} + \mathbb{T}_{p_1',F_K}F_K + \mathbb{E}_{p_1',F_\nu}F_{K,\nu}\right)\frac{\partial p_1}{\partial x}\end{aligned} \tag{4.58}$$

in terms of acoustic pressure p_1 and its first derivative $\frac{\partial p_1}{\partial x}$.

In the fourth step, the spatially resolved as well as the averaged solution are both now merged with corresponding form of the acoustic ideal gas law (Eq. (4.36a)) to compute the density fluctuation ϱ_1 and its spatial average

$$\begin{aligned}\varrho_1 &= \left(\mathbb{T}_{\mathbf{\Lambda}_1} + \mathbb{T}_{\mathbf{\Lambda}_2F_K}F_K + \mathbb{E}_{\mathbf{\Lambda}_1,F_\nu}F_{K,\nu}\right)\mathbb{G}_{T_1} \\ &+ \left[\mathbb{G}_{p_1} + \left(\mathbb{T}_{p_1} + \mathbb{T}_{p_1,F_K}F_K + \mathbb{E}_{p_1,F_\nu}F_{K,\nu}\right)\mathbb{G}_{T_1}\right] p_1 \\ &+ \left(\mathbb{T}_{p_1'} + \mathbb{T}_{p_1',F_K}F_K + \mathbb{E}_{p_1',F_\nu}F_{K,\nu}\right)\mathbb{G}_{T_1}\frac{\partial p_1}{\partial x}\end{aligned} \tag{4.59}$$

$$\langle\varrho_1\rangle = \overline{\mathbb{G}}_{\mathbf{\Lambda}_1,\mathbf{\Lambda}_2} + \overline{\mathbb{G}}_{p_1}p_1 + \overline{\mathbb{G}}_{p_1'}\frac{\partial p_1}{\partial x}. \tag{4.60}$$

The cross-sectional average of the transversal acoustic component v_1 vanishes in the integral form of the continuity of mass (Eq. (4.36b)).

Substituting the density and its axial derivative and replacing $\partial p_1/\partial x$ in

$$\frac{\partial \langle u_1 \rangle}{\partial x} = \overline{\mathbb{K}}_{\mathbf{\Lambda}_1,\mathbf{\Lambda}_2} + \overline{\mathbb{K}}_{p_1}\, p_1 + \overline{\mathbb{K}}_{p_1'}\, \frac{\partial p_1}{\partial x} + \overline{\mathbb{K}}_{u_1}\, \langle u_1 \rangle \tag{4.61}$$

by Equation (4.44) (step 6) finally leads to the second TATE

$$\frac{\partial \langle u_1 \rangle}{\partial x} = \overline{\mathbb{K}}_{\mathbf{\Lambda}_1,\mathbf{\Lambda}_2} - \underbrace{\frac{\overline{\mathbb{K}}_{p_1'}\mathbb{X}_{\mathbf{\Lambda}_1}}{\mathbb{X}_{p_1'}} + \overline{\mathbb{K}}_{p_1}}_{A_{21}}\, p_1 + \underbrace{\left[\overline{\mathbb{K}}_{u_1} + \frac{\overline{\mathbb{K}}_{p_1'}}{(1-f_\nu)\,\mathbb{X}_{p_1'}}\right]}_{A_{22}}\, \langle u_1 \rangle\,. \tag{4.62}$$

It describes the axial propagation of the acoustic variables p_1, u_1. Again, its stagnant mean flow equivalent formulation is given by Equation (2.1b) in Section 2.1. As in the first TATE (Eq. (4.44)), the corresponding matrix entries are marked by A_{21} and A_{22}. Here, first two terms show the impact of both closure terms $\mathbf{\Lambda}_{1,2}$. Assuming a description of those two modeling approaches in terms of u_1 and p_1, the system of ODEs reads

$$\frac{d}{dx}\begin{pmatrix} p_1 \\ \langle u_1 \rangle \end{pmatrix} = \boldsymbol{A}(x)\begin{pmatrix} p_1 \\ \langle u_1 \rangle \end{pmatrix}. \tag{4.63}$$

All three quasi one-dimensional models investigated in Chapters 7 and 8 can be drawn from this system of equations. Assuming zero contribution of mean flow (**IMP**), all gray-boxed terms in the TAPEs (Eqs. (4.36)) vanish. If the terms $\mathbf{\Lambda}_{1,2}$ are neglected (**MI**), all terms indexed correspondingly do not contribute to the system. Finally, for **MII** contributions of these terms occur in various steps of the derivation process, such that they affect all the four matrix entries in Equation (4.63).

4.5.4 Achieving High Modeling Accuracy

The derivation presented in the last section contains some simplifications that are not imperative for achieving an analytical system of differential equations. A more general version always leads to more complex results. Moreover, dropping two or more of these simplifications leads – especially due to the convolution of the right-hand side terms in steps 2 & 3 –

to a combination of these terms that cause an immense increase in complexity of some of the resulting terms. Thus, in the following sections, ideas for improving the physical description of the transport equations are presented separately. The reader should be aware of the possibility of combining some of the improvements.

4.5.4.1 Parabolic Mean Distribution

As stated in Section 4.3, an analytical solution of a laminar profile of a compressible fluid through a channel with non-isothermal walls is not known. Thus, a quadratic isothermal transversal profile is assumed for the mean velocity. Keeping the averaged value $\langle u_0 \rangle(x)$ as scaling parameter, the mean velocity follows Equation (4.16). Applying this approach into the mass conservation (Eq. (4.9a)) yields a similar profile for mean density and temperature. Following the arguments of Section 4.2, this variation is less drastic and can be neglected in a first approach. Applying this mean distribution only to the right-hand side terms is not consistent.

If the parabolic shape of the mean velocity is only taken into account for inhomogeneities on the right-hand side of Equations (4.36c) and (4.36e), these terms are not constant. Hence their convolution with the original GF yields

$$\begin{aligned}
&\int_0^1 (1-\hat{y}^2) G(y,\hat{y}) d\hat{y} = \\
&+ \frac{\left(\alpha_j^2 - 2\right)\sinh(y\alpha_j) + 4\sinh((1+y)\alpha_j) + \left(\alpha_j^2 - 2\right)\sinh((2+y)\alpha_j))}{4\alpha_j^2 \cosh(\alpha_j)\sinh(\alpha_j)} \\
&+ \frac{(2 + \left(y^2-1\right)\alpha_j^2 - 2\cosh(\alpha_j - y\alpha_j) + 2\alpha_j \sinh(\alpha_j - y\alpha_j))}{\alpha_j^2} \mathrm{H}(-1+y) \\
&\qquad - \frac{\left(2 + \left(y^2-1\right)\alpha_j^2 + \left(\alpha_j^2 - 2\right)\cosh(y\alpha_j)\right)}{\alpha_j^2} \mathrm{H}(y). \quad (4.64)
\end{aligned}$$

This expression including the Heaviside function $H(y)$ does not simplify significantly by applying the cross-sectional averaging. This expansion

increases the number of terms and computational costs by a factor of two.

The velocity profile also couples with the density fluctuation in the conservation of mass (Eq. (4.36b)). Thus, especially the pressure transport equation equivalent of Equation (4.62) is affected by changes in the transversal mean velocity profile $u(y)$.

Nevertheless, if u is a function of the y-direction, the problem specific GF changes as well. Applying a coordinate transformation, the differential operator of the axial momentum Equation (4.36c) reads

$$\left[\left(C - y^2\right) - \frac{\partial^2}{\partial y^2}\right] u_1(x, y). \tag{4.65}$$

C represents a constant consisting of various terms. The solution of such a system of equations is an integral combination of Gamma functions $\Gamma(y)$ and Weber $W(y)$ functions with complex-valued arguments of different magnitudes. Due to this integral form, deriving these equations goes beyond the scope of this thesis and is not presented here.

In general, integral solutions increase the computational effort compared to the determination of one of the hyperbolic functions of the solutions in Section 4.5.

Furthermore, the interaction of hydraulic and thermal y-profile, which leads to $F_{K,\nu}$ in Equation (4.52), has an extra parabolic contribution term. It originates from the substituted conservation of mass (Eq. (4.36b)). The convolution results in an equation that is too large to display in this context.

Summarizing, taking additionally the transversal density and temperature evolution into account leads to an enormous complexity in the system.

4.5.4.2 Spatially Distributed Modeling Terms

In Section 4.5.2, **MII** was simplified by substituting the averaged form of the stagnant mean solution instead of the y-dependent form. Originally,

the right-hand side term replaced by $\mathbf{\Lambda}_1$ is a function of $\alpha_{j,q}$, the $\mathcal{L}$ term of Equation (3.50) scaling the Arnott function and the y-coordinate.

Introducing the inhomogeneity

$$b(\hat{y}) = 1 - \frac{\cosh\left(\alpha_{j,q}\hat{y}\right)}{\cosh\left({}_1\alpha_{j,q}\right)} \tag{4.66}$$

in Equation (3.54) and averaging in cross-sectional direction yields

$$\int_0^1 \int_0^1 b(\hat{y}) G(y,\hat{y}) d\hat{y} dy = \tag{4.67}$$

$$\begin{aligned}
&\frac{1}{2(1+\exp\left(\alpha_j\right))(1+\exp(2\alpha_j))\alpha_{j,q}\alpha_j(-\alpha_{j,q}+\alpha_j)(\alpha_{j,q}+\alpha_j)} \Bigg[\\
&(\exp\left(\alpha_j\right)-1)(1+\exp(2\alpha_j))\alpha_{j,q}\alpha_j^2 \sinh^{-1}\left(\alpha_{j,q}\right) \\
&+ \alpha_{j,q}\Big[(1+\exp(2\alpha_j))\alpha_j^2(1+2\alpha_j+\exp\left(\alpha_j\right)(-1+2\alpha_j)) \\
&- \alpha_{j,q}^2\left(3+2\alpha_j+\exp(2\alpha_j)\left[1+2\alpha_j+4(-1+\alpha_j)\cosh\left(\alpha_j\right)-2\sinh\left(\alpha_j\right)\right]\right)\Big] \\
&- 2(1+\exp\left(\alpha_j\right))(1+\exp(2\alpha_j))\alpha_j^3\tanh\left(\alpha_{j,q}\right)\Bigg].
\end{aligned}$$

Compared to the resulting transport equation stemming from the momentum Equation (4.36c) using **MI** or **MII**, respectively, leads to an enormous increase in terms. These again have to be considered in the convolution of the right-hand side terms of the energy Equation (4.36e). As this integration is straightforward, the solution can be sought, but the computational costs increase immensely. This improvement in analytical description further comes along with a higher complexity of the system of equations, which are prone to implementation errors and numerical accuracy.

A comparison to two-dimensional computations might still yield advantages for the computing time of the one dimensional set, but the complexity of the system implies a high error rate for the implementation and a low accuracy due to numerical errors occurring because of the numerous terms.

4.6 Numerical Implementation of the TATEs

Nowadays, the validation and verification of the system of equations derived is processed numerically. The TATEs are passed to the numerical tool Mathematica®[2]. In a preliminary step, the equations were counterchecked for zero mean flow conditions by comparison to spatial distribution results produced with DeltaEC. In a second step, the computation of the scattering behavior was implemented. The structure of this program and the necessary theoretical considerations are presented in this section.

4.6.1 General Solution Technique

The linear transfer behavior of any (acoustic) two-port can be obtained from two given independent sets of transport variables $(a,\ b)$ at both sides. Due to the presented algebraic relations between transfer and scattering matrices, any of these notations can be chosen. Here the computation of the scattering matrix is shown.

Integrating Equation (3.25) for both states in one system of equations and multiplying both sides by the input signal matrix yields

$$\begin{bmatrix} \mathfrak{F}_{2a} & \mathfrak{F}_{2b} \\ \mathfrak{G}_{1a} & \mathfrak{G}_{1b} \end{bmatrix} \begin{bmatrix} \mathfrak{F}_{1a} & \mathfrak{F}_{1b} \\ \mathfrak{G}_{2a} & \mathfrak{G}_{2b} \end{bmatrix}^{-1} = \begin{bmatrix} t_{12} & r_{11} \\ r_{22} & t_{21} \end{bmatrix}. \tag{4.68}$$

Solving this system for the unknown parts at the right-hand side directly yields the matrix entries. In general, all of the terms are complex-valued and frequency dependent. The latter implies performing this procedure for each investigated frequency.

As the TATEs are ODEs of first-order and linear in the acoustic variables, the transfer behavior is also linear a priori. Thus creating a set of independent acoustic states is trivial[3]. As the solution of the ODE is unique, choosing two different conditions at one reference position and integrating over the element leads to two independent states. Shifting the phase of the acoustic perturbations in a transmission-affected system avoids the

[2] Mathematica V8, see [209]

[3] It is also feasible to determine the linear portion of nonlinear transfer systems by increasing the number of independent states and applying optimization algorithms to the overdetermined system.

problem of a determinant of the input signal matrix to become zero which might occur for randomly chosen conditions. Therefore the conditions at $x = 0$ are determined as follows. The amplitudes of acoustic pressure $|p_1|_{a/b}/\varrho c$ and velocity $|u_1|_{a/b}$ are set to unity. In order to cause the states to be independent, their relative phases are set to $\phi_a(u_1, p_1) = 0$ and $\phi_b(u_1, p_1) = \pi$ respectively.

4.6.2 Implementation

Before the TATEs can be solved numerically, the mean temperature distribution is computed from equation (4.33) for given reference temperatures at the hot and cold end using a shooting method [154]. For computational reasons, the solution is interpolated with second-order accuracy from stored tabulated data. As can be seen from Appendix A.2, the highest-order derivative of the mean temperature is $\partial^2 T_0/\partial x^2$, which justifies this approach.

Within a given mean temperature distribution, the TATE system is integrated from the cold reference end to the hot side of the pore. A standard Adams-Bashforth [154] integration scheme with an accuracy of 10^{-12} is used in combination of a maximum step size of 10^{-6}, which revealed parameter-independent results for the test cases presented in the following.

4.7 Advantages and Drawbacks of Mean Flow Inclusion

The system of equations derived in this chapter contains formulations that explicitly contain mean flow in terms of $\langle u_0 \rangle$. Such a set is denoted explicit in contrast to the Equations (2.1) of Rott [170] and Swift [187]. These TATEs of the **IMP** model are only affected by a mean flow controlled temperature profile $T_0(x) = f(\langle u_0 \rangle(x))$ and thus couple implicitly with $\langle u_0 \rangle(x)$.

As stated in Section 2.1, these implicit equations are physical for stagnant mean flow conditions in narrow pore geometries [80]. The Rott functions for various geometries have been derived [187] and even arbitrary

shapes are conceivable [105]. Some of these findings may be adapted to the system of transport equations derived. As closure terms are used in the derivation of the TATEs, the system of equations is an approximation of the actual physics. The validity of a direct adaption of the Rott functions for geometries other than the 2D channel by adjusting the α value of the differential operator is yet to be proven. However, the small differences in the shape of the Rott functions [187] and especially in their instability potentiality [72] facilitate a comparison of the results obtained for different pore geometries with good accuracy.

The accuracy of the explicit TATEs (Eqs. (4.63)) for the basic closure assumptions is partially demonstrated in Chapter 8. Especially the improvement over the implicit Equations (2.1) is clearly visible from the investigated cases. Nevertheless, future investigations are needed to confirm these observations for other cases.

Due to the numerous additional terms of the explicit TATEs (Eqs. (4.63)), the computational costs for the prediction of the scattering behavior increases with every iteration for the closure assumption. Tests showed that the computational time for one single evolution of the acoustic pressure and velocity was almost tripled for **MI** and fifteen times larger for **MII**. Using high-order interpolation and tabulated values for the prefactors of the TATEs (Eqs. (4.63)), for the computation of scattering matrices, should reduce this additional effort.

The complexity of the TATEs makes a physical interpretation of the different terms harder. In the implicit equations, the influence of viscous dissipation, thermal diffusion and the interaction leading to energy transfer is still visible. This is not true for the explicit TATEs. The convective terms, i.e. terms that have mean flow contribution, mix the latter two components and yield less physical insight. This effect is not based on the modeling approaches, but on the physics of the problem. Hence modeling the closure terms implies a cautious validation of the approaches. These considerations demonstrate that these explicit TATEs (Eqs. (4.63)) should be used with care. Improved accuracy requires increased computational costs. Finding a reasonable balance depends on the problem considered and demanded error limits.

5 CFD/SI - Time Domain Analysis of Thermoacoustic Scattering

Determining the frequency response of a certain acoustic problem setup using a combination of transient CFD simulations and system identification (SI) methods is a central issue of various research activities at the Lehrstuhl für Thermodynamik at the TU München [57, 63, 75, 88, 95, 192, 200]. The basic technique, which originates from system theory and signal processing, was adapted to acoustic SISO[1] problems by Polifke et al. [146] and Gentemann et al. [62]. The idea is to reconstruct the frequency-dependent transfer function by determining the unit impulse response from the time series of the in- and output signals. During the last decade, this method was expanded to MISO[2] systems [75, 88, 150]. Moreover, the input signal generation was optimized in terms of SI requirements, like ergodicity, entropy and energy content [57, 75].

The signal generation and SI are created for linear time-invariant systems that are described by a black-box model. Thus its application is decoupled from the type of the so-called identification experiment [107], which can be of experimental, numerical or analytical nature. Due to this flexibility, various numerical simulation tools may be applied to produce the responses of the investigated problems.

As the problem discussed is set up in the laminar flow regime, the impact of turbulent noise is negligible. All sources of error are induced by the combination of the numerical tools applied. The existing pre- and post-processing tools provide accurate results for such cases. The CFD/SI tool created by Huber [75] could be applied with minor changes. Only the main ideas of the SI process are repeated here. Interested readers are referred to the literature for a deeper insight into the method. Digital signal processing literature [107, 110, 116, 132] provides further informa-

[1] SISO – Single Input Single Output.
[2] MIMO – Multiple Input Multiple Output.

tion about time domain methods. Applications to acoustic problems are discussed in books about this special topic [67, 74].

Figure 5.1 illustrates the CFD/SI method, which is structured in two parts. This structure is retained in the remainder of this chapter, whereas the latter part is presented in a general form first. The accuracy of SI is highly related to the characteristic properties of the investigated time series that are mandatory for the applicability of the Wiener-Hopf Inversion (WHI). Thus the chosen details of the signal generation process are also discussed. The identification experiment in terms of a two-dimensional CFD simulation of a slab pore is detailed in the second section. There, the case setup, boundary and initial conditions are discussed. Finally, the post-processing methods applied to generate the SI signals are presented.

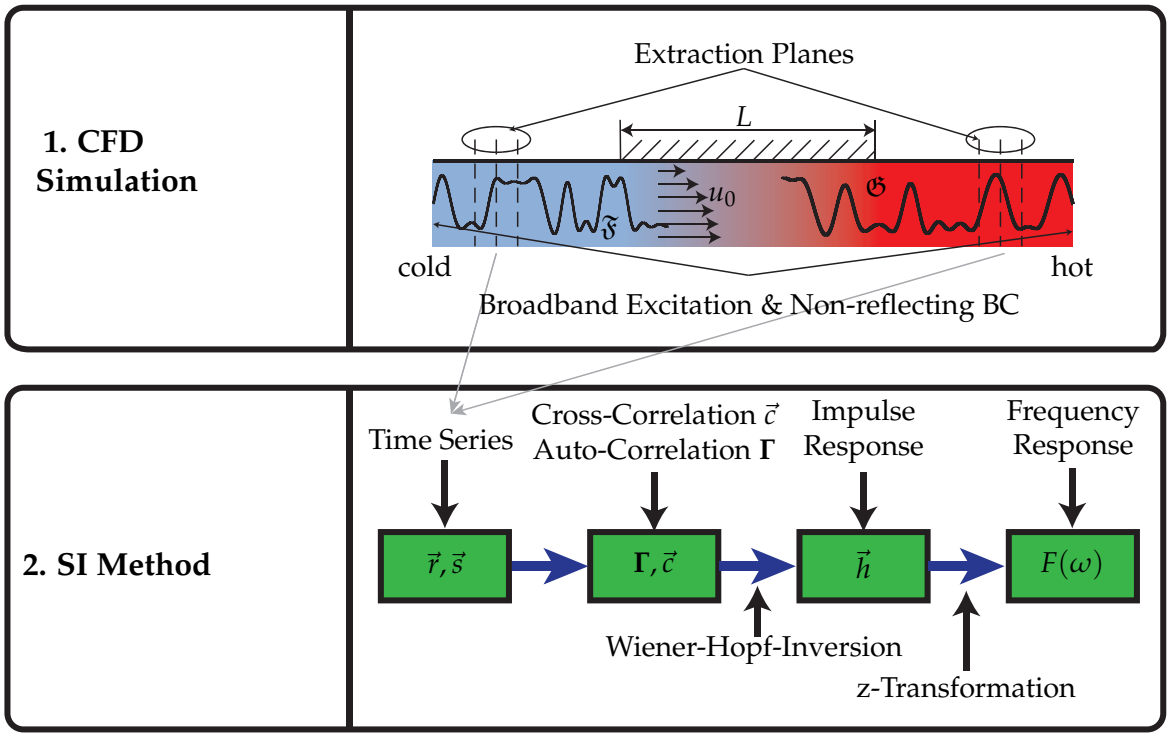

Figure 5.1: CFD/SI method schematics: The top part illustrates the identification experiment, i.e a CFD simulation excited by transient acoustic signals. The lower part presents the idea of the SI method. The signal correlations are formulated for obtaining the impulse response of the system, i.e. the time domain equivalent of the transfer function of the system.

5.1 System Identification

In general, if the suppression of unstable eigenmodes is possible inside an identification experiment – in this case the CFD simulation of a TA stack – predicting its scattering behavior for a single frequency is straightforward. The single frequency based technique described in Section 4.6 directly yields one set of scattering matrix coefficients. In mean flow affected CFD simulations, pressure and velocity conditions are usually fixed at different locations [142]. The two-source location method is preferred for such investigations. Forcing a sinusoidal excitation at the upstream velocity BC for generating one state and driving the pressure at the downstream end to yield a second state allows a direct application of Equation (4.68). The computational cost for this process scales linearly with the number of frequencies considered. Thus SI methods are used to recover the complete frequency response from one single simulation run in the time domain.

The CFD/SI method is restricted to linear time-invariant systems (LTI) [155]. A system is linear if the principle of superposition [107] can be applied. The time invariance of a system states that the output of the system does not depend on the actual time [155].

More background information of the CFD/SI method is presented in detail in various Ph. D. thesis (e.g. [75, 192]). Only the main equations of the process sketched in the second part of Figure 5.1 are given in the following. As stated in Section 3.2.4.1, the chosen scattering matrix notation is causal, which further simplifies the theory. In the first step of the SI process denoted by WHI, the time series obtained are stored in terms of signals $\vec{s}$ and responses $\vec{r}$. In a second step, the auto-correlation matrix $\mathbf{\Gamma}$ of the input signals and the cross-correlation vector $\vec{c}$ of the in- and output signals [74] are generated. Solving the Wiener-Hopf equation [208]

$$\vec{h} = \mathbf{\Gamma}^{-1}\vec{c}. \tag{5.1}$$

yields the unit impulse response (UIR) vector $\vec{h}$ of the approximated system. This UIR, the output of the system to a Dirac delta impulse, is the time domain equivalent of the frequency response $F(\omega)$, which is obtained by a z-transformation of $\vec{h}$ [110, 116].

As the WHI equation is the quintessence of the SI method, its functionality is considered in more detail. It approximates the discrete problem as an output error black-box model [155], i.e.

$$r_i = \sum_{k=0}^{\infty} h_k s_{i-k} + e_i. \tag{5.2}$$

The first term denotes the response of the system without noise. The second accounts for noise e imposed on the response signals. Neglecting contributions of large time scales, the length of $\vec{h}$ reduces and it becomes a finite impulse response (FIR).

The size of $\vec{h}$ is determined by two time lags τ. The discretized time step has to be considerably smaller than the minimum expected time lag τ_{min}. Usually, the time step applied in CFD simulations is controlled by even smaller time scales, for example turbulence, CFL-number, etc. For resolving this mismatch between these time scales, a reduction factor m is introduced, which accounts for the discrepancy of expected minimum time lag and temporal resolution. The maximum time lag considered limits the length of the FIR. Using this resolution, the length $K = mL$ of a discretized FIR has to be chosen such that at least the largest expected time lag τ_{max} can be captured by the FIR. The Wiener Filter has noise suppressing characteristics [63] that are reduced with increasing $t(K) \gg \tau_{\text{max}}$. Thus, the filter length mL has to be determined iteratively to find an optimum balance between noise suppression and system modeling.

The idea of the WHI method is to find a linear least squares optimum of the error-affected black-box model by minimizing the cost function

$$V(\vec{h}) = \sum_{i=L+1}^{N} e_i^2 \tag{5.3}$$

in terms of

$$\min_h \left(V(\vec{h}) \right). \tag{5.4}$$

For given $\vec{s}$ and $\vec{r}$, this problem has an analytical solution. Finding the root of its first derivative with respect to h_j yields the optimum UIR. Substituting Equation (5.2) into the right hand side directly yields the

Wiener-Hopf Equation (5.1). There, the sums of signals and responses are formulated in terms of cross-correlation vector $\vec{c}$

$$c_i = \frac{1}{N - mL + 1} \sum_{k=L}^{N} r(k)s(k - mi + 1) \quad \text{with } i = 1, 2, 3, ..., K \tag{5.5}$$

and auto-correlation matrix $\mathbf{\Gamma}$

$$\Gamma_{ij} = \frac{1}{N - mL + 1} \sum_{k=L}^{N} s(k - mi + 1)s(k - mj + 1) \quad \text{with } i, j = 1, 2, 3, ..., K. \tag{5.6}$$

This equation, also denoted as Wiener Filter [67], yields the linear least squares estimator for the FIR.

The solution method applied to Equation (5.1) has a certain impact on the resulting FIR. If iterative solvers are used, the noise content in the filter is partially suppressed by tolerating a certain residual value. This is equivalent to introducing a regression factor in this equation that accounts for a certain amount of errors. Thus a LSQR method [133] with a standard residual of 10^{-11} is applied to solve Equation (5.1).

The LSQR method is designed for sparse matrices. Applying this technique in the matrix inversion in Equation (5.1) makes a good decorrelation of the input signals $\vec{s}$ a crucial requirement to the signals. Here, the diagonal structure of the auto-correlation matrix is maximized by optimization of the reduction factor m. Considering each m-th signal data point only in Equation (5.6) causes a reduction in the off-diagonal contributions.

A second way of obtaining an optimized auto-correlation matrix relies on a good choice of the excitation signals. Thus, in MIMO systems, a good decorrelation of the input signals and a fast decorrelation of the signal itself accelerate the solution procedure. The auto-correlation matrix of a white noise signal reduces to the unity matrix $\mathbf{I}$ [116]. For a finite signal length N the frequency content is not constant. The identification of the corresponding transfer functions values might yield insufficient results.

An optimum signal is a trade off between this requirement and physical considerations. On the one hand, a high signal to noise ratio ensures a

good reconstruction quality. This implies the requirement for high signal amplitudes. On the other hand, the signals should stay in the linear limit, i.e.

$$p_1 \ll p_0, \tag{5.7a}$$

$$u_1 \ll \frac{p_0}{\varrho_0 c_0}, \tag{5.7b}$$

$$\varrho_1 \ll \frac{p_0}{c_0^2}. \tag{5.7c}$$

The pressure limit is given by nature while the other limits are derived from isentropic considerations that account for most acoustic problems [163]. These limits lead to maximum signal amplitude.

Huber [75] established quality measurements to determine the capabilities of amplitude limited signals used in the CFD/SI. He showed that a discrete random binary signal (DRBS) has higher quality measures than white noise and superimposed sinus overlays with comparable maximum amplitudes. DRBSs are defined as

$$x_n = X \operatorname{sign}(\mathrm{rand} - 0.5), \tag{5.8}$$

which yields $\pm X$, a value limited by Equations (5.7), for every time step. A low-pass filtering of this signal, which reduces the frequency content to a range of interest, yields increased spectral densities [75]. Such a prefilter can be exploited because the limited spatial resolution of a numerical simulation and dissipative effects [67] in acoustic simulations in the time domain themselves act as low-pass filter. Additionally, the TA effect operates in the low frequency regime, which is not affected by these low-pass filters. In combination with standard low-pass filters preliminary clocking period [107] techniques can be used to keep the signal constant for a certain amount of time after changing the sign of the signal.

5.2 CFD Simulation

In the last decade many different CFD codes were used in combination with the CFD/SI method. For this thesis, the open source code OpenFOAM[3] designed and implemented in its first stage by Jasak et al. [84]

[3] Version 2.1.x, August 2012

is used. The advantages of this code compared to a commercial tool are the free accessibility to the source code written in C++. It allows quick adaptations by object inheritance in the modular structured code. The growing community contributes to further developments of basic CFD solvers for classic fluid flow problems. This is the reason that bugs and errors are consequently resolved. This makes the application of OpenFOAM competitive to commercial simulation software for academic investigations. Nevertheless, no publications related to the simulation of acoustic phenomena using OpenFOAM are known to the author.

The results shown in Chapters 7 and 8 are generated using the standard compressible solver rhoPimpleFoam, a segregated solver using the PISO looping technique proposed by Issa [83]. Due to the better stability properties and the reduction of computational costs, this solver was preferred over the corresponding conjugate heat transfer solver. Preliminary tests revealed that for the observed circumstances the influence of the thermal oscillations inside the pore solid is negligible[4]. Test simulations carried out using standard turbulence models demonstrated that turbulent structures are negligible in the entire domain. Hence, the impact of turbulence modeling vanishes in the problems considered.

The incorporation of the influence of the solid on the mean temperature and velocity field is described in the following section, before the special BCs of this problem are explained in Section 5.2.3. Finally, Section 5.2.5 explains the post-processing methods applied.

5.2.1 Case Setup

The simulation domain displayed in Figure 5.2 corresponds to the setup described in Section 2.4. As the CFD code cannot handle two-dimensional problems, the z-direction of the computational domain is discretized by one cell. The total length scales are 0.5 mm in y-direction, which is equal to the pore width and 150 mm in x-direction. This length of approximately three times the stack length is prescribed to enable a reformation of plane wave acoustics. Only plane waves are detected by the

[4] Comparing the thermal diffusivities of air and celor yields a ratio much lower than unity. Thus ε_S in Equation (4.57) almost vanishes and so does the influence of the solid oscillation (see also Eq. (2.1b)).

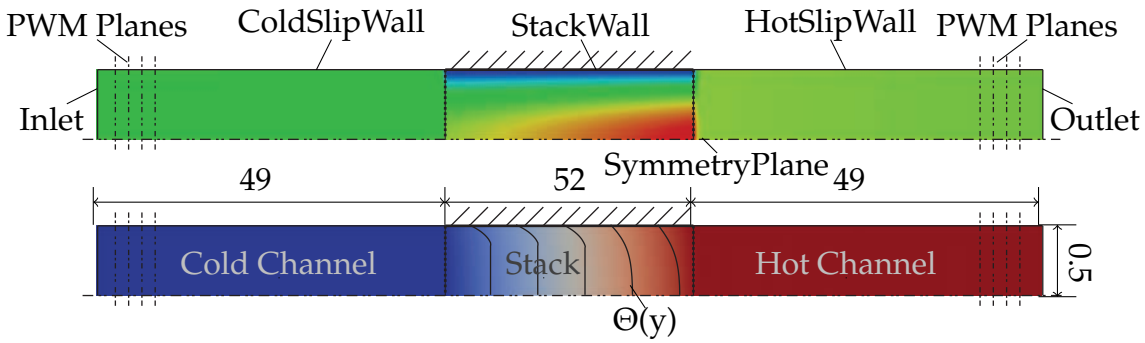

Figure 5.2: Domain of the CFD simulation: The two-dimensional region is 0.5 mm high and 150 mm wide. The top background color shows the axial mean velocity field while the bottom colors represent the mean temperatures.

filtering techniques applied at the non-reflecting BCs, which is treated in detail in the next section.

For a better overview, the axial dimension in Figure 5.2 is scaled by a factor of 0.02 with respect to the other coordinates. The background color of the top figure corresponds to the axial mean velocity u_0 for the maximum Ma considered. The two dotted lines indicate the location of the exit planes of the stack with a geometric length of 52 mm.

The bottom figure is colored in blue to red, indicating the mean temperature field of a case dominated by axial heat conduction. The regions, which are almost uni-colored are referred to as the "Hot" and "Cold Channel", while the pore region is denoted as "Stack". The transversal temperature profile is not identifiable from the uniformly color plot of the temperature, because it deviates less than 1 K from the center to the wall of the channel. Therefore, characteristic profiles $\Theta(y)$ are visualized by black lines along the stack. These curves all consist of a constant part near the center of the pore and a parabolic-like profile in the wall region. Although the L/D ratio far exceeds the thermal entry length [79], this profile has not reached the center line, because the thermal penetration velocity is of the same order as the convective scale and thus the increased temperature at the wall does not affect the profile across the complete channel width before it is convected out of the Stack.

The upstream end of the computational domain of all the three parts – "Cold Channel – Stack – Hot Channel" – is considered as a

"SymmetryPlane", which is physical for laminar and turbulent simulations using unsteady Reynolds averaged Navier-Stokes (URANS) equations. Due to the different nature of both Channels and the intermediate Stack, the opposite boundary is split into three parts: the "StackWall" is a no-slip wall with fixed temperature values, while the "ColdSlipWall" and "HotSlipWall" are adiabatic no-slip walls. The "Inlet" and "Outlet" are especially designed boundaries, see Section 5.2.3.

The Stack is resolved into cells that have a constant cell width $\Delta x = 10^{-4}$m. The cell height decays linearly in the positive y-direction. This results in a mesh size of 520×20 cells for this region. Using this cell size and an acoustic CFL-number less than unity (Eq. (2.3)) yields a simulation time step of $\Delta t = 1.25 \times 10^{-7}$ s. As the inflow and outflow conditions of the stack are multidimensional problems, a certain part of the Channels has to be resolved sufficiently (Figure 5.3) to capture the flow field in the vicinity of the inlet stagnation point. Furthermore, the flow field downstream of the stack has to be resolved up to the point where transversal differences in the flow field are negligible. Due to convection, the latter effect, which is of the order of [104]

$$\frac{L_d}{R} \approx 0.1\,\mathrm{Re}, \tag{5.9}$$

extends over a wider region than the first. For the maximum velocity considered here this approximation leads to

$$L_d \lessapprox 4 \times 10^{-3}\,\mathrm{m}. \tag{5.10}$$

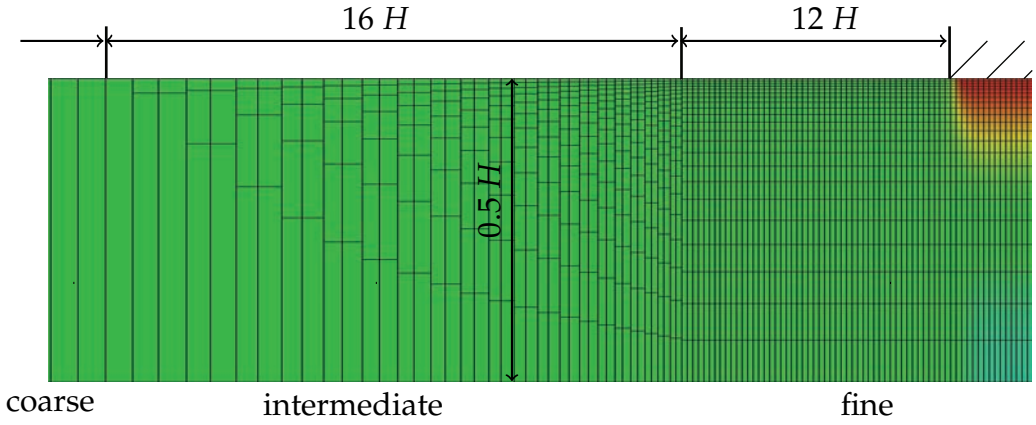

Figure 5.3: Zone of mesh refinement: the mesh is symmetric with respect to the center plane of the stack.

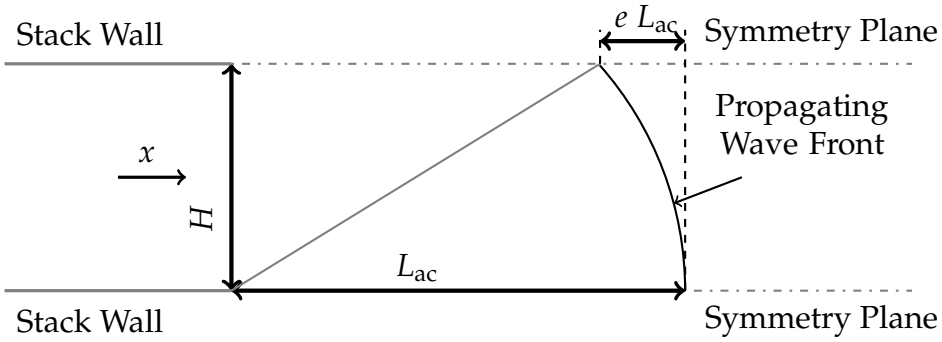

Figure 5.4: Measure of non-uniformity of a propagating wave front: In worst case conditions, the radially propagating wave front has a deviation of the maximum x-value at one side and the minimum x-value on te other symmetry plane. The ratio of this deviation to the distance to the distortions origin is defined as the measure of non-uniformity e.

Moreover, the re-formation of plane waves has to be taken into account. A geometrical estimate [85] yields a correlation for the measure of non-uniformity e. Consider a perturbation formed at the lower wall of the downstream end being transported radially in all directions. The information traveling along the pore axis reaches a certain position L_{ac} at the instant the characteristic wave reflects at the wall. The difference between both x-components related to L_{ac} characterizes the measure of acoustic non-uniformity e. Geometrical considerations directly result in

$$L_{ac} = \frac{H}{\sqrt{1-(1-e)^2}}. \tag{5.11}$$

For a deviation of 0.5%, this yields a ratio of $L_{ac}/H \approx 10$, which is almost equal to the hydrodynamic mean estimate. To capture these effects fully, the fine mesh resolution is continued for $12H$ into the Cold and Hot Channel, before a subsequent reduction in transversal direction is performed over $16H$. In this intermediate region, the axial cell width is stretched by a factor of 1.05 to a 20 times larger axial width. This leads to a cell size of $2\,\mathrm{mm} \times 0.5\,\mathrm{mm}$ in the coarse mesh that is spread across the main part of the Channels.

5.2.2 Material Properties

The material properties of the fluid are chosen according to the investigated problem. The operating fluid is air, which is considered as an ideal gas. All material properties are considered to be constant except for the viscosity and the thermal conductivity. In contrast to the approach of interpolating tabulated values, the latter parameters are computed using the Sutherland approach (Eq. (3.8)). Choosing the latter speeds up the numerical simulation by a factor of ten. The mean temperatures arising in the simulation revealed deviations in the computed acoustic quantities below 1%, which justifies a discrepancy to the one-dimensional modeling presented in Chapter 4.

5.2.3 Boundary Conditions

As discussed in Section 5.1, an increase in the decorrelation of the input signals decreases the computational costs and improves the results obtained from the SI procedure. Furthermore, potentially unstable acoustic modes inside the domain require an acoustic energy sink to prevent the CFD simulation from developping a self-excited instability. Here, BCs that permit a (partial) transmission of acoustic waves to the outside of the domain are preferred to other methods (see the review paper of Colonius and Lele [39]).

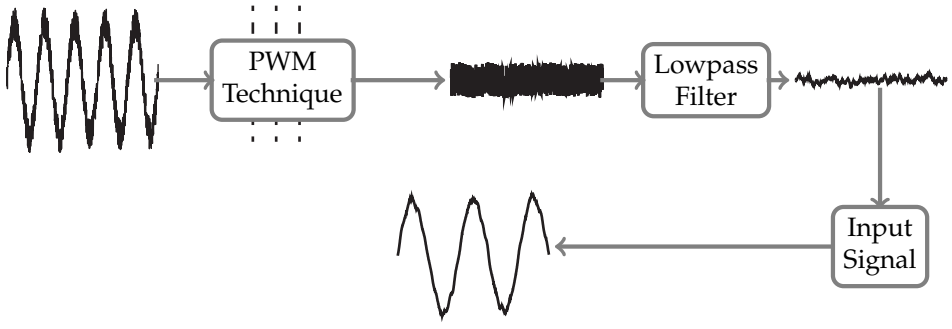

Figure 5.5: Sketch of boundary filtering: at first the PWM method filters out acoustic oscillations, before the PT1 filter behavior of the adapted LODI relations acts as lowpass filter. Finally, the input signal is superimposed to the actual boundary value.

The signal treatment at these BCs is sketched in Figure 5.5. Kreiss [97] proposed the so-called "local associated one-dimensional inviscid" (LODI) relations. This set of equations is a simplified version of the one-dimensional linearized equations of motion discussed in Section 3.1. Thompson [195, 196] used these LODI relations as an estimate of the waves entering and leaving the domain in the computation of BCs for inviscid flow problems. Based on his formulation Poinsot and Lele [142] derived a similar set for the application in compressible CFD simulations. These "Navier-Stokes based characteristic boundary conditions" (NSCBC), which suppress the reflections normal to the boundary, were further expanded by different authors [108, 213, 214] to additionally apply for transversal directions and species transport.

Here, a less sophisticated version was implemented. As the objective of this study was to investigate laminar flow problems coupled with acoustics, no problems that arise from combustion [141] or turbulence have to be taken into account. The distances from the Stack end to the inlet and outlet boundary is very large. In combination with the chosen symmetry conditions at the boundaries normal to the y-direction reduce possibly transported vorticity waves to a minimum. Moreover, the interaction between acoustic and vorticity waves is restricted to high Mach numbers. Still, small perturbations may approach the Outlet. Close investigations of the Hot Channel revealed negligible non-acoustic oscillations. Hence, the relevant fluctuations that approach the boundaries are assumed to propagate in isentropic conditions. This implies that only the reflectivity of the acoustic quantities of velocity and pressure have to be considered. General considerations lead to the conclusion that a well-posed set of BCs for a subsonic compressible flow problem consists of a pressure BC at the outlet and Dirichlet conditions for the velocity at the inlet of the domain [142]. To ensure this well-posedness, Rudy and Strickwerda [172] expanded the LODI relations by a relaxation term, such that the reflectivity of these BCs is not fully non-reflective [176, 181], especially in the low frequency range.

Polifke et al. [152] suggested an additional filter technique that improves the lowpass characteristic of the existing BCs based on filtering acoustic waves [148]. Kopitz et al. [94] developed such a characteristics based filter to extract the acoustic characteristic wave amplitudes at certain

monitor planes near the non-reflective boundary. An instantaneous area averaging yields the acoustic quantities by the application of a simple moving average technique in time [91]. These data are shifted by the characteristic acoustic time scale to the instant at which they arise at the boundary. Averaging over the monitor planes leads to a good estimate of the boundary normal acoustic quantity. Subtracting this value from its instant field value reduces the quantity, which has to be relaxed by its acoustic component. This process is referred to as "plane wave masking" and is explained in detail by Polifke et al. [152]. The combination of these two techniques was first applied by Kaess et al. [86] to form an acoustic impedance BC, which he demonstrated to be very accurate [88].

The last two steps sketched in Figure 5.5 describe the signal generation at the boundaries. An additional forcing term in the BCs facilitates the generation of characteristic wave amplitudes [88] traveling into the domain. Here, this method is used to insert the time line of the input signals at the corresponding BCs. Preliminary tests revealed a good agreement of desired and generated input signals for the chosen geometry.

5.2.4 Initial Conditions

The mean field quantities provide the steady state background information for the acoustic propagation mechanisms. As temperature and velocity directly couple with the TATEs (Eq. (4.36)), this information has to be adapted for all observed cases, i.e. changes in terms of Pe and Ma. In particular the non-constant temperature at the "StackWall" boundary has to be determined in a preliminary process to account for the mean heat conduction in the non-resolved solid domain. Starting with an approximate solution obtained from Equation (4.33), a conjugate heat transfer problem was solved by an iterative application of a finite element technique[5] on a computational domain containing the full fluid and solid part of one observed regenerator pore and its axial vicinity. The reference values at the cold inlet are fixed. For comparability, an averaged fluid Outlet temperature is sought. This condition is verified by adapting the temperature value at the hot end of the solid regenerator wall. It is found using a gradient-based method, allowing for a deviation of less than 1 K from

[5] Conjugate Heat Transfer Toolbox, Comsol 6.2 [40].

the required outlet value. The interface values inside the pore geometry of the solution are passed to the CFD solver using an overlay of a quadratic and an exponential fitting function for the temperature values of the StackWall.

The temperature of the fluid inside the pore is also initialized applying the corresponding BC values from the FE solution, whilst the Cold and Hot Channel are set to constant values. After computing the density values for the entire domain from the equation of state (Eq. (3.7)), the velocity field is also adapted according to an integral mass continuity (Eq. (3.1)) consideration in these regions. The inner region of the Stack is further manipulated assuming a quadratic profile with a mean velocity correlating with the temperature via Equation (3.1).

As these initial field values are only approximations, a further steady state computation is carried out before the transient solver is executed. Unfortunately, this steady state solution cannot be used as starting point for the CFD/SI simulation, because OpenFOAM reacts sensitively to a switch of solvers. Furthermore, the use of moving average methods for the determination of the acoustic quantities by the PWM technique necessitates to find a steady state which slightly deviates from the non-transient conditions. Thus, the simulation is run for at least a Stack flow through time before the acoustic excitation signals are switched on.

5.2.5 Post-Processing Methods and WHI Settings

The CFD simulations are run for a total computational time of 0.7 s. The signals and responses in terms of characteristic wave amplitudes are directly computed using the CFD solver and a sampling rate of 8.75×10^{-7} s. Thereby, the data from PWM planes and additionally defined monitor planes are used. A comparison of the computed signals revealed a lossless propagation of the plane characteristic waves through the intermediate and coarse mesh region of the Hot and Cold Channel. In order to eliminate numerical errors, the data of the monitor planes are mapped to the geometric ends of the Stack. The ends of these manipulated data is cut by 1ms from the beginning of recorded acoustic excita-

tion before they are passed to the WHI tool to improve the independence of transients.

The preliminary data manipulation results in signal lengths of $N \approx 80000$. All signals are pre-filtered using a low-pass filter with a cut of frequency of 100 Hz. A close investigation of the WHI filter length and the reduction factor yielded optimum parameters of $L = 100$ and $m = 25$, which are applied to all simulation cases considered.

6 Experimental Determination of Thermoacoustic Effects

The credibility of numerically acquired results is always dependent upon modeling assumptions. Different approaches of modeling a complex problem lead to increased reliability, but only experimental data support their validity. As stated in Section 2.2, for the investigated TA problem, no data are available in literature (to the author's knowledge).

Experimentally determining the acoustic fields under non-isentropic conditions is challenging. The characteristic wave amplitudes $\mathfrak{F}$ and $\mathfrak{G}$ cannot be measured by a direct method. Acoustic velocity fluctuations u_1 are computed from optical methods using LDA [20] or PIV [3, 23] methods. The coupling of the acoustic pressure p_1 to temperature T_1 and density ϱ_1 fluctuations by the linearized equation of state (4.36a) requires simultaneous investigation of these two quantities. p_1 cannot be determined directly in spatially resolved form. If possible, T_1 and ϱ_1 have to be captured for finding spatially resolved relations in terms of u_1, p_1. In addition, providing optical access to the region of interest is often challenging. Furthermore, generating simultaneous measurement data for different fields is cost-intensive and time demanding. Thus, this approach is out of the scope of this study.

Many acoustic investigation methods rely on approximating the acoustic field with analytical formulations which are fitted to local probe values. Investigating directed velocity fluctuations u_1 is straightforward by using constant temperature anemometry [76]. Dynamic pressure probes use piezoelectric sensor technology or classic capacitive microphones. Here, the latter are chosen for the construction of the cross-sectionally averaged acoustic state vectors providing reference data for the scattering behavior.

For the purpose of generating these data by applying the multi microphone method (MMM), an experimental apparatus is designed and set up. Its modular design further facilitates operating the test rig in a TA

standing wave engine configuration. The acoustic power produced inside the regenerator is not absorbed by any load. The driving effects inside the system are solely balanced by dissipative effects. For the purpose of separating the device from a heat pumping apparatus, it is still referred to as an "engine". The self-excited oscillations occurring thereby provide a qualitative demonstration of TA energy conversion using the regenerators. Moreover, a validation of the scattering matrix entries for one operating frequency by the time-dependent pressure data is possible.

The first two parts of this chapter discuss the theoretical background of the measurement technique applied and provide the link to theoretical information that can be drawn from the different measurements. The chapter concludes with a presentation of the design of the experimental apparatus in Section 6.3.

6.1 Multi Microphone Method

The MMM is a standard technique in duct-acoustics to determine the acoustic scattering behavior of acoustic multi-ports. In general, the application of the experimental MMM results in complex-valued transfer or scattering matrices. The idea is to determine the characteristic wave amplitudes at the ports of the investigated acoustic element by finding the optimum of an overdetermined system of equations that is estimated to fit the spatial profile of the acoustic pressure outside the element. This technique is a derivate of the two-source location method in reference to Section 4.6. The idea is to establish two independent acoustic states, which provide the information yielding the transfer matrix components of the considered acoustic two-port. In contrast to the application of this technique in the one-dimensional tool presented in Section 4.6, the up- and downstream values of p_1 and u_1 at the reference planes of the modeled element are not provided directly. They have to be found by reconstructing them from the measured data at the probing locations. The reconstruction is based on the mean temperature and velocity field in the measurement ducts, which has to be modeled.

6.1.1 Two Microphone Method and its Development

In 1979, To and Doige [198, 199] invented the two-load method, which was the first method to obtain transfer matrices experimentally. They demonstrated its capability for six geometries consisting of pipes, expansion and contraction chambers. The experimental setup was driven upstream of the measurement positions. Two independent states were created by applying a variable load at the opposite end of the measurement setup, which manipulated the acoustic impedance at the downstream end of their test rig. The pressure data were acquired using one microphone located at two varying positions inside each measurement channel.

In collaboration with Lung, Doige [109] further developed this method by applying the four-microphone two-load method. This reduced the minimum number of necessary measurements by a factor of two. The one-source two-load method, which theoretically always leads to independence of both states, reveals problems for certain frequencies because the two loads are not sufficiently different from each other for all frequencies observed.

Munjal and Doige [123] overcame this challenge by introducing a second acoustic source on the opposite side of the experiment. Based on this method, various geometries and configurations were investigated [126, 127, 134, 147]. Åbom and Bodén [4, 27] investigated the impact of measurement errors and derived limit spacings of the pressure sensors. Polifke and Paschereit [134, 147] proposed to increase the number of microphones to reduce the error content of the analytically described fields. At the Lehrstuhl für Thermodynamik of TU München this idea was implemented by Fischer [56] to investigate the acoustic transfer matrix of a swirl burner. The same method was also used by the group of Paschereit and Schueller to validate the analytical modeling of the acoustic transfer of different turbulent premixed burner configurations [135, 178, 179].

Minimizing the data error by applying a least squares fit method to the now overdetermined system improved the confidence of results by reducing the impact of measurement error of each pressure probe. Neunertf [126, 127] addressed the reconstruction error for thermally af-

fected measurements. He transformed the functional spatial expression of the estimated pressure profile to a chain of acoustic two-ports describing the wave characteristics between the measurement positions. By this method, he expanded the applicability of the MMM to arbitrary measurement regions with given acoustic transmission behavior. The latter methodology is applied to the current configuration, which is presented in the next section.

6.1.2 Multi Microphone Method in Non-Isentropic Conditions

The measurement setup is sketched in Figure 6.1. The goal of the MMM is to determine the scattering matrix for the acoustic black-box element based on the approximated spatial profile of the acoustic pressure p_1. Here, the investigated black-box two-port represents the thermoacoustic core, i.e. the combination of the TA stack and its adjacent heat exchangers. As stated before, generating two independent acoustic states yields a linear system of equations in terms of Equation (4.68) or its equivalent in pu-notation. The reference locations $x_{u,d,\mathrm{ref}}$ are defined by the upstream and downstream location of the interface between the acoustic two-port and the test rig. In many configurations, a direct access to the acoustic quantities at these locations is not realizable. Furthermore, the re-

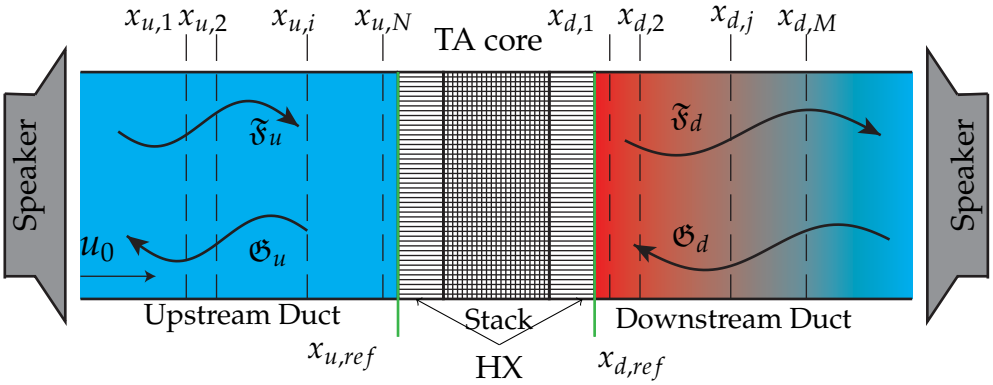

Figure 6.1: Sketch of the MMM applied to the present configuration. The investigated TA core is connected to an ambient duct at the upstream side and a hot duct with varying mean temperature at the downstream port. If mean flow is applied it flows from the ambient "Upstream Duct" to the heated "Downstream Duct". Both ducts are supplied with a speaker and various microphone probes in order to generate and determine two acoustic states at the reference positions $x_{u,d,\mathrm{ref}}$.

formation of plane waves discussed in Section 5.2.1 is not completed at these locations and local samples may contain transversal contributions. Therefore, the probes are located at distances $x_{u,d,k}$ several hydraulic diameters away from the reference planes. This displacement of the probes necessitates a reconstruction of the reference state vectors by analytically approximating a certain spatial characteristic of the acoustic wave transmission. As long as the isentropic condition (3.13) holds and taking into account the phase shift due to acoustic propagation (see Eq. (3.19)), probing of p_1 and u_1 at the same position is equivalent to acquiring the data of two quantities at different locations. Fitting the approximated acoustic transmission to the data obtained from further locations yields an optimized pressure profile. Multiple microphone adapters are inserted in the upstream and downstream[1] duct to reconstruct the acoustic state at the reference planes $x_{u,d,\mathrm{ref}}$. The ambient upstream duct contains $N = 5$ ports located at $x_{u,i}$, of which at most four are supplied with pressure sensors. The non-isothermal downstream duct also provides $M = 4$ probing locations that are all in use. Two loudspeakers located at the ends of those two ducts excite the system. Alternately driving these sources at the investigated frequencies yields two independent states. For these states, the acoustic properties at the reference positions have to be determined. The inactive loudspeaker at the non-excited side of the considered element has a positive impact on the reconstruction of the reference acoustic data, as it absorbs acoustic energy from the system. This leads to low reflection coefficients and small characteristic wave amplitudes of the reflected wave. No standing wave patterns with small local acoustic pressure amplitudes and piecewise constant phases can evolve in such configurations. Obtaining almost constant pressure amplitude profiles and continuous variations in phase in x-direction increases the accuracy of the measured signal. Especially a detectable change in phase between the pressure probes other than a multiple of π leads to robust results for the MMM.

[1] The denomination is similar to all previous chapters. "Upstream" is similar to the part at ambient conditions. "Downstream" indicates all components at a high temperature level. Mean flow is always directed from upstream to downstream conditions. Hence, speaking of "after the stack" also refers to the hot downstream part.

6.1.2.1 Approximating the Ambient Duct Acoustics

At first, the reconstruction of the acoustic state at the ambient reference position $x_{u,\mathrm{ref}}$ is explained. The spatial plane wave profile inside the upstream duct, in between two microphone adapters $(i,\ i+1)$, is determined by the transfer matrix

$$\begin{pmatrix} \frac{p_1}{\varrho_0 c} \\ u_1 \end{pmatrix}_{u,i+1} = \mathbf{T}_{i,i+1} \begin{pmatrix} \frac{p_1}{\varrho_0 c} \\ u_1 \end{pmatrix}_{u,i} . \tag{6.1}$$

The upstream reference plane, which is defined for reasons of comparability, does not coincide with any microphone position. The acoustic transfer between this location and the first microphone position is taken into account by $\mathbf{T}_{\mathrm{ref},1}$, denoting a simple duct element $\mathbf{D}$ characterized by the distance of the probes (Eq. (3.27)). Using these two matrix definitions $\mathbf{T}$, any measured acoustic pressure data at microphone position i correlates to the reference value by

$$\begin{pmatrix} \frac{p_1}{\varrho_0 c} \\ u_1 \end{pmatrix}_{\mathrm{u,ref}} = \mathbf{T}_{\mathrm{ref},1} \prod_{i=1}^{N} \mathbf{T}_{k,k+1} \begin{pmatrix} \frac{p_1}{\varrho_0 c} \\ u_1 \end{pmatrix}_{u,i} . \tag{6.2}$$

Using Equation (3.22), the transformation of these equations into the characteristic wave space yields

$$\begin{pmatrix} \mathfrak{F} \\ \mathfrak{G} \end{pmatrix}_{\mathrm{u,ref}} = \underbrace{\mathbf{\Omega} \mathbf{T}_{\mathrm{ref},1} \prod_{i=1}^{N} \mathbf{T}_{k,k+1} \mathbf{\Omega}^{-1}}_{\mathbf{M}_i^{-1}} \begin{pmatrix} \mathfrak{F} \\ \mathfrak{G} \end{pmatrix}_{u,i} . \tag{6.3}$$

Finally, summing up the corresponding characteristic wave amplitudes $\mathfrak{F}_i,\ \mathfrak{G}_i$ and applying Equation (3.18a) yields

$$\frac{p_1(x_{u,i})}{\varrho_0(x_{u,i}) c(x_{u,i})} = \mathfrak{F}_{u,\mathrm{ref}} \left(m_{11,i} + m_{21,i} \right) + \mathfrak{G}_{u,\mathrm{ref}} \left(m_{21,i} + m_{22,i} \right) , \tag{6.4}$$

where

$$\mathbf{M}_i = \begin{bmatrix} m_{11,i} & m_{21,i} \\ m_{21,i} & m_{22,i} \end{bmatrix} . \tag{6.5}$$

For more than two microphone measurements the resulting Equations (6.4) describe an overdetermined system for the unknown

variables $\mathfrak{F}_{u,\mathrm{ref}}$, $\mathfrak{G}_{u,\mathrm{ref}}$. Applying a Levenberg-Marquart Least-Squares fit method [154] yields an optimum solution by minimizing the microphone errors in terms of either phase and amplitude or real and imaginary part of the complex-valued $\mathfrak{F}_{u,\mathrm{ref}}$ and $\mathfrak{G}_{u,\mathrm{ref}}$.

6.1.2.2 Approximating the Non-Isothermal Duct Acoustics

In contrast to the ambient upstream part, the mean temperature $T(x)$ inside the hot duct decays from the heat exchanger towards the downstream end because of thermal losses through the insulated duct walls. Determining the matrix coefficients m for such non-isothermal mean conditions requires a more detailed consideration of the acoustic propagation in the measurement region. At first, the mean parameter field that serves as background information has to be considered. Here, in the absence of changes in cross-section and low Ma conditions, the determination of the mean temperature field is crucial for the analytical description of acoustic propagation from the reference plane $x_{d,\mathrm{ref}}$ to the microphones located at $x_{d,j}$. As shown in Appendix B.1, a detailed investigation of characteristic parameters allows a one-dimensional, cross-sectionally averaged description of the mean temperature distribution $T(x)$.

Due to different heat loss conditions, the estimated temperature distribution presented in Appendix B.1 is split into a linear and an exponentially decaying zone. The heat load-dependent temperature distribution is based on measured data from up to six distinct positions (Sec. 6.3), which the model parameters are fitted to. The continuous function $T(x)$ is discretized using a predefined temperature step ΔT. In his thesis Neunert [127] shows that depending on the shape of $T_0(x)$, a finer discretization of the profile improves the resulting fitting error of the determined

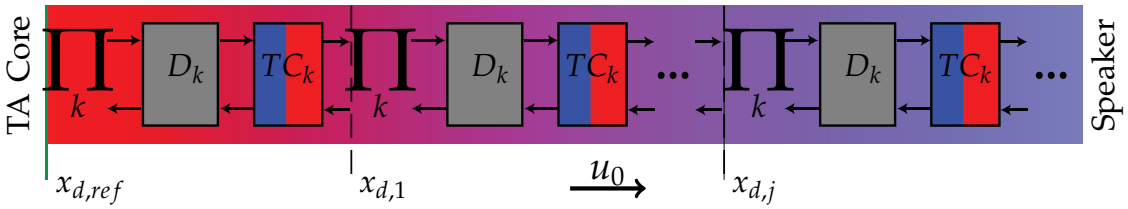

Figure 6.2: Network representation of the hot downstream measurement duct as a product of viscous duct and discrete temperature change elements.

characteristic wave amplitudes from up to 20% (modeling the temperature changes by one discrete step) to about 1%. This discretization enables expressing the transfer matrices similar to Equation (6.1) in terms of a combination of viscous duct **D** (Eq. (3.27)) and temperature change **TC** (Eq. (3.36)) elements. This expression is abbreviated by the Π-symbols in Figure 6.2.

The distances between predefined temperature changes ΔT correspond to the lengths l_k of the intermediate viscous ducts $\mathbf{D}_k$ between each temperature change $\mathbf{TC}_k$. Depending on the number of temperature changes K the transfer matrix between two positions j, $j+1$ becomes

$$\mathbf{T}_{j+1,j} = \prod_{k=1}^{K} \mathbf{D}_k \mathbf{TC}_k. \tag{6.6}$$

Using this formulation and forcing a pseudo temperature change ($\Theta = 1$) located at the microphone position permits the application of the set of Equations (6.4) in a similar way for the downstream measurement part. Hence, $\mathfrak{F}_{d,\mathrm{ref}}$ and $\mathfrak{G}_{d,\mathrm{ref}}$ can be approximated[2].

A typical result for this type of fitting method is displayed in Figure 6.3 for an Upstream excitation at a frequency of 140 Hz. The black crosses denote the measured pressure amplitudes. The phase values are provided as circles. Mean flow is directed from left to right. The hot Downstream Duct is much shorter than the cold Upstream Duct. The fitted pressure amplitude $|p_1|$ – depicted by the solid blue and red line – is normalized by the Upstream Duct value at the reference plane $p_1(x_{u,\mathrm{ref}})$. For plotting purposes, the axial distribution in Figure 6.3 is resolved using intermediate duct elements of a fixed length of 10 mm.

In both fitting regions $|p_1|$ varies for $\pm 15\%$ from their average value of approximately 1.2. The minimum values are very high and no pressure nodes ($|p_1| \ll 1$) occur. These values coincide with an almost constantly inclining phase value (dashed lines), representing a situation of a wave traveling against the positive mean flow direction. These conditions are typically met in downstream excited measurement situations. The combination of the non-driven speaker and its adjacent parts lead to

[2] The reader should be aware that the axial coordinates used in both regions point into opposite directions. The computation and accumulation of the transfer matrices should be processed carefully.

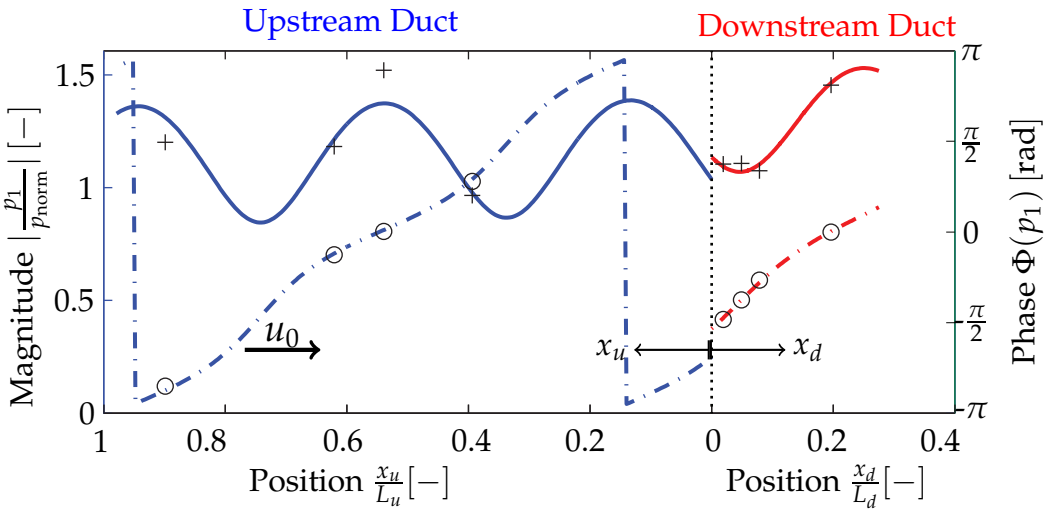

Figure 6.3: Typical pressure fit for the MMM at an excitation frequency of 140 Hz with four microphones at each side of the investigated acoustic element. Crosses and solid lines denote the experimental and analytically approximated magnitude of pressure p_1. Phases of p_1 are denoted by circles and dashed lines respectively. Blue lines indicate the Upstream Duct, red lines the hot Downstream Duct. The black dashed line indicates both reference planes.

a small reflection coefficient. This non-zero, frequency-dependent coefficient causes a reflected wave which slightly modulates the pressure in phase and magnitude.

Comparing the measured data to the fit, the phases match better than the amplitude values. This phenomenon is always found, if the fitting is carried out for the real and imaginary part of the set of Equations (6.4). The larger discrepancies in the magnitude values are observed for all measurement conditions. Using four microphones leads to a good reliability of the data fit for most investigated frequencies.

6.1.3 Reconstruction from TA Core Data

In Chapters 4 and 5, the acoustic transmission of the regenerator was considered analytically and numerically without the adjacent heat exchangers. This is not possible in the experimental setup. The mean temperature is maintained by the heat exchangers. Thus, a direct investigation of the scattering behavior of the TA stack is impossible. An indirect method has to be applied, in which the heat exchangers are reconstructed from separate measurement campaigns. The reconstruction is illustrated in

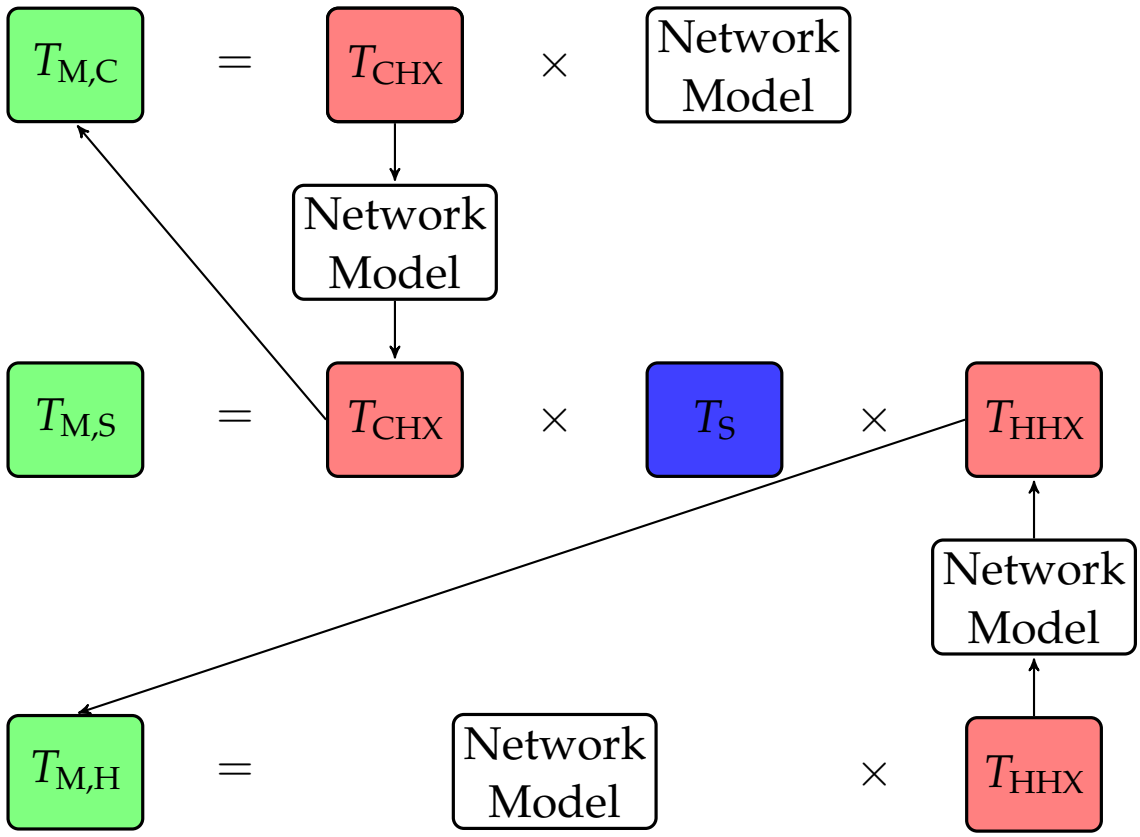

Figure 6.4: Reconstruction of the scattering matrix of a stack (blue) from the measured data (green). At first, the scattering matrices of the heat exchangers (red) have to be determined. Separate measurements and an assumed network model facilitate an approximation of the cold heat exchanger at ambient conditions. This measurement is fitted by a network model. Using this approach, the same procedure leads to a model for the hot heat exchanger. Finally the scattering matrix of the stack is determined from the measured transfer matrix and two heat exchanger models.

Figure 6.4. The output of the MMM is a transfer matrix $\mathbf{T}_{M,S}$. It describes the acoustic behavior of all three components, i.e. the regenerator and its adjacent heat exchangers ($\mathbf{T}_{CHX/HHX}$). These scattering matrices have to be determined separately ($\mathbf{T}_{M,C/H}$) while keeping the operating conditions similar. Here it is assumed that the interaction of these components can be separated. Using this approach, an accurate determination of the periphery of the regenerator leads to a comparable result for the scattering behavior of the stack. Some of the neglected issues are mentioned concisely:

- Any hydrodynamic interaction at the interface of any components is suppressed. For example, the inlet temperature of the hot HX is not

changed by direct thermal contact with the stack. Further, the formation of streaming vortices might also be retarded by an adjacent component.

- The increased blockage due to geometrical changes of the free surfaces at the contact plane is assumed to have no effect. Imagine a stack of plates at perfect contact to a matrix of squared ducts with the same porosity and hydraulic diameter. No theoretical area change occurs, but the flow field is changed by the displacement due to the face areas of the solid separating the ducts.
- Variations in mean conditions due to the enhanced heat conduction by the solid contact are small. For example, the axial temperature profile inside the heater is equal for both configurations – the stack mounted and unmounted in contact to the heater. This assumption is supported by high thermal resistance due to the non-planar surfaces of the adjacent components.

These assumptions imply that the heat input from the heat exchangers into the solid stack material is constant over the cross-section of the regenerator.

At first the scattering matrix $\mathbf{T}_{\mathrm{CHX}}$ of the cold heat exchanger is determined. Its acoustic transmission at ambient conditions is investigated leading to the experimental data $\mathbf{T}_{\mathrm{M,C}}$. These data have to be corrected by a representation of the components between the heat exchanger and the downstream reference plane. Here a network model consisting of ducts and area changes of geometrical equivalence to reality is chosen. Inverting the network model transfer matrix leads to the reconstructed $\mathbf{T}_{\mathrm{CHX}}$ of the cold heat exchanger. The matrix inversion in the computation of the transfer matrix of the stack

$$\mathbf{T}_{\mathrm{S}} = {\mathbf{T}_{\mathrm{CHX}}}^{-1} \mathbf{T}_{\mathrm{M,S}} {\mathbf{T}_{\mathrm{HHX}}}^{-1} \tag{6.7}$$

are highly susceptible to numerical issues. Thus, a more robust approach is preferred: the scattering matrix is modeled in terms of a combination of acoustic two-port elements, optimized such that the optimization parameters represent the reality and describe the acoustic transmission as accurately as possible. This network representation is provided in detail in Appendix B.2.

The network model of $\mathbf{T}_{\mathrm{ColdHX}}$ is also used for the determination of $\mathbf{T}_{\mathrm{HotHX}}$. This matrix is computed from a MMM measurement of both heat exchangers mounted without the stack ($\mathbf{T}_{\mathrm{M,H}}$). Using the similar procedure as for $\mathbf{T}_{\mathrm{ColdHX}}$ the transfer matrix of the hot heat exchanger is determined. The final network representation of this component is also given in Appendix B.2.

6.2 Mode Shape, Onset and Limit Cycles of TA Engines

So far, the chapter dealt with the experimental determination of acoustic scattering matrices. For demonstrating the energy conversion from heat to acoustic power, the modular design of the test rig facilitates operating it in a thermoacoustic standing wave engine mode. The calibrated microphones are expected to deliver absolute pressure data with a standard deviation of approximately 5%. The pressure record of the operating TA engine enables a quantitative comparison to other test rigs. Another idea is to provide a validation case to the scattering matrices determined so far for one operating frequency. The mode shape at operating conditions as well as the growth rate at the onset yield data that are reproducible with a predicted scattering matrix of the TA regenerator. For completeness, the limit cycle of the thermoacoustic engine is briefly presented.

When the acoustic power amplification exceeds the dissipative losses and the Rayleigh criterion [157] is fulfilled for a certain eigenfrequency, the system becomes unstable. This so-called onset of instability is discussed in many TA publications (e.g. [12, 35, 66, 212, 217]). Figure 6.5 shows the experimentally determined onset of a TA standing wave engine from Penelet et al. [136] for different mean temperature gradients $\frac{\partial T}{\partial x}$ across the stack. The amplification of an unstable mode is characterized by the growth rate α, which is the imaginary part of the frequency. In contrast to thermoacoustic instabilities caused by combustion, in which the cycle increment [75, 144] defined by

$$\mathrm{CI} = \exp\left(-\frac{\alpha}{f}\right) - 1 \tag{6.8}$$

can reach factors of unity or higher [151, 192], the cycle increment in TA engines is comparatively small. For the two dashed and dot-dashed

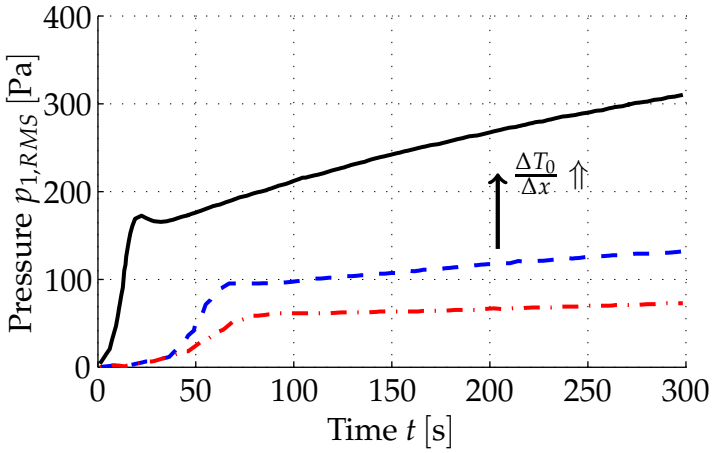

Figure 6.5: Typical onset of a TA engine (adapted from [136]). An increase in $\Delta T_0/\Delta x$ leads to higher growth rates and limit cycle amplitudes.

cases, the limit cycle is reached after approximately 60 s, which corresponds to almost 1000 periods at the operating frequency of $f \approx 150$ Hz. The CI of the high temperature gradient conditions causes a steep incline for the first 30 s before saturation effects occur. In Section 7.2.2, these values are compared to the data from experiments.

One-dimensional network models investigating acoustic stability problems predict the complex-valued eigenfrequencies of a modeled system. The scattering behavior of TA stacks is implemented into such a tool. The model results for the first eigenfrequency of the complete modeled TA apparatus allow for a quantitative comparison to the cycle increment obtained experimentally.

6.3 Experimental Setup

This chapter presents the technical realization of the experimental test rig which applies the discussed methodology. Both setup conditions treated so far are considered: the apparatus operating as a standing wave TA engine with stagnant mean velocity[3] and the modified setup for mean flow affected MMM measurements are presented. Both configurations have common components. At first the TA engine and its parts are described,

[3] This restriction arises from the technical incorporation of mean flow into the system. The damping inside the air supply causes too high damping ratios to obtain unstable modes.

before the additional modules mounted for determining the scattering behavior are explained.

6.3.1 TA Engine Setup

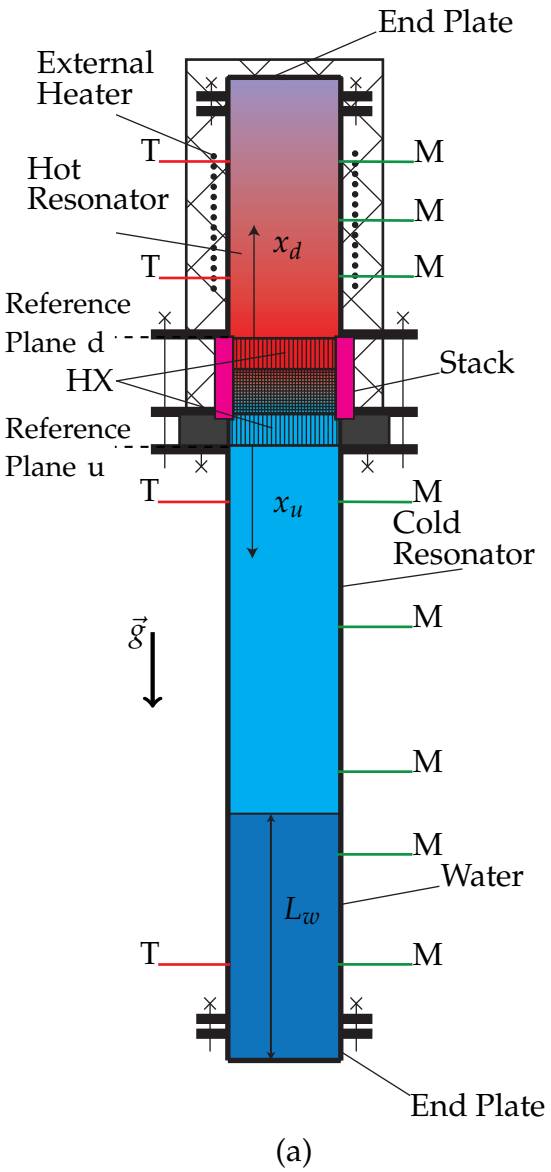

(a)

Num.	Dist. [m]	Standard Mic
Upstream		
1	0.0475	
2	0.9845	A
3	1.3485	B
4	1.5525	D
5	2.2475	F
Downstream		
6	0.0475	H
7	0.1225	L
8	0.1965	C
9	0.4915	M

Num.	Dist. [m]	TC Type
Upstream		
1	0.0475	N
2	2.2475	N
Downstream		
3	47.5	N
4	0.1965	N
5	0.4065	K
6	0.6875	K
Water Cooling		
7	in	J
8	out	J

(b)

Figure 6.6: TA engine setup: figure (a) displays a sketch of the apparatus configuration. T and M mark thermocouple and microphone positions. Table (b) contains the distances of those measurement tools with respect to their reference planes at $x_{u,d}$.

Figure 6.6a displays a sketch of the apparatus in TA engine mode. To avoid any buoyancy effects inside the acoustic measuring object caused

by imperfect cross-sectional mean temperature distribution, the setup is positioned upright with the hot end on top of the cold parts. The test rig consists of two resonators denoted as hot and cold and the TA core defined in the last chapter. The cold and hot resonators are made of a quadratic steel duct with a free surface area of $0.0025\,\mathrm{m}^2$ and a wall thickness of $0.01\,\mathrm{m}$. All parts, if not mentioned separately, are made of steel using norm parts whenever possible.

6.3.1.1 Resonators and End Plates

The hot duct is $0.24\,\mathrm{m}$ in length and contains microphone adapters (M), which can optionally be replaced by M24 screws. The relative distance of these adapters to the reference planes are displayed together with the thermocouple locations in Table 6.6b. The adapters are designed such that a water cooled microphone probe from Fischer [55] is placed near the wall of the duct. The shielded N-type thermocouple tips with $2\,\mathrm{mm}$ diameter are centered inside the duct. To minimize thermal losses, the duct is wrapped in two layers of insulation: A solid high temperature insulation[4] of $2\,\mathrm{cm}$ thickness shields the resonator inside a mineral wool layer of $6\,\mathrm{cm}$ that is coated with aluminum foil. Transversal thermal losses through the duct walls are minimized by an external electric resistance heater, capable of producing up to $500\,\mathrm{W}$ thermal power. This causes a linear axial temperature decay for $x_d \lesssim x_8$ controlled by the inner heater on the one end and the losses at the end plate on the other end.

This mineral wool insulated cap with an inner duct length of $0.05\,\mathrm{m}$ is identical to the upstream end and flanged to the hot downstream resonator, such that reflections are minimized at the resonator contact plane. One central hole drilled into the top end plate facilitates the insertion of a thermocouple with variable axial position inside the duct. Furthermore, twelve M2 tapped holes allow the hot air to leave the setup in the subsequent experiments including mean flow.

The cold resonator with a total length of $2.3\,\mathrm{m}$, which is maintained at ambient temperature, contains two control thermocouples of N type. In all measurements, the average temperature deviation does not exceed

[4] PROMAFORM-1260 [156].

1 K. The operation frequency is variable, because the resonator can be partially filled with colorized water. Using such a fluid facilitates the determination of the surface level inside an opaque hose mounted to the upstream end of the resonator. A change in the level of the water column causes a variation of operating conditions. The operating conditions presented in Section 7.2 correspond to a fixed water level of $L_w = 1.1\,\mathrm{m}$.

6.3.1.2 Heat Exchangers

The basis of the cold heat exchanger displayed in Figure 6.7b is a commercial lamellar, water cooled heat exchanger[5] with an average plate distance of 1.4 mm. The cooling fins made of copper are 0.25 mm thick. The originally circular cross-section of $D = 100\,\mathrm{mm}$ was filled with an aluminum based two-component epoxy to maintain the inner cross-section of 25 cm^2 and inside squared shape of the regenerator. Two supply pipes of $D = 10\,\mathrm{mm}$ cross the remaining area. They cause smooth changes in

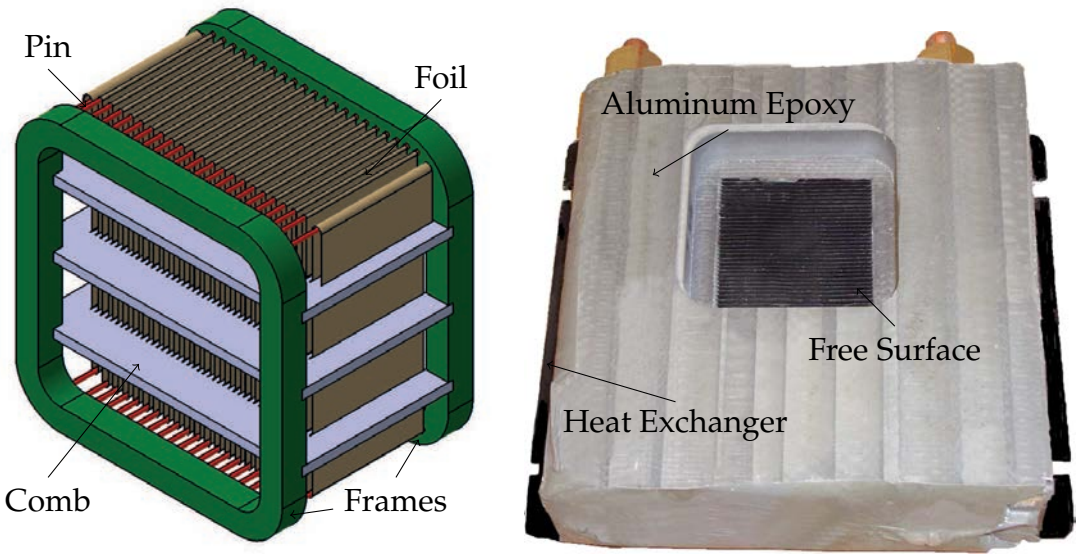

Figure 6.7: The hot (a) and cold (b) heat exchanger. The electrically supplied heater is handmade and consists of a 0.1 mm thick foil, which is bended over stainless steel pins. The cold heat exchanger is a partially epoxy filled standard lamellar liquid-gas heat exchanger.

[5] Lytron 6105 [111].

cross-sectional area in the center of the remaining 30 plates with a length 30 mm.

The plates of the hand made, electrically supplied heater on top of the regenerator consist of an approximately 1.5 m × 20 mm × 0.1 mm stainless steel foil[6]. This foil is depicted in brown color in Figure 6.7a. It is wrapped around 1 mm stainless steel wire (red) at each turn. Three high temperature resistive ceramic combs maintain a quasi equidistant cross-sectional spacing of the foils. The stainless steel pins and ceramic combs are embedded in two ceramic main frames. Due to the frames, the free surface expands to a square section with 0.055 m edge length. External tests showed that the heater is capable of producing up to 800 W thermal power. The network model representation of both heat exchangers is given in Appendix B.2.

6.3.1.3 Regenerator

The regenerator and the heater are framed inside a specially designed ceramic duct to avoid electrical short circuits between the resonator ducts and the electric heater. This duct is colorized in pink in Figure 6.6a. It is fixed together with the cold heat exchanger between three steel flanges. The part located near the heater is machined such that the heating foils

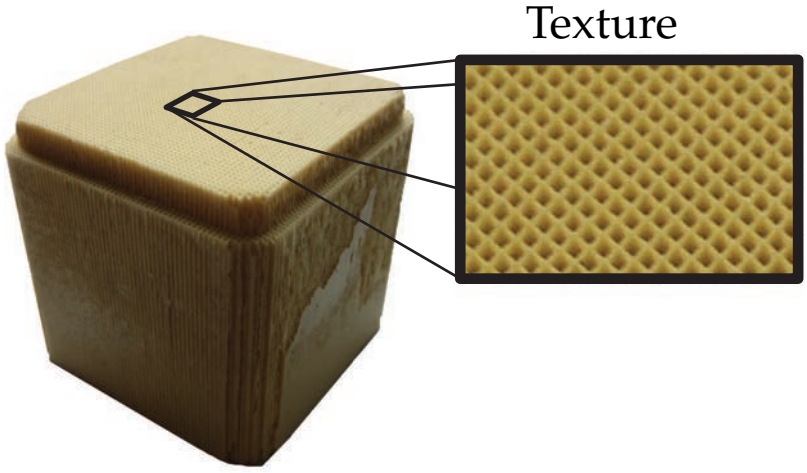

Figure 6.8: Picture of the regenerator. The cordierite ceramic consists of quadratic shaped pores with a hydraulic diameter of approximately 0.8 mm.

[6] High nickel alloy 8000210.

are – under ideal conditions – in direct contact to the pore ends. The quadratic regenerator with a total length of 52 mm and a width of 55 mm consists of a catalyts celor® substrate [42]. The material properties of this quadratic pore shaped substrate are similar to those of cordierite. A cell density 900 *cpsi* and a wall thickness of about 6.35×10^{-4} m yield a porosity (Eq. (3.20)) of $\phi = 0.8$ and a hydraulic radius of $y_0 \approx 0.48$ mm for the substrate. The latter value is computed assuming ideal straight quadratic pore channels, despite the fact that such substrates have rough walls to increase the catalytic contact area.

6.3.2 Multi-Microphone-Method Setup

For the MMM measurement campaigns all components of the apparatus operating in TA engine mode are used. Thus, the hot and cold resonators and the intermediate TA core are only partially displayed in the MMM setup sketched in Figure 6.9. Only additional parts are completely shown.

The hot resonator is elongated by a 0.24 m long, rock wool insulated duct containing an extra microphone adapter located at x_9. Using this extension, the MMM can be processed with four microphones in both the data acquisition sections. The axial temperature distribution is expected to decay exponentially in this region (App. B.1). Thus, the 0.24 m long T-joint that couples the loudspeaker side branch into the system is at a lower temperature level than the first three microphones. The 80 W speaker is additionally shielded by a small portion of cooled air transporting the heated gas to the main duct and through the opened bore holes – in this configuration – in the upper end plate.

The upstream loud speaker is similarly connected to the (empty) ambient resonator duct. The air cooling the speaker and the fluid entering the apparatus from the bottom end plate via twelve mounted hoses of $d_h = 1$ mm is controlled by two flow meters with a limited mass flow rate of $\approx 3.2\,\mathrm{g\,s^{-1}}$ at ambient conditions, which is higher than the investigated operating points of $\dot{m} \lesssim 1.8\,\mathrm{g\,s^{-1}}$. The small long hoses cause strong damping inside the air supply. Thus, the average flow field inside the

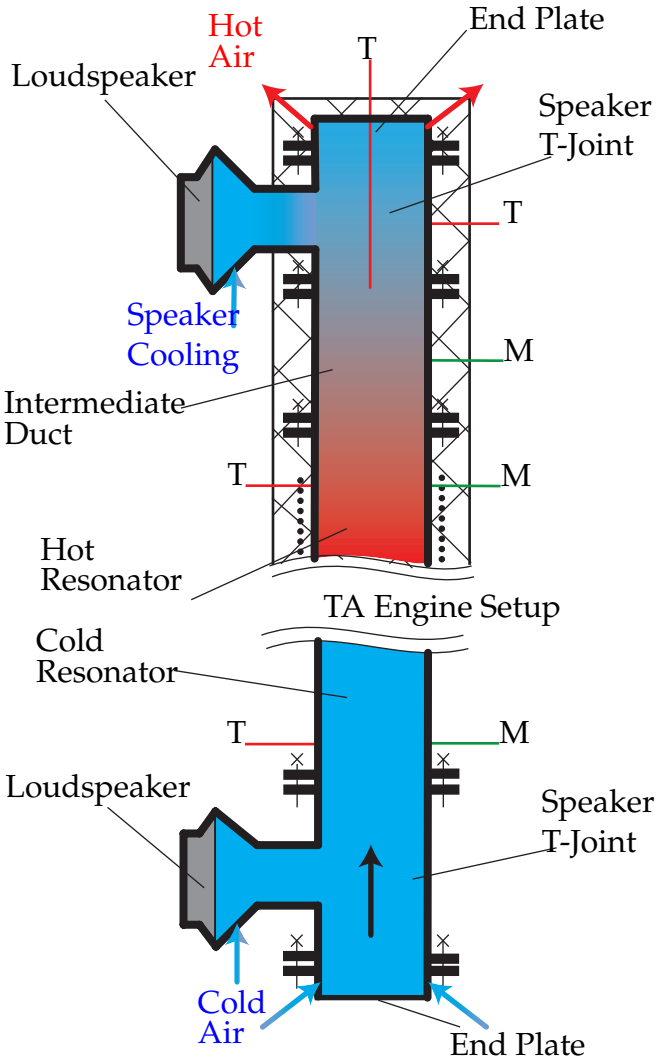

Figure 6.9: Sketch of the MMM setup. Those parts of the apparatus that are also used in the TA engine setup are omitted. Both resonators are supplied by a speaker that is mounted in combination with a T-joint. For data acquisition purposes, the hot resonator is elongated by an isolated duct. In case of mean flow, the flow direction points from the bottom to the top.

measurement setup is almost decoupled from the air supply upstream of the feeding hoses.

6.3.3 Measurement Processs

The thermocouples controlling the temperature distribution inside the setup are connected to a cold-junction compensated external data ana-

lyzer[7] reading all temperature values using a sampling rate of $\Delta t = 1\,\mathrm{s}$. As soon as the collected parameters vary less than $5\,\mathrm{K\,min^{-1}}$, the state is assumed to be steady. The deviation of the stack outlet temperature to the value of the first thermocouple behind the heater is lower than 5 K for the downstream stack temperature range of up to 500 K.

The analysis is conducted over a frequency range of 5 Hz to 600 Hz in constant steps of 5 Hz. The speakers drive the acoustic field inside the setup for a minimum of 3 times the data acquisition period at each frequency. The excitation amplitude is controlled by a preliminary equalizing loop, whereas the maximum measured pressure magnitude obtained for each frequency is calibrated to $30 \pm 5\,\mathrm{Pa}$. Due to the mid range characteristics of the speakers, especially the lowest frequencies of $5\,\mathrm{Hz} \leq f \leq 25\,\mathrm{Hz}$ can not be maintained at this level. Each data acquisition loop is followed by an idle time of several seconds to ensure undisturbed initial conditions.

The signals obtained from the pressure sensors – here capacitive microphones [65] are used – are amplified to $1\,\mathrm{mV\,Pa^{-1}}$ before they are read out by a sequential AD interface card at a sampling rate of $8000\,\mathrm{s^{-1}}$, leading to a temporal resolution of more than 12 points for the maximum investigated frequency of 600 Hz.

The time series are band pass filtered and transformed to frequency space using an FFT-algorithm. The peak frequency data detected in the frequency band of $\pm 5\,\mathrm{Hz}$ around the current frequency of excitation are stored for later post-processing. A calibration process similar to Fischer [55] compensates the impact of the sequential data acquisition delay.

6.3.3.1 Quality Estimations

Åbom and Bodén [4, 27], demonstrated that the achieved measurement quality is sensitive to various issues. As shown by Fischer [55], all parameters influencing the data fitting process are crucial for obtaining accurate results. This section discusses the preliminary quality predictions for the measurement method. Estimations from literature as well as considerations of problem-dependent error impacts are presented.

[7] Agilent 34970A [6].

The intended analytical temperature distribution based on up to 4 local sensors seems to be a rough estimate. The profile affects the acoustic transport in two ways: some parts of the characteristic waves are reflected with the factor $\frac{\Theta-1}{2}$ at the approximated temperature changes, and the actual $k^{\pm}$ (Eq. (3.28)) inside the duct is modified by the temperature-dependent speed of sound. Both, the reflection error and the error in transport speed scale with $\pm\sqrt{\frac{\Delta T}{T}}$. This leads to an error impact of less than 1% in the final computation of the scattering matrices.

Due to the direct impact on the fitting process, the MMM results are more sensitive to the acquired pressure data. The accuracy of these values depends on the signal to noise ratio, the microphone accuracy, the data acquisition system and the quality of the calibration coefficients.

The first and second errors can be reduced by repeatedly varying the microphone positions [123] and averaging over several measurement campaigns. The calibration causes constant offset errors that sum up during the averaging process. As the calibration relies on the accuracy of the reference microphone[8], the complete data set depends on the accuracy of this pressure sensor and the reproducibility of its data. The latter strongly depends on the observed frequency. Measurements obtained from other applications revealed that data below 100 Hz [55] have to be considered carefully because the error exceeds a reliable range.

Due to the questionable reliability of the data, a cautious consideration of the statistics of the fitting process is necessary. Translating determined deviations from the fitting in characteristic wave space into the scattering matrix notation is not straightforward. The dimensional error quantities of the least square fit method are not directly comparable to the error in transmission prediction. Also, a non-dimensionalization by normalizing the quantities with the computed characteristic wave amplitudes, or reference pressures, only leads to comparable results for traveling wave conditions. Such conditions occur if highly absorbing conditions at the opposite side of the acting speaker are generated. Processing all error quantities and their combinations from the fitting procedure to the final scattering matrix notation is very time consuming and increase the re-

[8] Here microphone M is chosen.

quired active storage. Thus, a different approach is used to determine a quality measure for the scattering matrix obtained experimentally. This method is inspired by the bootstrapping technique [14] applied to the CFD/SI method by Foeller [57] and Tay [192]. It uses random parts of signals to find confidence intervals for the results. In contrast to the bootstrapping technique, the data is considered in the frequency domain. Further, all possible data sets and no random selection is used. The idea is to fit the mode shape to a reduced number of pressure sensors by sequentially removing some microphone data columns from the fitting process. A stochastic analysis of all resulting reference wave amplitudes leads to a complex-valued variation in the determined scattering matrix coefficients. Summing up over all possible combinations leads to a mean value, which is identical to the fit achieved by taking all data into account. Moreover, statistical data like standard deviation and maximum error are computed from these results. As these data are dimensionless, their magnitude is a comparable measure for the accuracy of the data. These values are plotted in terms of error bars in the experimentally determined scattering matrices presented in Section 7.1.4.3.

7 Thermoacoustic Interaction in Zero Mean Flow Conditions

This thesis uses and cross-validates three different methods to investigate the TA effect. The cross-sectionally averaged scattering behavior is considered experimentally, semi-analytically and by the application of multi-dimensional CFD simulations. The methods used are validated for stagnant mean flow conditions and the accuracy of the different approaches is discussed in Section 7.1. The application of the predicted scattering behavior is used in the second section to show the predictability of typical operating conditions of the experimental setup in the TA engine mode. An investigation of the instability potentiality of the reference test case concludes the present chapter. Due to its low computational costs, the one-dimensional model approach derived in Chapter 4 facilitates a parameter variation in terms of this potentiality. The IP of deviating mean parameter provides an insight into the capabilities for different configurations.

7.1 Scattering Behavior of Thermoacoustic Stacks

This section presents the scattering matrices obtained by experimental data (**EXP**), one-dimensional numerical modeling (**IMP**, **MI** and **MII**) and CFD/SI methods (**CFD**), respectively. For improved clarity in presenting the data graphically, the results of these three different approaches are displayed separately in Sections 7.1.1 and 7.1.3. Furthermore, in Section 7.1.2 it is shown that the results correspond to the predictions of a simplistic analytical model in the limit of high frequencies. Finally, an error analysis of the methods applied is performed.

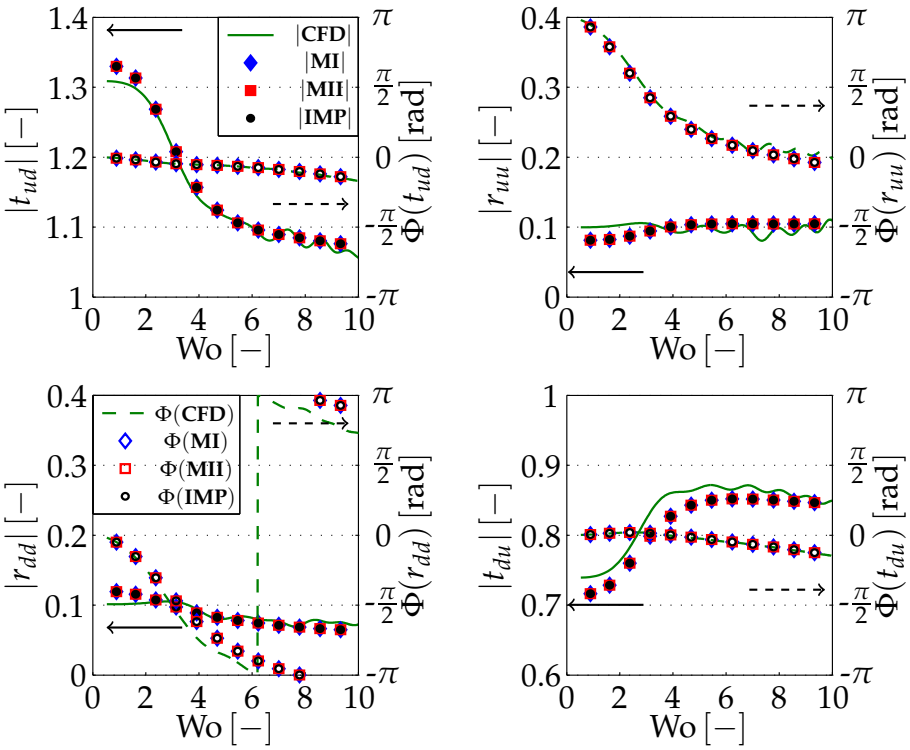

Figure 7.1: Scattering matrix obtained from one-dimensional models and **CFD** data. The data overlap in a wide region. The gain of the transmission coefficients is shown in solid lines for the **CFD** data and as filled markers for the one-dimensional models. The reflected characteristic wave components dominate the matrix. The phase values, illustrated with dashed lines and empty symbols match well in all four elements.

7.1.1 One-Dimensional Models and CFD/SI Data

In the following, the results of the one-dimensional models (**MI**, **MII**) from Chapter 4 are compared to the solutions obtained by the implicit model **IMP** of Peter in't panhuis et al. [80]. The two models including mean flow are both based on the TATEs (Eqs. (4.36)) and differ in their closure assumptions for the terms denoted by $\mathbf{\Lambda_i}$. **MI** neglects these terms, while **MII** approaches them in terms of an cross-sectional average of the solution for stagnant mean flow. Considering zero mean flow reduces the TATEs (Eqs. (4.36)) to the basic set of equations for the **IMP** model. Hence this section will show a correct implementation with respect to the implicit model. Furthermore, the **CFD** data (Chap. 5) of the reference case (Section 2.4) with vanishing mean flow are used for validation. Figure 7.1 depicts the magnitude (gain) values of the models **IMP**,

MI and **MII** with filled symbols. The gain obtained from the CFD/SI method is displayed by a green solid curve. All these values scale with the left-hand side vertical axis of the four plots in Figure 7.1. The blank symbols represent the phase values of the model data, scaling with the right-hand side vertical axis. The color and shape are the same as for its magnitude value. The dashed line describes the phase values of the **CFD**. For reasons of generality, all data are plotted versus the Womersley number Wo of the reference (cold) side. As stated in Section 4.2, Wo is proportional to the hydraulic radius and the square root of the frequency. The transformation from this space into the Lautrec number La space is linear (Eq. (4.7)) and provides similar insight.

The gain and phase values of the transmission coefficients t_{ud}, t_{du} as well as the reflection coefficients r_{uu}, r_{dd} displayed in Figure 7.1 match very well. As expected, all one-dimensional modeling approaches predict identical scattering values. Both phases $\Phi(t_{ud})$ and $\Phi(t_{du})$ of **CFD** and these models completely overlap in the displayed range. This also accounts for the phase of the characteristic wave reflected at the cold upstream side. Only the reflected hot wave phase $\Phi(r_{dd})$ deviates perceptibly for Wo > 6, but is acceptable because of the corresponding gain value.

Concerning the magnitude values of the scattering matrix coefficients, two observations can be made:

- In contrast to the one-dimensional models, the **CFD** solution for higher frequencies contains wiggles. These are artificial products of the SI [58] (also Fig. 7.4). Considering the one-dimensional model of Rott [170], these wiggles are not reproducible by the steady decaying Rott functions (Eqs. (7.8)) displayed in Swift's textbook [187]. Approximating this region by a polynomial least-square fit should result in an accurate match with the one-dimensional model data.

- At low frequencies (Wo < 1), the **CFD** solution tends to underestimate the TA interaction. The transmission coefficients are closer to unity and the corresponding characteristic wave is amplified less with a maximum gain deviation of 0.02 in the low Wo limit of t_{ud}. The low frequency region of the reflection coefficients experiences a

similar tendency with respect to a value around 0.1. The simulated signal length of 0.7 s (Sec. 5.2.5) contains an insufficient amount of information about low frequencies. The limit frequency from sampling theory [155] $f_{\text{samp}} = T^{-1}$ states that Womersley number values of $\text{Wo} \lessapprox 0.2$ cannot be resolved by the system identification. As the accuracy of the SI decreases even before this value is reached, the data in the region of $\text{Wo} < 1$ also start to deviate from reality. SI tests on varying time series of the signal revealed that the changes in the scattering matrix which is related to the TA effect evolve with increasing signal length. The hump in the range of $\text{Wo} \lesssim 5$ rises linearly with the simulation time. This results in a square root convergence in the Womersley space. Thus, and due to the predictable tendency, the improvement in the resulting scattering matrix data by using longer time signals has to be balanced by rising computational costs.

Altogether, both methods match very well. This leads to a certain reliability of the accuracy of the results obtained. Furthermore the existence of implementation bugs in the components of the one-dimensional tool that are not affected by mean flow is excluded. As the one-dimensional models are considered to be exact, and due to the immense reduction in computational costs, the parameter variation for stagnant mean flow conditions in Section 7.3.1 is investigated using the one-dimensional formulation of Chapter 4. If mean flow occurs, the **CFD** solution is the least error-prone and the most reliable. It is selected as the reference solution whenever parallel plate configurations are investigated.

7.1.2 Analytical Limits

The reliability of results is often demonstrated in terms of limit value investigations. If an effect is known to converge to a defined value, reaching these values with the models used corroborates the correctness of the approach. Hence, Figure 7.2 compares the scattering matrix results obtained from the **CFD** data to the matrix values computed from the rudimentary network model presented in Figure 3.2 of Section 3.2.4. The latter is incapable of reproducing the TA effect. This network representation

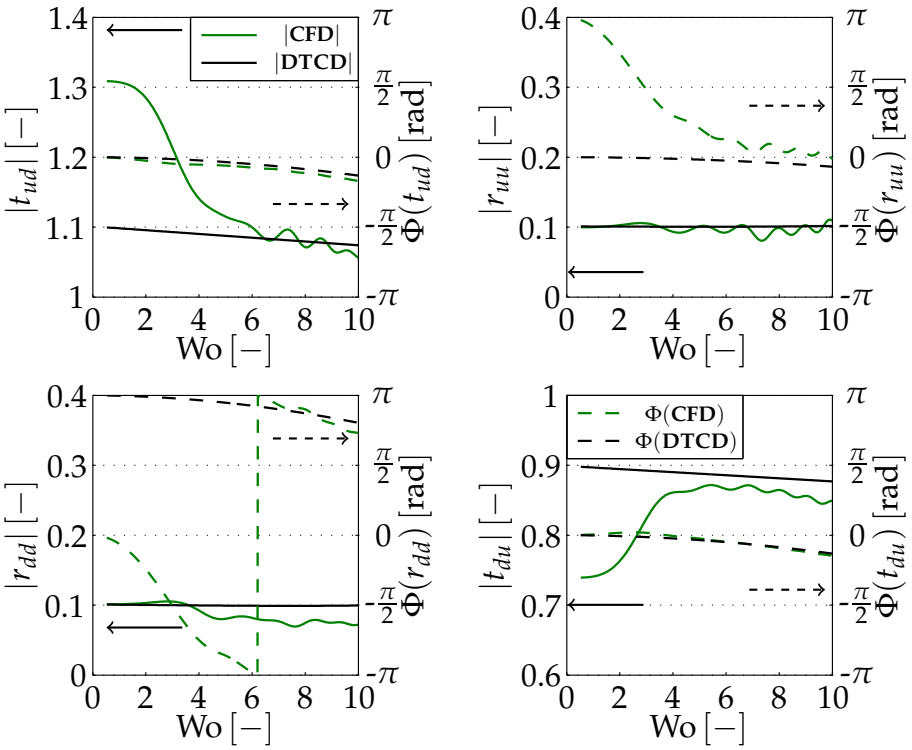

Figure 7.2: Scattering matrix of the TA regenerator vs. a simple model approach (**D-TC-D**). The latter consists of the network representation displayed in Figure 3.2: two discrete area changes combined with a hot and a cold viscous duct on the upstream and downstream end of a temperature step.

is from now on referred to as **D-TC-D** model. It serves as a validation model in the high frequency limit, where the impact of acoustic boundary layers is negligible. The TA regenerator scattering matrix converges asymptotically to the data of this model. It consists of two area changes at both ends modeling the area change due to the porosity $\Phi = 0.95$[1]. The TA pore itself is modeled by a hot and cold viscous duct at in- and outlet temperature. These ducts are connected by a temperature change at the center of the pore. As thermo-viscous interaction is not modeled – for example by a time lag model[2] – the TA amplification cannot be captured.

The phases in the zero frequency limits are considered first. The transmission coefficients $\Phi(t_{ud})$, $\Phi(t_{du})$ are dominated by the time lag τ caused

[1] These area changes are symmetric to the center of the stack and not part of the model. Hence, they do not affect the scattering matrix.

[2] Typical delay models, like the n-τ models as used by Kopitz [95] are not applicable here, because the delay is not dominated by a frequency independent, for example convective, time scale.

by the propagation through the stack. For such waves the low frequency limit of the phase tends to zero because

$$\lim_{\mathrm{Wo} \to 0} \Phi = \lim_{f \to 0} 2\pi f \tau = 0. \tag{7.1}$$

The phases of the reflection coefficients do not correlate to a time lag and thus do not necessarily approach zero. The discrete temperature change at the center of the resonator , i.e. $x = 26\,\mathrm{mm}$, causes a phase shift of π for the hot reflected wave r_{dd}. The cold reflected wave r_{uu} does not undergo this phase shift. In contrast, the **CFD** results, as well as all other data obtained, display a phase shift in r_{uu}. This is the typical behavior of an area change. As the TA effect is strong in this region, a blocking by the viscous boundary layer and an additional phase shift in the r_{dd} element by the thermal wall interaction might be the reasons for this discrepancy. However, no physical or mathematical explanation can be given. This difference in $\Phi(r_{dd})$ vanishes with increasing frequency. The simple approach is a valid limit for the right end of the horizontal axis of all phase coefficients in Figure 3.2.

The amplitude values of this model are governed by the discrete temperature change. Using Equation (3.36), a change in mean temperature T_0 from 300 K to 450 K leads to scattering matrix values of

$$\mathbf{S}_{TC} = \begin{bmatrix} 1.101 & 0.101 \\ -0.101 & 0.899 \end{bmatrix}. \tag{7.2}$$

The two coefficients of reflection, i.e. the off-diagonal entries in the scattering matrix, show an absolute value of the order of 0.1. The wave transmitted from upstream to downstream increases by approximately 10% in amplitude, while the wave transmitted from downstream is reduced by this amount. As shown in Figure 3.4 the acoustic power balance of this element stays neutral.

The magnitude values of the reflection coefficients of both approaches vary little. The greater deviations between **D-TC-D** and **CFD** data in the hot reflection coefficient r_{dd} with increasing Womersley numbers arise from the choice of temperature-independent thermophysical gas parameters (μ, K) for the simple model. The gain of the transmission coefficient

t_{ud} is also slightly affected by this effect. It almost converges to the simplified solution when the thermo-viscous boundary layer interaction, but is reduced to a too low value for Wo > 8. For lower amplitudes both transmission coefficients deviate from the **D-TC-D** model. The differences indicate that a characteristic wave, which is transmitted from the cold to the hot part (t_{ud}), is amplified by the TA effect, while its counterpart (t_{du}) is damped when traveling against a positive temperature gradient. As this effect is larger for low Wo, a TA apparatus should maintain the first characteristic wave, while suppressing the latter to avoid the elimination of acoustic energy. These operating conditions are typical for traveling wave engines.

7.1.3 Comparison with Experimental Results

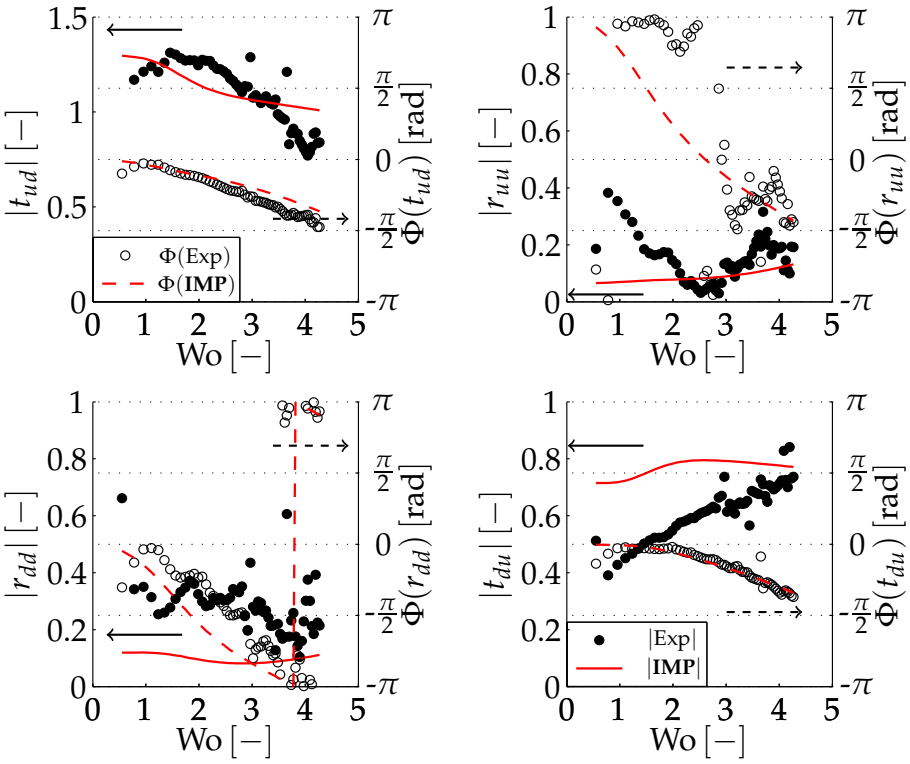

Figure 7.3: Experimental data vs. combined **IMP** data for qudratic shaped pores and reconstructed heat exchangers. Despite the deviation from the predicted data, similar trends are clearly visible. The measurement error in the low frequency range impedes an identification of the TA hump in this region.

Although detailed accurate numerical simulations usually describe the physics with high reliability, experimental data are considered to be most credible. Figure 7.3 depicts the data obtained for the complete TA core by the MMM presented in Section 6.1. The filled dots designate the measured gain values, while the blank circles describe the phase. These data are compared to the **IMP** results. These are manipulated using the reconstructed scattering matrices of the heat exchangers (Sec. 6.1.3). Here, the **IMP** results are obtained by inserting the proper Rott functions for quadratic shaped pores. While **CFD** and **IMP** of slab stacks match well for zero mean flow, choosing the latter reduces the error impact induced by differences in cross-sectional geometry.

The measured phase of the transmission coefficients match very well for a wide region. This is due to the corresponding delay being governed by the timescale of the wave traveling through the media without any interference. The high frequency data are also in good agreement with the reference data. Contrarily there is a huge mismatch for the scattering matrix coefficients for Wo $\lesssim 2$. In comparison to the **IMP** data, the experimental setup experiences a certain blocking that increases for low frequencies. Parts of the characteristic waves are reflected and thus increase the contribution of $|r|$ while the transmission coefficient gains $|t|$ are reduced. This frequency dependent reflectivity is not accounted for by analytical models of discrete area or temperature changes. Thus it can not be reproduced in the reconstruction model of the heat exchangers. Swift [187] discusses the impact of wall roughness on the TA boundary layer interaction. He observes that especially for rough walls the impact of viscous dissipation and, in a similar manner, thermal diffusion increases. This effect can also be attributed to a partial blocking of the regenerator pores leading to a stronger reflection at low frequencies. A second reason for these contrary tendencies is due to the applied pressure sensors. As stated in Section 6.3.3.1, the capacitive signal conversion technique is sensitive to frequency. Low frequency data are affected by non-statistical errors. This low Wo region is expected to be influenced by unidentified impacts and measurement errors. They impede a quantitative comparison to the data obtained numerically.

Nevertheless, the phase of the reflection coefficient $\Phi(r_{uu})$, which does not coincide with the **D-TC-D** model discussed in the last chapter, occurs

in a similar manner. Furthermore, the TA amplification in $|t_{ud}|$ is still visible. In the next chapter, the author focuses on tendencies that the effects experience when experimental data is affected by mean flow. Only these tendencies are taken into consideration.

7.1.4 Accuracy of Applied Methods

In the last chapter, three different methods for obtaining the scattering matrix of a TA regenerator were compared. Regardless of the good qualitative agreement, these results have to be verified and validated because of the lack of comparable data in the published literature. Thus, this chapter discusses model and measurement errors as well as the accuracy of the techniques applied.

In contrast to the domains considered with the numerical tools, the experimental setup investigates the real physical TA regenerator. Thus errors stemming from inadequate model assumptions of the regenerator do not affect this measurement. However, the modeling approaches of the MMM procedure, the approximated geometry and its thermal field nevertheless induce a certain potential of model error.

The numerically investigated domains on the other hand are simplified with respect to the technical device. No inlet/outlet interference like the formation of jets at the expansion or streaming effects are considered. Also the assumed axial mean temperature profile inside the regenerator is independent of losses to the exterior. In contrast to the approximated data of the one-dimensional models, all mean data is available from the **CFD** simulation. Some error impact is related to the geometric restriction of the investigated computational domain. As stated in Section 2.4, the influence of the openings and multi-dimensional effects are not captured by the two-dimensional consideration of a single pore. Furthermore, buoyancy is a priori neglected. As the error impact of the approaches arises from different sources, a quantitative comparison is impossible. Determining the error impact of elements of the methods applied and thereby obtaining a certain credibility of the acquired data is the only way of supporting the cross-validation and verifying the choice of the reference method.

7.1.4.1 Quasi One-dimensional Modeling

The quasi-one-dimensional model of Rott [170] was shown to be exact for long pores and for stagnant mean conditions by in't panhuis et al. [81]. Following the derivation of Chapter 4 and neglecting u for a pore with vanishing ratio of length scales ε, the resulting mathematical description of the acoustic transport is exact for ideal conditions. As long as the mean flow is a quantity of second order and the pore is not affected by any losses, which are not considered here, the modeling approach described in this thesis is still valid. For stagnant mean flow conditions, all errors in scattering matrix data are related to the numerical discretization and provided thermophysical material data. The high accurate integration scheme in combination with a step size of 10^{-5} yields a very precise result. Thus, the tabulated data, which are stored with a precision of 10^{-4}, induce the largest errors of similar magnitude into the equations.

Due to the restrictive assumptions mentioned, this high accuracy is only valid for the stagnant mean flow case. As soon as $\dot{m} > 0$, the error, which clearly stems from false closure assumptions, increases. Quantifying the accuracy is restricted to a comparison to data obtained by other approaches.

7.1.4.2 CFD and SI

The CFD simulation reveals a good agreement with the **IMP** model (see Figure 7.1). As the configuration considered exactly matches the BCs of the 1D problem, the modeling error is supposed to be of the same order of magnitude. Entrance effects and inlet/outlet area changes are also not considered. Moreover, the temperature variation at the interface to the solid material is not taken into account. As a laminar mean flow regime is considered, the impact of turbulent noise is negligible. Because the complete stack height in the experiment is two orders larger than the hydraulic pore radius (Sec. 6.3.1.3) and the conductivity of the fluid and the solid regenerator component are small in the experiment, inhomogeneities due to losses to the exterior play a minor role. Thus, these assumptions can be considered to introduce negligible error.

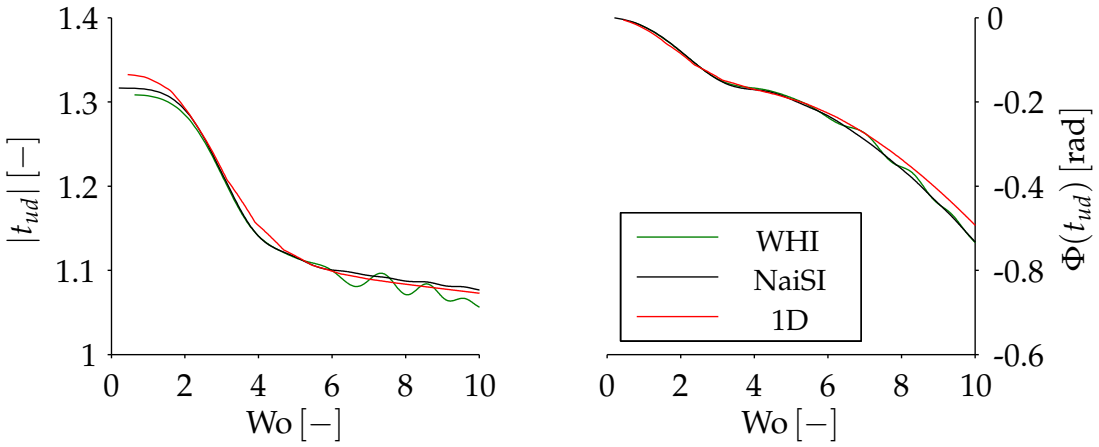

Figure 7.4: Validation of t_{ud} obtained by the WHI method (green) against the improved SI method NaiSI (black) and the one-dimensional approach (red).

The accuracy of the SI tool (Sec. 5.1) depends on the signal quality, the noise level and the choice of identification parameters. As TA amplification is dominated by the gain of the transmission coefficient t_{ud}, this parameter is validated separately in Figure 7.4. Here, the transmission coefficient obtained by the method described in Chapter 5 (green) is compared to the quasi one-dimensional solution (red) and a result obtained by the so-called NaiSI method (black) [57][3]. This method is based on time domain methods and regularization techniques [10]. The latter accounts for the error content in the data and thus yields a more precise solution for a similar set of signals and responses.

The discrepancy of the results obtained is very low for the investigated stagnant mean conditions. The wiggles occurring in the WHI prediction are completely smoothed by the regularization technique in the NaiSI data. The phase values stick to the WHI results. They indicate a reduction in transport velocity. This is a possible indicator for numerical dispersion in the CFD code [78]. This phase error does not affect the low Wo region. Here, slight deviations can be seen. Finally, the estimated lack of amplitude of the WHI for low frequencies is slightly improved by the NaiSI method. The predicted values are closer to the magnitudes of the

[3] NaiSi stands for "Novel and improved System identification". The development of this method was the scope of an ongoing research activity at the Chair of Thermodynamics at TU München. The tool was not available during the data generation process.

1D values. However, as the time series is still too short, they cannot reach this limit.

Summarizing, the WHI deviations in magnitude are up to 2% in the region of the wiggles. The accuracy in the low frequency range is restricted by the length of the investigated time series. All discrepancies result from the SI errors and discretization errors[4] in the CFD simulation. These discrepancies are not related to mean flow and in combination with the qualitative agreement to the experimental data. The choice of the WHI solution as reference data is justified.

7.1.4.3 Impacts of Measurement Error and Credibility of Experimental Data

The experimental data show larger deviations than other methods. Thus, the impact of possible errors is investigated in more detail.

Reconstruction Faults

The models applied and optimized for the consideration of the adjacent heat exchangers and geometrical changes inside the TA core are not perfect. The parameters listed in Appendix B.2 allow only an approximate reconstruction of the acoustic scattering behavior of the heat exchangers. The assumed mean temperature profile $T_0(x)$ is computed using four measurement nodes. Moreover, as the error margins of numerical data are of the same order as for the experimentally acquired data of the TA core, some effects may not be captured. If these are physical, but not identifiable, their impact on the overall measured scattering behavior cannot be taken into account. The dominant decay and rise of the magnitude values of the scattering matrix data detected for Wo < 2 in Figure 7.3 is one of the three possibly uncaptured phenomena, which might be physical. A higher real viscous and thermal damping inside the narrow geometries of the TA core could, on the one hand, cause a stronger decay in the transmission coefficients $|t|$. On the other hand, it would affect both transmission coefficients in the same way for zero

[4] In this context the discretization errors refer to the chosen discretization schemes and the numerical dispersion related to the solution techniques applied. Resolution errors from too coarse meshing or time stepping are expected to play a less significant role.

mean velocity. This also accounts for the qualitative impact of losses due to area changes. A further physical effect, which is not taken into account, is the strong reflection at low frequencies discussed in Section 7.1.3. No acoustic element description is known to the author that predicts this phenomenon and can be incorporated into the network representation of the reconstruction process.

Data Acquisition

The measurement chain for the MMM includes microphones, signal amplifiers, an analog/digital interface and numerous cables and connectors. All these components contribute a certain error to the system. Åbom and Bodén [4] showed that the MMM is sensible to the accuracy of the measurement instrumentation as well as to the location of data acquisition. For the two-microphone method, they required a relative microphone distance s of

$$0.1 < s\frac{\pi(1-\mathrm{Ma}^2)\omega}{c} < 0.8, \tag{7.3}$$

which is violated by a factor of up to approximately three. Here, the use of more than two microphones for the pressure fit balances this potential error source.

Especially the wiring connections and the pressure sensors are error prone. These potentially systematic but unrepeatable errors can lead to non-physical results notwithstanding a change of microphone orderings and repeating the experiment [193]. Figure 7.5 depicts the relative amplitude and phase deviation of six (out of eight) microphones from the fitted pressure profiles over Womersley number for a) upstream and b) downstream excitation. Each value displays the error of the microphone with respect to the fitting through three microphones at each side, which are exemplarily depicted for a frequency of 140 Hz in Figure 6.3. These values are non-dimensionalized by the acoustic pressure fit quantity that is computed for the ends of the TA core. Choosing a different set of microphones will lead to very similar results. The expected random deviation for a stochastic amplitude and phase error only occurs for Womersley numbers of $\mathrm{Wo} > 3$. These values are larger than the rest. These errors are balanced by the averaging procedure described in Section 6.3.3.1. In

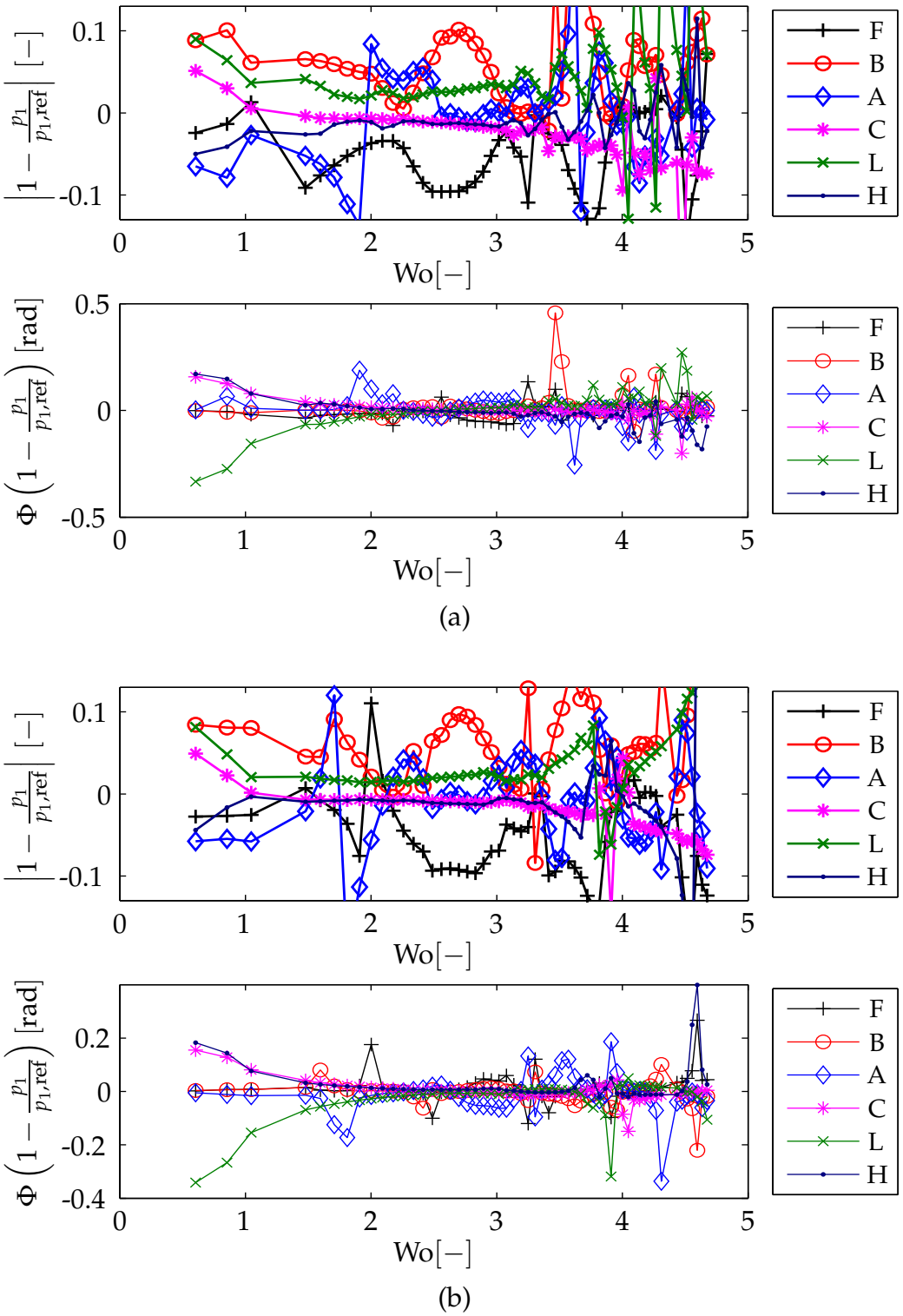

Figure 7.5: Microphone deviations from fit profiles for a) upstream and b) downstream excitation. Some sensors reveal non-statistical deviations in the Wo < 3 region.

contrast to this, almost all microphones display a clear trend to overestimate (or respectively underestimate) the magnitude and phase when they fall below a certain frequency. Microphones B and L, for example, always record higher values than predicted by the fitted profile for $\mathrm{Wo} < 3$. This tendency of a consistent over- or underestimation can also be observed for the phase at low frequencies. The deviation is neither linked to the position of the active speaker nor to the microphone location. This trend in both quantities – gain and phase – is expressed in terms of systematic errors in the scattering matrices that are not balanced by any averaging process. As the origin could not be identified by a variation of the microphones and is not reproducible, the author expects this deviation to be part of the data acquisition system.

As discussed so far, an interpretation of the impact of the systematic error on the scattering behavior is very difficult. Taking the microphone errors into account by weighing them in different variations does not lead to quantitative conclusions considering their impact on the predicted scattering matrix value. Hence, the method of predicting the scattering matrix values with varying combinations of microphone data (Sec. 6.3.3) is chosen. It is the only method to at least provide a qualitative estimate of the accuracy of the results obtained in terms of scattering matrix values. Using this method allows to determine statistical data as maximum error and standard deviation, which are considered in the next section.

Measurement Errors

Figures 7.6 and 7.7 display the maximum error and standard deviation [91] of the measured zero mean flow scattering matrix. The eye-catching discrepancy of the low frequency magnitudes (blue lines) supports the statement that the accuracy of microphone measurements below 100 Hz[5] is not satisfactory. Except for some frequencies the amplitude error decreases with increasing Wo. These exceptions are not restricted to fluid-dynamic eigenfrequencies of the system. Observations during the measurement campaigns revealed that these deviations in the maximum error and the standard deviation displayed in Figure 7.7 correspond to a resonance frequency of the complete setup. For these frequencies the ex-

[5] $\mathrm{Wo} < 1.64$ in the present configuration.

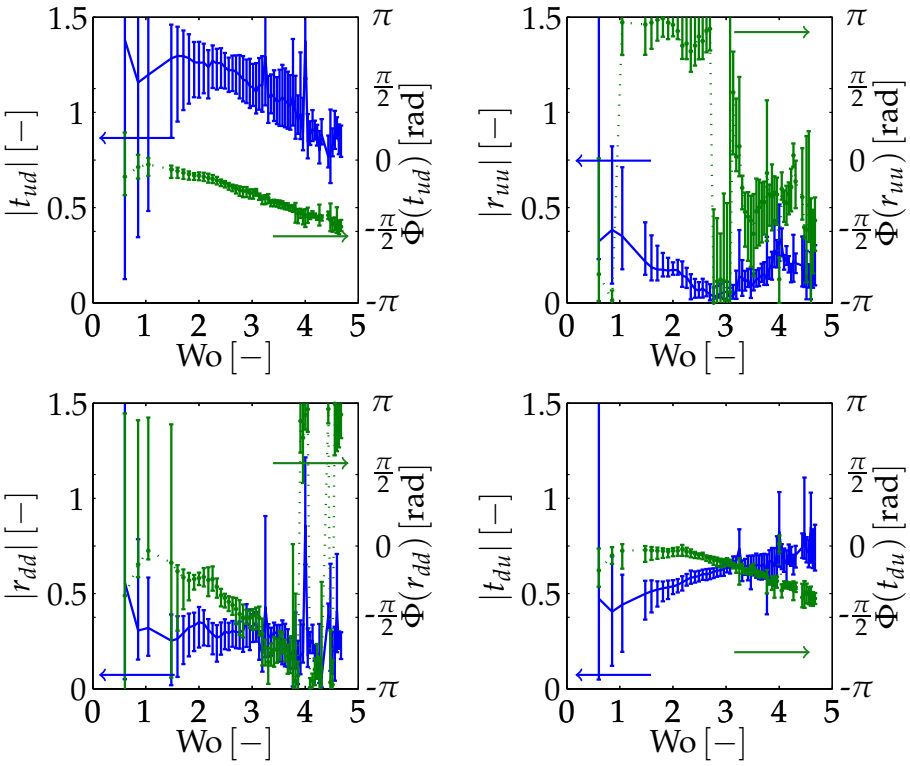

Figure 7.6: Maximum error of measurements for the TA core obtained by successively omitting one microphone in each measurement duct. The magnitude error in the low frequency range is attributed to the microphone errors and the low excitation amplitudes of the speakers.

ternal sound level increases far above the standard value and loose parts mounted at the exterior of the apparatus begin to vibrate.

As expected from the good qualitative overlap with the numerical data, the phase error (green curves) of the transmission coefficients is small. This is attributed to the fact that the phase of a wave traveling through a dissipative duct is almost unaffected by errors of the estimated damping coefficient d than its magnitude value (Eq. (3.28)). The errors decrease with increasing changes in amplitude. This is due to the ratio of the measurement error to the actual acoustic pressure magnitude. The complex-valued error quantitiy is constant while the excitation is limited by the speakers. At low frequencies, the used forcing elements were not capable of generating the demanded power level of 50dB. Thus, in this region the error ratio increases. As the error ratio impact can be split up for the characteristic wave amplitude, this effect also explains the comparatively higher error values in the off-diagonal coefficients. The higher error for

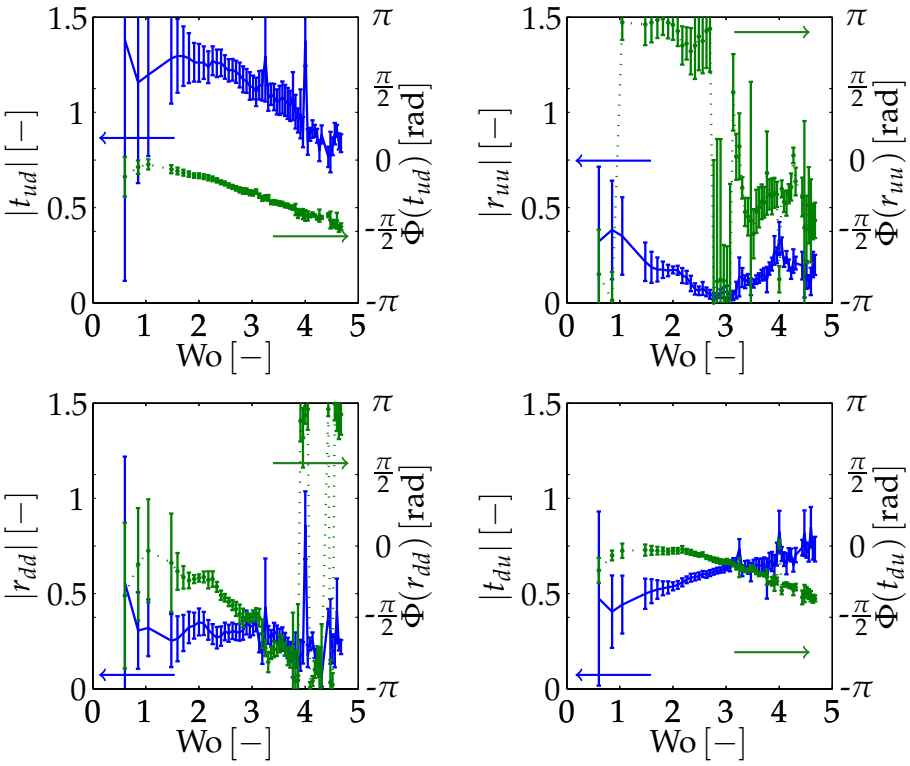

Figure 7.7: Standard deviation of experimental data. Compared to the maximum error, the standard deviation is relative small. This indicates that most parts of the error content is statistical which leads to an acceptable performance of the measurement method.

the phase values of r_{uu} and r_{dd} is related to the smaller contribution of the reflected waves with respect to the recorded noise.

Altogether, the observed error margins are acceptable for comparing the experimental and numerical results in a qualitative manner. The high frequency regime even allows for a quantitative validation of the numerical data. When the frequencies reach low values (Wo $\lessapprox$ 1.6), the experimental data have to be interpreted with caution because of the large errors. Furthermore, tests on other geometries (not presented here) showed that even though they seem to reach values higher than 20%, the average trends remain always comparable.

7.1.4.4 Minor Sources of Errors

The analysis of the methods applied showed a good reliability of the data obtained by all the three methods. This comparability is further influenced by minor discrepancies. Determining the real contribution of these differences is beyond the scope of this thesis. They are presented as possible sources of error in this section.

The test rig is operating at atmospheric conditions. Consequently, everyday fluctuations in atmospheric conditions, for example humidity take effect on the system's acoustic measurement hardware. Moreover, due to design reasons, the microphones are not accurately fixed in their positions. The positioning may change slightly during the measurement campaign. The power supply of the electric heaters is controlled manually. This leads to a power input accuracy lower than 98%. The error of control thermocouples, which are used to maintain a certain temperature distribution, is of the order of 1 K. Although the approximated temperature profile (App. B.1) has been validated empirically, the lack of information about the real multi-dimensional mean temperature field inside the measurement duct causes a certain uncertainty. The temperature of the mains water, which is used to maintain the upstream duct at ambient conditions, changes in time. Deviations of up to 5 K were observed during the measurement campaigns. Finally, it has to be stated that the combination of acoustic oscillations and hot temperatures causes a fast material aging of the internal heater and its surrounding components. Especially the ceramic parts are subjected to deterioration at every measurement campaign. This leads to a change in geometrical conditions as well as losses due to imperfect sealing.

The CFD simulation is also subjected to errors. The open source code OpenFOAM used in the present thesis has rarely been used for aeroacoustic simulations [117, 118, 191]. There is no publication available treating acoustic propagation under non-isothermal conditions. Thus, its accuracy has only been tested to some extent. Kunzer [101] investigated different discretization schemes for incompressible solvers. These were tested in the thesis of Stich. He solved generic compressible test cases by using a PISO looped solver. Altogether, the investigation revealed much higher numerical diffusivity than other codes [58]. The use of the

segregated solver is also expected to induce a certain relative time lag of pressure, velocity and temperature oscillation. Also, the computation of the thermophysical properties causes small discrepancies to experimental and one-dimensional data. Finally, although the temperature profiles were sufficiently resolved, the investigation of higher Pe cases is limited by the mesh resolution. In this case, local refinement will not only cause an increasing number of degrees of freedom, but also a necessity of reducing the time step to maintain an acoustic CFL-number lower than unity.

The one-dimensional numerical tool is expected to be the least error-prone. The usage of a fine discretization and a higher-order integration scheme only induces small errors. The highest numerical errors occur for low frequencies [72]. The computation of the matrix coefficients of $\mathbf{A}$ (Eq. (4.63)) for every step causes an error accumulation, which leads to unphysical results. A preliminary computation of these components in combination with interpolation at the current position circumvents this problem.

7.2 Thermoacoustic Engine Operation Mode

Two states of the TA engine setup facilitate a validation of the scattering matrices obtained. The cycle increment [75, 192] in the linear onset of the engine is comparable to the data obtained from the eigenfrequency analysis of a network model. The limit cycle delivers qualitative information about the ratio of losses, higher-order modes and damping inside the system. Moreover, the reconstructed mode shape of the first eigenmode allows a comparison of the reference plane data to the predicted values obtained by numerical and experimental techniques. All the time-dependent data presented in this chapter refer to the signal depicted in Figure 7.8. The measurement data for this plot are obtained for one TA engine operation point ($L_w = 1.1\,\mathrm{m}$). An average temperature difference of approximately 100 K was preset over the stack by controlling the power supply of the inner heater.

The onset was produced by dismounting a plug at a central position in the cold channel, such that all instabilities break down. As soon as all

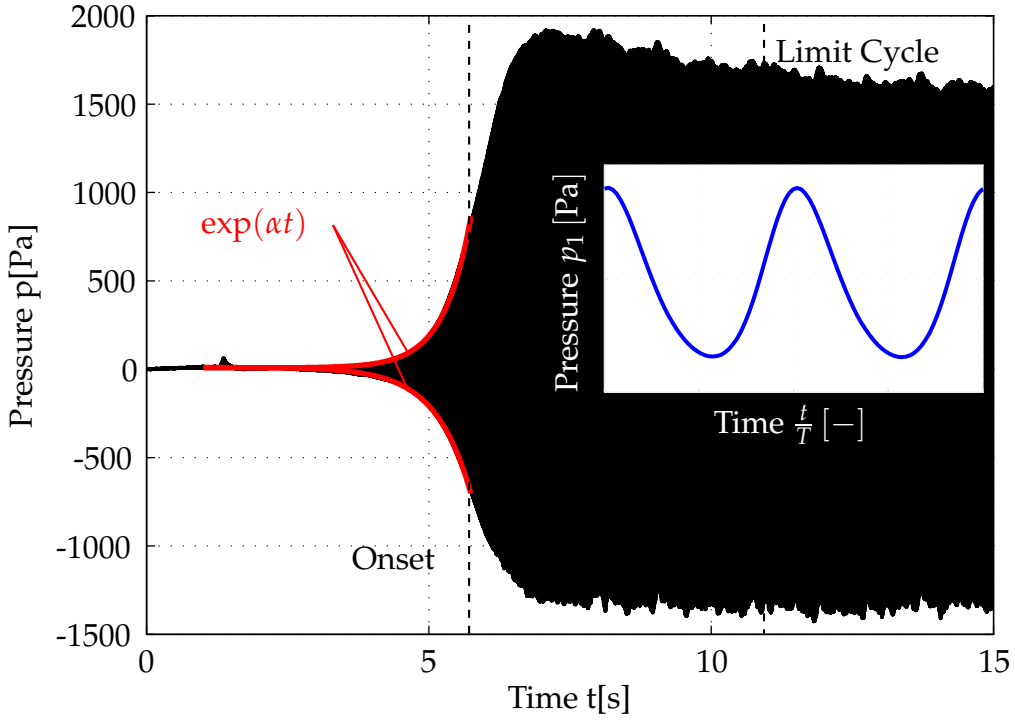

Figure 7.8: The onset and limit cycle of the TA engine setup for a water level of 1.1 m. Peak amplitudes of 2 kPa are reached at a temperature difference of 100 K.

fluctuations die out, the plug is mounted and the unstable mode evolves again until the limit cycle is reached. The first seven seconds displayed in Figure 7.8 are considered as the onset region, where linear TAs dominate the acoustic amplification and nonlinear effects do not affect mean conditions. The blue curve displayed inside the graph depicts two periods of the limit cycle region. It is reached after approximately 12 s.

7.2.1 Mode shape of the First Eigenmode

The mode shape of a certain geometry defines the spatial distribution of the frequency-filtered acoustic pressure and velocity. This distribution is obtained applying the reconstruction technique described in Section 6.1.2. Both ends of the standing wave engine are closed. This demands a $\lambda/2$-mode for the first eigenfrequency of the setup. Furthermore, solid walls postulate $u_1|_{x=0,L} = 0$, which coincides with a vanishing acoustic pressure gradient at these locations for $\mathrm{Ma} = 0$. The state vectors resulting at the reference planes $x_{u,d,\mathrm{ref}}$ provide one set of outgoing

characteristic wave amplitudes that has to match to those computed from the product of the predicted scattering matrix and the incoming waves. Under optimum conditions, the scattering matrix even allows a coupled mode shape solution for the complete setup. These criteria are investigated in detail and discussed here.

The black curves in the magnitude (top) and phase (bottom) plot of Figure 7.9 show the reconstructed mode shape of the first eigenfrequency obtained for the configuration described in Section 6.3.1. The curve fitting with respect to the microphone data (red circles) was processed such that the cold and hot sides were treated separately using the optimiza-

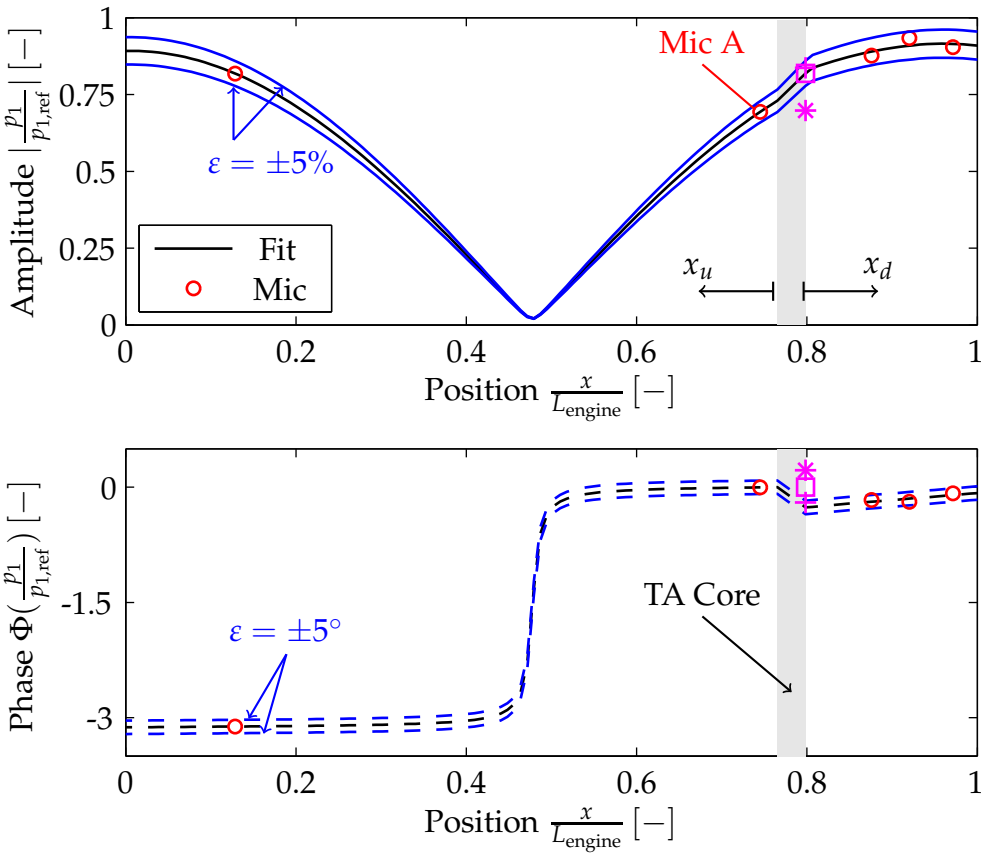

Figure 7.9: The mode shape of the first eigenmode of the TA engine operation mode (top magnitude, bottom phase). The eigenfrequency corresponds to a Womersley number of Wo ≈ 1.7 The black curves depict the reconstructed mode shape obtained by applying the fitting technique described in Section 6.1 to the cold and hot side microphones separately. The colored markers (∗, □, +) of the predicted behavior only partially hit the 95% confidence interval of the magnitude and 5° phase error deviation of the fitted curves.

tion method described in Section 6.1.1. The curves in the TA core region are linear interpolations and no computed intermediate values. The blue curves describe the confidence intervals of 95% for the magnitude curve and a $\pm 5^\circ$ discrepancy to the dashed phase plot. All five microphone measurements (red circles) are within this range. These microphones are not located near the pressure antinode of the profile. The measured pressure data has high amplitude values and hence, the reconstructed mode shape is not affected by the standing wave pattern. Due to the use of two microphones at the cold side, the fitting problem (Eq. (6.4)) with two complex-valued degrees of freedom is not overdetermined. Thus, this part of the curves coincides with the measurement values. The microphones are known to predict the most accurate results for ambient conditions, which also provide the most reliable mean quantity data. Detailed tests revealed that these measurements can lead to errors of $2-3\%$. The hot curve fit was obtained using a measurement based linear temperature distribution according to

$$T_0(x) = 400\,\mathrm{K} - 50\,\mathrm{K}\frac{x_d}{L_d} \tag{7.4}$$

and a temperature stepping of 1 K for each discrete change in mean temperature. Due to the increased number of microphones, the problem becomes overdetermined. The fitting to the less accurate mean temperature data in the downstream ($0.8 < x/L_{\mathrm{engine}} < 1$) lead to clearly visible deviations.

As both ends of the engine are completely sealed, a typical $\lambda/2$ mode shape is expected with both ends having a zero gradient in $|p_1|$. Moreover, the pressure at these locations is expected to oscillate with a phase difference of π. The upstream pressure gradient at $x = 0$ almost reaches zero. This indicates that: a) the fit is in good accordance to the measurement data in the frequency range below the cut-on frequency of transversal modes and b) the water column in the duct causes a hard wall reflection coefficient of

$$\left.\frac{\mathfrak{F}}{\mathfrak{G}}\right|_{x=0} \approx 1. \tag{7.5}$$

In contrast to this good match of fit and estimated pressure profile, the downstream tangent of $|p_1(L_{\mathrm{engine}})|$ is slightly negative. Combined with the phase shift of these positions of more than π, this indicates a certain

error in the predicted fit. This discrepancy may originate from different reasons: i) the estimated temperature distribution is not accurate enough. ii) Although the pressure sensors are water cooled, the heating causes a certain impact on the output data. iii) A bad preparation of the microphone leads to deviations from the calibrated state.

The quality of the three prediction tools is compared in terms of the magenta colored markers in Figure 7.9. They denote the pressure values predicted by computing the hot downstream value from the upstream reference state. For this purpose, the scattering matrix values obtained using the MMM ($*$), the CFD/SI method ($\square$) and the one-dimensional prediction tool ($+$) for the first eigenfrequency Wo $\approx$ 1.65 are extracted. Next, applying Equations (3.24) and (3.26) these values are transformed into transfer matrix data in *pu* notation. Finally multiplying the acoustic state vector of the upstream plane by these matrices yields the predicted p_1 values at the downstream end of the stack. The experimental results ($*$) show the strongest deviation. The measurement error at the operating point of Wo $\approx$ 1.65 is too large to produce reasonable results. The predicted pressure amplitudes of the **CFD** data ($\square$) match to the predicted shape on the hot left side. This is not valid for the phase value. It deviates half as much as the experimental data, but the confidence interval is not captured. This deviation is related to the different cross-sectional shapes of the pores. As shown later (Fig. 7.12), the impact of this parameter causes the largest deviations in this region. Using the right cross-sectional shape values obtained from the one-dimensional model **IMP** ($+$) leads to a match within the confidence intervals. Here and in the next section, the scattering matrix was obtained for quadratic pore shapes of equal hydraulic radius R. Apart from the validation of experimental results in Section 7.1.3, this adaption is presented only in this section.

7.2.2 Thermoacoustic Onset

The pressure data displayed in Figure 7.8 are recorded in the cold duct at the position of microphone A, which is denoted "Mic A" in Figure 7.9. The reconstructed mode shape leads to a factor of $\approx$ 1.3 between the pressure value at the downstream antinode and the measured value at location A. However, as the cycle increment in the linear acoustic regime

is independent of the amplitude values, the consideration of the pressure at any location should lead to the same results.

The red curves in Figure 7.8 display an exponential fit of the hull curve connecting the positive and negative peak values of the measurement. The exponential prefactor, the growth rate α, of both curves deviates by approximately $\pm 10\%$ from the mean value of $1.4\,\mathrm{s}^{-1}$. The value of the cycle increment of 1.3×10^{-2} is of the same order of magnitude as the CI of the engine of Penelet et al. [136]. The maximum CI of the black curve in Figure 6.5 is smaller by a factor of two.

For comparability, a network model[6] of the lossless engine was created to numerically predict the instability of the setup in terms of its first complex-valued eigenfrequency. The same scattering matrix as used in Section 7.2 is implemented. The data of the corresponding scattering matrix were obtained from the quasi one-dimensional model described in Chapter 4. As stagnant mean flow conditions prevail, the solution of in't panhuis et al. [81] (Sec. 7.1.4.1) in combination with Rott functions for quadratic pores can be applied to produce the data series. These data columns were fitted to analytical expressions with a precision of 10^{-3} in the region of $\pm 40\,\mathrm{Hz}$ around the expected first eigenfrequency.

This lossless network model revealed a CI three times higher than the fitted experimental value. An estimation of damping by viscous friction in the test-rig was determined in separate tests at ambient conditions. The damping ratio for different length configurations was determined by exciting the experimental apparatus with a small explosive. Applying spectral methods to the time line of the recorded pressure data yielded damping ratios for the eigenfrequencies of the system. These test showed that the cycle increment of the first eigenfrequency at ambient conditions was about $\mathrm{CI} \approx -2 \times 10^{-2}$. If this damping effect is assumed to occur in the network model in the same way, the predicted CI has to be corrected by adding both cycle increments (Eq. (6.8)). Using this approach, the real and imaginary parts of the predicted complex-valued first eigenfrequency matched with high accuracy to the experimental values.

[6] taX v0.9 [106].

7.2.3 Limit Cycle Oscillations

The mode shape displayed in Figure 7.9 was obtained from the complex-valued pressure data of the first eigenfrequency in the limit cycle region. Limit cycle oscillations occur if nonlinear effects consume the amplification power. Some of these nonlinear mechanisms cause an energy shift to higher modes [187]. A further reduction of the power is restricted to the increasing impact of nonlinear acoustic terms. Second-order contributions in the enthalpy transport change the energy balance of the linear system. This effect and changes in the heat transfer coefficient at the heaters lead to a variation of the axial mean temperature distribution inside the TA stack [187]. The thermal relaxation time for these changes is orders of magnitudes larger than the acoustic time scales[7]. This causes a delay of the system response and the peak pressure magnitudes reached after about eight seconds in the observed case slightly decreases until a steady axial temperature profile is reached.

A consideration of the hull curves in the onset and limit cycle reveals a shift of the amplitude values of approximately $+250\,\mathrm{Pa}$. This suggests an increase in mean pressure when the engine operates in the limit cycle. A close investigation of moving average values of the data set demonstrates that this deviation is a result of the superposition of multiple frequencies that slightly vary in time.

The blue curve in Figure 7.8 displaying two periods of the first eigenfrequency indicate a non-negligible contribution of higher harmonics to the acoustic signal in the limit cycle. In contrast to the linear acoustic regime of the onset, where only the first and second eigenfrequency can be identified in the frequency spectrum, these higher harmonics can also easily be recovered from Figure 7.10. This figure displays the frequency-related pressure magnitude values obtained by a standard fast Fourier transform (FFT) of the limit cycle region. The first harmonic at $f_I \approx 106\,\mathrm{Hz}$ contains the major energy of the acoustic signal and all higher harmonic amplitudes reveal an exponential decrease, which are typically observed in TA limit cycles [11, 184, 217]. Sakamoto et al. [173] attribute their occurrence to the strong nonlinearity of higher mode standing waves, which is not

[7] The stagnant fluid thermal relaxation time is reduced by the acoustic oscillations inside the pores.

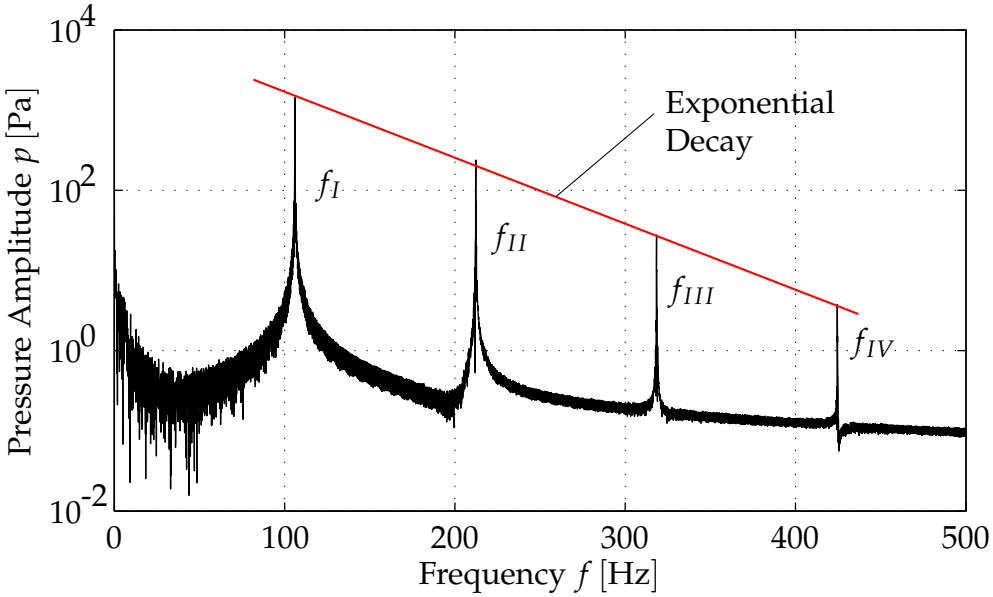

Figure 7.10: FFT of the TA engine in its limit cycle. The first four eigenfrequencies are easily detectable. The steep decay of the amplitude values in the vicinity of the eigenfrequencies indicates low damping inside the system.

physically explained. The numerical model of Watanabe et al. [204, 216] showed these higher harmonics. Their decay rate did not follow exponential decrease. Naugolikh et al. [125] explain the energy shift to the next harmonics based on the Korteweg-de Vries-Burgers equation [221] where the solutions for special conditions reveal an exponential amplitude relation.

In the present work, the amplitude of the second eigenfrequency is slightly higher than the value expected from the exponential decay. This is due to the fact that the second eigenfrequency f_{II}, like the first, experiences an amplification by the TA effect with an overcritical temperature gradient. The lower amplitude of $|p_1(f_{II})|$ compared to the $|p_1(f_I)|$ is due to the higher Lautrec numbers La at this frequency. This coincides with a lower TA interaction over the stack (compared to Section 1.3).

A good qualitative measure for the damping inside the system is the determination of the damping coefficient by the full width at half maximum [54]. The steep drop of the frequency content in the vicinity of the harmonics indicate a very low damping inside the engine (compare to Sec. 7.2.2). The TA amplification is mainly balanced by the second-order

heat transfer effects and turbulent dissipation caused by the high pressure amplitude itself.

7.3 Instability Potentiality of Thermoacoustic Stacks and Regenerators

As stated in Section 3.2.5, the instability potentiality (IP) derived from the scattering matrix of the TA regenerator is a good predictor for the behavior of a complete TA apparatus. In combination with assumed small losses at the reflecting ends, the demonstrated neutral and passive behavior of ducts, discrete area and temperature changes indicate a tendency of passive behavior for both resonator components. The only potentially unstable elements are the heat exchangers and the TA regenerator. A detailed investigation of the heat exchanger scattering matrices might lead to maximum eigenvalues higher than unity. The eigenvalues $\lambda_{\max}$ of the stack will not be reached. This statement is based on the fact that, if a heat exchanger exposed to stagnant mean flow conditions would cause comparable or even higher limit cycles than those of TA engines. Such setups would be more common because of the reduced number of components.

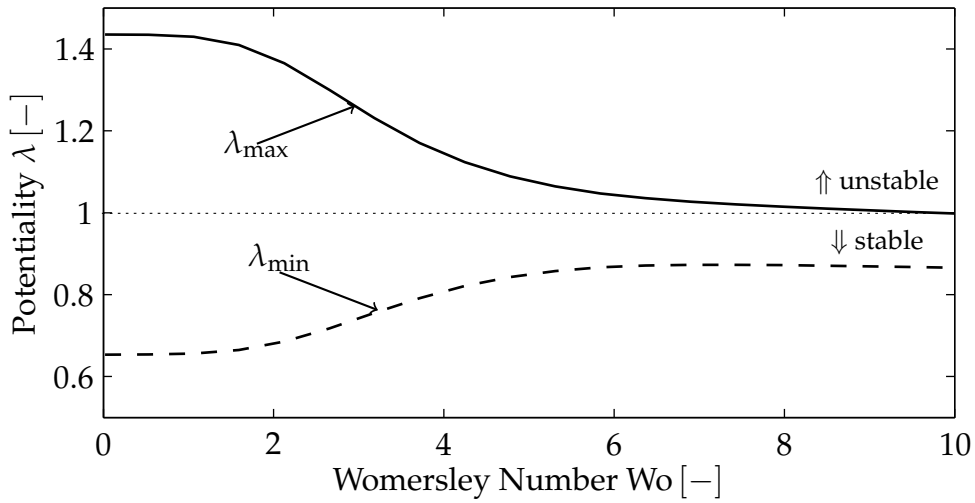

Figure 7.11: Maximum and minimum instability potentiality of the TA regenerator in reference configuration. The maximum eigenvalue $\lambda_{\max}$ predicts a potentially unstable behavior, $\lambda_{\min} < 1$ states that certain configurations yield acoustic power reduction over the regenerator.

As no such application is known to the author[8], the deviation from unity of the maximum eigenvalue $\lambda_{\max}$ of heat exchangers is expected to be at least an order of magnitude lower than the value occurring in TA regenerators.

The maximum (solid line) and minimum (dashed line) eigenvalues of the TA regenerator operating under reference conditions are depicted in Figure 7.11. They are computed using the one-dimensional model values of the scattering matrix displayed in Figure 7.1. This model is also used for the parameter variation in the next chapter. The dotted line indicating unity splits the potentially unstable region from the potentially stable region in this plot. The maximum and minimum eigenvalues describe energy values. They may be compared to the square of the magnitude of the scattering matrix elements. Qualitative relations can be drawn for the frequency limits. They reveal some insight about the dominating components of the TA regenerator.

Next, the low Wo limit eigenvalues depicted in Figure 7.11 are investigated. We compare these values to the scattering matrix data for this limit displayed in Figure 7.2. A short glance at this figure reveals, that suppressing a hot to cold traveling characteristic wave amplitude $\mathfrak{G}_d$ should lead to maximum power amplification, while suppressing $\mathfrak{F}_u$ cause maximum acoustic power reduction. Neglecting the contributions of the reflection coefficients Equation (3.47) reads

$$\eta_{\max} = \frac{c_d \varrho_{0,d}}{c_u \varrho_{0,u}} |t_{ud}|^2 \qquad = 1.46 > \lambda_{\max}, \tag{7.6}$$

$$\eta_{\min} = \frac{c_u \varrho_{0,u}}{c_d \varrho_{0,d}} |t_{du}|^2 \qquad = 0.62 < \lambda_{\min} \tag{7.7}$$

for these approaches. The contributions of the reflection coefficients lead to variations of these data, that lead to te eigenvalues of Figure 7.11. The corresponding eigenvectors of $\lambda_{\max,\min}$ coincide with this simplified investigation. They nearly point into the direction of one of the incoming characteristic wave amplitudes $\mathfrak{F}_u$ and $\mathfrak{G}_d$ [73]. Hence, a systems operating with contributions of mostly one characteristic wave amplitude

[8] The reader should be aware that strictly speaking this is only valid for stagnant mean flow conditions. Mean flow interactions in the area expansions downstream of heat exchangers may lead to instabilities in technical applications. However, shear layer induced mechanisms arise after a transition to turbulent flow conditions.

leads to maximum/minimum acoustic power amplification. Qualitative explanations provided by various authors [31, 187] support this finding. Traveling wave engine engines for example always try to suppress the hot to cold traveling wave in the region of the regenerator.

In the high frequency limit of Figure 7.11 $\lambda_{\max}$ almost reaches unity. This is not valid for the t_{ud} element of the scattering matrix, which is larger by approximately 0.05, but the phase shift of r_{uu} towards zero causes a negative contribution in terms of IP. In contrast to this behavior, the lower eigenvalue is not affected by the reflection coefficients. It reaches the same values as t_{du} which still is stable. As shown by Holzinger et al. [72], the reduced impact of the TA energy conversion in the transmission coefficients (Fig. 7.2) lead to a higher impact of the reflection coefficients to the maximum eigenvalue. With Womersley number increasing above $\mathrm{Wo} > 1$, the corresponding eigenvector shifts to a mixed state of incoming waves causing an optimum standing wave condition at the stack.

The distance to unity is larger for $\lambda_{\min}$ than for $\lambda_{\max}$ in this central Wo sector. These distances do not necessarily scale with the ratio of unstable to stable states. A consideration of the acoustic power output to input ratio of Holzinger et al. [72] showed for $\mathrm{Wo} = 1$ that as long as the characteristic wave amplitude entering the system from the cold side is larger than the hot counter part, the system is unstable for any relative phase, although the distance of λ_i to the neutral state is almost equal. Even if this wave relation is violated, most of the states are active and increase the acoustic power inside the system.

7.3.1 Influence of Mean Parameters

The investigation of the acoustic instability potentiality in the preceding section reveals some insight in the coupling of scattering matrices and IP for TA regenerators for the reference case. These operating conditions depend on parameters that can easily be retrieved from the set of Equations (2.1). The Rott functions $f_{K,\nu}$ depend on the Womersley number Wo and the cross-sectional shape of the regenerator. A change in geometry may yield an improved energy conversion for the technical application in question. The different value returned from the Rott's func-

tions $f_{K,\nu}$ for one frequency is related to their scaling with Pr. The use of different fluids may significantly change the IP of the problem. Viscous dissipation and thermal diffusion both also scale with mean pressure p_0. A pressurization leads to changes in the scattering behavior. Finally, the TA amplification term scales with mean temperature T_0. The investigation of different temperature differences over the stack should influence the IP of the TA regenerator. For yielding a certain insight into the impact of those parameters, they are varied in the next sections. Combinations of parameter variations, which might lead to optimum conditions, are beyond the scope of this work and not considered here.

7.3.1.1 Influence of the Cross-Sectional Pore Shape

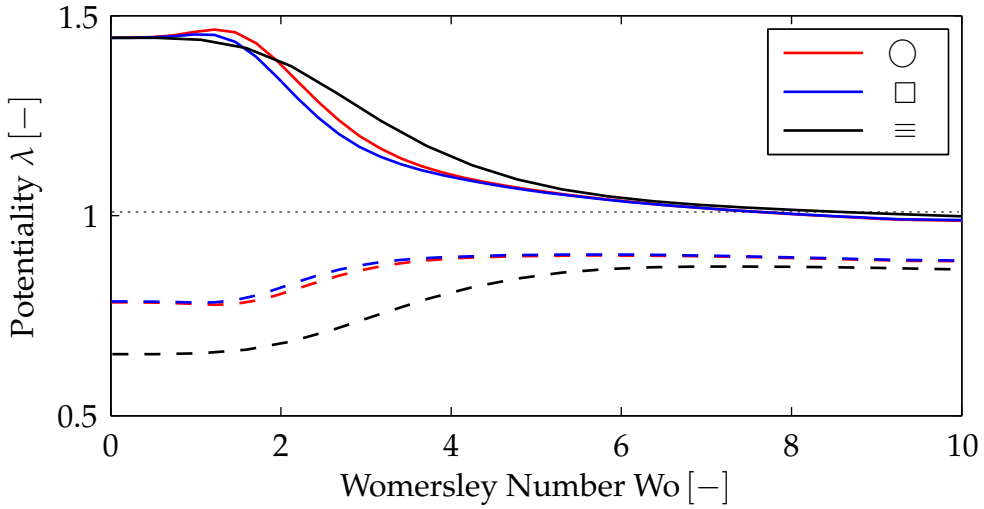

Figure 7.12: Maximum and minimum IP for different cross-sectional shapes in the reference configuration. In the region of $1 \lesssim \mathrm{Wo} \lesssim 4$, where Rott's functions deviate most [187], the maximum potentiality varies. The minimum potentialities of the circular (◯) and quadratic (□) shaped pores are higher than for slab pores.

The viscous Rott's functions describing slab stacked (≡), quadratic (□) and circular shaped pores (◯) are defined by [187]

$$f_{\nu,\equiv} = \frac{2\tanh\left(\frac{1+i}{2}\mathrm{Wo}\right)}{(1+i)\mathrm{Wo}}, \tag{7.8a}$$

$$f_{\nu,\square} = 1 - \frac{64}{\pi^4}\sum_{m,n\mathrm{odd}} \frac{1}{m^2n^2\left(1 - 2i\left[\frac{\pi}{4\mathrm{Wo}}\right)^2(m^2+n^2)\right]}, \tag{7.8b}$$

$$f_{\nu,\bigcirc} = \frac{2J_1\left[(i-1)\mathrm{Wo}\right]}{(i-1)\mathrm{Wo}\,J\left[(i-1)\mathrm{Wo}\right]}. \tag{7.8c}$$

If the thermal penetration depth δ_K is considered, the Womersley number Wo is replaced by the Lautrec number La. As these dimensionless numbers scale with the square root of the Prandtl number Pr (Tab. 4.1), their ratio is fixed by the chosen operating fluid. Especially the real values of these functions deviate for $1 \lesssim \mathrm{Wo} \lesssim 5$. Their impact on the IP is mainly restricted to this region.

Figure 7.12 depicts $\lambda_{\mathrm{min,max}}$ for these three cross-section geometries. The high and low frequency values of the profiles of both quantities stay unaffected. Circular and quadratic pores lead to almost equal eigenvalues except for a small intermediate Wo region.

The peak IPs are reached by circular pores for $\mathrm{Wo} \approx 1.5$. The radial symmetry of the boundary layers improves the energy conversion with respect to the axial symmetric shapes occurring in the other profiles. The lower performance of the slab pores profile at the region of maximum IP is due to the lower change in phase for $f_{\equiv}$. The smoother phase change of the parallel plate geometry coincides with larger magnitude values of the Rott function. Thus, while the circular pores are favorable for low Wo, slab geometries lead to a better performance for applications operating at $\mathrm{Wo} > 2$. The higher amplitude values of $f_{\equiv}$ also increase the impact in A_{12} and A_{21} of the set of transport Equation (2.1), which strongly contribute to λ_{min}. The higher damping causes lower minimum eigenvalues over the entire Womersley number range.

7.3.1.2 Material Properties of the Fluid

The ratio of viscous diffusion to thermal conductivity is a characteristic quantity for many energy conversion processes. Here, the Prandtl number Pr is not just a scaling factor for the TA interaction term A_{22} of Equation (2.1a). It also determines the value of the thermal Rott function f_K for a given Womersley number Wo and thus has an impact on the full system of Equations (2.1). In Figure 7.13 this impact is investigated in terms of a change in the heat conduction K of air. The standard case (black) of $\mathrm{Pr} \approx 0.7$ is depicted for orientation purposes. This value is

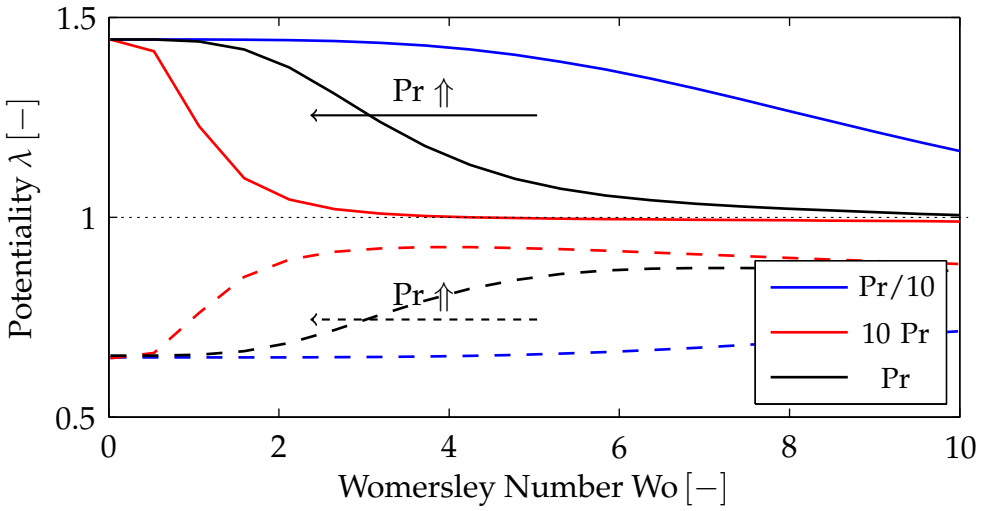

Figure 7.13: Prandtl number variations for a slab pore operating with air. Lower Pr cause a wider Womersley number range of high IP. λ_{min} has a maximum in the medium Wo range, which becomes more distinct for high Pr.

varied over one order of magnitude. The drastic change displays the limits reachable for mixtures of noble gases and refrigerants like R-12 [124]. Most gases fall in this parameter range. As shown in Figure 7.13, a change in Pr does not affect the limit values of λ_i. The solid blue curve depicting λ_{max} for low Pr also tends to unity for high frequency values. The stable eigenvalues behave slightly different. The minimum eigenvalues of high Prandtl numbers Pr experience a maximum value in the range of Wo ≈ 2. A reduction in Pr causes a wider frequency spread, in which the maximum IP deviates far from unity. Using mixtures with low Pr leads to a better performance for equal operating frequencies [202]. Keeping this in mind, the reader should be aware that the speed of sound of these mixtures often strongly deviates from c in air and thus, the operating frequency of an apparatus changes remarkably.

7.3.1.3 Impact of Mean Pressure

Many technical applications operate under pressurized conditions in order to increase the power density [185]. Figures 7.14 depicts the influence of a change in mean pressure of up to ten times the standard conditions. These results are traceable by considering the set of Equations (2.1). The TA conversion term A_{22} is considered to be almost unaffected by changes

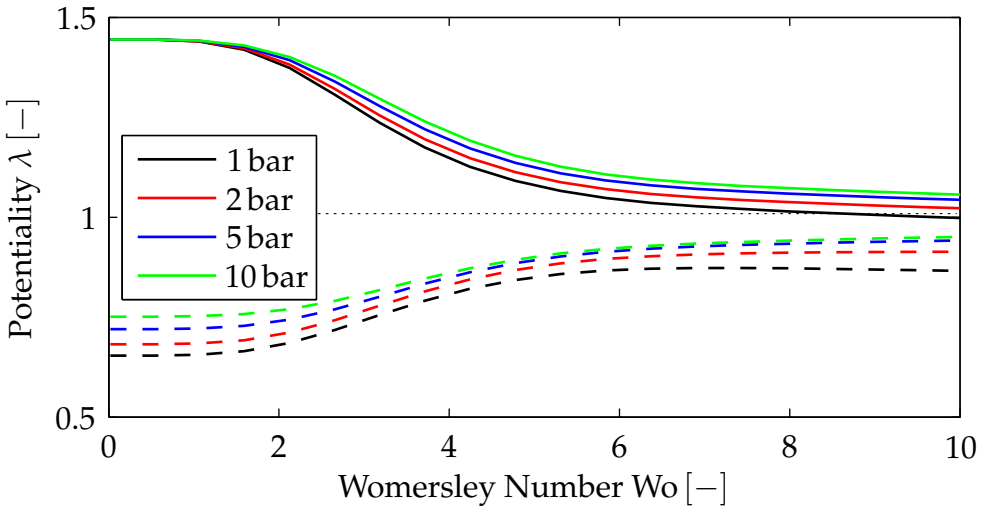

Figure 7.14: IP of different pressurization levels. The viscous diffusion increases with p_0. The eigenvalues become slightly lower.

in p_0. Hence, this dominating term causes similar IPs for all four cases. The only terms directly scaling with mean pressure are those containing viscous dissipation A_{12} and the thermal diffusion A_{21}. While the latter component decreases with p_0, the viscous component becomes stronger and thus causes higher damping. Since the Prandtl number Pr of air is lower than unity, an increase causes higher IPs for pressurized systems. This tendency further supports the utilization of pressurized setups, which already experience higher performance values because of the higher power densities being transported through the regenerator.

7.3.1.4 Variation of the Mean Temperature Gradient

The combination of mean temperature and its gradient in the TA interaction term A_{22} in Equation (2.1b) supports the idea of a strong dependency on this parameter. The influence of $\partial T_0/\partial x$ and $\beta = T_0^{-1}$ can easily be separated by varying two of the following three parameters:

1. Adapting the compressibility β in terms of mean temperature level $T_0(x)$ while keeping the temperature gradient $\partial T_0/\partial x$ constant;

2. Changing the mean temperature gradient $\partial T_0/\partial x$ by varying the hot downstream temperature T_d;

3. Changing the mean temperature gradient $\partial T_0/\partial x$ by changing the stack length L_S for a given temperature difference ΔT_0.

Here, the first two variations are carried out. Surprisingly, a shift of the temperature profile for $\pm 100\,\mathrm{K}$, which corresponds to the first variation, changes the eigenvalues mainly due to the temperature dependency of the thermophysical parameters of the fluid. The IP profile of the acoustic two-port still almost matches the reference case displayed as the black curves in Figure 7.15. On the one hand, this is due to the relatively small changes of compressibility from $3/4$ to $3/2$. This nevertheless should cause changes in viscosity μ, thermal conductivity K etc. On the other hand, the right hand side viscous friction term A_{12} of Equation (2.1a) also scales with this factor and balances these changes. It leads to an unaltered behavior.

Changing the hot mean temperature affects both, the compressibility β and $\partial T_0/\partial x$, but as changes in β have little impact on the result, it can be considered as a change of the second parameter. The linear scaling of the TA interaction term A_{22} in Equation (2.1b) with the mean temperature gradient $\partial T_0/\partial x$ indicates a linear relation between $\lambda_i - 1$ and this parameter. A qualitative consideration of the low frequency limits of Figure 7.15, which displays this variation type from $5\,\mathrm{K}/L < \Delta T_0/L_S <$

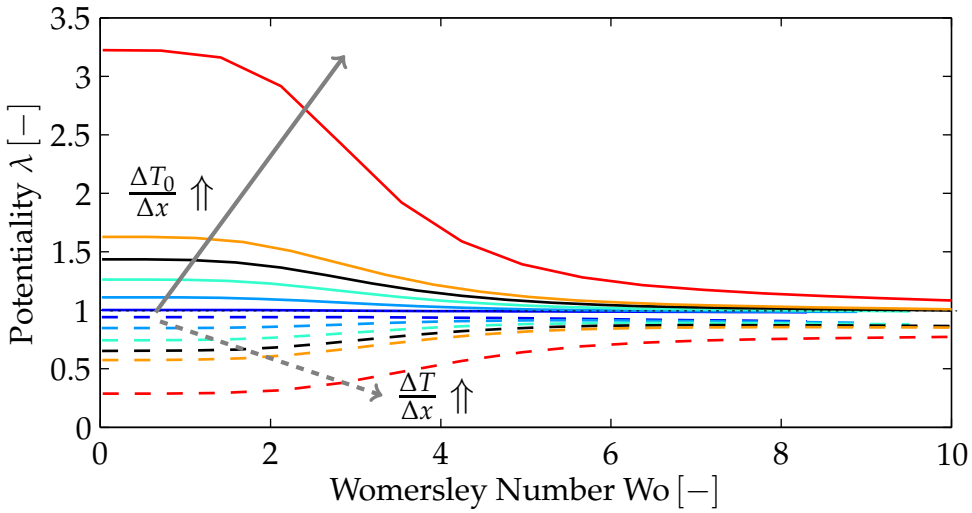

Figure 7.15: Mean temperature dependency of the IP. The spread of the limit curves inclines with increasing T_0. A higher driving gradient linearly scales with $\lambda_{\max} - 1$.

$300\,\mathrm{K}/L$, yields a linear relation between $\lambda_{\max} - 1$ and the temperature gradient. The blue colored curves denote a temperature gradient of 5 K (dark blue), 10 K and 50 K (light blue) per stack length L. The distance between the orange colored $200\,\mathrm{K}/L$ and the reference case depicted in black is as large as the distance between the former curve and the maximum IP of $300\,\mathrm{K}/L$. No saturation limit is reached for the investigated temperature gradients. It is expected that the maximum acoustic power output ratio always scales linearly with an increase in temperature difference. The power output is further affected by diffusion. Such effects are taken into account by the **D-TC-D** model treated in Section 7.1.2. Figure 3.4 shows that if dissipative effects are taken into account in the ducts, both eigenvalues **D-TC-D** decrease from unity for higher Womersley numbers Wo. Hence, considering $\mathrm{Wo} > 0$, the offset of the linear scaling with the temperature gradient changes. The offset follows the decaying lines of the eigenvalues $\lambda_{D-TC-D,max}$ of the simplified model. The linear scaling factor is computed from $\lambda_{\max} - \lambda_{\text{D-TC-D,max}}$ for varying Womersley numbers and temperature gradients.

The variation of the regenerator length for constant temperatures at both ends was also investigated for reasons of completeness. However, the change in the results verified that the impact of the change in β is negligible compared to a variation of the temperature gradient.

The temperature gradient affects the TA interaction locally. One might expect that a change in the temperature profile $T_0(x)$ caused by mean flow u_0 or higher-order effects could lead to other IPs than the ones shown here. For implicit modeling (**IMP**), mean flow changes only result in an adaption of $T_0(x)$. However, due to the linear scaling of the relevant term, the overall impact of different mean temperature profiles $T_0(x)$ neither affects the scattering matrices nor the IP of TA regenerators. Impacts of mean flow, which are captured by the other demonstrated models, are investigated in the next chapter. As the observed influences do not change the nature of the scattering matrices and low Ma affect the IP computation by $1 \pm \mathrm{Ma}^{-1}$, their impact on IP is not considered for these cases.

8 Impact of Mean Flow on the Scattering Behavior of Thermoacoustic Stacks

As discussed in Section 2.4, the mean flow has a strong impact on the axial distribution of the mean temperature. The profile changes from linear to exponential. Traditional modeling approaches (**IMP**) take this change in mean quantities into account, without considering the impact of mean velocity u_0 in detail in the acoustic transport equations . However, variations in the spatial profile of $T_0(x)$ for the same inlet and outlet conditions $T_{u,d}$ lead to small changes in the predicted scattering matrix of a TA regenerator. This approach underestimates the impact of mean flow on the scattering behavior. The one-dimensional models derived in Chapter 4 consider in addition the direct coupling of mean velocity $u_0(x)$ and the acoustic quantities in the TAPEs (Eqs. (4.36)). This chapter demonstrates the higher accuracy of these new models **MI**, **MII** for the prediction of acoustic scattering matrices of stacks that are affected by mean flow. It is organized as follows: at first, Section 8.1 shows the MMM data for three different mean flow configurations and discusses the observed impact of mean flow. In a second step, the same configurations are investigated using CFD/SI methods. Finally, Section 8.3 provides a validation of the one-dimensional models **MI** and **MII** for two cases that vary in Peclet number Pe (Eq. (4.32)): a heat conduction dominated, mean flow affected case $\mathrm{Pe}_{\mathrm{lin}}$ and the same case with a temperature field arising from the mixed convection and conduction influence comparable to experimental conditions $\mathrm{Pe}_{\mathrm{exp}}$. The **CFD** results are chosen as reference solution because of their robustness. These results are also compared to the stagnant mean flow case. It is shown that especially in the low Womersley number Wo region and for larger Peclet numbers Pe, the more accurate modeling approaches improve the predicted scattering behavior with respect to the **CFD** solutions.

8.1 Experimental Mean Flow Results

Determining the influence of mean flow on the scattering behavior of TA regenerators is one of the main goals of this thesis. Trends in experimental data – as long as their nature is physical and they are no experimental artifacts – have to be captured by numerical approaches. Therefore, the results obtained are reconsidered in a first step. Figure 8.1 displays scattering matrices of the experimentally investigated TA core for three different mean flow conditions without the application of the reconstruction method discussed in Section 6.1.3. The black markers denote the amplitude (+) and phase (○) values for stagnant mean conditions, i.e. the case denoted Pe_0. The blue symbols depict a case with a mean

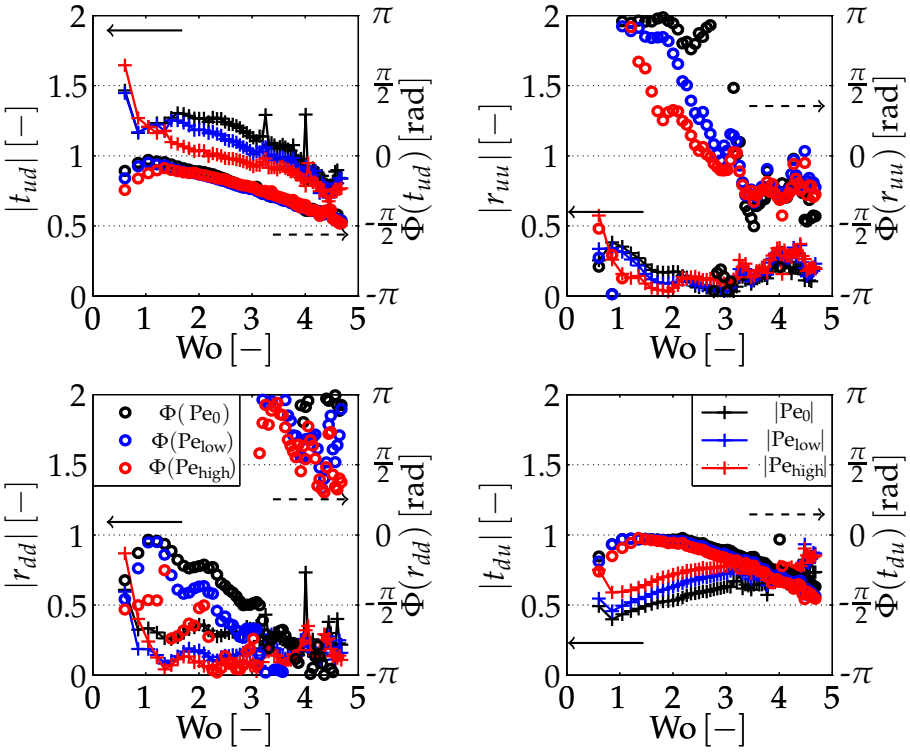

Figure 8.1: Scattering matrices obtained experimentally using the MMM in the presence mean flow u_0. Three cases are investigated: No mean flow (Pe_0, black markers), moderate mean flow of ($\mathrm{Pe}_{\mathrm{low}} \approx 15$, blue markers) and high mean flow ($\mathrm{Pe}_{\mathrm{high}} \approx 30$, red markers). The latter configurations correspond to mean flow velocities at the ambient upstream inlet of $u_0 = 0.05\,\mathrm{m\,s^{-1}}$ and $u_0 = 0.1\,\mathrm{m\,s^{-1}}$. Higher Peclet numbers Pe lead to a lower impact of the TA effect in the transmission coefficients t_{ud} and t_{du}.

flow of $\dot{m} \approx 88.8\,\mathrm{mg\,s^{-1}}$, which is denoted by $\mathrm{Pe_{low}}$. This Peclet number of $\mathrm{Pe} \approx 15$ is equivalent to an inlet mean flow velocity of a stack pore of $u_0 \approx 0.05\,\mathrm{m\,s^{-1}}$ or a reference Mach number of $\mathrm{Ma} \approx 1.5 \times 10^{-4}$. The $\mathrm{Pe_{high}} \approx 30$ data in red correspond to operating conditions occurring with equal temperature difference and twice the air mass flow rate ($\dot{m} \approx 176\,\mathrm{mg\,s^{-1}}$). The mean field conditions at the ambient upstream (reference) end of the stack stay constant. This also accounts for the mean flow velocity $u_0 \approx 0.1\,\mathrm{m\,s^{-1}}$ and $\mathrm{Ma} \approx 3 \times 10^{-4}$. The latter configuration corresponds to the maximum mean flow feed, the air supply of the experimental setup can provide.

The phase Φ of all scattering matrix coefficients is only marginally affected by mean flow. The phases of the reflection coefficients vary stronger than those of the transmission coefficients, especially for very small magnitude values. This indicates that these deviations may be related to measurement errors.

The reflection coefficient amplitudes $|r|$, especially the cold entry $|r_{uu}|$ are similar for all the three cases. The inaccuracy of the data in the low frequency limit ($\mathrm{Wo} \to 0$) was discussed in Section 7.1.4. The stagnant flow values of $|r_{uu}|$ and $|r_{dd}|$ were larger than predicted by the numerical simulation (Sec. 7.1.3) over the entire Womersley number range. In the mean flow affected conditions, a similar overestimation of the reflection coefficient amplitudes can be stated.

The high frequency limit of all three mean flow cases coincide. Phase and magnitude values of the mean flow affected case match the stagnant flow conditions. In this region, the impact of the TA effect is negligible. Therefore, the scattering matrix values are dominated by viscous dissipation and the change in mean temperature ΔT over the stack. The changes in wave number (Eq. (3.28)) are negligible due to its maximum relative change of less than 1%. Hence, the similar high frequency data of the cases prove that ΔT of all three cases is the same.

In contrast to the high frequency range TA energy conversion plays an important role in the low frequency regime. Here, especially the impact on the transmission coefficients t is reduced with increasing mean flow. When the Womersley number Wo drops below a value of four, increas-

ing mass flow rates cause a stronger trend towards unity for both $|t_{ud}|$ and $|t_{du}|$. This trend supports empirical observations [158, 159, 187] that the performance of a TA device drops with increasing mean flow and stops working before the temperature profile is "blown off". The observed deviations in gain of more than 10% justify invoking direct mean flow interaction in one-dimensional prediction tools, although closure assumptions have to be drawn and the numerical effort increases.

8.2 CFD/SI Mean Flow Results

The **CFD** results of stagnant mean flow (black) and the $\mathrm{Pe}_{\mathrm{high}}$ case are displayed in Figure 8.2. The intermediate case $\mathrm{Pe}_{\mathrm{low}}$ is skipped here. Instead, a second cases with the same upstream u_0 conditions as $\mathrm{Pe}_{\mathrm{high}}$ is displayed. They only differ in their mean temperature profile. $\mathrm{Pe}_{\mathrm{lin}}$

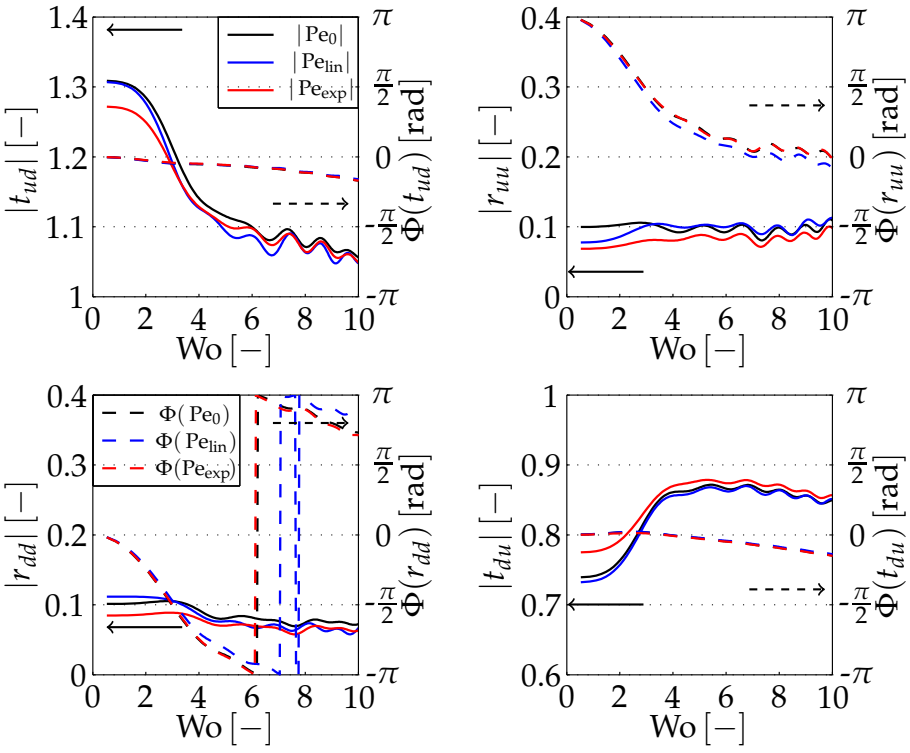

Figure 8.2: Scattering matrices obtained using the CFD/SI method for zero mean flow (black) and mean flow velocity of $u_0 = 0.1\,\mathrm{m\,s^{-1}}$ (red and blue). The latter two cases differ in their mean temperature profile, a conduction dominated case $\mathrm{Pe}_{\mathrm{lin}}$ (red) and a convection/diffusion case $\mathrm{Pe}_{\mathrm{exp}}$ depicted in blue.

denotes a configuration which is dominated by axial heat conduction. This limit case may be realized using copper regenerators. Using such a material leads to an almost linear temperature distribution along the pore. The stagnant mean flow conditions displayed in black in Figure 2.3 experience the same averaged temperature profile as $\mathrm{Pe}_{\mathrm{lin}}$ depicted in blue. The convection/conduction mixed case $\mathrm{Pe}_{\mathrm{exp}}$ is affected by operating conditions similar to $\mathrm{Pe}_{\mathrm{high}}$. This change is equivalent to replacing the regenerator made of copper by a ceramic component based on cordierite while keeping all reference conditions constant. As depicted by the blue graph in Figure 2.3, the temperature distribution has an approximately exponential contour. Such a configuration leads to regions of higher products of $u_0 \frac{\partial T}{\partial x}$ and the additional terms accounted for in **MI** and **MII** may have a stronger impact on the scattering behavior of the TATEs.

The mean flow independent phase values of the transmission coefficients t_{ud} and t_{du} detected in the experimental investigation is reproduced by the CFD/SI method. The signal propagation over the stack is dominated by the axial average of the speed of sound. It further scales with the mean velocity in terms of $1 \pm \mathrm{Ma}$. As the maximum Mach number in the $\mathrm{Pe}_{\mathrm{exp}}$ configuration equals $\mathrm{Ma} \approx 3 \times 10^{-4}$ this impact is negligible. The phases of the reflection coefficients $\Phi(r)$ are not influenced by any changes in transport velocity $c \pm u_0$. Thus, no clear trend is visible in Figure 8.2 from the three investigated cases.

At first the amplitude changes from the stagnant flow case Pe_0 to the convection dominated case $\mathrm{Pe}_{\mathrm{exp}}$ are examined. The trends detected in the experimental investigation are captured. All curves in Figure 8.2 overlap in the Womersley region of $\mathrm{Wo} > 6$. When the frequency is decreased, the transmission coefficients $|t|$ in the $\mathrm{Pe}_{\mathrm{exp}}$ case show a clear reduction in magnitude. The decrease of $|t_{ud}|$ especially affects traveling wave engines, which try to suppress all other components. A reduction of 5% $|t_{ud}|$ causes a 25% reduction in efficiency and should be taken into account in the prediction models. In this region, the gain values of the reflection coefficients $|r|$ also decrease by a small amount, which matches the experimental investigations qualitatively.

The scattering matrix of the $\mathrm{Pe}_{\mathrm{lin}}$ case is a mixture of both cases investigated so far. In the low frequency limit, all gain values match the stagnant mean flow conditions. When the Womersley number Wo is increased, the curves start to tend to the $\mathrm{Pe}_{\mathrm{exp}}$ scattering matrix coefficients until they overlap in a region of $3 < \mathrm{Wo} < 6$.

These observations facilitate two statements. The contribution of the gray boxed mean flow terms in the TATEs (Eqs. (4.36)), which account for the convective transport of acoustic quantities, increases with decreasing Womersley number. Furthermore, the interaction of changes in mean temperature $T_0(x)$ and mean velocity $u_0(x)$ affects the impact of these terms. If a linear temperature gradient occurs, the scattering matrix of the stack stays almost unaffected.

8.3 1D-Modeling of Mean Flow Affected Regenerators

In the last section, the **CFD** data revealed a mean flow dependency of the acoustic scattering behavior. This especially applies to regenerators operating at low Wo conditions. The prediction of scattering values for other configurations consumes a lot of computational resources. The use of less compute intensive tools, like the quasi-one dimensional tool developed in Chapter 4 is preferable as long as their accuracy is acceptable. In the following, the results obtained by these two methods are compared for the cases demonstrated in the previous section. The impact of considering mean flow terms is presented in terms of a validation of the models **MI** and **MII** against the implicit model **IMP**. Validating the scattering matrices resulting from these explicit models against data obtained from CFD and the implicit model gives an idea about the adequacy of the closure assumptions for the modeled terms $\mathbf{\Lambda}_i$ (Eqs. (4.36)).

8.3.1 Heat Conduction Dominated Conditions

The green curves (solid for gain and dashed for phase) depicted in Figure 8.3 represent the frequency-dependent scattering matrix of a TA regenerator exposed to an almost linear mean temperature gradient and $\mathrm{Ma} \approx 3 \times 10^{-4}$. The symbols denote the scattering matrix predictions

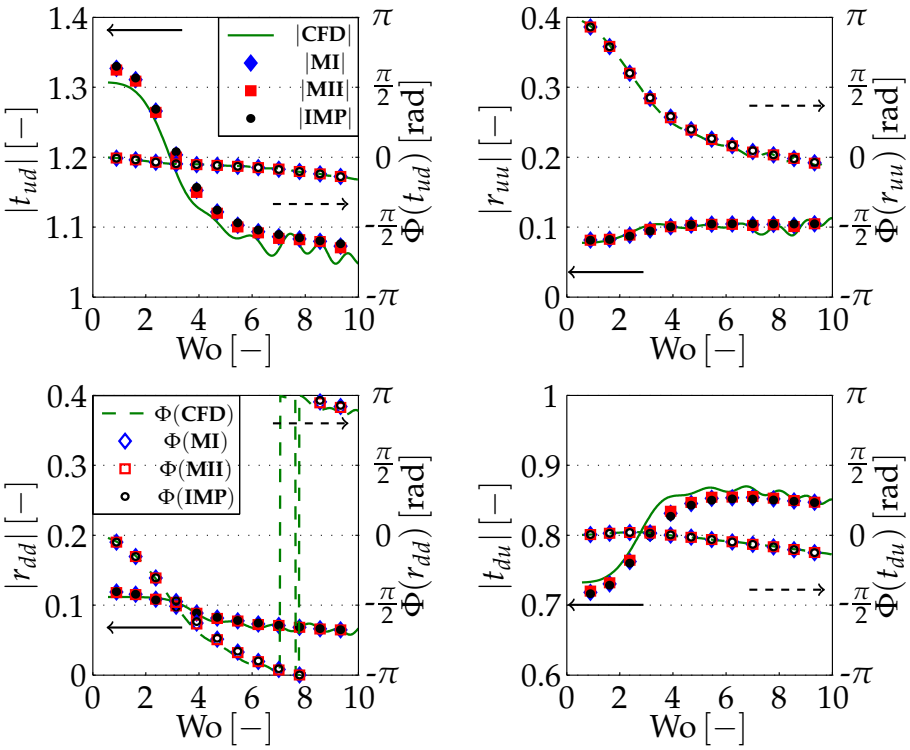

Figure 8.3: One-dimensional models **MI**, **MII** and **IMP** vs. **CFD** data for Ma $\approx 3 \times 10^{-4}$ and a vanishing Pe – the $\mathrm{Pe}_{\mathrm{lin}}$ case. While the implicit model does not react to mean flow, both explicit models show a (very) small reduction in TA interaction in the transmission coefficients.

of the models **MI**(♦) and **MII**(■), which consider u explicitly, and the precursor of these models, the indirectly affected model **IMP**(•). Filled symbols represent gain values, while empty marker stand for the phases of the matrix elements, respectively. Except for small deviations in the region of $1 \lesssim \mathrm{Wo} \lesssim 4$, all three modeling approaches predict the same scattering matrix data. This coincides with a negligible impact of all gray boxed terms in the TAPEs (Eqs. (4.36)).

In general, it can be stated that for this configuration the increased computational effort of the explicit method derived in Chapter 4 is not justified by an improvement in prediction precision. The change in $|t_{ud}|$ in the range of $1 \lesssim \mathrm{Wo} \lesssim 6$, which is captured with higher precision, is of the order of the estimated accuracy achieved for the different methods. Computing the scattering matrix values at a single frequency using one processor of a standard desktop PC takes about thirty seconds. The improvement of the enhanced models **MI** and **MII** comes along with an

increased computational effort by a factor of about three and twenty, respectively.

8.3.2 Peclet Number Controlled Conditions

The validity of the quasi one-dimensional models is presented in Figure 8.4. The $\mathrm{Pe}_{\mathrm{lin}}$ configuration discussed in the last section cannot be obtained in the experimental setup. The operating conditions of $\mathrm{Pe}_{\mathrm{exp}}$ reproduce the operating conditions inside the test rig. This configuration causes stronger deviations in the scattering matrix if mean flow is present (Fig. 8.2). As stated in Section 7.3.1.4, neither the IP, nor the scattering matrix coefficients are affected by a change in mean temperature profiles if mean flow vanishes. Moreover, replacing the y-dependent mean quantities by their cross-sectional averaged quantities is expected to influence

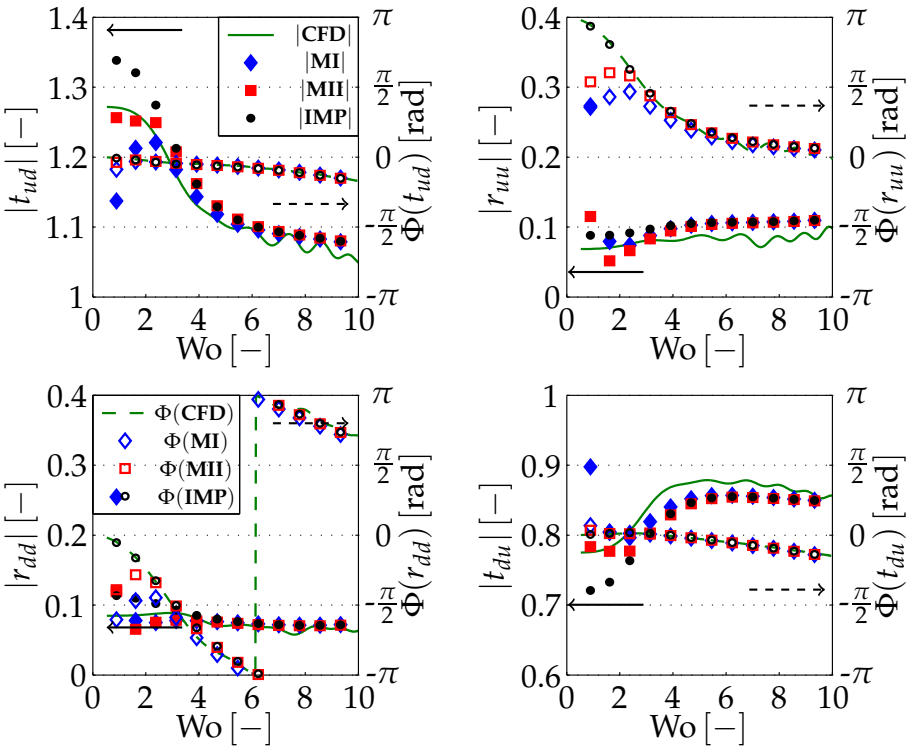

Figure 8.4: One-dimensional models **MI**, **MII** and **IMP** vs. **CFD** data for a convection influenced pore: scattering matrix coefficients of the $\mathrm{Pe}_{\mathrm{exp}} \approx 30$ case. The implicit model still performs similar to previous curves. **MI** overpredicts the amplitude reduction of $|t|$. **MII** matches with a reasonable accuracy for these values. The reflection phases of the latter deviate from **CFD**.

the operating point $\mathrm{Pe}_{\mathrm{lin}}$ with its linear axial temperature profile $T_0(x)$ to some extent. The interaction of acoustic transport variables scaling with a product of those mean quantities is the origin of the deviations between $\mathrm{Pe}_{\mathrm{lin}}$ and $\mathrm{Pe}_{\mathrm{exp}}$.

The ratio of convective to conductive fluxes of $\mathrm{Pe} \approx 30$ in the latter case causes a very steep temperature profile and non-constant axial gradients in u_0 and T_0. Six of the new terms in Equations (4.36) include a combination of these quantities. Among these terms are $\mathbf{\Lambda}_i$, which are modeled by different closure assumptions in **MI** and **MII**. The impact and capabilities of these closure assumptions can be drawn from the differences in resulting scattering matrix data.

Using the same colors and markers, Figure 8.4 displays the acoustic scattering matrices of all three one-dimensional models and the corresponding **CFD** solution for $\mathrm{Pe}_{\mathrm{exp}}$ operating conditions. Although the deviations from the reference solution increase at very small frequencies most tendencies are captured well by the quasi one-dimensional models. In total, a higher complexity of the model improves the solution. The implicit model **IMP** captures all four phases of the predicted **CFD** results over the entire range of Wo. When the TA mechanisms cause a certain phase deviation from the predominant time delay of simplified network approaches (Fig. 7.2), these phases still match the reference solution. In contrast, the changes in gain for low $\mathrm{Wo} \lesssim 3$ are not predicted by this model, because it neglects direct mean flow coupling in the derivation. This accounts for the increase/decrease of the transmission coefficients $|t_{ud}|/|t_{du}|$ induced by the TA effect. The **IMP** magnitude values deviate by up to 0.1 from the reference **CFD** values.

The explicit models take into account the coupling terms between mean velocity and acoustic quantities in Equations (4.36). They vary in their closure assumption for $\mathbf{\Lambda}_i$. Modeling these two terms is the main simplification in the final set of equations. If so, the differences obtained in scattering matrix values compared to **CFD** reflect the influence of these two terms.

In contrast to **IMP**, the model **MI**, which neglects the terms $\mathbf{\Lambda}_i$, does not capture the phases Φ of the reflection elements r depicted in Figure 8.4.

Especially the low frequency region, i.e. Wo < 3, is not captured at all because deviations in Φ of up to $-\pi$ occur in this region. The crucial transmission coefficients $|t|$ match for a wider region than for the **IMP** model. Contrary to all other results obtained, the model tends to the lower limit values of the temperature change (Eq. (7.2)) presented in Figure 7.2. This means that the TA effect is predicted to totally break down for low frequencies using this closure assumption. The reference simulation does not share this trend. Thus, the closure terms $\mathbf{\Lambda}_i$ need to be considered.

Only **MII** takes these terms into account. Although the closure assumption is simplified severely, the transmission gain values match very well in the critical region of Wo < 3. The absolute deviation in $|t_{ud}|$ and $|t_{du}|$ between the quasi one-dimensional model and the **CFD** data is reduced by one order of magnitude, while the phase of these components stays comparable to **CFD**. The phase and gain error of the reflection coefficients is also reduced by a factor of approximately two. The errors still increase with decaying Womersley numbers Wo.

Summarizing the validation of the one-dimensional models, a stepwise improvement in prediction accuracy is visible for the enhanced modeling of **MI** and **MII**. Taking into account mean flow in the TAPEs (Eqs. (4.36)) is crucial for a better prediction. Especially a valid closure assumption for the terms $\mathbf{\Lambda}_i$ is necessary for a good description of the low Womersley region of cases with high Peclet numbers. Modeling these terms by a cross-sectional average of the **IMP** solution, i.e. **MII**, causes a reduction of 50% in magnitude error relative to **MI**. Except for the low frequency limit, **MII** performs very accurate. In this region, the more sophisticated approaches discussed in Section 4.5.4 have to be used for achieving high accuracy.

9 Conclusions and Outlook

The impact of laminar mean flow on acoustic scattering in TA regenerators has been investigated. A quasi one-dimensional approach was presented. Two closure assumptions were derived for an analytical approach. The accuracy of the modeling approaches has been validated against CFD data and results obtained experimentally for one test configuration.

The validation succeeded for stagnant mean flow conditions with only little deviation for scattering matrix measurements as well as reconstruction of the operating conditions of the experimental test rig in engine operation mode. Due to the lack of reliability of the multi microphone measurements, the CFD solution was chosen as reference solution for a validation of the quasi one-dimensional approach.

The second part of the validation was then carried out for mean flow affected pores. The experimental data, **CFD** results and the analytical modeling revealed two key findings:

1. The TA effect occurring in regenerators is affected by mean flow velocity u_0. For the settings considered, the transmission coefficients of the scattering matrices showed an increasing sensitivity to mean flow for Mach numbers of $\mathrm{Ma} > 1.5 \times 10^{-4}$. The change of TA interaction is stronger if combinations of steep axial gradients in mean flow velocity $u_0(x)$ and mean temperature $T_0(x)$ occur inside the pore. Thus, linear temperature profiles produce more acoustic power than convection-affected distributions $T_0(x)$, which, for example, occur in fluid/solid material combinations of air inside a ceramic regenerator. Linear temperature profiles are maintained by stack materials providing high conductivity. Such configurations show a TA scattering behavior similar to stagnant mean flow conditions. This is not valid for convection dominated cases. The investigated combinations of mean flow and mean temperature distribu-

tion cause a certain decay in the TA interaction. This corroborates the observations of other publications [158, 159].

2. The experimental results and multi-dimensional CFD simulations show a good agreement in the trends observed. These trends in the **CFD** solution data can also be predicted by the quasi one-dimensional model. To find a good agreement, mean flow contribution has to be taken into account in the linearization process. Further, adequate closure assumptions have to be chosen. Here, especially in the low Wo region, the advanced **MII** model showed better agreement than **IMP** and **MI**. Only for very low Womersley numbers Wo all tested closure assumptions fail. For the best model, **MII** this failure is restricted the phase of the reflection coefficients. Higher complexity leads to higher accuracy, but is also accompanied by an increase in computational effort. The same challenges arise with a more detailed description of the mean flow field.

The quasi one-dimensional model can be applied in numerical prediction tools in the early stage of the development of new technical setups. The TA transport ODEs predict the spatial distribution of cross-sectionally averaged acoustic pressure and velocity distributions. Their validity is independent of nonlinear effects as long as they only affect mean quantities. Thus the quasi one-dimensional models yield accurate predictions of the acoustic performance of any TA device that is affected by mean flow.

The low-order model improves the prediction of acoustic transfer of all devices marked by green dots in Figure 1.2 depicting the TA iceberg analogy. It enables a more accurate prediction of the performance of devices affected by unwanted or deliberate mean flow. Streaming effects inside TA traveling wave applications can cause mean flow velocities comparable to the cases investigated in Chapter 8. These effects per se lead to a reduction in conversion efficiency by causing losses and storing energy in second-order terms. The investigated examples show that these reductions are even increased by the direct impact of mean flow on the acoustic transport equations. This shows the necessity of suppressing mean flow in such devices. The suppressing characteristic of mean flow velocity may also be used to stabilize systems. For example, a small amount of

mean flow circulating in pipes entering and leaving the hydrogen storage of a fuel cell car can prevent the system from going unstable. Such a measure improves the security of the energy supply in mobile applications. Modeling the losses inside the supply system carefully facilitates the application of the one-dimensional model derived to determine the necessary amount of mean flow to stabilize the system. Finally, the direct application of mean flow inside thermoacoustic devices may still be advantageous to traditional methods. Especially in waste heat conversion, where the heat is fed to the device by enthalpy flow, the direct conversion of heat into acoustic power is attractive for potential application. The omission of one heat exchanger reduces the costs of the device. These have to be balanced by the decrease in energy conversion efficiency, which is implied by the occurrence of mean flow inside the regenerator. Additionally, reducing the losses inside the system by omitting the heat exchanger may even lead to an improved performance of the overall setup. Computing this situation with the one-dimensional tool leads to an accurate prediction of the expected efficiency of the system.

The low computational costs allow for a fast determination of the acoustic transfer for various configurations. Furthermore, applying it in combination with the instability potentiality as optimization tool facilitates drawing a map that indicates the positive or negative impact of mean flow. The influence of several mean parameters shown in Section 7.3 demonstrates the multi-dimensionality of such a map. Tabulation methods and optimization algorithms should be applied to ensure a fast determination of promising operating conditions. Nevertheless, a technical device operating with deliberate mean flow that improves the TA power conversion performance remains unknown. The investigation of possible fields of application is left to future research activity.

Finally, this thesis provides contributions that facilitate the understanding of the impact of mean flow on the TA effect. So far, Sondhauss and Rijke type applications were clearly separated. Extending the use of the former to the convective mean flow regime merges their applicability. This thesis does not show the differences and similarities of these energy conversion mechanisms. A close investigation may yield a combined application or demonstrate a familiarity of both effects that is not known

today. It may lead to a new nomenclature distinguishing between conduction and convection dominated acoustic power conversion.

Supervised Theses

Im Rahmen dieser Dissertation entstanden am Lehrstuhl für Thermodynamik der TU München in den Jahren 2007 bis 2012 unter wissenschaftlicher, fachlicher und inhaltlicher Anleitung des Autors die im Folgenden aufgeführten studentischen Arbeiten. In ihnen wurden verschiedene Fragestellungen zur Wärmeübergangsbestimmung und Thermoakustik untersucht. Ergebnisse aus diesen Arbeiten können in Teilen in das vorliegende Dokument eingeflossen sein. Der Autor dankt hiermit nochmals explizit allen ehemals betreuten Studenten für ihr Engagement bei der Unterstützung dieser wissenschaftlichen Arbeit.

Associated with this Ph. D. thesis are a number of "student theses" (Semesterarbeiten, Diplomarbeiten, Bachelor theses or Master theses) that were supervised by the author of the present work. These theses were prepared at the Lehrstuhl für Thermodynamik at TU München in the years 2007 through 2012 under the close supervision of the present author. Various issues were investigated concerning heat transfer problems as well as thermoacoustic questions. Some parts of these supervised theses may have been incorporated into the present thesis. The author would like to express his sincere gratitude to all formerly supervised students for their commitment supporting this research project.

Student	**Thesis**
Alexander Avdonin	*Determination of the Acoustic Power Generation Potentiality of One-Dimensional Acoustic Elements*, Semesterarbeit, filed in July 4th, 2011.
Armin Baumgartner	*One-Dimensional Modeling of the Thermoacoustic Effect Considering Mean Flow*, Diplomarbeit, filed in November 15th, 2011.

Stefan Erschen	*Konstruktion einer Thermoakustischen Maschine zur Untersuchung des Wärmeübergangs in einer pulsierenden Strömung* (in German), Semesterarbeit, filed in August 24th 2009.
Viktor Fleischer	*Simulation und Systemidentifikation des thermoakustischen Effekts* (in German), Semesterarbeit, filed in April 26th, 2010.
Richard Gurtner	*Implementierung eines 1-D Modells zur Stabilitätsanalyse thermoakustischer Stacks* (in German), Semesterarbeit, filed in June, 8th 2010.
Vera Hoferichter	*Gittergenerierung und Optimierung zur Untersuchung thermoakustischer Grenzschichtphänomene* (in German), Semesterarbeit, filed in August 31st, 2011.
Thomas Kaiser	*Numerical Simulation and System Identification of Thermoacoustics*, Semesterarbeit, filed in May 1st, 2011.
Claude Labonte & Tobias Sachsenhauser	*Numerische Parameterstudie des Wärmeübergangs in pulsierenden Strömungen* (in German), Semesterarbeit, filed in November 30st, 2007.
Jürgen Loth	*Thermische Identifikation und Optimierung eines Thermoakustik Prüfstandes* (in German), Semesterarbeit, filed in June 15th, 2011.
Christina Mauter	*Aufbau und Inbetriebnahme eines Prüfstandes zur Quantifizierung thermoakustischer Grenzschichteffekte* (in German), Semesterarbeit, filed in Apritl 25th, 2011.
Johannes Schäfer	*Implementation of Non-Reflecting LODI Boundary Conditions with Plane Wave Masking in OpenFOAM* , Semesterarbeit, filed in April 15th, 2011.
Jürgen Stich	*Optimierung akustischer Simulationen für Finite Volumen basierte sequentielle Löser* (in German), Semesterarbeit, filed in June 29, 2011.

Maximilian Sperling	*Numerical Computation of Acoustic Transfer in the Low Frequency Regime*, Diplomarbeit, filed in November 15, 2012.
Constanze Temmler	*Numerische Untersuchungen zum Einfluss der Festkörperwärmeleitung bei thermoakustischen Grenzschichtphänomenen* (in German), Bachelorthesis, filed in September 31st, 2011.

References

[1] K. Abdoulla, Z. Yu, and A. J. Jaworski. Design of a Low-Cost Two-Stage Thermoacoustic Electricity Generator for Rural Communities in Developing Countries. In *Proceedings of the 19th International Congress on Sound and Vibration, Vilnius, Lithuania*, July 2012.

[2] A. S. Abduljalil, Z. Yu, and A. J. Jaworski. Selection and Experimental Evaluation of Low-Cost Porous Materials for Regenerator Applications in Thermoacoustic Engines. *Materials & Design*, 32(1): 217–228, 2011.

[3] P. Aben, P. Bloemen, and J. Zeegers. 2-D PIV Measurements of Oscillatory Flow Around Parallel Plates. *Experiments in Fluids*, 46:631–641, 2009.

[4] M. Åbom and H. Bodén. Error Analysis of Two–Microphone Measurements in Ducts with Flow. *Journal of the Acoustical Society of America*, 83(6):2429–2438, 1988.

[5] J. A. Adeff, T. J. Hofler, A. A. Atchley, and W. C. Moss. Measurements with Reticulated Vitreous Carbon Stacks in Thermoacoustic Prime Movers and Refrigerators. *Journal of the Acoustical Society of America*, 104(1):32–38, 1998.

[6] Agilent Technologies, Inc. *Agilent 34970A Users Guide*, 2003.

[7] P. R. Alemela. *Measurement and Scaling of Acoustic Transfer Matrices of Premixed Swirl Flames*. Ph. D. thesis, Technische Universität München, München, Germany, 2009.

[8] M. Altenbokum. Das Phänomen Thermoakustik: Praktische Anwendungen. *Kälte, Luft und Klimatechnik*, 12:26–28, 2008.

[9] W. P. Arnott, H. E. Bass, and R. Raspet. General Formulation of Thermoacoustics for Stacks Having Arbitrarily Shaped Pore Cross Sections. *Journal of the Acoustical Society of America*, 90:3228–3237, 1991.

[10] R. Aster, B. Borchers, and C. Thurber. *Parameter Estimation and Inverse Problems*. Academic Press, 2nd edition, 2012.

[11] A. A. Atchley, H. E. Bass, and T. J. Hofler. Development of Nonlinear Waves in a Thermoacoustic Prime Mover. In M. F. Hamilton and D. T. Blackstock, editors, *Frontiers in Nonlinear Acoustics: Proceedings of the 12th ISNA*, pages 603—-608. Elsevier Science, London, 1990.

[12] A. A. Atchley. Analysis of the Initial Buildup of Oscillations in a Thermoacoustic Prime Mover. *Journal of the Acoustical Society of America*, 95(3):1661–1664, 1994.

[13] Y. Aurégan and R. Starobinski. Determination of Acoustical Energy Dissipation/Production Potentiality from the Acoustical Transfer Functions of a Multiport. *Acta Acustica*, 85(6):788–792, 1999.

[14] B. B. Efron and R. Tibshirani. *An Introduction to the Bootstrap*. Chapman & Hall, 1993.

[15] S. Backhaus and G. W. Swift. A Thermoacoustic Stirling Heat Engine. *Nature*, 399(6734):335–338, 1999.

[16] S. Backhaus and G. W. Swift. Fabrication and use of Parallel Plate Regenerators in Thermoacoustic Engines. In *Proceedings of the 36th Intersociety Energy Conversion Engineering Conference, Savannah, USA*, pages 453–458, 2001.

[17] S. Backhaus and G. W. Swift. New Varieties of Thermoacoustic Engines. In *Proceedings of the 9th International Congress on Sound and Vibration, Orlando, USA*, pages 8–11, 2002.

[18] S. Backhaus and G. W. Swift. An Acoustic Streaming Instability in Thermoacoustic Devices Utilizing Jet Pumps. *Journal of the Acoustical Society of America*, 113(3):1317–1324, 2003.

[19] S. Backhaus, G. W. Swift, and R. S. Reid. High-Temperature Self-Circulating Thermoacoustic Heat Exchanger. *Applied Physics Letters*, 87(1):14102–14102, 2005.

[20] H. Bailliet, P. Lotton, M. Bruneau, V. Gusev, J. Valière, and B. Gazengel. Acoustic Power Flow Measurement in a Thermoacoustic Resonator by Means of Laser Doppler Anemometry (L.D.A.) and Microphonic Measurement. *Applied Acoustics*, 60(1):1–11, 2000.

[21] H. Bailliet. Fascicule de Cours. In *Ecole d'été de thermoacoustique, Roscoff, France*, pages 453–458, 2001.

[22] T. C. Bammann, C. Q. Howard, and B. Cazzolato. Review of Flow-Through Design in Thermoacoustic Refrigeration. In *Proceedings of the Australian Acoustical Society Conference, Busselton, Australia*, pages 357–361, November 2005.

[23] A. Berson, M. Michard, and P. Blanc-Benon. Measurement of Acoustic Velocity in the Stack of a Thermoacoustic Refrigerator Using Particle Image Velocimetry. *Heat and Mass Transfer*, 44:1015–1023, 2008.

[24] R. B. Bird, W. E. Stewart, and E. N. Lightfoot. *Transport Phenomena*. Wiley, New York, 2nd edition, 2001.

[25] G. Bisio and G. Rubatto. Sondhauss and Rijke Oscillations—Thermodynamic Analysis, Possible Applications and Analogies. *Energy*, 24(2):117–131, 1999.

[26] P. Blanc-Benon, E. Besnoin, and O. Knio. Experimental and Computational Visualization of the Flow Field in a Thermoacoustic Stack. *Comptes Rendus Mécanique*, 331(1):17–24, 2003.

[27] H. Bodén and M. A. bom. Influence of Errors on the Two-Microphone Method for Measuring Acoustic Properties in Ducts. *Journal of the Acoustical Society of America*, 79(2):541–549, 1986.

[28] D. Bohn and E. Deucker. An acoustical model to predict combustion driven oscillations. In *20th International Congress on Combustion Engines*, 1993.

[29] E. Buckingham. On Physically Similar Systems: Illustrations of the Use of Dimensional Equations. *Physical Review*, 4(4):345–376, 1914.

[30] R. L. Carter and K. T. Feldman. An Acoustically Resonant Stirling Engine. pages 166–169, 1963.

[31] P. H. Ceperley. A Pistonless Stirling Engine—The Traveling Wave Heat Engine. *Journal of the Acoustical Society of America*, 66(5):1508–1513, 1979.

[32] H. Chaitou, P. Nika, and G. Layes. A New Numerical Optimization Approach For Standing-wave Thermoacoustic Engines. In *Proceedings of the 19th International Congress on Sound and Vibration, Vilnius, Lithuania*, July 2012.

[33] Chart BioMedical. QDrive-The Sound Choice. www.qdrive.com, 2012.

[34] B. M. Chen, Y. A. Abakr, P. H. Riley, and D. B. Hann. Development of Thermoacoustic Engine Operating by Waste Heat from Cooking Stove. *AIP Conference Proceedings, Sydney, Australia*, 1440(1):532–540, 2012.

[35] G. B. Chen and T. Jin. Experimental Investigation on the Onset and Damping Behavior of the Oscillation in a Thermoacoustic Prime Mover. *Cryogenics*, 39(10):843–846, 1999.

[36] B.-T. Chu. On the Generation of Pressure Waves at a Plane Flame Front. *International Symposium on Combustion*, 4(1):603–612, 1953.

[37] J. R. Clement and J. Gaffney. Thermal Oscillations in low Temperature Apparatus. *Advances in Cryogenic Engineering*, 1:302–306, 1953.

[38] K. D. Cole, J. V. Beck, A. Haji-Sheikh, and B. Litkouhi. *Heat Condiction Using Green's Functions*. CRC Press, 2nd edition, 2011.

[39] T. Colonius and S. K. Lele. Computational Aeroacoustics: Progress on Nonlinear Problems of Sound Generation. *Progress in Aerospace Sciences*, 40(6):345–416, 2004.

[40] COMSOL Multiphysics GmbH. *COMSOL Multiphysics Users Guide*, June 2012.

[41] C. Constanda. *Solution Techniques for Elementary Partial Differential Equations*. CRC Press, 2nd edition, 2010.

[42] Corning GmbH. Corning Thin-Wall Substrates, August 2012.

[43] B. de Kees. Multi-Stage Travelling Wave Thermoacoustics in Practice. In *Proceedings of the 19th International Congress on Sound and Vibration, Vilnius, Lithuania*, July 2012.

[44] M. M. Denn. *Process Fluid Mechanics*. Prentice-Hall Englewood Cliffs, NJ, 1980.

[45] A. P. Dowling. The Calculation of Thermoacoustic Oscillations. *Journal of Sound and Vibration*, 180(4):557–581, 1995.

[46] A. P. Dowling. Thermoacoustics and Instability. In *Proceedings of the 6th International Congress on Sound and Vibration, Copenhagen, Denmark*, 1999.

[47] A. P. Dowling and J. E. Ffowce-Williams. *Sound and Sources of Sound*. Ellis Horwoood, 1983.

[48] D. G. Duffy. *Green's Functions with Applications*. Chapman & Hall/CRC, 2001.

[49] E. N. Economou and P. Fulde. *Green's Functions in Quantum Physics*, volume 7. Springer-Verlag New York, 1979.

[50] S. Evesque and W. Polifke. Low-order acoustic modelling for annular combustors: Validation and inclusion of modal coupling: Power for land, sea and air. In *Proceedings of ASME Turbo Expo 2002 Power for Land, Sea and Air*, July 2002.

[51] K. T. Feldman. *A Study of Heat Generated Pressure Oscillations in a Closed end Pipe*. Ph. D. thesis, University of New Mexico, College of Engineering, Bureau of Engineering Research, 1965.

[52] K. T. Feldman. Review of the Literature on Sondhauss Thermoacoustic Phenomena. *Journal of Sound and Vibration*, 7(1):71–82, 1968.

[53] K. Feldman Jr. Review of the Literature on Rijke Thermoacoustic Phenomena. *Journal of Sound and Vibration*, 7(1):83–89, 1968.

[54] R. Feynman, R. Leighton, and M. Sands. *The Feynman Lectures on Physics, Vol. I: The New Millennium Edition: Mainly Mechanics, Radiation, and Heat*. Basic Books, 2011.

[55] A. Fischer. *Hybride, thermoakustische Charakterisierung von Drallbrennern*. Ph. D. thesis, Technische Universität München, 2004.

[56] A. Fischer, C. Hirsch, and T. Sattelmayer. Comparison of multi-microphone transfer matrix measurements with acoustic network models of swirl burners. *Journal of Sound and Vibration*, 298(73-83): 73–83, 2006.

[57] S. Föller and W. Polifke. Advances in Identification Techniques for Aero-Acoustic Scattering Coefficients from Large Eddy Simulation . In *Proceedings of the 18th International Congress on Sound and Vibration, Rio de Janeiro, Brasil*, 2011.

[58] S. Föller and W. Polifke. Identification of Aero-Acoustic Scattering Matrices from Large Eddy Simulation: Application to a Sudden Area Expansion of a Duct. *Journal of Sound Vibration*, 331(13): 3096–3113, 2012.

[59] A. M. Fusco, W. C. Ward, and G. W. Swift. Two-Sensor Power Measurements in Lossy Ducts. *Journal of the Acoustical Society of America*, 91(4):2229–2235, 1992.

[60] S. Garrett. Thermoacoustic Engines and Refrigerators. *American Journal of Physics*, 72:11–17, 2004.

[61] A. Gentemann and W. Polifke. Scattering and Generation of Acoustic Energy by a Premix Swirl Burner. In *Proceedings of the International Gas Turbine and Aeroengine Congress & Exposition, Montreal, Quebec, Canada*, 2007.

[62] A. M. G. Gentemann, A. Fischer, S. Evesque, and W. Polifke. Acoustic Transfer Matrix Reconstruction and Analysis for Ducts with Sudden Change of Area. In *Proceedings of the 9th AIAA/CEAS Aeroacoustics Conference and Exhibit, Hilton Head, USA*, 2003.

[63] A. Gentemann. *Identifikation von akustischen Transfermatrizen und Flammenfrequenzgängen mittels Strömungssimulation*. Ph. D. thesis, Technische Universität München, 2006.

[64] O. S. Graham and A. P. Dowling. Low-Order Modelling of the Response of Ducted Flames in Annular Geometries. In *Proceedings of ASME Turbo Expo 2012, No. GT2012-68698, Copenhagen, DK*, 2012.

[65] G.R.A.S. Sound & Vibration. *1/4-inch Pressure Microphone Type 40BP*, 2004.

[66] M. Guedra, G. Penelet, P. Lotton, and J. Dalmont. Theoretical Prediction of the Onset of Thermoacoustic Instability from the Experimental Transfer Matrix of a Thermoacoustic Core. *Journal of the Acoustical Society of America*, 130(1):145–152, 2011.

[67] D. Havelock, S. Kuwano, and M. Vorländer. *Handbook of Signal Processing in Acoustics*, volume 1. Springer Verlag, 2008.

[68] H. Helmholtz. *On the Sensations of Tone*. Dover Publications, 1954.

[69] B. Higgins. On the Sound Produced by a Current of Hydrogen Gas Passing Through a Tube. *Journal of Natural Philosophy and Chemical Arts*, 1:129, 1802.

[70] O. Hireche, C. Weisman, D. Baltean-Carlès, P. Le Quéré, and L. Bauwens. Low Mach Number Analysis of Idealized Thermoacoustic Engines with Numerical Solution. *Journal of the Acoustical Society of America*, 128:3438, 2009.

[71] T. Hofler. *Thermoacoustic Refrigerator Design and Performance*. Ph. D. thesis, University of California, San Diego, 1986.

[72] T. Holzinger and W. Polifke. Optimization of Thermoacoustic Stacks for Maximum Generation of Acoustic Energy. In *Proceedings of the 19th International Congress on Sound and Vibration, Vilnius, Lithuania*, July 2012.

[73] T. Holzinger, T. Emmert, and W. Polifke. Optimization of Thermoacoustic Regenerators for a Maximum Generation of Acoustic Energy. *(sbmitted to) Journal of the Acoustical Society of America*, 2013.

[74] Y. Huang, J. Benesty, and J. Chen. *Acoustic MIMO Signal Processing*, volume 1. Springer Berlin, Germany, 2006.

[75] A. Huber. *Impact of Fuel Supply Impedance and Fuel Staging on Gas Turbine Combustion Stability*. Ph. D. thesis, Technische Universität München, 2009.

[76] G. Huelsz and F. López-Alquicira. Hot-Wire Anemometry in Acoustic Waves. *Experiments in Fluids*, 30:283–285, 2001.

[77] G. Huelsz and E. Ramos. On the Phase Difference of the Temperature and Pressure Waves in the Thermoacoustic Effect. *International Communications in Heat and Mass Transfer*, 22(1):71–80, 1995.

[78] F. Ihlenburg. *Finite Element Analysis of Acoustic Scattering*, volume 132. Springer, 1998.

[79] D. P. Incropera, Frank P.and DeWitt. *Fundamentals of Heat and Mass Transfer*. John Wiley & Sons, 2002.

[80] P. in't panhuis, S. Rienstra, J. Molenaar, and J. Slot. Weakly Nonlinear Thermoacoustics for Stacks with Slowly Varying Pore Cross-Sections. *Journal of Fluid Mechanics*, 618:41–70, 2009.

[81] P. H. M. W. in't panhuis. *Mathematical Aspects of Thermoacoustics*. Ph. D. thesis, Technische Universiteit Eindhoven, 2009.

[82] P. H. M. W. in't panhuis, S. W. Rienstra, and J. Molenaar. Systematic Derivation of the Weakly Non-Linear Theory of Thermoacoustic Devices Version II. Technical report, Dep. of Mathematics and Computer Science Technische Universiteit Eindhoven, 2009.

[83] R. I. Issa. Solution of the Implicitly Discretised Fluid Flow Equations by Operator-Splitting. *Journal of Computational Physics*, 62(1): 40–65, 1985.

[84] H. Jasak. *Error Analysis and Estimation for the Finite Volume Method with Applications to Fluid Flows*. Ph. D. thesis, University of London, 1996.

[85] C. Jörg. Estimation of Rehomogenization of Acoustic Fields in Ducts. Private Communication, 2011.

[86] R. Kaess, A. Huber, and W. Polifke. A Time-Domain Impedance Boundary Condition for Compressible Turbulent Flow. In *Proceedings of the 14th AIAA/CEAS Aeroacoustics Conference (29th AIAA Aeroacoustics Conference), May 2008, Vancouver, Canada*, 2008.

[87] R. Kaess, W. Polifke, T. Poinsot, N. Noiray, D. Durox, T. Schuller, and S. Candel. CFD-Based Mapping of the Thermo-Acoustic Stability of a Laminar Premix Burner. In *Proceedings of the Summer Program*, 2008.

[88] R. Kaess. *Thermoacoustic Stability Analysis from Open Loop Transfer Functions based on LES*. Ph. D. thesis, Technische Universität München, 2010.

[89] M. Karlsson and M. Åbom. Aeroacoustics of T-Junctions - An Experimental Investigation. *Journal of Sound and Vibration*, 329(10): 1793–1808, 2010.

[90] O. D. Kellogg. *Foundations of Potential Theory*, volume 31. Dover Publications, 2010.

[91] J. F. Kenney and E. S. Keeping. *Mathematics of Statistics*, volume 1. Van Nostrand, 1947.

[92] G. R. Kirchhoff. Über den Einfluss der Wärmeleitung in einem Gase auf die Schallbewegung. *Annalen der Physik*, 134(6):177–193, 1868.

[93] C. T. Knipp. A Possible Standard of Sound. *Physical Reviews*, 12: 491–492, 1918.

[94] J. Kopitz, E. Bröker, and W. Polifke. Characteristics-Based Filter for Identification of Acoustic Waves in Numerical Simulation of Turbulent Compressible Flow. In *Proceeding of the 12th International Congress on Sound and Vibration, Lisbon, Portugal*, 2007.

[95] J. Kopitz. *Kombinierte Anwendung von Strömungssimulation, Netzwerkmodellierung und Regelungstechnik zur Vorhersage thermoakustischer Instabilitäten*. Ph. D. thesis, Technische Universität München, 2007.

[96] H. A. Kramers. Vibrations of a Gas Column. *Physica*, 15 (11–12): 971–984, 1949.

[97] H.-O. Kreiss. Initial Boundary Value Problems for Hyperbolic Systems. *Communications on Pure and Applied Mathematics*, 23(3):277–298, 1970.

[98] R. A. Kruger, D. R. Reinecke, and G. A. Kruger. Thermoacoustic Computed Tomography-Technical Considerations. *Medical Physics*, 26(9):1832–1837, 1999.

[99] P. Kuchment and L. Kunyansky. Mathematics of Thermoacoustic Tomography. *European Journal of Applied Mathematics*, 19(02):191–224, 2008.

[100] P. K. Kundu and I. M. Cohen. *Fluid Mechanics*. Elsevier Academic Press, 3rd edition, 2004.

[101] C. Kunzer. Untersuchung der numerischen Eigenschaften unterschiedlicher Diskretisierungsschemata in OpenFOAM. Master's thesis, Technische Universität München, 2011.

[102] R. Lacombe, P. Moussou, S. Foeller, G. Jasor, W. Polifke, and Y. Aurégan. Experimental and Numerical Investigations on the Whistling Ability of an Orifice in a Flow Duct. In *Proceedings of 17th International Congress on Sound and Vibration, Cairo, Egypt*, 2010.

[103] L. D. Landau and E. M. Lifshitz. *Fluid Mechanics*. Pergamon, 1959.

[104] H. Langhaar. Steady Flow in the Transition Length of a Straight Tube. *Journal of Applied Mechanics*, 9(2):55–58, 1942.

[105] C. Lawn. A Linear 1D Model for the Thermoacoustic Effect in the Presence of Mean Flow. In *Proceedings of the 19th International Congress on Sound and Vibration, Vilnius, Lithuania*, July 2012.

[106] R. Leandro, A. Huber, and W. Polifke. *taX Manual*, 2012.

[107] L. Ljung. *System Identification*. Wiley Online Library, 1999.

[108] G. Lodato, P. Domingo, and L. Vervisch. Three-Dimensional Boundary Conditions for Direct and Large-Eddy Simulation of Compressible Viscous Flows. *Journal of Computational Physics*, 227 (10):5105–5143, 2008.

[109] T. Y. Lung and A. G. Doige. A Time-Averaging Transient Testing Method for Acoustic Properties of Piping Systems and Mufflers with Flow. *Journal of the Acoustical Society of America*, 73(3):867–876, 1983.

[110] R. Lyons. *Understanding Digital Signal Processing*. Prentice Hall PTR, 2004.

[111] Lytron GmbH. Lytron, July 2012.

[112] C. Marx. Über das Tönen erhitzter gläserner Röhren. *Journal für Praktische Chemie*, 22(1):129–135, 1841.

[113] D. Marx and P. Blanc-Benon. Numerical Simulation of Stack-Heat Exchangers Coupling in a Thermoacoustic Refrigerator. *AIAA Journal*, 42(7):1338–1347, 2004.

[114] G. F. McLaughlin and J. J. Keller. Thermoacoustic oscillations in combustion chambers of gas turbines. *AIAA Journal*, 12(33):2280–2287, 1995.

[115] P. Merkli and H. Thomann. Thermoacoustic Effects in a Resonance Tube. *Journal of Applied Mechanics*, 70:161–177, 1975.

[116] S. Mitra and Y. Kuo. *Digital Signal Processing: a Computer-Based Approach*, volume 2. McGraw-Hill New York, 2006.

[117] M. Miyamoto, Y. Ito, K. Takahashi, T. Takami, T. Kobayashi, A. Nishida, and M. Aoyagi. Numerical Study on Sound Vibration of an Air-Reed Instrument with Compressible LES. *arXiv preprint arXiv:1005.3413*, 2010.

[118] M. Miyamoto, Y. Ito, K. Takahashi, T. Takami, T. Kobayashi, A. Nishida, and M. Aoyagi. Applicability of Compressible LES to Reproduction of Sound Vibration of an Air-Reed Instrument. In *Proceedings of 20th International Symposium on Music Acoustics, Sydney and Katoomba, Australia*, 2010.

[119] P. J. J. Montgomery and S. L. Garrett. Low-Cost Thermoacoustic Co-Generator for Biomass-Burning Cook Stoves. *Journal of the Acoustical Society of America*, 128(4):2347–2347, 2010.

[120] M. J. Moran, H. N. Shapiro, D. D. Boettner, and M. Bailey. *Fundamentals of Engineering Thermodynamics*. Wiley, 2010.

[121] I. Müller and W. Müller. *Fundamentals of Thermodynamics and Applications: with Historical Annotations and Many Citations From Avogadro to Zermelo*. Springer, 2009.

[122] M. L. Munjal. *Acoustics of Ducts and Mufflers*. John Wiley & Sons, 1987.

[123] M. L. Munjal and A. G. Doige. Theory of a Two Source-Location Method for Direct Experimental Evaluation of the Four-Pole Parameters of an Aeroacoustic Element. *Journal of Sound and Vibration*, 141(2):323–333, 1990.

[124] National Institute of Standards and Technology (NIST). NIST Chemistry WebBook, November 2008.

[125] K. A. Naugolnykh and L. A. Ostrovsky. *Nonlinear Wave Processes in Acoustics*. Cambridge Univ Pr, 1998.

[126] U. Neunert, C. Hirsch, and T. Sattelmayer. A Novel Approach to Determine the Acoustic Transfer Matrices of Laminar Flat Flames. In *Proceedings of the 4th European Combustion Meeting, Vienna, Austria*, April 2009.

[127] U. Neunert. *Thermoakustische Stabilität einer Reisemobilheizung*. Ph. D. thesis, Technische Universität München, 2010.

[128] J. A. L. a. Nijeholt, M. E. H. Tijani, and S. Spoelstra. Simulation of a Traveling-Wave Thermoacoustic Engine Using Computational Fluid Dynamics. *Journal of the Acoustical Society of America*, 118(4): 2265–2270, 2005.

[129] D. Noda and Y. Ueda. Temperature Difference Required for the Operation of a Vaporized-Water Thermoacoustic Engine. In *Proceedings of the 19th International Congress on Sound and Vibration, Vilnius, Lithuania*, July 2012.

[130] J. R. Olson and G. W. Swift. Similitude in Thermoacoustics. *Journal of the Acoustical Society of America*, 95(3):1405–1412, 1994.

[131] J. R. Olson and G. W. Swift. Acoustic Streaming in Pulse Tube Refrigerators: Tapered Pulse Tubes. *Cryogenics*, 37(12):769–776, 1997.

[132] A. V. Oppenheim, R. W. Schafer, J. R. Buck, et al. *Discrete-Time Signal Processing*, volume 2. Prentice Hall Upper Saddle River, 1989.

[133] C. C. Paige and M. A. Saunders. A Bidiagonalization Algorithm for Sparse Linear Equations and Least-Squares Problems. Technical report, DTIC Document, 1978.

[134] C. O. Paschereit and W. Polifke. Investigation of the Thermo-Acoustic Characteristics of a Lean Premixed Gas Turbine Burner. In *Proceedings of the International Gas Turbine and Aeroengine Congress & Exposition*, 1998.

[135] C. O. Paschereit, B. B. H. Schuermans, W. Polifke, and O. Mattson. Measurement of transfer matrices and source terms of premixed flames. *J. Eng. Gas Turbines and Power*, 124(2):239–247, April 2002. Originally published as ASME 99-GT-133.

[136] G. Penelet, V. Gusev, P. Lotton, and M. Bruneau. Experimental and Theoretical Study of Processes Leading to Steady-State Sound in Annular Thermoacoustic Engines. *Physical Review E*, 72 (1):016625/1–13, 2005.

[137] G. Penelet, S. Job, V. Gusev, P. Lotton, and M. Bruneau. Dependence of Sound Amplification on Temperature Distribution in Annular Thermoacoustic Engines. *Acta Acustica united with Acustica*, 91(3): 567–577, 2005.

[138] G. Petculescu and L. A. Wilen. Thermoacoustics in a Single Pore with an Applied Temperature Gradient. *Journal of the Acoustical Society of America*, 106(2):688–694, 1999.

[139] A. Pinaud. Über eine neue Art der Ton-Erzeugung. *Annalen der Physik*, 118(13):610–618, 1837.

[140] G. Pénelet. Introduction à la Thermoacoustique. In *Ecole d'été de thermoacoustique, Roscoff, France*, pages 1–56, 2001.

[141] T. Poinsot and D. Veynante. *Theoretical and Numerical Combustion*. RT Edwards, Inc., 2005.

[142] T. Poinsot and S. K. Lele. Boundary Conditions for Direct Simulations of Compressible Viscous Flows. *Journal of Computational Physics*, 101(1):104–129, 1992.

[143] W. Polifke. Combustion Instabilities. In *Advances in Aero-Acoustics and Applications, Von Karman Institute for Fluid Dynamics, Brussels, Belgium*, Von Karman Institute, 2004.

[144] W. Polifke. Low-Order Analysis Tools for Aero- and Thermo-Acoustic Instabilities. In *Advances in Aero-Acoustics and Thermo-Acoustics, Von Karman Institute for Fluid Dynamics, Brussels, Belgium*, 2010.

[145] W. Polifke. Thermo-Acoustic Instability Potentiality of a Premix Burners. In *European Combustion Meeting, ECM2011, Munich, Germany*, 2011.

[146] W. Polifke and A. Gentemann. Order and Realizability of Impulse Response Filters for Accurate Identification of Acoustic Multi-Ports from Transient CFD. *International Journal of Acoustics and Vibration*, 9(3):139–148, 2004.

[147] W. Polifke and C. O. Paschereit. Determination of Thermo-Acoustic Transfer Matrices by Experiment and Computational Fluid Dynamics. *ERCOFTAC Bulletin*, 38, September 1998.

[148] W. Polifke and C. Wall. Non-Reflecting Boundary Conditions for Acoustic Transfer Matrix Estimation with LES. *Combustion Turburbulence Research, Annual Research Briefs*, pages 345–356, 2002.

[149] W. Polifke, C. O. Paschereit, and K. Döbbeling. Constructive and destructive interference of acoustic and entropy waves in a premixed combustor with a choked exit. *Int. J. of Acoustics and Vibration*, 6(3):1–38, 2001.

[150] W. Polifke, A. Poncet, C. O. Paschereit, and K. Döbbeling. Reconstruction of Acoustic Transfer Matrices by Instationary Computational Fluid Dynamics. *Journal of Sound and Vibration*, 245(3):483–510, 2001.

[151] W. Polifke, A. Fischer, and T. Sattelmayer. Instability of a Premix Burner with Nonmonotonic Pressure Drop Characteristic. *Journal of Engineering for Gas Turbines and Power*, 125:1–8, 2003.

[152] W. Polifke, C. Wall, and P. Moin. Partially Reflecting and Non-Reflecting Boundary Conditions for Simulation of Compressible Viscous Flow. *Journal of Computational Physics*, 213:437–449, 2006.

[153] T. L. Pollès, M.-X. François, P. Duthil, and J.-P. Thermeau. Le Froid venu du Son. *La Gazette du Vide*, 18:14–16, 2010.

[154] W. H. Press, S. A. Teukolsky, W. T. Vetterling, and B. P. Flannery. *Numerical Recipes: The Art of Scientific Computing*. Cambridge University Press, 3rd edition, 2007.

[155] J. G. Proakis and D. G. Manolakis. *Digital Signal Processing*, volume 99. Macmillan Publishing Company, New York, 1996.

[156] Promat GmbH. Promaform, June 2012.

[157] L. Rayleigh. *The Theory of Sound*, volume I & II. Macmillan and Co., 1878.

[158] R. S. Reid. *Open Cycle Thermoacoustics*. Ph. D. thesis, Los Alamos National Laboratory, 2000.

[159] R. S. Reid, W. C. Ward, and G. W. Swift. Cyclic Thermodynamics with Open Flow. *Physical Review Letters*, 80:4617–4620, 1998.

[160] S. W. Rienstra and A. Hirschberg. An Introduction to Acoustics. *Eindhoven University of Technology*, 2001.

[161] P. L. Rijke. Notiz über eine neue Art, die in einer an beiden Enden offenen Röhre enthaltene Luft in Schwingungen zu versetzen. *Annalen der Physik*, 183(6):339–343, 1859.

[162] P. Riley. Stove for Cooking, Refrigeration and Electricity. http://www.score.uk.com/, 2009.

[163] T. D. Rossing, editor. *Springer Hand Books of Acoustics*. Springer Science+Business Media, LLC New York, 2007.

[164] N. Rott. Damped and Thermally Driven Acoustic Oscillations in Wide and Narrow Tubes. *Zeitschrift für angewandte Mathematik und Physik*, 20:230–243, 1969.

[165] N. Rott. Thermally Driven Acoustic Oscillations. Part II: Stability Limit for Helium. *Zeitschrift für angewandte Mathematik und Physik*, 24:54–72, 1973.

[166] N. Rott. The Heating Effect Connected with Non-linear Oscillations in a Resonance Tube. *Zeitschrift für angewandte Mathematik und Physik*, 25:619–634, 1974.

[167] N. Rott. Thermally Driven Acoustic Oscillations, Part III: Second-Order Heat Flux. *Zeitschrift für angewandte Mathematik und Physik*, 26:43–49, 1975.

[168] N. Rott. The Description of Simple Waves by Particle Displacement. *Zeitschrift für angewandte Mathematik und Physik*, 29:178–189, 1978.

[169] N. Rott. The Mutual Penetration of Simple Waves in Gases. *Zeitschrift für angewandte Mathematik und Physik*, 29:462–472, 1978.

[170] N. Rott. Thermoacoustics. In *Advances in Applied Mechanics*, volume 20, pages 135–175. Elsevier, 1980.

[171] N. Rott and G. Zouzoulas. Thermally Driven Acoustic Oscillations, Part IV: Tubes with Variable Cross-section. *Zeitschrift für angewandte Mathematik und Physik*, 27:197–224, 1976.

[172] D. H. Rudy and J. C. Strikwerda. A Nonreflecting Outflow Boundary Condition for Subsonic Navier-Stokes Calculations. *Journal of Computational Physics*, 36(1):55–70, 1980.

[173] S. Sakamoto and Y. Watanabe. The Experimental Studies of Thermoacoustic Cooler. *Ultrasonics*, 42(1–9):53–56, 2004.

[174] A. O. Santillán and R. R. Boullosa. Acoustic Power and Heat Fluxes in the Thermoacoustic Effect due to a Travelling Plane Wave. *International Journal of Heat and Mass Transfer*, 40(8):1835–1838, 1997.

[175] H. Schlichting, K. Gersten, E. Krause, H. Oertel, and K. Mayes. *Boundary-Layer Theory*. Springer Verlag, 8th edition, 2000.

[176] T. Schönfeld and T. Poinsot. Influence of Boundary Conditions in LES of Premixed Combustion Instabilities. *Annual Research Briefs*, pages 73–84, 1999.

[177] B. Schuermans. *Modelling and Control of Thermoacoustic Instabilities*. Ph. D. thesis, Ecole Polytechnique Federale De Lausanne, 2003.

[178] B. Schuermans, F. Bellucci, V. Guethe, F. Meili, P. Flohr, and C. O. Paschereit. A detailed analysis of thermoacoustic interaction mechanisms in a turbulent premixed flame. In *Int'l Gas Turbine and Aeroengine Congress & Exposition*, Atlanta, GA, U.S.A., June 14-17 2004.

[179] B. B. H. Schuermans, W. Polifke, and C. O. Paschereit. Modeling Transfer Matrices of Premixed Flames and Comparison with Experimental Results. In *Int'l Gas Turbine and Aeroengine Congress & Exposition*, Indianapolis, Indiana, USA, 1999.

[180] B. B. H. Schuermans, W. Polifke, C. O. Paschereit, and J. H. van der Linden. Prediction of acoustic pressure spectra in combustion systems using swirl stabilized gas turbine burners. In *Proceedings of the IGTI*, Munich, Germany, May 13-16 2000. ASME.

[181] L. Selle, F. Nicoud, and T. Poinsot. Actual Impedance of Nonreflecting Boundary Conditions: Implications for Computation of Resonators. *AIAA Journal*, 42(5):958–964, 2004.

[182] C. Sondhauss. Über die Schallschwingungen der Luft in erhitzten Glasröhren und in gedeckten Pfeifen von ungleicher Weite. *Annalen der Physik*, 155(1):1–34, 1850.

[183] S. R. Stow and A. P. Dowling. Thermoacoustic oscillations in an annular combustor. In *Proceedings of ASME Turbo Expo 2001 Power for Land, Sea and Air*, New Orleans, Louisiana, June 4-7 2001. ASME.

[184] G. W. Swift. Analysis and Performance of a Large Thermoacoustic Engine. *Journal of the Acoustical Society of America*, 92(3):1551–1563, 1992.

[185] G. W. Swift. Thermoacoustic Engines and Refigerators. *Encyclopedia of Applied Physics, Testing Equipment-Mechanical to Topological Phase Effects*, 21:22–28, 1995.

[186] G. W. Swift. Streaming in Thermoacoustic Engines and Refrigerators. In *AIP Conference Proceedings, Adelaide, Australia*, December 2000.

[187] G. W. Swift. *Thermoacoustics- A Unifying Perspective for Some Engines and Refrigerators*. Acoustical Society of America, 2002.

[188] G. W. Swift and S. Backhaus. A Resonant, Self-Pumped, Circulating Thermoacoustic Heat Exchanger. *Journal of the Acoustic Society of America*, 116 (5):2923–2938, 2004.

[189] G. W. Swift and W. C. Ward. Simple Harmonic Analysis of Regenerators. *Journal of Thermophysics and Heat Transfer*, 10(4):652–662, 1996.

[190] K. W. Taconis. Vapor-Liquid Equilibrium of Solutions of 3He in 4He. *Physica*, 15:738, 1949.

[191] K. Takahashi, M. Miyamoto, Y. Ito, T. Takami, T. Kobayashi, A. Nishida, and M. Aoyagi. Numerical Analysis on 2D and 3D Edge Tones in Terms of Aerodynamic Sound Theory. In *Proceedings of 20th International Congress on Acoustics, Sydney, Australia*, 2010.

[192] L. R. Tay-Wo-Chong Hilares. *Numerical Simulation of the Dynamics of Turbulent Swirling Flames*. Ph. D. thesis, Technische Universität München, 2012.

[193] J. R. Taylor. *An Introduction to Error Analysis: the Study of Uncertainties in Physical Measurements*. Universal Science Books, 1997.

[194] P. Testud, Y. Aurégan, P. Moussou, and A. Hirschberg. The Whistling Potentiality of an Orifice in a Confined Flow Using an Energetic Criterion. *Journal of Sound and Vibration*, 325(4):769–780, 2009.

[195] K. W. Thompson. Time Dependent Boundary Conditions for Hyperbolic Systems. *Journal of Computational Physics*, 68(1):1–24, 1987.

[196] K. W. Thompson. Time Dependent Boundary Conditions for Hyperbolic Systems, II. *Journal of Computational Physics*, 89(2):439–461, 1990.

[197] H. Tijdeman. On the Propagation of Sound Waves in Cylindrical Tubes. *Journal of Sound and Vibration*, 39(1):1–33, 1975.

[198] C. W. S. To and A. G. Doige. A Transient Testing Technique for the Determination of Matrix Parameters of Acoustic Systems, I: Theory and Principles. *Journal of Sound and Vibration*, 62(2):207–222, 1979.

[199] C. To and A. Doige. A Transient Testing Technique for the Determination of Matrix Parameters of Acoustic Systems, II: Experimental Procedures and Results. *Journal of Sound and Vibration*, 62(2):223–233, 1979.

[200] A. Ulhaq, S. Hemchandra, L. Tay-Wo-Chong, and W. Polifke. Multiple-Input, Single-Output Approach for Identification of Laminar Premixed Flame Dynamics from Direct Numerical Simulation. In *Proceedings of the 19th International Congress on Sound and Vibration, Vilnius, Lithuania*, July 2012.

[201] V.-G. V. und Chemieingenieurwesen (GVC), editor. *VDI-Wärmeatlas*. VDI-Verlag, Düsseldorf, 8th edition, 2007.

[202] B. Ward, J. Clark, and G. W. Swift. DeltaEC Version 6.2 Users Guide. Technical report, Los Alamos National Laboratory, 2008.

[203] W. Ward and G. Swift. Design Environment for Low–Amplitude Thermoacoustic Engines. *Journal of the Acoustical Society of America*, 95(6):3671–3674, 1994.

[204] M. Watanabe, A. Prosperetti, and H. Yuan. A Simplified Model for Linear and Nonlinear Processes in Thermoacoustic Prime Movers. Part I. Model and Linear Theory. *Journal of the Acoustical Society of America*, 102(6):3484–3496, 1997.

[205] N. T. Weiland. *Feasibility Analysis of an Open Cycle Thermoacoustic Engine with Internal Pulse Combustion*. Ph. D. thesis, Georgia Institute of Technology, 2004.

[206] J. Wheatley, T. Hofler, G. W. Swift, and A. Migliori. An Intrinsically Irreversible Thermoacoustic Heat Engine. *Journal of the Acoustical Society of America*, 74(1):153–170, 1983.

[207] J. Wheatley, G. W. Swift, and A. Migliori. The Natural Heat Engine. *Los Alamos Science*, 14:2–47, 1986.

[208] N. Wiener. Extrapolation, Interpolation, and Smoothing of Stationary Time Series: with Engineering Applications. *Journal of the American Statistical Association*, 47(258), 1949.

[209] Wolfram Research. Mathematica, June 2012.

[210] A. S. Worlikar and O. M. Knio. Numerical Simulation of a Thermoacoustic Refrigerator. *Journal of Computational Physics*, 127(2): 424–451, 1995.

[211] A. S. Worlikar, O. M. Knio, and R. Klein. Numerical Simulation of a Thermoacoustic Refrigerator: II. Stratified Flow Around the Stack. *Journal of Computational Physics*, 144(2):299–324, 1998.

[212] T. Yazaki, A. Iwata, T. Maekawa, and A. Tominaga. Traveling Wave Thermoacoustic Engine in a Looped Tube. *Physical Review Letters*, 81:3128–3131, October 1998.

[213] C. S. Yoo and H. G. Im. Characteristic Boundary Conditions for Simulations of Compressible Reacting Flows with Multi-Dimensional, Viscous and Reaction Effects. *Combustion Theory and Modelling*, 11(2):259–286, 2007.

[214] C. S. Yoo, Y. Wang, A. Trouvé, and H. G. Im. Characteristic Boundary Conditions for Direct Simulations of Turbulent Counterflow Flames. *Combustion Theory and Modelling*, 9(4):617–646, 2005.

[215] G. Y. Yu, E. C. Luo, W. Dai, and J. Y. Hu. Study of Nonlinear Processes of a Large Experimental Thermoacoustic Stirling Heat Engine by Using Computational Fluid Dynamics. *Journal of Applied Physics*, 102(7):074901, 2007.

[216] H. Yuan, S. Karpov, and A. Prosperetti. A Simplified Model for Linear and Nonlinear Processes in Thermoacoustic Prime Movers. Part II. Nonlinear Oscillations. *Journal of the Acoustical Society of America*, 102(6):3497–3506, 1997.

[217] S. Zhou and Y. Matsubara. Experimental Research of Thermoacoustic Prime Mover. *Cryogenics*, 38(8):813–822, 1998.

[218] J. Zierep. *Theoretical Gasdynamics*. Springer-Verlag, 1978.

[219] F. Zink, J. Vipperman, and L. Schaefer. CFD Simulation of a Thermoacoustic Engine with Coiled Resonator. *International Communications in Heat and Mass Transfer*, 37(3):226–229, 2010.

[220] F. Zink, J. Vipperman, and L. Schaefer. CFD Simulation of Thermoacoustic Cooling. *International Journal of Heat and Mass Transfer*, 53(19–20):3940–3946, 2010.

[221] D. Zwillinger. *Handbook of Differential Equations*. Academic Press, 3rd edition, 1998.

A Details of the Derivation of the Quasi 1D-Model

This chapter contains details of the derivation shown in Chapter 4. The special non-dimenzionalization technique applied yields a dimensionless system of equations in different orders of ε, i.e. the pore aspect ratio. Due to this ratio such terms of higher order are later neglected and, for better readability, presented in the main text with abbreviations $A_i\left(\mathcal{O}\left(\varepsilon^2\right)\right)$. In the following chapter, these terms are presented. The derivation of the quasi one-dimensional explicit TAPEs (Eqs. (4.63)) causes an increase in number of terms of the implicit solution. For the purpose of giving an overview of the derivation steps, these terms are accumulated to replacement parameters. In the second part of this chapter, these parameters are given in detail.

A.1 Higher Order Terms in the Dimensionless NSEs

The formulation of the LNSEs (Eqs. (4.9)) contain various terms $A_i\left(\mathcal{O}\left(\varepsilon^2\right)\right)$ which are later neglected.

The second and higher order contribution in ε to the axial momentum Equation (4.9b) reads

$$A_1\left(\mathcal{O}\left(\varepsilon^2\right)\right) = \varepsilon^2\left[\frac{\kappa}{\mathrm{Wo}^2}\left(2\frac{\partial^2 u}{\partial x^2}+\frac{\partial^2 v}{\partial x \partial y}\right)+\frac{\kappa}{\mathrm{Wo}_\zeta^2}\left(\frac{\partial^2 u}{\partial x^2}+\frac{\partial^2 v}{\partial x \partial y}\right)\right] + \varepsilon^3\frac{\kappa}{\mathrm{Wo}^2}\frac{\partial^2 v}{\partial x^2}. \tag{A.1}$$

The spatial derivatives and the scaling with Wo indicate the origin of the terms. All terms in $A_1\left(\mathcal{O}\left(\varepsilon^2\right)\right)$ result from viscous stress tensor τ_{ij}.

The transversal momentum Equation (4.9c) is multiplied by ε to obtain zeroth order information. Thus,

$$A_2\left(\mathcal{O}\left(\varepsilon^2\right)\right) = \varepsilon^2\left[\varrho\frac{Dv}{Dt} + \frac{\kappa}{\mathrm{Wo}^2}\left(2\frac{\partial^2 v}{\partial y^2} + \frac{\partial^2 u}{\partial x \partial y}\right) + \frac{\kappa}{\mathrm{Wo}_\zeta^2}\left(\frac{\partial^2 v}{\partial y^2} + \frac{\partial^2 u}{\partial x \partial y}\right)\right] + \varepsilon^3\left[\frac{3\kappa}{\mathrm{Wo}^2}\frac{\partial^2 v}{\partial x \partial y} + \frac{\kappa}{\mathrm{Wo}_\zeta^2}\left(\frac{\partial^2 u}{\partial x^2} + \frac{\partial^2 v}{\partial x \partial y}\right)\right] \tag{A.2}$$

additionally contains the substantial derivative of the transversal velocity.

Both the fluid energy conservation (Eq. (4.9d)) and the solid energy conservation (Eq. (4.9f)) further include the axial thermal conductivity term in

$$\begin{aligned} A_3\left(\mathcal{O}\left(\varepsilon^2\right)\right) &= \varepsilon^2\left[\frac{2\kappa}{\mathrm{Wo}^2}\left(\left[\frac{\partial v}{\partial y} + \frac{\partial u}{\partial x}\right]^2 + \frac{\partial u}{\partial y}\frac{\partial v}{\partial x}\right)\right. \\ &\quad \left. + \frac{\kappa}{\mathrm{Wo}_\zeta^2}\left(\frac{\partial v}{\partial y} + \frac{\partial u}{\partial x}\right)^2 + \frac{\kappa}{2\mathrm{La}^2}\frac{\partial^2 T}{\partial x^2}\right] + \varepsilon^4\frac{\kappa}{\mathrm{Wo}^2}\frac{\partial v}{\partial y}^2, \\ A_4\left(\mathcal{O}\left(\varepsilon^2\right)\right) &= \varepsilon^2\frac{\kappa}{2\mathrm{La}_\mathrm{S}^2}\frac{\partial^2 T}{\partial x^2}, \end{aligned} \tag{A.3}$$

which is of higher order in ε. This is in accordance to the approach for the thermodynamic cycle stated in Section 1.2. It states that changes of the thermodynamic state in the vicinity of a thermo-viscous acoustic boundary layer are governed by transversal heat conduction, while the axial contribution is negligible.

A.2 Abbreviations for the Analytical Approaches

The abbreviations introduced in Section 4.5.3 follow a nomenclature based on the original equation and contributing terms.

A.2.1 Axial Momentum Equation

Comparing Equations (4.36c) and (4.39) under consideration of Equation (4.37) directly leads to

$$\mathbb{X}_{p_1} = \frac{(1-\gamma)\,T}{i\kappa - \mathrm{Ma}\frac{\partial T}{\partial x}}, \tag{A.4}$$

$$\mathbb{X}_{\Lambda_1} = \frac{(1-\gamma)\,T\Lambda_1}{i\kappa - \mathrm{Ma}\frac{\partial T}{\partial x}}. \tag{A.5}$$

A.2.2 Energy Equation

Substituting the solution of Equation (4.39) into Equation (4.36e) leads to the abbreviations

$$\mathbb{E}_{p_1} = \frac{T\left(\left(-1+\gamma\right)\kappa - ic_p\mathrm{Ma}\gamma\frac{\partial T}{\partial x}\right)}{c_p\left(\kappa - i\mathrm{Ma}\frac{\partial T}{\partial x}\right)}, \tag{A.6}$$

$$\mathbb{E}_{p_1,F_\nu} = 0, \tag{A.7}$$

$$\mathbb{E}_{p_1'} = -\frac{\left(\mathrm{Ma}\left(-1+\gamma\right)T^2\right.}{c_p\left(i\kappa + \mathrm{Ma}\frac{\partial T}{\partial x}\right)}, \tag{A.8}$$

$$\mathbb{E}_{p_1',F_\nu} = -\frac{\mathbb{X}_{p_1}\frac{\partial T}{\partial x}}{i\kappa + \mathrm{Ma}\frac{\partial T}{\partial x}}, \tag{A.9}$$

$$\mathbb{E}_{\Lambda_2} = \frac{i\left(-1+\gamma\right)T\Lambda_2}{c_p\left(\kappa - i\mathrm{Ma}\frac{\partial T}{\partial x}\right)}, \tag{A.10}$$

$$\mathbb{E}_{\Lambda_1,F_\nu} = \frac{-\mathbb{X}_{\Lambda_1}\frac{\partial T}{\partial x}}{i\kappa + \mathrm{Ma}\frac{\partial T}{\partial x}}. \tag{A.11}$$

Here, the terms $\mathbb{E}_{\Lambda_2}$ and $\mathbb{E}_{\Lambda_1,F_\nu}$ vanish for **MI**. After combining the energy Equations (4.36e) and (4.36f) the new variables occurring are

$$\mathbb{T}_{p_1} = \left(\mathfrak{Pr}\mathbb{E}_{p_1} + \mathbb{E}_{p_1,F_\nu}\left(-1 + \frac{f_{K,\nu}}{f_K}\right)\right)\mathbb{E}_{\epsilon_S}, \tag{A.12}$$

$$\mathbb{T}_{p_1'} = \left(\mathfrak{Pr}\mathbb{E}_{p_1'} + \mathbb{E}_{p_1',F_\nu}\left(-1 + \frac{f_{K,\nu}}{f_K}\right)\right)\mathbb{E}_{\epsilon_S}, \tag{A.13}$$

$$\mathbb{T}_{\Lambda_1} = -\left(\mathbb{E}_{\Lambda_1,F_\nu}\mathbb{E}_{\epsilon_S}\right) + \frac{\left(\mathfrak{Pr}\mathbb{E}_{\Lambda_2}f_K + \mathbb{E}_{\Lambda_1,F_\nu}f_{K,\nu}\right)\mathbb{E}_{\epsilon_S}}{f_K}, \tag{A.14}$$

$$\mathbb{T}_{p_1,F_K} = \frac{\mathbb{E}_{p_1,F_\nu}\left(f_K - f_{K,\nu}\right)\mathbb{E}_{\epsilon_S} + \mathbb{E}_{p_1} f_K \left(1 - \mathfrak{Pr}\mathbb{E}_{\epsilon_S}\right)}{f_K}, \tag{A.15}$$

$$\mathbb{T}_{p_1',F_K} = \frac{\mathbb{E}_{p_1',F_\nu}\left(f_K - f_{K,\nu}\right)\mathbb{E}_{\epsilon_S} + \mathbb{E}_{p_1'} f_K \left(1 - \mathfrak{Pr}\mathbb{E}_{\epsilon_S}\right)}{f_K}, \tag{A.16}$$

$$\mathbb{T}_{\Lambda_2 F_K} = \frac{\mathbb{E}_{\Lambda_1,F_\nu}\left(f_K - f_{K,\nu}\right)\mathbb{E}_{\epsilon_S}}{f_K} + \mathbb{E}_{\Lambda_2}\left(1 - \mathfrak{Pr}\mathbb{E}_{\epsilon_S}\right). \tag{A.17}$$

It needs to be emphasized that all of these terms include contributions of $\mathbb{E}_{\epsilon_S}$ indicating of the fluid-solid interaction. This index is discharged. Again, Equations (A.14) and (A.17) are zero for the less accurate model **MI**.

A.2.3 Gas Law

The first substitution process of the resulting energy Equation (4.58) and momentum Equation (4.39) into the ideal gas Equation (4.36a) yields two new parameters

$$\mathbb{G}_{p_1} = \frac{\gamma}{\left(-1+\gamma\right)T}, \tag{A.18}$$

$$\mathbb{G}_{T_1} = \frac{-1}{\left(-1+\gamma\right)T^2}, \tag{A.19}$$

which are combined to

$$\overline{\mathbb{G}}_{p_1} = \mathbb{G}_{p_1} + \left(\mathbb{E}_{p_1,F_\nu} + \mathbb{T}_{p_1} + \mathbb{T}_{p_1,F_K} - \mathbb{T}_{p_1,F_K} f_K - \mathbb{E}_{p_1,F_\nu} f_{K,\nu}\right)\mathbb{G}_{T_1}, \tag{A.20}$$

$$\overline{\mathbb{G}}_{p_1'} = \left(\mathbb{E}_{p_1',F_\nu} + \mathbb{T}_{p_1'} + \mathbb{T}_{p_1',F_K} - \mathbb{T}_{p_1',F_K} f_K - \mathbb{E}_{p_1',F_\nu} f_{K,\nu}\right)\mathbb{G}_{T_1}, \tag{A.21}$$

$$\overline{\mathbb{G}}_{\Lambda_1,\Lambda_2} = \left(\mathbb{T}_{\mathbf{\Lambda}_1} + \mathbb{T}_{\mathbf{\Lambda}_2 F_K} + \mathbb{E}_{\mathbf{\Lambda}_1,F_\nu} - \mathbb{T}_{\mathbf{\Lambda}_2 F_K} f_K - \mathbb{E}_{\mathbf{\Lambda}_1,F_\nu} f_{K,\nu}\right)\mathbb{G}_{T_1} \tag{A.22}$$

in the cross-sectional averaging process. Again the last term is zero for **MI**.

A.2.4 Conservation of Mass

Finally, all derived formulas are substituted in the conservation of mass (4.36b), and the intermediate values

$$\overline{\overline{\mathbb{k}}}_{\langle u_1 \rangle} = \frac{-i\frac{\partial T}{\partial x}}{(-1+\gamma)\,T^2\left(\kappa + i\mathrm{Ma}\frac{\partial T}{\partial x}\right)}, \tag{A.23}$$

$$\overline{\overline{\mathbb{k}}}_{\langle u_1' \rangle} = \frac{i}{\left((-1+\gamma)\,T\left(\kappa + i\mathrm{Ma}\frac{\partial T}{\partial x}\right)\right)}, \tag{A.24}$$

$$\overline{\overline{\mathbb{k}}}_{\langle \varrho_1' \rangle} = \frac{-i\left(-\left(\mathrm{Ma}T^3\right) + \mathrm{Ma}\gamma T^3\right)}{(-1+\gamma)\,T^2\left(\kappa + i\mathrm{Ma}\frac{\partial T}{\partial x}\right)}, \tag{A.25}$$

result in the coefficients

$$\overline{\mathbb{K}}_{u_1'} = -\frac{(f_\nu - 1)\,\overline{\overline{\mathbb{k}}}_{\langle u_1 \rangle}\mathbb{X}_{p_1}}{(f_\nu - 1)\,\overline{\overline{\mathbb{k}}}_{\langle u_1' \rangle}\mathbb{X}_{p_1} - \overline{\mathbb{G}}_{p_1'}\overline{\overline{\mathbb{k}}}_{\langle \varrho_1' \rangle}}, \tag{A.26}$$

$$\begin{aligned}\overline{\mathbb{K}}_{\mathbf{\Lambda}_1,\mathbf{\Lambda}_2} = &-\frac{\overline{\mathbb{G}}_{p_1'}\overline{\overline{\mathbb{k}}}_{\langle \varrho_1' \rangle}\mathbb{X}_{\mathbf{\Lambda}_1} f_\nu'}{(f_\nu - 1)\,\overline{\overline{\mathbb{k}}}_{\langle u_1' \rangle}\mathbb{X}_{p_1} - \overline{\mathbb{G}}_{p_1'}\overline{\overline{\mathbb{k}}}_{\langle \varrho_1' \rangle}} \\ &- \frac{(f_\nu - 1)\left(\mathbb{X}_{p_1}\left(\overline{\mathbb{G}}_{\mathbf{\Lambda}_1,\mathbf{\Lambda}_2} - \overline{\overline{\mathbb{k}}}_{\langle \varrho_1' \rangle}\frac{\partial \overline{\mathbb{G}}_{\mathbf{\Lambda}_1,\mathbf{\Lambda}_2}}{\partial x}\right) + \overline{\mathbb{G}}_{p_1'}\overline{\overline{\mathbb{k}}}_{\langle \varrho_1' \rangle}\frac{\partial \mathbb{X}_{\mathbf{\Lambda}_1}}{\partial x}\right)}{(f_\nu - 1)\,\overline{\overline{\mathbb{k}}}_{\langle u_1' \rangle}\mathbb{X}_{p_1} - \overline{\mathbb{G}}_{p_1'}\overline{\overline{\mathbb{k}}}_{\langle \varrho_1' \rangle}},\end{aligned} \tag{A.27}$$

$$\begin{aligned}\overline{\mathbb{K}}_{p_1'} = &\frac{\overline{\mathbb{G}}_{p_1'}\left[(f_\nu - 1)\left(\mathbb{X}_{p_1} + \overline{\overline{\mathbb{k}}}_{\langle \varrho_1' \rangle}\frac{\partial \mathbb{X}_{p_1}}{\partial x}\right) + \mathbb{X}_{p_1}\overline{\overline{\mathbb{k}}}_{\langle \varrho_1' \rangle}\frac{\partial f_\nu}{\partial x}x\right]}{(f_\nu - 1)\,\overline{\overline{\mathbb{k}}}_{\langle u_1' \rangle}\mathbb{X}_{p_1} - \overline{\mathbb{G}}_{p_1'}\overline{\overline{\mathbb{k}}}_{\langle \varrho_1' \rangle}} \\ &- \frac{(f_\nu - 1)\,\overline{\overline{\mathbb{k}}}_{\langle \varrho_1' \rangle}\mathbb{X}_{p_1}\left(\overline{\mathbb{G}}_{p_1} + \frac{\partial \overline{\mathbb{G}}_{p_1'}}{\partial x}\right)}{(f_\nu - 1)\,\overline{\overline{\mathbb{k}}}_{\langle u_1' \rangle}\mathbb{X}_{p_1} - \overline{\mathbb{G}}_{p_1'}\overline{\overline{\mathbb{k}}}_{\langle \varrho_1' \rangle}},\end{aligned} \tag{A.28}$$

$$\overline{\mathbb{K}}_{p_1} = \frac{(f_\nu - 1)\,\mathbb{X}_{p_1}\left(\overline{\mathbb{G}}_{p_1} - \overline{\overline{\mathbb{k}}}_{\langle \varrho_1' \rangle}\frac{\partial \overline{\mathbb{G}}_{p_1}}{\partial x}\right)}{(f_\nu - 1)\,\overline{\overline{\mathbb{k}}}_{\langle u_1' \rangle}\mathbb{X}_{p_1} - \overline{\mathbb{G}}_{p_1'}\overline{\overline{\mathbb{k}}}_{\langle \varrho_1' \rangle}}. \tag{A.29}$$

The second transport ODE of the acoustic variables (see Eqs. (4.63)) is denoted in terms of these coefficients. The term $\overline{\mathbb{K}}_{\mathbf{\Lambda}_1,\mathbf{\Lambda}_2}$ contains the terms differing in the different model derivations.

B Experimental Modeling Approaches

The experimental investigation of TA regenerators in Chapter 6 necessitates the introduction of two modeling approaches. The hot downstream data acquisition region is governed by non-negligible changes in mean temperature T. As the test rig only allows for local temperature probing, the axial distribution is modeled. The scattering matrices obtained include the acoustic transmission behavior of the adjacent heaters. This transmission behavior is reconstructed from separate measurements. As the final solution is — to some extent — sensitive to this data, the reconstructed scattering matrices are modeled analytically before they are applied to obtain a set of data comparable to numerical results.

B.1 Approximated Temperature Distribution Inside the Downstream Duct

The temperature field inside the hot regenerator and its prolongation is multi-dimensional. A consideration of dimensionless numbers is necessary to allow for a one-dimensional consideration of the temperature profile. The temperature field has been investigated in detail in the semesterarbeit of Loth. All data values are taken from this thesis.

The hot resonator part of the duct is supplied with heat from an external heater. Thus, the cross-sectional average of the mean temperature can be approximated by a linear distribution in the axial direction

$$T_{\mathrm{lin}}(x) = a_1 + a_2 x. \tag{B.1}$$

This does not account for the extension part containing the standard microphone adapter "M". Here, a closer investigation has to be carried out. The combined heat transfer coefficient through the insulated duct wall related to its hydraulic diameter reaches values of

$$k \approx 0.125\,\mathrm{W\,m^{-2}\,K^{-1}}. \tag{B.2}$$

Considering the corresponding Biot number yields a negligible contribution of the transversal heat conduction. Hence the governing equation describing the steady state axial temperature distribution inside the hot duct is approximated by

$$a\frac{\partial^2 T}{\partial x^2} + u\frac{\partial T}{\partial x} + \frac{2k}{Ka}(T - T_\infty) = 0. \tag{B.3}$$

The general solution of this problem reads

$$T_{\text{exp}}(x) = T_\infty + C_1 \exp(b_1 x) + C_2 \exp(-b_2 x), \tag{B.4}$$

where b_i are problem-dependent parameters and C_i are integration constants that have to be determined by local temperature data.

The contact plane of both regions located at x_L yields the coupling condition

$$T_{\text{exp}}(x_L) = T_{\text{lin}}(x_L). \tag{B.5}$$

The temperature distribution is described by three parameters that have to be determined by local temperature data.

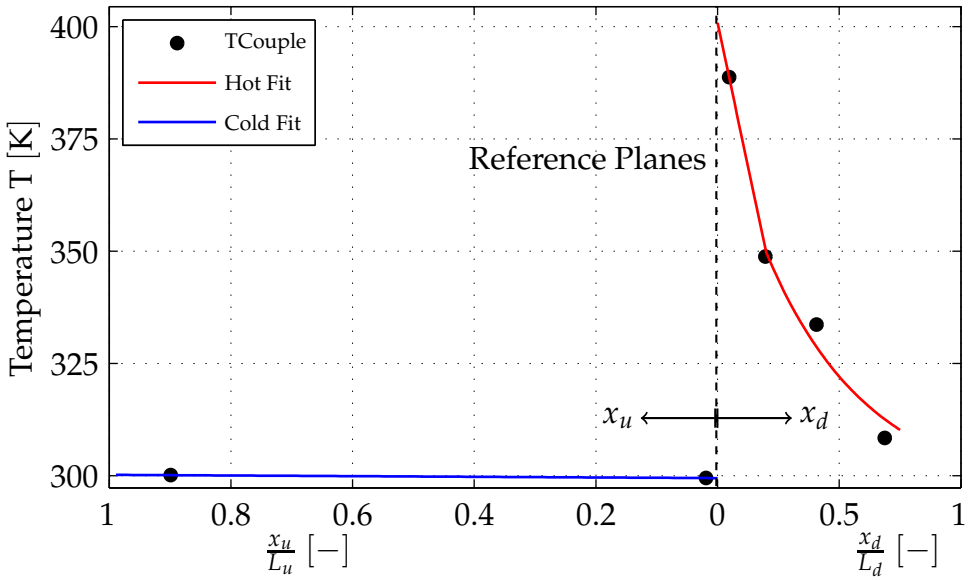

Figure B.1: Typical temperature fit for MMM measurements. The blue curve depicts the temperature distribution inside the ambient upstream duct. The red graph follows the temperature profile derived, which is linear for $x_d \lesssim 0.2$. The black dots denote the time averaged thermocouple data.

A typical temperature distribution obtained by fitting to additional data points is displayed in Figure B.1 The black dots denote the measurement data the curves are fitted to. The overlay of fit and measurement data indicate a good agreement of approximated temperature distribution and measured thermocouple data.

B.2 Reconstructed Network Representations of the heaters

As discussed in Section 6.1.3, the scattering matrix of a TA regenerator cannot be obtained by direct measurements. The heaters maintain the temperature gradient and their acoustic transfer behavior contributes to the measurement of the TA core. Their impact needs to be determined by separate investigations. These reveal a vanishing influence of mean flow in the scattering matrix values of the heaters, which is thus neglected. For geometrical comparison of the data, the reader is referred to Figures 6.7 in Section 6.3.1.2. The maximum variation of the optimized characteristic geometric scales with respect to their real measure is below 5%.

Ambient heater

The network model representing the ambient heater consists of three duct elements separated by two area changes depicted in Figure B.2. Two additional area changes that represent the solid area of the plates. The temperature change over the heater is not taken into account, assuming

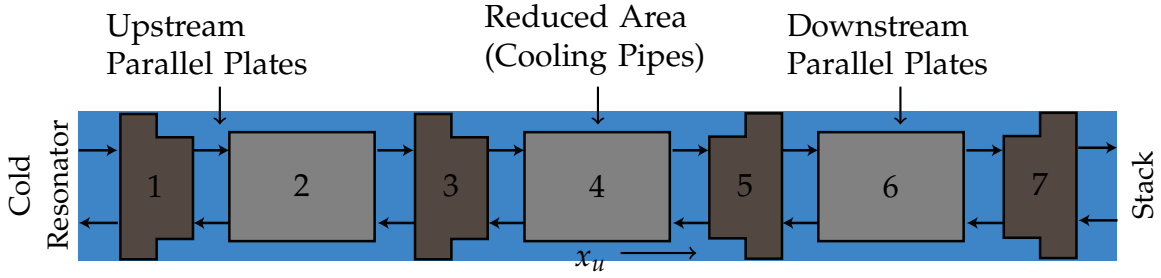

Figure B.2: Network representation of the ambient heater. The inner area changes account for the cooling pipes. The numbering relates the two-ports to the data listed in Table B.1.

good thermal contact. Accounting for the temperature induced reflection yields no improvement in reconstructing the data.

A sketch of the combination of these acoustic two-ports is depicted in Figure B.2. All relevant data for this and the following models are listed in Table B.1.

Item	Type	Data	Description
1	**AC**	$\alpha \approx 1.03$	From resonator to heater
2	**D**	$L = 7\,\mathrm{mm}$ $y = 1\,\mathrm{mm}$	heater between finns
3	**AC**	$\alpha \approx 1.1$	Contraction due to cooling pipes
4	**D**	$L = 7\,\mathrm{mm}$ $y = 1\,\mathrm{mm}$	heater between finns
5	**AC**	$\alpha \approx 0.9$	Expansion to standard heater area
6	**D**	$L = 7\,\mathrm{mm}$ $y = 1\,\mathrm{mm}$	heater between finns
7	**AC**	$\alpha \approx 0.97$	heater to TA stack

Table B.1: Geometrical parameters of the network representation of the cold heater. **AC** denotes area changes. **D** stands for viscous duct elements.

Figure B.3 displays the scattering matrices of a measured scattering matrix of the ambient heater (black dots) and the corresponding reconstruction model (red lines). The latter is corrected by a duct model representing the missing heater and regenerator in the measurement. The transmission coefficients match for a wide region. Due to the small amplitude values, the measured reflection coefficient data are not trustworthy.

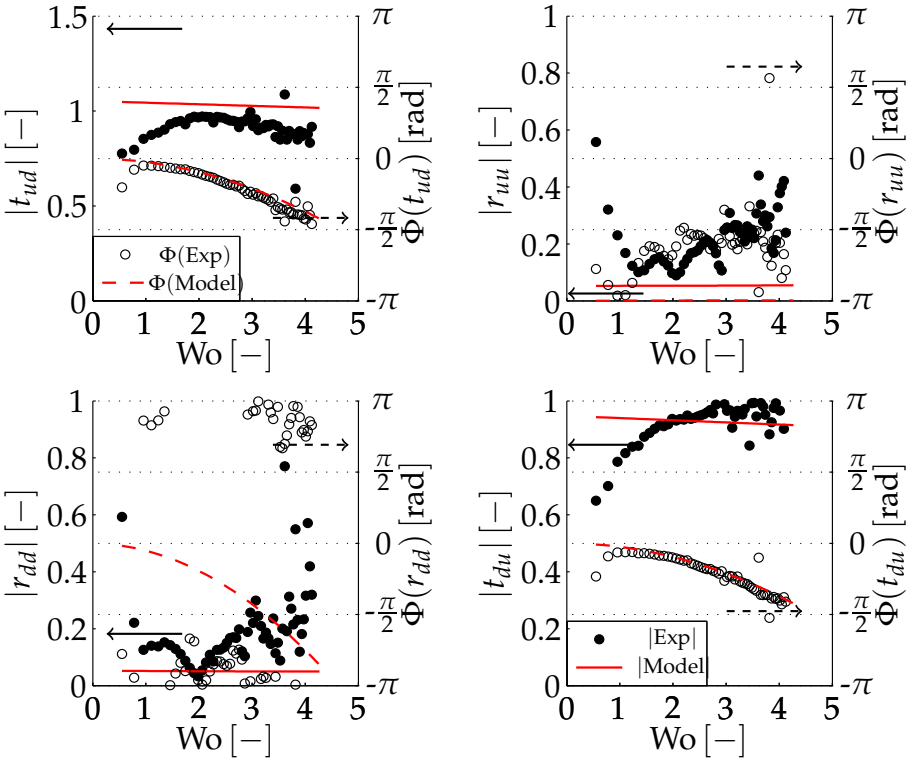

Figure B.3: Experimental data vs. model data of the cold heater. The model data is corrected by a duct representing the lengths of the missing heater and regenerator.

Hot Downstream heater

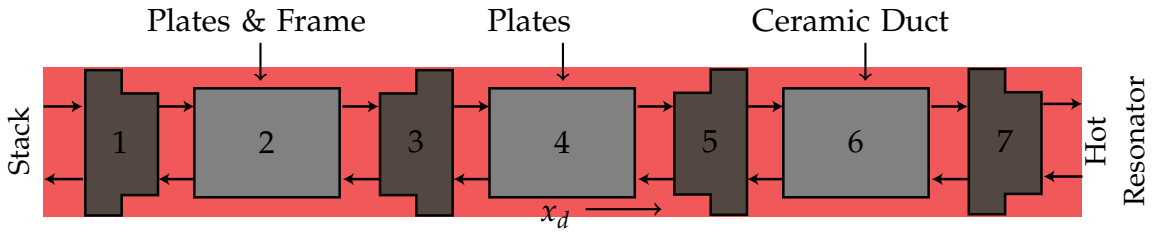

Figure B.4: Network representation of the Hot heater. The inner area changes account for Area chnges due to the frames and difference in length between the heating plates and distance between the frames.

The TA regenerator is partially inserted into the ceramic frame of the downstream heater. Figure B.4 displays the the approximated combination of acoustic two-port elements modeling the acoustic transmission of the heater. It is represented by four area changes connected by viscous duct elements. The first accounts for the change from TA stack to the heat exchanger. The heating part containing the metal foils is followed by a cross-section equivalent to the the ceramic frame. This element is followed by the second heater frame. Furthermore, an additional ceramic duct part needs to be considered. The same argument that is stated for the cold heater also good holds for neglecting thermal changes in this component. Table B.2 lists the characteristic parameters of the acoustic elements.

The models of both heat exchangers are similar. So is their scattering behavior, Thus a validation of the scattering matrices of the heater model is not presented here.

Item	Type	Data	Description
1	**AC**	$\alpha \approx 0.73$	From TA stack to heater
2	**D**	$L = 20\,\text{mm}$ $y = 7\,\text{mm}$	Heater between foils
3	**AC**	$\alpha \approx 1.55$	Contraction to ceramic frame
4	**D**	$L = 3\,\text{mm}$ $y = 22.5\,\text{mm}$	Heater frame
5	**AC**	$\alpha \approx 0.65$	Expansion to ceramic duct area
6	**D**	$L = 2\,\text{mm}$ $y = 27.5\,\text{mm}$	Ceramic duct
7	**AC**	$\alpha \approx 1.13$	Contraction to resonator duct area

Table B.2: Geometrical parameters of the network model representing the heater. **AC** denotes area changes. **D** stands for viscous duct elements.